Development of an Uncertainty Quantification methodology for Multi-Physics Best Estimate analysis and application to the Rod Ejection Accident in a Pressurized Water Reactor

Gregory Delipei

université PARIS-SACLAY

ÉCOLE POLYTECHNIQUE
UNIVERSITÉ PARIS-SACLAY

NNT : 2019SACLX078

Thèse de doctorat

Développement d'une méthodologie de Quantification d'Incertitudes pour une analyse Mutli-Physique Best Estimate et application sur un Accident d'Éjection de Grappe dans un Réacteur à Eau Pressurisée

Thèse de doctorat de l'Université Paris-Saclay
préparée à Ecole Polytechnique

Ecole doctorale n°573 Interfaces: Approches Interdisciplinaires / Fondements, Applications et Innovation (INTERFACES)
Spécialité de doctorat : Mathématiques appliquées

Thèse présentée et soutenue à Saclay, le 04/10/2019, par

GREGORY KYRIAKOS DELIPEI

Composition du Jury :

Emmanuel GOBET Professeur, École Polytechnique (CMAP)	Président
Bertrand IOOSS Ingénieur de Recherche, Electricité de France (Research and Development Division)	Rapporteur
Kostadin IVANOV Professeur, North Carolina State University (Burlington Laboratory)	Rapporteur
Herve MONOD Directeur de Recherche, Institut National de la Recherche Agronomique	Examinateur
Clementine PRIEUR Professeur, Université Grenoble Alpes	Examinateur
Mathieu SEGOND Ingénieur de Recherche, Framatome	Examinateur
Josselin GARNIER Professeur, École Polytechnique (CMAP)	Directeur de thèse
Jean-Charles Le Pallec Ingénieur de Recherche, CEA	Co-Encadrant de thèse
Benoit Normand Ingénieur de Recherche, CEA	Co-Encadrant de thèse

Acknowledgments

First and foremost, I would like to express my gratitude and deepest appreciation to my thesis Director Josselin Garnier and my supervisors at CEA Jean-Charles Le Pallec and Benoit Normand. With their guidance, support and patience during these three years, they were not only the catalyst for the completion of this thesis but also a driving force for me to invest and dive deep into the subject. I feel very lucky and I hope that we will have the chance to collaborate again in the future.

I would like to express my sincere gratitude to all the members of my thesis jury: the president E. Gobet and the examiners H. Monod, C. Prieur and M. Segond. Additionally, I am very thankful to my two reviewers B. Iooss and K. Ivanov for their instructive corrections and comments that helped improve significantly the quality of this work.

This thesis could not have been completed without the contributions at both scientific and personal level of C. Patricot, J-M. Martinez, E. Royer and A. Boulore. They were following the thesis from its beginning to its end and formed a working group for which I could not feel more proud to be a part of. Their excellent scientific background brought on the table significant insights on all the aspects of the thesis and they helped me to deal with the strong multidisciplinary needs of my thesis. Additionally, I would like to thank also K. Ammar and A. Calloo for spending a significant amount of their time for suggestions and corrections during the thesis even if they were not directly involved.

I am very thankful to all the people in SERMA for creating a wonderful working environment. I would like to thank the SERMA/LPEC laboratory directors during this thesis: F. Damian and C. Guenaut that were always very helpful and understanding. I would like to thank also the friends and colleagues in SERMA that through daily discussions contributed their significant part in this thesis. From unofficial corrections, suggestions and advises to relaxing discussion about all aspects of the PhD life. From all of them, I namely thank Dominic, Paolo, Esteban and Vito. I am deeply thankful also to my friends outside of the laboratory and more particularly Christonikos, Revekka, Apostolis and Nikos for their constant support during this long journey.

I am eternally grateful to the person for whom I was the most burden and I really do not know at moments how she withstood me: my partner at life Nikoleta. Her help at all levels can not be measured and I feel very lucky and proud to have her next to me. In a world of increasing uncertainty she is where I find my certainty.

Finally, my parents and my brother are the last pillar and cornerstone during not only these three years, but all my life. Their constant support during good and rough times and their naive optimism for my future is everything.

ἕν οἶδα, ὅτι οὐδέν οἶδα

Socrates

List of Abbreviations

ALARA	As Low As Reasonable
ANN	Artificial Neural Network
ANOVA	Analysis of Variance
BE	Best Estimate
BEPU	Best Estimate Plus Uncertainties
BLUE	Best Linear Unbiased Estimator
CDF	Cumulative distribution function
CHF	Critical Heat Flux
CLT	Central Limit Theorem
DNB	Departure from Nucleate Boiling
DNBR	Departure from Nucleate Boiling Ratio
DOE	Design of Experiments
ESE	Enhanced Stochastic Evolutionary
GLM	Generalized Linear Model
HSIC	Hilbert-Schmidt Independence Criterion
HZP	Hot Zero Power
IBE	Improved Best Estimate
IDRM	Input Dimension Reduction Method
LHS	Latin Hypercube Sampling
LOCA	Loss of Coolant Accident
LOO	Leave One Out
MLE	Maximum Likelihood Estimation
MST	Minimum Spanning Tree
OAT	Once At a Time
PC	Pearson Coefficient
PCA	Principal Components Analysis
PCC	Partial Correlation Coefficient

PCE	Polynomial Chaos Expansion
PCMI	Pellet Cladding Mechanical Interaction
pdf	Probability density function
PIRT	Phenomena Identification and Ranking Table
PLS	Partial Least Squares
PRCC	Partial Rank Correlation Coefficient
PWR	Pressurized Water Reactor
REA	Rod Ejection Accident
RKHS	Reproducing Kernel Hilbert-Schmidt
SA	Simulated Annealing
SC	Spearman Coefficient
SCRAM	Safety Control Rod Axe Man
SRC	Standardized Regression Coefficient
SRRC	Standardized Rank Regression Coefficient
UAM	Uncertainty Analysis Modeling benchmark
UQM	Uncertainty Quantification Methodology

Contents

List of Figures

List of Tables

Introduction

The conceptual evolution of nuclear reactors for power generation is fundamentally linked with safety preservation of individuals, society and environment. The main safety objectives is to ensure that the radiological exposure during normal operation is as low as reasonably achievable (ALARA concept) and is mitigated in case of accidents. The basic principle for attaining this objective is the defense in depth, where different levels of protection are introduced including successive safety barriers. The integrity of the barriers is ensured by some safety criteria based on physical quantities.

Since severe accidents cannot be reproduced in a reactor, numerical codes are used to model the main underlying physical phenomena with reasonable approximations and hypothesis. The computational advancements of the last decades lead to the development of modelings that take into account the most important phenomena improving the understanding of the underlying physics and increasing the precision of their predictions. These modelings and the associated numerical codes are called Best-Estimate (BE) and are used in industrial applications since they have an affordable computational cost.

While the precision of the results improve there are still many approximations and hypothesis in the calculations that induce errors in forms of bias and variance. It became thus obvious that in order to be confident about the safety analyses these errors or uncertainties must be treated in a consistent framework with BE modeling. This framework is called Best Estimate Plus Uncertainties (BEPU) and is currently a field of increasing research internationally. While this concept was initially used for thermal-hydraulics safety calculations of LOCA transients it is being expanded in a broader spectrum of physics and for different reactor conditions. The Rod Ejection Accident (REA) in Pressurized Water Reactors (PWR) is a design basis multi-physics transient for which a BEPU is carried out in this thesis.

REA transients occur in a PWR reactor when a control rod is violently ejected from the core due to mechanical malfunction. This inserts positive reactivity in the core and the power starts increasing followed by a fuel temperature increase. This leads to a Doppler negative feedback that creates a power peak. The power then continues to decrease and when the heat generated in the core reaches the coolant a second negative feedback from the moderator is added reducing even further the power. During the whole duration of the REA there is the possibility to loose the first safety barrier (cladding). It is evident that a multi-physics coupling of BE codes is necessary in order to capture correctly the strong interactions between neutronics, fuel-thermomechanics and thermal-hydraulics. In order to ensure the safety of the reactor during a REA an uncertainty analysis must be performed focusing on quantities of interest for the safety such as: the fuel temperature, stored enthalpy in the fuel, cladding temperature and Departure from Nucleate Boiling Ratio (DNBR). Many sources of uncertainties are identified in a REA uncertainty analysis. The main ones can be grouped in the following categories :

- Modeling : The theoretical equations describing a phenomenon include some assumptions and simplifications. Besides that, the use of physical models and correlations induce further errors.
- Input data : Physical (e.g. cross-sections) and technological (e.g. geometries) quantities in the physical models and equations are uncertain. Additionally, boundary and initial conditions are also uncertain. Experimental measurements are usually used to quantify the above mentioned sources of uncertainties introducing potential correlations.

– Nodalization : It involves the different steps for solving a specified modeling introducing errors and uncertainties. The phase space of the equations is discretized and the geometry is homogenized. Sometimes a smaller scale geometry is employed inducing scaling effects. Numerical algorithms are used to solve the equations on the selected discretization. These algorithms converge to approximate solutions.

Challenges and objectives

In this thesis we study the multi-physics uncertainty analysis for REA in a PWR core. The BE modeling available in CEA is used with a coupling of APOLLO3 ® (neutronics) and FLICA4 (thermal-hydraulics).

The main objective is to develop an uncertainty quantification methodology for the multi-physics BE modeling of REA. Each coupled physic includes various uncertain inputs and thus the inputs dimension can be potentially very large and with dependencies. Additionally, different outputs of interest must be considered with also potential large dimension (e.g. functional 2D fields) and non-linear behaviors. This creates many challenges accentuated by the fact that the computational cost for a multi-physics BE modeling limits the number of possible code evaluations. A lot of progress has been made so far in the statistical analysis for these kind of problems with application in a variety of fields including dimension reduction, global sensitivity analysis, surrogate modeling and many others.

We select to model different uncertain inputs spanning neutronics, fuel-thermomechanics and thermal-hydraulics. The uncertainty quantification methodology that we will develop must include at least the following steps :

- Input - Output Identification.
- Input Uncertainty Quantification.
- Uncertainty Propagation.
- Global Sensitivity Analysis.

A second objective of the thesis is to improve the BE modeling in terms of its uncertainty representation. A Best Effort coupling scheme for REA analysis is available at CEA. This includes ALCYONE V1.4 code for a detailed modeling of fuel-thermomechanics behavior. However, it has a very high computational cost and its use in uncertainty quantification for REA is prohibitive. One of the main REA modeling differences between BE and Best Effort coupling is the treatment of the gap heat transfer H_{gap}. In FLICA4 a constant value is used as an input of the code while in ALCYONE V1.4 is calculated taking into account the fuel-cladding gap behavior. For improving the BE modeling a methodology for calibrating a simplified analytic H_{gap} model using decoupled ALCYONE V1.4 REA calculations is developed.

Thesis structure

The thesis is divided in 4 Chapters. In Chapter 1 an overview of nuclear reactor physics is provided. Neutronics, fuel-thermomechanics and thermal-hydraulics are discussed from basic notions for each one of them to their modeling options used in the thesis context. An emphasis is given on REA and its different multi-physics aspects. The coupling framework developed at CEA is presented and the two available BE and Best Effort coupling schemes are presented. The Chapter ends with details about BEPU historical evolution, including the different developed methodologies.

In Chapter 2 an overview of the state of the art of statistical tools used for uncertainty analysis is provided. This Chapter covers a large variety of topics :

- Input Uncertainty Quantification.
- Uncertainty Propagation.

- Dimension Reduction.
- Surrogate models.
- Design of Experiments.
- Sensitivity Analysis.
- Model Calibration.

The Chapter ends with some recent works in uncertainty analysis and the use of the different methods in nuclear application.

In Chapter 3 we develop the Uncertainty Quantification Methodology (UQM) on a small scale core (MiniCore) representative of a PWR core. This core cannot allow physical conclusions but it can be used for testing and evaluating the different statistical tools in an environment relatively close to a PWR core. Various modelings are considered starting from separate stand-alone studies in neutronics, thermal-hydraulics and fuel-thermomechanics up to the BE coupling. We use the MiniCore for the development of the H_{gap} model calibration methodology. The H_{gap} model is then introduced in the BE modeling. The UQM is tested on this Improved Best Estimate (IBE) modeling. The Chapter ends with comparisons between the Best Effort and the IBE modelings for the predicted H_{gap} evolution during the REA.

In Chapter 4 we apply the two methodologies developed in Chapter 3 in a large scale PWR core. First, the UQM is applied for the BE modeling. Second, the H_{gap} model calibration methodology is applied and the resulting H_{gap} models are used to establish the IBE modeling. The results of the two methodologies are analyzed and physical conclusions are drawn. The UQM is then applied on the IBE modeling. The Chapter ends with some complementary studies concerning the IBE thermal-hydraulics modeling options in an uncertainty analysis context. The impact on a large variety of outputs up to functional $3D$ fields is investigated.

Finally, the thesis ends with some general conclusions together with some interesting perspectives for future works.

Chapter 1

Context of the thesis

1.1 Introduction

The main objective of the thesis is to develop and apply an Uncertainty Quantification Methodology (UQM) for multi-physics coupling modeling of a Rod Ejection Accident(REA) in a Pressurized Water Reactor (PWR). The REA involves a strong interaction between three different disciplines or 'physics': neutronics, fuel-thermomechanics and thermal-hydraulics. The computational advancements of last decades lead to the development of Best Estimate (BE) codes that take into account the most important phenomena of the underlying physics with a reasonable precision.

The REA occurs in a PWR reactor when a control rod is violently ejected from the core due to mechanical malfunction. A power pulse is created and depending on the core initial conditions it can be very violent and it can damage the reactor. The power initially increases followed by a fuel temperature increase in the core. This creates a negative Doppler feedback and the corresponding power peak. The power then decreases something accentuated by a second negative feedback due to the coolant (water). This happens at a latter stage of the transient when the heat produced in the fuel reaches the coolant increasing its temperature and reducing its density. After around 1-2 seconds the SCRAM[1] safety mechanism injects all the control rods in the core ending the transient. During the whole duration of the REA there is the possibility to loose the first safety barrier (cladding). The correct modeling of these different phenomena and their interactions necessitate the multi-physics coupling of neutronics, fuel-thermomechanics and thermal-hydraulics BE codes. This increases the computational cost and creates many challenges for the uncertainty quantification.

In this Chapter we present the context surrounding the thesis. We start by giving some basic insights about PWR nuclear reactors design in Section 1.2. We describe how PWR function and their main components. Since we study the REA it is important to first introduce the related physics. In Sections 1.3 - 1.5 we detail the neutronics, fuel-thermomechanics and thermal-hydraulics modeling. For all the physics we adopt the same structure:

1. Definition of some basic notions.
2. Description of the theoretical equations.
3. Details about the modeling of the equations.
4. Presentation of the BE codes used to model the equations: APOLLO3 ® (neutronics), ALCYONE V1.4 (fuel-thermomechanics) and FLICA4 (thermal-hydraulics).

In Section 1.7 we combine the presented elements so far to detail the REA with its different multi-physics aspects. In Section 1.7 we discuss the coupling framework used in this thesis to model the REA. In Section 1.8 we take a step back and give an overview of the general Best Estimate Plus Uncertainty (BEPU) framework introducing the aspect of uncertainty quantification. Finally, in Section 1.9 we highlight the main motivations and challenges of this thesis.

1.2 PWR nuclear reactors design

Nuclear reactors are systems in which nuclear fission chain reactions are controlled and sustained. Their applications vary a lot, from submarines propulsion to medical isotopes production but their main application is for energy production in installations called nuclear power plants. The nuclear power plants are similar to conventional power plants where a heat source vaporizes water. The vapor feeds the turbine connected with the generator and electricity is produced. The main difference is that the heat source is provided by fission nuclear chain reactions. Fission is an exothermic reaction occurring when an atom interacts with a neutron and then splits in two fragments releasing energy. Heavy atoms have more probability to undergo fission and a typical example used in nuclear reactors is uranium 235 (U-235). The heavy atoms are located in the fuel region of the reactor's core. The energy released by fission of one atom U-235 is around 203 MeV and is distributed among the fission fragments, beta radiation, gamma photons, antineutrons and neutrons as seen in table 1.1.

[1] Emergency shutdown of the reactor by inserting all the control rods

Table 1.1: U-235 fission reaction energy distribution in MeV

Fission fragments	166
Antineutrinos	10
Prompt gamma photons	8
Beta radiation (electrons)	7
Delayed gamma photons	7
Neutrons	5
Total	**203**

Fission produces in average 2.5 neutrons[2] that in their turn will induce new fissions and thus create nuclear chain reactions. The neutrons are released at high energy whilst the fission reaction is more likely to be induced by neutrons of low energy. For this reason a material called moderator (usually water) surrounds the fuel and its main role is to slow down the neutrons through scattering. The heat produced by fission is extracted from the core with the use of coolant (usually water). The different combinations of fuel-moderator-coolant and core conditions lead to many different concepts of nuclear reactors. From those various concept the most frequently used and the one which we focus on is the PWR. A typical PWR design can be seen in figure 1.1.

The fuel is a composition of uranium 238 and 235 (typically $3-5\%$ of U-235) while the coolant and the moderator are water. The fuel is located in a vessel pressurized at 155bars in order to not have boiling of water. The water driven by the pumps enters from the bottom at an average temperature of $290°C$ and exits from the top at an average temperature of $330°C$. Afterwards, it passes through the steam generator where it transfers energy to water being pressurized at 75bars with a saturation temperature of $290°C$. Steam is produced that is then fed to the turbine-generator system to produce electricity. The pressurizer is a component that controls the pressure in the primary circuit (the reactor core and the loop of the water circulation). All this system is surrounded by a containment building in order to protect the environment in case of a hypothetical accident. A typical electrical power of a PWR is 1300MW with an efficiency of 33% (Rankine cycle).

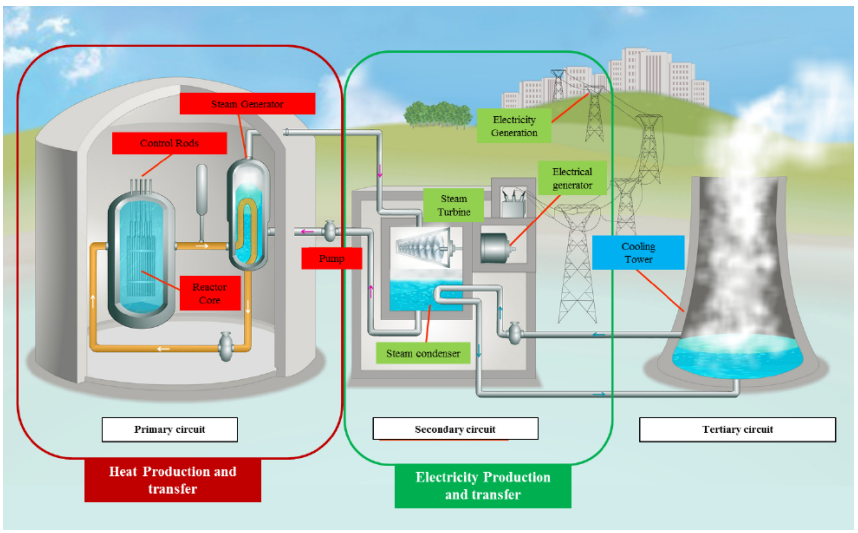

Figure 1.1: Typical PWR design [1].

The reactor's core has three different scales. The fuel pin scale (about 1cm in diameter) is the smallest component and consists of small fuel pellets stacked in long tubes (about 4m long) called fuel pins. The fuel pins have an external region called cladding made from zirconium alloys which is used mainly to avoid radioactive products dispersion in the coolant. There is a gap between fuel and cladding for mechanical reasons that is filled with helium at 10-30bars pressure in order to increase the heat transfer from the fuel to the cladding.

The next scale is the fuel assembly (about 20cm length) where an assembly is a 17x17 array (typical

[2]For U-235 nucleus.

composition) of fuel pins, guide tubes (tubes where the control rods enter) and an instrumental tube as seen in figure 1.2. The fuel assemblies have some structural materials to hold together the fuel pins and they are the parts used to insert or extract fuel from the core. The water circulates in the space between the fuel pins.

The last scale is the core itself (about 4m in diameter) which is usually composed of 193 fuel assemblies and can be seen in figure 1.3. The control rods, consisting of neutron absorbent materials, are inserted in the core from the top and into the guide tubes in order to sustain the fission chain reaction. The positioning of those rods is such as to create a power flux as flat as possible.

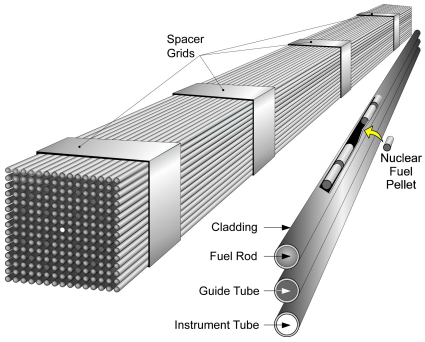

Figure 1.2: PWR fuel assembly and pin [2].

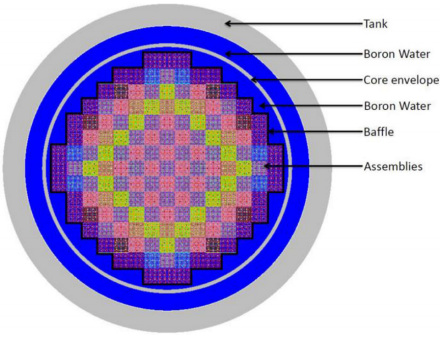

Figure 1.3: Typical PWR core composition [3].

The safety of nuclear reactors is of utmost importance. Three physical safety barriers can be identified in the PWR core, ensuring the confinement of radioactive material [8]. The fuel rod, the pressurized vessel and the containment building. Safety calculations and analyses are used to simulate and predict the behavior of these barriers under both normal and accidental conditions. Such analyses of nuclear reactor's core physics lead to the identification of three different physics. The first one is neutronics related to the power generation, which is proportional to the neutron flux. The second one is fuel-thermomechanics related to the heat diffusion into the fuel pin and its mechanical behavior. The third one is thermal-hydraulics, related to the extraction of heat from the coolant and to the distribution of the coolant in the whole core. The phenomena in each physics are governed by different set of equations that usually are solved by different codes. While for some applications stand-alone physics can be considered, for transients where the interactions between physics can be very strong a multi-physics coupling framework is necessary. An example of such transient is the REA studied in this thesis. Before getting into more details about REA it is important to get some insights about each interacting physic and the codes used for their modeling.

1.3 Neutronics modeling

1.3.1 Basics

The field of neutronics deals with the calculation of the neutrons density in time and space for the whole reactor's core. In order to understand the underlying equations we first present some basic notions of neutron physics based on [9], [4] and [10].

1.3.1.1 Neutron spectrum

The neutrons are produced at two significantly different timescales creating two neutron categories. The first are called prompt neutrons and they are generated at an order of 10^{-14}s mainly from neutron induced fission and spontaneous fission. The second are called delayed neutrons and they are emitted by specific nuclei of the fission fragments, called precursors, at varying timescales from few milliseconds to minutes depending on the precursor. There are more than 200 precursors that usually are grouped in groups of 6-8 with similar average half-lives for modeling purposes. The delayed neutron fraction is the percentage of neutrons emitted as delayed per fission and for U-235 is around 0.6%. The slowing down of neutrons from the high energies at which they are typically emitted to lower energies where the fission is more probable can be seen as a source of

neutrons at different energies. This phenomenon gives rise to the neutron spectrum of figure 1.4 for a PWR. During the slowing down process the neutrons have high probabilities to be absorbed at intermediate energies due to capture resonances that will be detailed later.

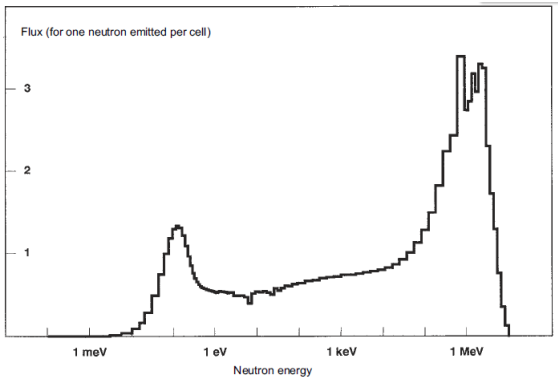

Figure 1.4: Typical neutron spectrum in a PWR [4].

The hump at high energies is the neutrons emitted by fission and follows the Maxwell distribution of equation 1.1 with T around 1.3 MeV. The hump at low energies corresponds to the slowed down neutrons also called thermalized and is usually described by the Maxwell distribution of thermal agitation.

$$\chi(E)dE = \frac{2\pi}{(\pi T)^{\frac{3}{2}}}\sqrt{E}\, exp(-\frac{E}{T})dE \tag{1.1}$$

In neutronic analysis the quantity aimed to be calculated is the angular flux defined in equation 1.2. It is the number of neutrons located in $\vec{r}$, with energy E, moving in a direction of solid angle $\vec{\Omega}$ at instant t where, $n(\vec{r}, E, \vec{\Omega}, t)$ is the neutron density and υ is the neutron velocity.

$$\psi(\vec{r}, E, \vec{\Omega}, t) = n(\vec{r}, E, \vec{\Omega}, t)\upsilon \tag{1.2}$$

The integration of the angular flux for all directions leads to the scalar flux:

$$\phi(\vec{r}, E, t) = \int_{4\pi} \psi(\vec{r}, E, \vec{\Omega}, t)d^2\vec{\Omega} \tag{1.3}$$

1.3.1.2 Cross-sections and reaction rates

Each U-235 fission, as mentioned, produces in average 2.5 neutrons of high energy. During their lives these neutrons will interact with the surrounding materials in many different ways. The microscopic cross-sections represent the probability of the different possible reactions between the neutron and an atom's nucleus and are measured in barns (10^{-24}cm^2). Intuitively it represents the effective surface around the nucleus in which the neutron will interact. The larger is the surface the higher is the probability of the reaction to occur. Microscopic cross-sections depend on the nucleus and the energy of the incident neutron. The main cross-sections concerning a nuclear reactor core are:

- Scattering: After the interaction the nucleus remains as it was. In elastic scattering the neutron only changes angle while in inelastic scattering the neutron loses also energy and a photon is emitted.
- Capture: The nucleus absorb the neutron and decays with photons emission.
- Fission: As described previously, the nucleus splits in two fragments with release of radiation and neutrons.

The macroscopic cross-section for reaction i (Σ_i) is defined in equation 1.4. It can be seen as the probability of a neutron moving in a straight line to interact with a nucleus of the surrounding materials in an infinitesimal distance through reaction i. It is measured in cm^{-1} and its inverse is the neutron mean distance without interaction (mean free path).

$$\Sigma_i(\vec{r}, E, t) = \sigma_i(E) N_k(\vec{r}, t) \tag{1.4}$$

Where:

- $\sigma_i(E)$ is the microscopic cross-section for reaction i.
- $N_k(\vec{r}, t)$ (nuclei/cm^3) is the nucleus k concentration at a specific location and instant.

Since the cross-sections represent probabilities they can be summed giving rise to synthetic microscopic and macroscopic cross-sections. From those the most used are the absorption and total cross-sections. The former is the sum of capture and fission as seen in equations 1.5 - 1.6 and the latter is the sum of all the cross-sections.

$$\sigma_a = \sigma_f + \sigma_c \tag{1.5}$$

$$\Sigma_a = \Sigma_f + \Sigma_c \tag{1.6}$$

Some microscopic cross-sections show regions of resonances around specific energies related to the nucleus excitation levels. This is can be observed in figure 1.5 created with SCALE [11] code using ENDF-VII microscopic cross-sections library [12]. The treatment of those resonances is a fundamental aspect in neutronics modeling.

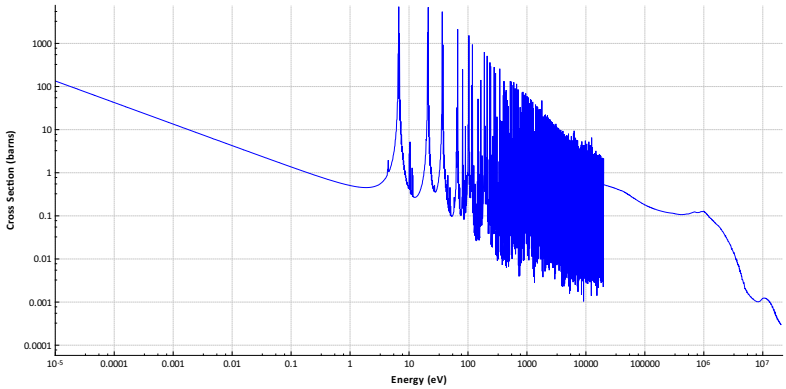

Figure 1.5: U-238 capture microscopic cross-section.

An important quantity related to cross-sections is the reaction rate for reaction i defined in equation 1.7. It is the number of neutron interactions with matter through reaction i per unit volume and time and it is measured in cm^{-3}s^{-1}.

$$\tau_i(\vec{r}, E, t) = \Sigma_i(\vec{r}, E, t) \phi(\vec{r}, E, t) \tag{1.7}$$

1.3.1.3 Criticality and reactivity

The balance of the neutronic population of the reactor is described by the effective multiplication factor k_{eff} defined as the ratio between the production and disappearance of neutrons:

$$k_{eff} = \frac{Production}{Absorption + Leakage}$$

The production of neutrons is due to fission, the absorption is all the possible reactions induced by the neutron that do not create another neutron and the leakage is the neutrons escaping the core without being absorbed. Using the effective multiplication factor we can define three different states of the reactor:

- $k_{eff} = 1$: The reactor is critical and the neutron population is constant.
- $k_{eff} > 1$: The reactor is super-critical and the neutron population increases.

- $k_{eff} < 1$: The reactor is sub-critical and the neutron population decreases.

An important quantity derived from the multiplication factor is the static reactivity defined as:

$$\rho = \frac{k_{eff} - 1}{k_{eff}}$$

It can be seen as a relative comparison between the state of the reactor and its critical state. It is used in neutron kinetics because it is a good measure of modifications in the neutron population. To give an example related to the REA, if the reactor is critical and a control rod is ejected then there is an insertion of positive reactivity. Less absorbent materials are present in the reactor and thus the effective multiplication factor increases. The reactivity is measured in pcm[3] or 10^{-5}.

The reactor's reactivity (ρ) and its effective delayed neutron fraction (β_{eff}) have a major importance in kinetics calculations. The β_{eff} is representing the whole core and is related to its modeling. It can be seen as a sum of the delayed neutron fraction in different regions weighted by the corresponding neutron flux. The importance of ρ and β_{eff} can be highlighted through point kinetics analysis where the reactor is averaged to a point and thus only temporal variations are taken into account. The results of this approach shows that for positive injected reactivity $\rho - \beta_{eff} < 0$ the neutronic population increase is governed by delayed neutrons timescales and thus can be manageable. However, for $\rho - \beta_{eff} > 0$ the neutronic population increase is governed by prompt neutrons leading to rapid power increase. This is called a supercritical prompt driven transient and as we will see it can occur during a REA. A useful expression of the reactivity is as a ratio with the effective delayed neutron fraction ρ/β_{eff} measured in dollars \$.

1.3.1.4 Mechanisms of reactivity change

During the reactor's life variations in reactivity occur. The main physical phenomena inducing these variations are:

- **Fuel composition evolution:** The fissile nuclei are consumed during the reactor operation reducing its reactivity. Some fission products can produce fissile nuclei through their decay chains resulting in a reactivity increase. The sum of these two effects during the reactor's life, in general, has a negative impact on reactivity.

- **Fission poisons:** Fission, either directly or through fission fragments decay, produces nuclei with strong neutron capture cross-section that decrease the reactivity. These nuclei are called fission poisons and the most important ones in PWR are Xe-135 and Sm-149. Particularly Xe-135 is produced directly from fission and from fission fragments decay while it is consumed by neutron induced capture and beta decay. During reactor's shutdown the neutron flux rapidly decreases and Xe-135 increases reaching its peak in 8 hours. For similar reasons in regions where the flux is tilted towards one region, the region with higher flux will exhibit a decrease in Xe-135 while the other region an increase. This initially enhances the flux tilt but after few hours it can reverse it creating spatial oscillations. In PWR this phenomenon can occur axially in the assemblies where the control rods are inserted [13].

- **Reactor's conditions change:** During accidents the materials temperatures and densities can change rapidly and induce reactivity modifications. The most important ones are: the fuel temperature increase resulting in the increase of neutron capture called Doppler effect (detailed in Section 1.3.1.5) and the moderator density decrease and temperature increase. In PWR for safety reasons all these effects must have a negative impact on reactivity.

The reactor during nominal operation is maintained at a critical state. Since the above mentioned phenomena alter the reactivity of the core, different mechanisms are used to counterbalance and control these reactivity variations:

- **Control rods:** They consist of nuclei with high neutron absorption cross-section and they are inserted from the top in the fuel assemblies guide tubes. They are extracted slowly with reactor's life to compensate the decrease in reactivity due to fuel composition evolution.

[3] From french "pour cent mille".

- **Burnable poisons:** Some fuel pins can be replaced by absorbent pins that consist of nuclei with high neutron absorption cross-section that deplete with the reactor's life (usually gadolinium Gd or boron B). They are used for the initial reactivity excess at the reactor start in order to keep the global reactivity effect negative. With time their concentration become negligible.
- **Soluble boron:** Quantities of boric acid (neutron absorbent) are dissolved in the coolant. It has a more uniform and precise impact in the core than the control rods but is limited by the safety requirement to maintain a negative density reactivity effect in the coolant. It is used in conjunction with control rods for slow reactivity variations.

1.3.1.5 Doppler effect

The microscopic cross-sections at T=0K can be represented by analytic expressions on a continuous energy range. These cross-sections thus assume the target nucleus to be immobile but in reality the nucleus is always in thermal agitation due to its real temperature. This agitation affects the relative velocity between the nucleus and the neutron which in its turn affects the microscopic cross-section. While the effect for most nuclei and energy ranges is negligible, for heavy nuclei and in the region of resonances the effect is very important and must be taken into account. This phenomenon is called Doppler effect and it tends to decrease the amplitude and increase the width of the resonance.

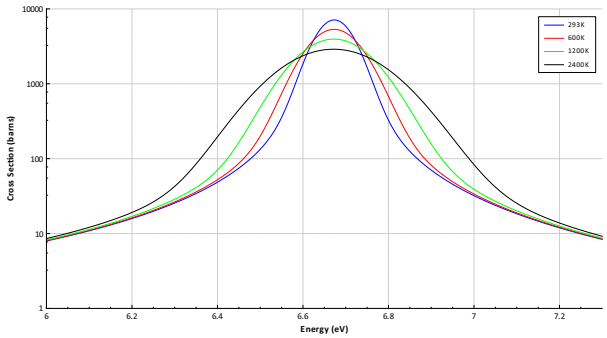

Figure 1.6: Doppler effect on U-238 capture resonance at 6.67eV

The widening of the resonance is more important than the decrease in amplitude and thus the resulting effect is an increase of the interactions. The modeling of this effect is called Doppler broadening of the microscopic cross-sections. In a PWR the Doppler effect is more prominent in the capture cross-section of U-238 as can be seen in figure 1.6[4]. This effect is crucial during transients where a sharp power increase is followed by a fuel temperature increase. The Doppler effect then will act as a feedback by injecting negative reactivity and moderating the transient.

1.3.2 Transport and evolution equations

The field of neutronics, as mentioned, deals with the calculation of the neutrons density in time and space for the whole reactor's core. There are two types of coupled fundamental equations describing the neutrons density spatial and temporal evolution. They are going to be presented based on [9].

1. Transport (Boltzmann) integro-differential equation describing the balance between the production and disappearance of neutrons. The solution of the equation is the neutronic angular flux $\psi(\vec{r}, E, \vec{\Omega}, t)$. It can also be expressed in an integral form.
2. Generalized evolution (Bateman) equations describing the isotopic evolution in the core during its whole life. The solutions of the equations are the nuclei concentrations $N_k(\vec{r}, t)$. A simplification of these equations are used in transient calculations where only the precursors concentrations are taken into account. In these calculations it is assumed that due to the small time period considered the isotopic state does not change [14].

[4]Created with SCALE using ENDF-VII library.

The transport integro-differential equation is established in an elementary volume $D = d\vec{r}\,dE\,d\vec{\Omega}$ around the point $P = (\vec{r}, E, \vec{\Omega})$.

$$\begin{aligned}\frac{1}{v}\frac{\partial\psi(\vec{r},E,\vec{\Omega},t)}{\partial t} =& -\vec{\Omega}\nabla\psi(\vec{r},E,\vec{\Omega},t)\\ &-\sum_k\Big(N_k(\vec{r},t)\sigma_{t,_k}(E)\psi(\vec{r},E,\vec{\Omega},t)\Big)\\ &+\sum_k\left(N_k(\vec{r},t)\int_0^\infty dE'\int_{4\pi}\sigma_{s,k}(E'\to E,\vec{\Omega}'\to\vec{\Omega})\psi(\vec{r},E',\vec{\Omega}',t)d\vec{\Omega}'\right)\\ &+\frac{1}{4\pi}\sum_k\left(N_k(\vec{r},t)\int_0^\infty\nu_{p,k}(E')\sigma_{f,k}(E')\chi_{p,k}(E'\to E)\phi(\vec{r},E',t)dE'\right)\\ &+\frac{1}{4\pi}\sum_k\nu_{p,f,k}\lambda_{f,k}N_k(\vec{r},t)\chi_{p,f,k}(E)\\ &+\frac{1}{4\pi}\sum_k\lambda_{d,k}N_k(\vec{r},t)\chi_{d,k}(E)\\ &+S_{ext}(\vec{r},E,\vec{\Omega},t)\end{aligned} \tag{1.8}$$

- The first term on the left side is the derivative of the angular flux variation with respect to time.
- The first term on the right side is neutrons escaping D through its boundaries (leakage).
- The second term on the right is the disappearance of neutrons due to either absorption or scattering to a different state (E, Ω) through nucleus k. $N_k(\vec{r}, t)$ is the nucleus concentration and $\sigma_{t,_k}$ the total microscopic cross-section of nucleus k for an incident neutron of energy E.
- The third term on the right side is the neutrons reaching the state (E, Ω) due to scattering from all the other angles and energies. The transfer microscopic cross-section $\sigma_{s,k}(E' \to E, \vec{\Omega}' \to \vec{\Omega})$ represents this probability for nucleus k.
- The fourth and fifth terms on the right are the production of prompt neutrons from fission reactions induced by neutrons and by spontaneous fission of nucleus k. The average number of prompt neutrons emitted by fission of nucleus k for an incident neutron of energy E' is $\nu_{p,k}$. Additionally, $\sigma_{f,k}(E')$ is the corresponding fission microscopic cross-section and $\chi_{p,k}(E' \to E)$ the emitted neutron spectrum. The average prompt neutrons emitted from spontaneous fission of nucleus k is $\nu_{p,f,k}$ with $\lambda_{f,k}$ the fission decay constant and $\chi_{p,f,k}$ the emitted neutrons spectrum.
- The sixth term on the right is the production of delayed neutrons due to decay of precursors, where $\lambda_{d,k}$ is their decay constant and $\chi_{d,k}$ the delayed neutrons fission spectrum.
- The seventh and last term on the right accounts for all the possible external neutron sources present in D.

As in the case of neutrons in transport equation the evolution equations are a balance between production and disappearance of the different nuclei $N_k(\vec{r}, t)$.

$$\begin{aligned}\frac{dN_k(\vec{r},t)}{dt} =& +\sum_{m\neq k}\left(\sum_q\int_0^\infty\sigma_{q,k\leftarrow m}(E)\phi(\vec{r},E,t)dE\right)N_m(\vec{r},t)+\sum_{m\neq k}\lambda_{m\to k}N_m(\vec{r},t)\\ &-\lambda_kN_k(\vec{r},t)-\left(\sum_q\int_0^\infty\sigma_{q,k}(E)\phi(\vec{r},E,t)dE\right)N_k(\vec{r},t)\end{aligned} \tag{1.9}$$

- The first term on the left is the rate of change in time of the nucleus k concentration.
- The first term on the right is the production of nucleus k by nuclear reaction q on nucleus m induced by an incident neutron of energy E. The corresponding microscopic cross-section is $\sigma_{q,k\leftarrow m}$.

- The second term on the right is the production of nucleus k due to decay of nucleus m, with $\lambda_{m\to k}$ its corresponding decay constant.

- The third term on the right is the disappearance of nucleus k due to decay with λ_k its decay constant.

- The fourth and last term on the right is the disappearance of nucleus k through nuclear reaction q induced by a neutron of energy E. The corresponding microscopic cross-section is $\sigma_{q,k}$.

The derivation of the equations includes some basic assumptions:

1. The neutrons population in the reactor is sufficient large in order to be able to define the neutron's density. In a typical reactor the order of magnitude of the neutron's population is 10^8 neutrons/cm^3 satisfying this hypothesis.

2. The neutron-neutron interactions are negligible in comparison to the neutron - materials interaction in the reactor. This essentially means that the neutrons density is orders of magnitudes smaller than the density of the materials in the reactor and thus the probability for the neutron to interact with an atom of the materials is orders of magnitude higher than to interact with another neutron. This hypothesis leads to the linear form of the transport equation.

3. The relativistic effects of neutrons are negligible. In fact the maximum kinetic energy of the neutrons in a reactor is about 2MeV and thus satisfies this hypothesis.

4. The neutrons decay to protons is negligible. The decay period of this reaction is in the order of 10 minutes while the neutrons average life time in the reactor is $10^{-5} - 10^{-3}$s satisfying this hypothesis.

5. The gravity effect is neglected (straight paths for particles).

There are two broad methods for the solution of the equations: the Monte Carlo and the deterministic. In the Monte Carlo the equations are not solved directly but through simulations of random walks of neutrons. Each possible neutron event is sampled through distributions from the moment it appears until its absorption. With the simulation of large number N of neutrons paths their density population converges to the solution with a rate of $\frac{1}{\sqrt{N}}$. In the deterministic approach the equations are solved by phase space discretization introducing further approximations. In this thesis we use the deterministic neutronic code APOLLO3®. For this reason in the following Section we focus on the deterministic approach and the different modeling options relevant to APOLLO3®.

1.3.3 Deterministic modeling

The deterministic approach consists in discretizing the phase space of the equations [13], [15]. The combined discretized meshes needed for the space (core volume), the solid angle (sphere of surface 4π), the energy ($1e^{-2}eV - 2e^{+6}eV$) and the time is more than 10^{16} meshes. This discretization size is far too large for the computational power currently available. To this purpose a three step approach is adopted. Before detailing each phase space discretization we will describe the general aspects of the different steps presented in figure 1.7.

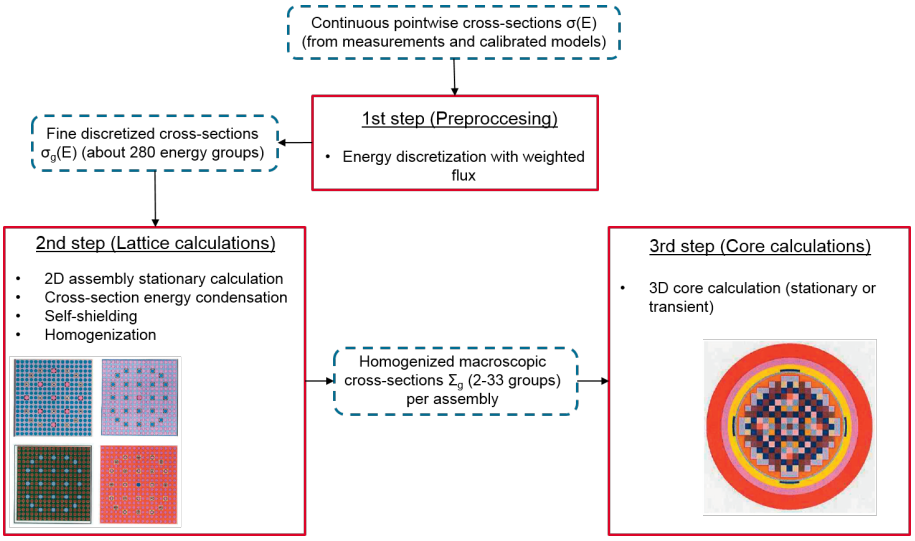

Figure 1.7: Three step deterministic neutronics calculation scheme.

In the first step the microscopic cross-sections are condensed from continuous pointwise to a multi-group discrete energy mesh (about 280 energy groups) based on typical neutron spectrum.

In the second step the so called "lattice" calculations are performed. They are usually horizontal 2D assembly calculations on the previous discretized energetic mesh. These calculations are performed for each assembly of the core with an infinite medium hypothesis and leakage adjustment. The result of the calculations are condensed in energy and homogenized in space cross-sections that preserve the reaction rates. It is important to notice that during this process self-shielding is performed in order to take into account the flux reduction in the resonances peaks of the cross-sections that will reduce the reaction rates as well. This step is performed for different core isotopic states resulting from the solution of the evolution equations and for various core conditions (fuel temperature, moderator temperature, etc.) [14]. The typical result of the second step is multigroup macroscopic cross-sections of few energy groups (2-33 groups for PWR) for each assembly in a multiparametric tabulation form.

The third step is a full core 3D calculation where each assembly is homogenized and represented by its macroscopic cross-section. The transport equation or an approximation of it is solved (e.g. Diffusion equation). This calculations scheme has some limitations mainly coming from the infinite medium hypothesis in the second step and the different approximated solvers of the 3D transport equation in the third step.

Since in any deterministic calculation the cross-sections are in a multigroup format it is useful to present the multigroup form of the transport equation. If we consider $\mathcal{G}$ energy groups with bounds $[\mathrm{E_g}, \mathrm{E_{g+1}}]$ for $\mathrm{g} \in \mathcal{G}$ the multigroup angular flux of each group is defined as:

$$\psi^g(\vec{r}, \vec{\Omega}, t) = \int_{E_g}^{E_{g+1}} \psi(\vec{r}, E, \vec{\Omega}, t) dE \tag{1.10}$$

The multigroup nuclear data are described by a superscript g and the multigroup approximation of the transport equation can be expressed as:

$$
\begin{aligned}
\frac{1}{v^g}\frac{\partial\psi^g(\vec{r},\vec{\Omega},t)}{\partial t} =& -\vec{\Omega}\nabla\psi^g(\vec{r},\vec{\Omega},t) \\
&-\sum_k\left(N_k(\vec{r},t)\sigma^g_{t,k}\psi^g(\vec{r},\vec{\Omega},t)\right) \\
&+\sum_{g'}\sum_k\left(N_k(\vec{r},t)\int_{4\pi}\sigma^{g'\to g}_{s,k}(\vec{\Omega}'\to\vec{\Omega})\psi^{g'}(\vec{r},\vec{\Omega}',t)d\vec{\Omega}'\right) \\
&+\frac{1}{4\pi}\sum_{g'}\sum_k\left(N_k(\vec{r},t)\nu^{g'}_{p,k}\sigma^{g'}_{f,k}\chi^{g'\to g}_{p,k}\phi^{g'}(\vec{r},t)\right) \\
&+\frac{1}{4\pi}\sum_k\nu_{p,f,k}\lambda_{f,k}N_k(\vec{r},t)\chi^g_{p,f,k} \\
&+\frac{1}{4\pi}\sum_k\lambda_{d,k}N_k(\vec{r},t)\chi^g_{d,k} \\
&+S^g_{ext}(\vec{r},\vec{\Omega},t)
\end{aligned}
\tag{1.11}
$$

Three different types of calculations can be identified based on the treatment of time:

- The stationary calculation, where the time dependent terms of the transport equation are omitted ($\frac{1}{v^g}\frac{\partial\psi^g(\vec{r},\vec{\Omega},t)}{\partial t}$, $\frac{1}{4\pi}\sum_k\nu_{p,f,k}\lambda_{f,k}N_k(\vec{r},t)\chi^g_{p,f,k}$, $\frac{1}{4\pi}\sum_k\lambda_{d,k}N_k(\vec{r},t)\chi^g_{d,k}$).
- The so called Burn-up calculations, where the isotopic evolution of the materials (Bateman equations) are calculated during the whole life of the reactor while the power does not vary much (load of the power plant).
- The transient calculations, in short time scales where strong variations of important quantities can occur. For these calculations the initial state of the reactor prior to the transient is calculated by Burn-up calculations and then the kinetic equations are used.

In the following Sections we are going to detail the phase space discretization for the deterministic modeling of transport equation and the different types of calculations related to the time parameter concerning the thesis.

1.3.3.1 Energy discretization

The first two steps in the deterministic approach handle the energy discretization in order to produce multigroup cross-sections. It is quite challenging due to the large energy bounds (from meV to MeV) and to the complicated behavior of the microscopic cross-sections in different energetic regions with the presence of sharp resonances. A big effort is made across the world to create nuclear data libraries based on measurements. These libraries store microscopic cross-sections parameters for a large variety of isotopes and permit their pointwise reconstruction in the whole energy domain. Besides that, they also store neutronic kinetic parameters, fission yields (fission fragments probability), radioactive decay constants, quantities for other particles interaction with matter and uncertainties. More details can be found in [12] and [16]. Some of the most currently used nuclear data libraries are:

- ENDF/B-VII.1: United States Evaluated Nuclear Data Library.
- JEFF-3.2: Joint Evaluated Fission and Fusion File.
- JENDL-4.0: Japanese Evaluated Nuclear Data Library.
- BROND-2.2: Russia Evaluated Nuclear Data Library.
- CENDL-3.1: Chinese Evaluated Nuclear Data Library.

The pointwise reconstruction of the cross-sections is carried out using various nuclear formalisms based on "R matrix" [17]. The most used formalisms are the single or multilevel Breit-Wigner and the Reich-Moore. The obtained cross-sections are at T=0K and the Doppler broadening is applied

in order to calculate the pointwise cross-sections at different temperatures of interest. These cross-sections can be used directly in Monte Carlo codes but for deterministic ones an initial cross-section preprocessing is necessary. This is the 1st step of the deterministic approach where the goal is to condense the cross-section from pointwise to few hundred groups selected in an optimum way to include the most important resonances. The pointwise-multigroup cross-section comparison can be seen for two resonances of U-238 capture in figure 1.8 plotted with SCALE. This step is performed once per type of reactor under study.

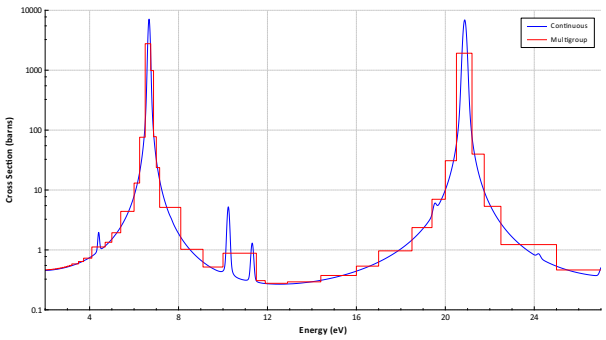

Figure 1.8: U-238 capture multigroup microscopic cross-section

The condensation in energy group g, for nucleus k and reaction i is performed by a weighting of the pointwise cross-section with the pointwise neutron flux of equation 1.12. Since the flux cannot be known prior to solving the transport equation, a "representative" in a macroscopic sense neutron spectrum (e.g. Maxwellian) $\phi_M(E)$ is used. Examples of codes that are used for this purpose are NJOY, CALENDF, AMPX and PREPRO. The codes provide also finer, in terms of energy discretization, cross-section information that will be used in the self shielding process of the second step. The results are stored in a multigroup library.

$$\sigma_{i,k}^{g} = \frac{\int_g \sigma_{i,k}(E)\phi_M(E)dE}{\int_g \phi_M(E)dE} \tag{1.12}$$

The second step, as mentioned, consists in a further condensation of the cross-sections in energy and an homogenization in space. It is a case depended calculation[5] at an assembly level with an infinite medium hypothesis (reflective boundary conditions). It aims at conserving the reaction rates between the initial heterogenous assembly geometry and the resulting homogenous one. The different stages of this calculation are well describted in [18] and can be summarized as:

1. **Self shielding:** It is a phenomenon with both energy and space aspects. The flux in the resonances of the cross-sections exhibits a strong decrease that must be modeled in order to obtain correct reaction rates and not overestimate them. Besides that, spatially some fuel regions can see more neutrons and thus have large differences in flux. The energy aspect is treated through the finer cross-section information stored in the first step while the spatial aspect by considering different concentric fuel regions. This process is applied for specific resonant nuclei and the result is an adjustment of their microscopic cross-section to take into account the local depression of the neutrons flux.

2. **Condensation:** The transport equation is solved at the finer multigroup level. The flux obtained is used to further condensate the microscopic cross-section to few groups. If the index g corresponds to the initial fine energy structure and index G to the condensed one the condensation is expressed by equation 1.13 where i is the reaction and k the nucleus.

$$\sigma_{i,k}^{G} = \frac{\sum_g \sigma_{i,k}^{g}\phi^{g}}{\sum_g \phi^{g}} \tag{1.13}$$

3. **Homogenization:** The assembly is homogenized both spatially and isotopically either in the whole assembly or in subregions by preserving important quantities of interest. There is

[5] It has to be performed for each different reactor modeling

the possibility to treat some isotopes of interest separately, typically this is done for poison isotopes (Xe, Sm). The desired quantities to be preserved are the reaction rates in the homogenization region and the flux currents at the boundaries. Different approaches exist to derive the homogenized macroscopic cross-sections [13] taking into account discontinuities between assemblies. A rather simplistic approach for illustration purposes is:

$$\Sigma_{i,R}^{G} = \frac{\sum_r \Sigma_{i,r}^{G} \phi_r^G V_r}{\sum_r \phi_r^G V_r} \tag{1.14}$$

The second step is performed for the different core assemblies, for various assembly isotopic states calculated by solving the evolution equation and for different temperature and density conditions. For each assembly a multiparametric cross-section library is produced that will be used in the third step where the core calculations would be performed. Examples of codes treating the second step lattice calculations are SCALE [11], APOLLO2 [18] and APOLLO3® [19].

The first two steps of the deterministic approach handle mainly the energy discretization with some aspects of space and solid angle through the homogenization phase. In the third step the heterogeneities of the assemblies are lost and they are instead represented by the condensed homogenized macroscopic cross-sections obtained in step 2. These quantities will be used to perform the different deterministic calculations at the core level where the space, solid angle and time discretizations will be addressed.

1.3.3.2 Solid angle discretization

There are different methods used to treat the solid angle discretization $\vec{\Omega}$ for the solution of transport equation in lattice and core calculations [15]. Some of them treat at the same time both solid angle and space.

- **Spherical harmonics (P_N):** The flux angular dependence is expanded in spherical harmonics that are truncated at an order N.
- **Simplified spherical harmonics (SP_n):** In general the P_N equations are quite complicated to solve and thus most of the codes solve a simplified version of them (SP_N). The assumption of locally plane geometry is applied corresponding to a $1D - P_N$ with slow variations in space. The spherical harmonics become now the Legendre polynomials.
- **Diffusion approximation:** It is the method used in this thesis. The transport equation is simplified. The main assumption is that the angular flux does not depend much on the direction $\vec{\Omega}$ and that the flux is mainly from scattering, something not true near sources or sinks.
- **Discrete ordinates (S_N):** The solid angle is discretized in N directions covering the 4π solid angle and approximating the integral by a quadrature.
- **Collision probabilities (P_{ij}):** It is based on the calculations of probabilities for a neutron in one region i to undergo a collision in a different region j. It treats both solid angle and space and solves the integral form of transport equation.
- **Method of Characteristics (MOC):** It treats both space and solid angle. It solves the integral form of transport equation using S_N trajectories on non structured homogeneous meshes [9].

For lattice calculations (2nd step) MOC and P_{ij} are typically used while S_N, SP_N and Diffusion are used in core calculations (3rd step).

1.3.3.3 Space discretization

Space is discretized in meshes of different sizes axially and radially. The way in which the flux and currents are calculated inside the meshes and on the boundaries creates different discretization methods [9]:

- **Finite differences:** It is the classical way used to solve differential equations. The geometry is discretized and the derivatives in the transport equation are approximated by a first order Taylor expansion computed on two neighboring points.
- **Nodal:** It is also called finite volume method and is based on a semi-analytic resolution of the equation in a volume. Usually a polynomial approximation is used for the solution. The solution is obtained first by integrating in each direction (x,y,z) to calculate transverse leakages and then integrating in the whole volume to obtain the integral flux.
- **Finite elements:** It is the method used in the thesis. The geometry is discretized in volumes and the solution is expanded on a polynomials basis of chosen order. The unknowns now are the coefficients of the flux on this basis. The convergence depends on the degree of the basis and the mesh size.

All of the methods are used for core calculations in conjunction with the corresponding solid angle discretization method. Finite differences and Nodal methods are mainly used with Diffusion approximation while Finite elements are used for all the solid angle methods.

1.3.3.4 Stationary calculations

The stationary transport equation is solved for a given core isotopic state and condition. In general the stationary transport equation has solution only when the reactor is at a critical state. In order to obtain solutions for non critical states an unknown variable λ is used:

$$\begin{aligned}\vec{\Omega}\nabla\psi^g(\vec{r},\vec{\Omega}) = &-\sum_k\left(N_k(\vec{r})\sigma_{t,k}^g\psi^g(\vec{r},\vec{\Omega})\right)\\ &+\sum_{g'}\sum_k\left(N_k(\vec{r})\int_{4\pi}\sigma_{s,k}^{g'\to g}(\vec{\Omega}'\to\vec{\Omega})\psi^{g'}(\vec{r},\vec{\Omega}')d\vec{\Omega}'\right)\\ &+\frac{1}{\lambda}\frac{1}{4\pi}\sum_{g'}\sum_k\left(N_k(\vec{r})\nu_{p,k}^{g'}\sigma_{f,k}^{g'}\chi_{p,k}^{g'\to g}\phi^{g'}(\vec{r})\right)\end{aligned} \tag{1.15}$$

It is an eigenvalue problem with the largest eigenvalue equal to the effective multiplication factor $\lambda = k_{eff}$. The corresponding eigenfunction is the angular flux solution. For convenience purposes the steady-state transport equation can be written in a form of operators:

$$T\phi = \frac{1}{\lambda}F\phi \tag{1.16}$$

Where:

- T is a disappearance multigroup operator.
- F is the multigroup production operator.

This eigenvalue problem is solved through power iterations [20] as described in the following algorithm.

Power iterations algorithm

1: Initialize λ^0, ϕ^0, and convergence criteria $\epsilon_\lambda, \epsilon_\phi$ and $n = 1$
2: **while** $(\lambda^{(n)} - \lambda^{(n-1)} > \epsilon_\lambda)$ & $(\|\phi^{(n)} - \phi^{(n-1)}\| > \epsilon_\phi)$ **do**
3: Compute angular flux: $T\phi^{(n)} = \frac{1}{\lambda^{(n-1)}}F\phi^{(n-1)}$.
4: Compute $\frac{\lambda^{(n)}}{\lambda^{(n-1)}} = \frac{\|F\phi^{(n)}\|}{\|F\phi^{(n-1)}\|}$.
5: $n = n + 1$
6: **end while**

1.3.3.5 Burn-up calculations

Nuclei isotopic compositions change with time during the reactor's life due to transmutations by nuclear reactions and due to radioactive decay. A quantity describing the historical usage of the fuel is the Burn-up measured in MWd/t[6]. The concentrations of nuclei thus vary in space and time

[6] Megawatt days per ton of fuel nuclei.

following the evolution equations 1.9. The equations for different isotopes can be lumped into the following matrix notation for a time step Δt:

$$\frac{\Delta N}{\Delta t} = S + AN \tag{1.17}$$

Where S is a direct source term while A is the matrix representing the nuclear reactions and decay. If the flux solution during the whole reactor history is known at different time steps a Runge-Kutta numerical scheme can be used to solve the equations. This is not usually the case since the evolutions equations are coupled with the transport equation. In this case, a sequential approach is adopted where the solution of the flux at time step n is used to compute the new concentrations at time step $n+1$ that will update the transport equation. Predictor-corrector techniques can be used to anticipate the flux variation in the interval.

1.3.3.6 Transient calculations

Transient calculations aim to describe the reactor's behavior under accidental situations where for a short period of time large flux variations can occur. For these short time periods the Burn-up evolutions of the nuclei are not considered, only the precursors are taken into account due to their important role in the delayed neutron production. The precursors are grouped in 6-8 groups of similar disintegration periods ranging from 50μs to 50s. The multigroup transport equation and the precursors evolution equations are expressed in equations 1.18a and 1.18b respectively.

$$\begin{aligned}
\frac{1}{\upsilon^g}\frac{\partial \psi^g(\vec{r},\vec{\Omega},t)}{\partial t} =& -\vec{\Omega}\nabla\psi^g(\vec{r},\vec{\Omega},t) \\
&- \sum_k \left(N_k(\vec{r},t)\sigma^g_{t,k}\psi^g(\vec{r},\vec{\Omega},t)\right) \\
&+ \sum_{g'}\sum_k \left(N_k(\vec{r},t)\int_{4\pi}\sigma^{g'\to g}_{s,k}(\vec{\Omega}'\to\vec{\Omega})\psi^{g'}(\vec{r},\vec{\Omega}',t)d\vec{\Omega}'\right) \\
&+ \frac{1}{4\pi}\sum_{g'}\sum_k \left(N_k(\vec{r},t)\nu^{g'}_{p,k}\sigma^{g'}_{f,k}\chi^{g'\to g}_{p,k}\phi^{g'}(\vec{r},t)\right) \\
&+ \frac{1}{4\pi}\sum_k \nu_{p,f,k}\lambda_{f,k}N_k(\vec{r},t)\chi^g_{p,f,k} \\
&+ \frac{1}{4\pi}\sum_k \lambda_{d,i}C_i(\vec{r},t)\chi^g_{d,i}
\end{aligned} \tag{1.18a}$$

$$\frac{dC_i(\vec{r},t)}{dt} = +\sum_k \left(N_k(\vec{r},t)\beta^k_i\sum_{g'}\nu^{g'}_{t,k}\sigma^{g'}_{f,k}\phi^{g'}(\vec{r},t)\right) - \lambda_i C_i(\vec{r},t) \tag{1.18b}$$

Where:

- C_i is each precursor group concentration.
- β^k_i the precursors delayed neutron fraction.
- λ_i the precursors decay constant.

The solution of these equations is performed in the third step of the deterministic resolution method. In the second step together with the homogenized macroscopic cross-section for each assembly of the reactor the kinetic quantities are also homogenized in effective quantities representing the heterogeneities of the assembly. This leads to the effective delayed neutrons and decay constants.

Two categories of methods for the solution of the above system of equations exist:

- **Neutron flux form - amplitude separation**: The neutron flux $\phi(\vec{r}, E, t)$ space and time variations are decomposed in two functions. Function a that represents rapid amplitude variations in broad discretization regions ($\vec{R}$). Function f that represents mainly slow amplitude variations (T) in the form of the flux. The flux becomes then $\phi(\vec{r}, E, t) = a(\vec{R}, E, t)f(\vec{r}, E, T)$. Depending on the T and $\vec{R}$ size different methods are defined. The most general is the Multi-Fidelity method and corresponds to the use of large discretization regions for $\vec{R}$ and large time steps for T. The Improved Quasi static method follows the amplitude variations in the whole core ($a(t)$) using point kinetics and updates the flux form on large time steps T. The point kinetics method where the flux form is not updated and the core is averaged over energy, space and angle resulting in a simplified set of equations that represent average variations in time of important quantities. With this method local effects are not accessible something very important for transients like REA [1].

- **Direct discretization**: It consist in discretizing the equations 1.18a and 1.18b and is the method used in this thesis. The equations are integrated in time with finite time discretization. Assumptions are made on the form of the variation of parameters inside each time step. The velocities are considered constant while the cross-sections are considered to vary lineary. The flux is discretized using a theta scheme, where depending on the θ value a Crank-Nikolson scheme or implicit scheme can be used. Usually in transient calculation a mix of those two options are used. The Crank-Nikolson is used in the phase of the power increase and the implicit scheme when the power decreases. The precursors equation 1.18b is formally integrated by considering linear flux variation in the time step. The spatial behavior of the flux is projected on a basis of finite elements. The integration now is possible for each time step and the solution is obtained by solving a linear system of size $N \times G$, where N the number of points in the finite elements and G the number of energy groups.

1.3.3.7 Boundary conditions

For the solution of the equations boundary conditions must be imposed. In neutronics deterministic modeling the angular flux is described at the boundaries of the studied geometry. Assuming a domain $V \in \mathbb{R}^3$ and its boundary $S = \partial V$ the angular flux of on the boundary is $\psi(\vec{r_s}, E, \vec{\Omega}, t)$ with $\vec{r_s} \in S$. Considering $\vec{n_e}$ the unit outward normal vector on S the albedo β is defined as :

$$\beta = \frac{\int_{\vec{n_e}\cdot\vec{\Omega}<0} |\vec{\Omega} \cdot \vec{n_e}| \psi(\vec{r_s}, E, \vec{\Omega}, t) d\vec{\Omega}}{\int_{\vec{n_e}\cdot\vec{\Omega}>0} \vec{\Omega} \cdot \vec{n_e} \psi(\vec{r_s}, E, \vec{\Omega}, t) d\vec{\Omega}} \tag{1.19}$$

The albedo is the ratio between the neutrons current entering and exiting through S. Based on this definition three different boundary conditions are defined:

- $\beta = 0$: Void condition where no neutrons are assumed to be reflected in V. It is used mainly for the core calculations.
- $\beta = 1$: Reflective condition where all the neutrons are reflected into V with a solid angle symmetrical to the outgoing. It is used for the lattice calculations representing the infinite medium approach.
- $0 < \beta < 1$: A fraction of the neutrons are reflected. If the solid angle at which they are reflected is uniformly distributed then it is called diffusion condition.

Besides the neutronic boundary conditions there are also thermal and hydraulic conditions that need to be defined. They concern the effective fuel temperature strongly related with the Doppler effect, the moderator density and the moderator temperature. The macroscopic cross-sections are tabulated using these quantities and once they are provided, usually as a result of other codes, the core state can be defined and the equations can be solved. For the moderator density and temperature there is no ambiguity. For the fuel temperature the problem is that its radial distribution inside the fuel pellet is not uniform. The neutronic modeling cannot take this into account since the pellet is homogenized. If the radial temperature is calculated from thermal modeling of the fuel pellet on discretized radial meshes then different expressions exist to compute an effective fuel temperature representing the radial temperature profile. The Rowlands expression is used in this thesis defined by the fuel temperature in the center T_c^f and the external surface of the pellet T_s^f:

$$T_{eff}^{R} = \frac{4}{9}T_{c}^{f} + \frac{5}{9}T_{s}^{f} \tag{1.20}$$

The effective Rowlands temperature T_{eff}^{R} is based on a parabolic profile of the fuel temperature. This is not always true and Santamarina [21] proposed a different expression that is adequate for both parabolic and non-parabolic temperature profiles. More details about both expressions can be found in [22].

1.3.4 APOLLO3® code

The code used for the neutronics modeling in this thesis is APOLLO3® [19] developed at CEA in a common project between CEA, Framatome and EDF. This project concerned the development of state of the art codes for nuclear reactor physics with improved accuracy, flexible architecture and high computation capabilities. APOLLO3® is a deterministic neutronic code that can perform both lattice and core calculations including most of the methods for energy, space, angle and time discretization previously described. It is used for evolution calculations to reach the reactor's initial state prior to the REA and for the transient core calculations. The 3D kinetics method is used with two group Diffusion [23] as described in equations 1.21a and 1.21b. The cross-sections are homogenized at an assembly level using APOLLO2 code [18]. For the space discretization RTN Finite Element of 1st order are used. Void boundary conditions are considered.

$$\begin{aligned}\frac{1}{\upsilon^{g}}\frac{\partial\phi^{g}(\vec{r},t)}{\partial t} &= +\nabla D^{g}\,\vec{\nabla}\,\phi^{g}(\vec{r},t) - \Sigma_{t}^{g}\phi^{g}(\vec{r},t) + \sum_{g'=1}^{2}\Sigma_{s}^{g'\to g}\phi^{g'}(\vec{r},t) \\ &\quad + \chi_{p}^{g}\sum_{g'=1}^{2}(1-\beta^{g'})\nu^{g'}\Sigma_{f}^{g'}\phi^{g'}(\vec{r},t) + \sum_{i=1}^{6}\lambda_{i}\chi_{i,d}^{g}C_{i}(\vec{r},t)\end{aligned} \tag{1.21a}$$

$$\frac{dC_{i}(\vec{r},t)}{dt} = +\sum_{g'=1}^{2}\beta_{i}^{g'}\nu^{g'}\Sigma_{f}^{g'}\phi^{g'}(\vec{r},t) - \lambda_{i}C_{i}(\vec{r},t) \tag{1.21b}$$

Where:

- D^{g}, Σ_{t}^{g} and Σ_{f}^{g} are the diffusion coefficient, the total macroscopic cross-section and the fission macroscopic cross-section for group g.
- $\Sigma_{s}^{g'\to g}$ is the transfer cross-section from group g' to g.
- χ_{p}^{g}, $\nu^{g'}$ and β^{g} are the fission prompt spectrum, the average neutrons emitted through fission and the the total effective delayed neutron fraction for group g.
- A total of 6 precursor groups are considered with C_{i}, λ_{i}, $\chi_{i,d}^{g}$, β_{i}^{g} their concentration, effective decay constant, delayed neutron spectrum and effective delayed neutron fraction. The total effective delayed neutron fraction is obtained by $\beta^{g} = \sum_{i=1}^{6}\beta_{i}^{g}$.

.

1.4 Fuel-thermomechanics modeling

1.4.1 Basics

The power generated in the reactor's fuel rods affects the conditions of the fuel pellets, cladding and the gap between them. In PWR the fuel pellets are made from uranium oxide UO_{2}, the cladding from a zirconium alloy (Zircalloy IV among the different ones) and the gap is filled with helium due to its high thermal conductivity. Thermal, irradiation and chemical phenomena impact both the mechanical aspects of fuel rods (stress and strains) and the head conduction. These phenomena range from the atomic scale to the fuel pellet macroscopic scale. Their modeling is very important for the fuel rod integrity, which is as mentioned the first safety barrier, in both nominal and accidental situations [24]. In this Section we are going to describe some basic fuel-thermomechanical notions and phenomena based on [25] and [5].

1.4.1.1 Fuel pellet behavior

- **Cracking:** With the first power increase a radial temperature gradient induces a differential thermal expansion leading to cracking of the fuel pellet radially and axially. The gap between the fragmented pellet and the cladding reduces enhanced by their thermal expansion. This leads to an increased heat conduction and thus a decrease of fuel temperature in the beginning of the fuel rods life in the reactor. Besides that, the cracks increase the fuel external surface facilitating the release of fission products in the gap affecting the conductivity.

- **Densification:** During the initial irradiation phase ($< 10GWd/t$) the generated fission products interact with the small pores leading to diffusion of vacancies on the grain boundaries. The fabrication porosity is reduced and the fuel density increases about 1% with a corresponding shrinkage of the pellet. This phenomenon slows down the fuel-to-pellet gap closure. Some of the important quantities for densification are: burn-up, fabrication porosity, radial temperature and fission rate.

- **Swelling and gas releases:** The fission products are generated along the irradiation of the fuel. They can be solid or gas and contribute to the increase of fuel volume. This phenomenon is called swelling. In general, the gaseous fission products contribution is much more important than the solid one. The fuel volume evolution after $15GWd/t$ is dominated by swelling.

  Fission gases (e.g. Xe, Sm) precipitate into bubbles in intragranular or intergranular spaces. The also diffuse towards the grain boundaries. The gases generated closer to the fuel surfaces can be released in the free spaces of the rod by athermal diffusion. The gas releases increase constantly with irradiation due to the fission products and fuel surface evolution. This is the main gas release mechanism up to $30GWd/t$. At higher burn-up the gas releases rate accelerates due to the activation of thermal mechanisms. The result of the fission gas releases is an increase in the internal fuel rod pressure and a decrease the gap conductivity.

- **Thermal expansion:** An increase in temperature of fuel leads to its expansion. It is an important contributor to the closing of the gap between fuel pellet and cladding. Axially the thermal expansion gives an "hourglass" shape in the fuel pellet.

- **Creep:** It is a slow irreversible deformation of the fuel pellet due to stresses. Irradiation and temperature have an important impact on creep.

- **High burn-up structure:** On the fuel periphery there is more Pu-239 production during fuels life due to epithermal neutron absorption in U-238 resonances. Fission of Pu-239 atoms results in an increased burn-up in this region and thus high fission products concentration. Additionally, the lower temperature in the periphery induces slower fission products diffusion and defects annealing. Around $40GWd/t$ restructuring of this region occurs, where the grains divide into smaller ones and the porosity increases up o 10%. This new microstructure is called high burn-up structure or 'rim effect' and affects significantly the fission gas releases.

1.4.1.2 Cladding behavior

- **Creep:** The differential pressure between coolant and gap pressure compress the cladding. The fast neutron flux and temperature impact the resulting creep deformation.

- **Thermal expansion:** As fuel pellet, cladding exhibits thermal expansion but with a slower temperature rate.

- **Oxidation:** The water interacts by oxidation with the Zr of the external cladding surface creating an external zircon oxide layer up to $120\mu m$. This layer has poor conductivity modifying thus the thermal transfer between clad and coolant. Additionally, it is an exothermic reaction increasing the cladding temperature.

$$Zr + 2H_2O \rightarrow ZrO_2 + 2H_2$$

  The hydrogen produced from the reaction can form hybrids reducing the ductility of the clad and causing embrittlement. Oxidation increases with coolant temperature increase.

- **Cladding damage:** Fast neutrons cause microstructural defects reducing the cladding ductility.

1.4.1.3 Fuel-cladding gap

Initially, due mainly to cladding creep down, fuel swelling and thermal expansion, the gap closes around 30 GWd/t as seen in figure 1.9. The contact occurs first at the edges of the "hourglass" shaped fuel pellet and then the cladding continuous to deform to take exactly the shape of the pellet. This is called pellet cladding mechanical interaction (PCMI). The gap stays closed for a period and the cladding follows the fuel swelling. At the end of the fuel's life the gap re-opens. The gap width and its properties (pressure, fission gases) have a significant impact on the thermal conductivity of the fuel pin. In transient situations, PCMI can lead to cladding failure. The temperature gradient increases rapidly and the corresponding fuel swelling and fission gas releases induce high tensile stresses on the cladding that may lead to its ballooning and burst.

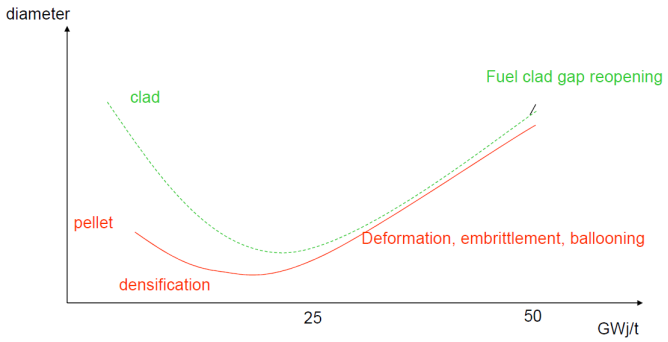

Figure 1.9: Fuel-cladding gap width evolution with Burn-Up.

A simplified synthetic presentation of the main phenomena affecting the fuel rod behavior can be seen in figure 1.10.

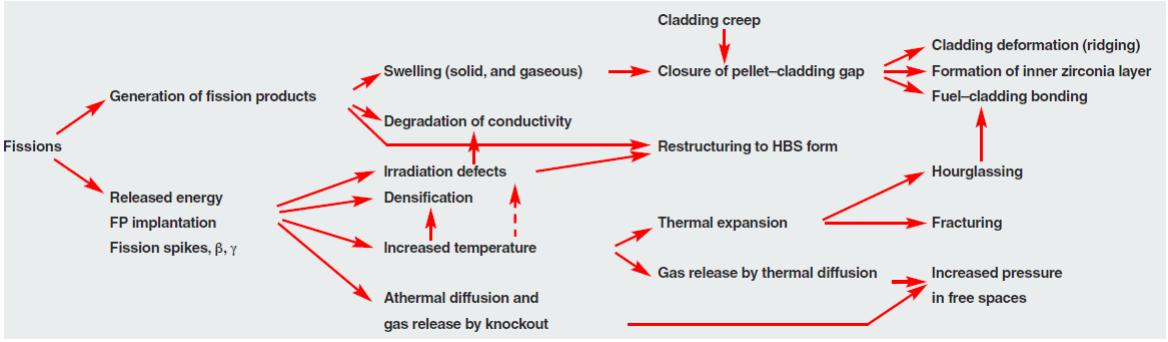

Figure 1.10: Fuel rod main phenomena during irradiation [5].

1.4.2 Thermomechanical equations

The fuel rod behavior is governed by two equations representing the mechanical and thermal phenomena [26]. Mechanically different states emerge due to loadings of thermal, mechanical and chemical origins in the different parts of the rod related to the basic phenomena described previously. Each state is described by displacements in relation to its previous state that satisfy the static mechanical equilibrium constraint of equation 1.22. Thermally the heat equation (1.23) describes the temperature spatial and temporal evolution in the fuel rod. Both equations are coupled since the mechanical displacements affect the efficiency of the heat distribution in the rod and the temperature variations impact the loadings.

$$\nabla\overline{\overline{\sigma}} = 0 \tag{1.22}$$

$$\rho(\vec{r})c_p(\vec{r})\frac{dT(\vec{r})}{dt} - \nabla\lambda(\vec{r})\nabla T(\vec{r}) = P_v(\vec{r}) \tag{1.23}$$

Where:

- $\overline{\overline{\sigma}}$ is the stress tensor and ρ is the density.
- c_p is the specific heat capacity and λ is the thermal conductivity.
- T is the temperature and P_v is the volumetric power generation.

The basic assumptions for the derivation of these equations are:

1. Quasi static mechanical behavior of the fuel rod
2. Isotropic heat flux diffusion

There many ways to model the above mentioned equations. In the following Section we will focus on the modeling aspects relevant to ALCYONE V1.4 code since it is the code used in this thesis for the fuel-thermochanics modeling.

1.4.3 Modeling

The two equations are quite general and in order to solve them different physical and empirical models are used to represent the contribution of each phenomenon. The different models are defined separately for the phenomena in the fuel pellet, the cladding and the gap between them [27], [28].

1.4.3.1 Mechanical

The constitutive mechanical laws describe the relation between stress and strain. Strain is directly linked with the displacements. For example in radial direction $e^r = \frac{du^r}{dR}$ with e^r, u^r, R the radial strain, radial displacement and the radius. The total induced differential strain can be decomposed in elastic and non-elastic parts:

$$\frac{d\overline{\overline{\epsilon}}_t}{dt} = \frac{d\overline{\overline{\epsilon}}_e}{dt} + \frac{d\overline{\overline{\epsilon}}_i}{dt} \tag{1.24}$$

The relation between stress and elastic strain is:

$$\frac{d\overline{\overline{\sigma}}}{dt} = \underline{\underline{C}} : \frac{d\overline{\overline{\epsilon}}_e}{dt} \tag{1.25}$$

Finally we can combine both equations to:

$$\frac{d\overline{\overline{\sigma}}}{dt} = \underline{\underline{C}} : \left[\frac{d\overline{\overline{\epsilon}}_t}{dt} - \frac{d\overline{\overline{\epsilon}}_i}{dt}\right] \tag{1.26}$$

Where $\underline{\underline{C}} = f(E,\nu)$ is the 4th order elastic tensor of the material which is a function of ν the Poisson's ratio and of E the Young's modulus that depends on temperature and porosity. With this definition we can define the different stress-strain equations for fuel and cladding by introducing their inelastic strain contributions. For the fuel it is the cracking, creep, swelling and thermal expansion. In the swelling term solid and gas swelling together with the densification are taken into account.

$$\frac{d\overline{\overline{\sigma}}_f}{dt} = \underline{\underline{C}}^f : \left[\frac{d\overline{\overline{\epsilon}}_{f,t}}{dt} - \frac{d\overline{\overline{\epsilon}}_{f,crack}}{dt} - \frac{d\overline{\overline{\epsilon}}_{f,creep}}{dt} - \frac{d\overline{\overline{\epsilon}}_{f,swell}}{dt} - \frac{d\overline{\overline{\epsilon}}_{f,thermal}}{dt}\right] \tag{1.27}$$

- **Cracking**

  Once the yield stress is reached the development of micro-cracking until the rupture is modeled by a linear softening stress strain law. The strain will increase as the stress decreases until zero when the rupture occurs. The yield stress criterion is defined as:

$$F_{crack} = \overline{\overline{n}}_i : \left[\overline{\overline{\sigma}}_f - \overline{\overline{R}}_f(\overline{\overline{\epsilon}}_{f,crack}))\right] = 0 \tag{1.28}$$

Where $\overline{\overline{R}}_f$ is the tensile strength tensor and is the above mentioned linear function of the inelastic cracking strain tensor $\overline{\overline{\epsilon}}_{f,crack}$. The strain rate can be calculated by the consistency of the above equation described as $dF = 0$ for the conditions between the yield stress reach and the rupture.

$$\overline{\overline{n}}_i : \frac{d\overline{\overline{\epsilon}}_{f,crack}}{dt} = \frac{\overline{\overline{n}}_i : \frac{d\overline{\overline{\sigma}}_f}{dt}}{\overline{\overline{n}}_i : \frac{d\overline{\overline{R}}_f}{d\overline{\overline{\epsilon}}_{f,crack}} : \overline{\overline{n}}_i} \tag{1.29}$$

Where $\underline{\underline{\underline{E}}}^{crack} = \frac{d\overline{\overline{R}}_f}{d\overline{\overline{\epsilon}}_{f,crack}}$ is the 4th order tensor softening modulus. More details are provided in [29] and [1].

- **Creep**

  The creep strain rate in the fuel is modeled by an incompressible viscoplastic formulation:

$$\frac{d\overline{\overline{\epsilon}}_{f,creep}}{dt} = \frac{3}{2}\frac{d\epsilon^{eq}_{f,creep}(\sigma^{eq}_f, \tau_f, T_f, p_f)}{dt}\frac{S_f}{\sigma^{eq}_f} \tag{1.30}$$

  Where:

  - σ^{eq}_f is the Von-Mises equivalent stress.
  - $S_f = \overline{\overline{\sigma}}_f - \frac{1}{3}tr(\overline{\overline{\sigma}}_f)\mathbb{I}$ is the deviatoric stress tensor with $\mathbb{I}$ the identity tensor.
  - $\epsilon^{eq}_{f,creep}$ is the equivalent plastic strain deformation. It is a function of the Von-Mises equivalent stress, the fission reaction rates τ_f, fuel temperature T_f and fuel porosity p_f.

- **Swelling**

  The swelling strain rate is the sum of the solid swelling, densification, and gas swelling.

$$\frac{d\overline{\overline{\epsilon}}_{f,swell}}{dt} = \frac{d\overline{\overline{\epsilon}}_{f,ss}}{dt} + \frac{d\overline{\overline{\epsilon}}_{f,d}}{dt} + \frac{d\overline{\overline{\epsilon}}_{f,gs}}{dt} \tag{1.31}$$

  The solid swelling depends on the fission products evolution and thus is modeled by a function of fuel density ρ_f and burn-up evolution $\frac{dBU}{dt}$.

$$\frac{d\overline{\overline{\epsilon}}_{f,ss}}{dt} = \frac{1}{3}A\rho_f\frac{dBU}{dt}\mathbb{I} \tag{1.32}$$

  The densification is a function of burn-up $f(BU)$:

$$\frac{d\overline{\overline{\epsilon}}_{f,d}}{dt} = \frac{1}{3}\frac{df(BU)}{dt}\mathbb{I} \tag{1.33}$$

  The porosity evolution due to densification is calculated by the empirical correlation of equation 1.34, where P_0 is the fabrication porosity and G is the solid fission product swelling.

$$P = \frac{P_0 - G}{1 - G} \tag{1.34}$$

  The gas swelling strain rate is modeled by a set of differential equations describing its generation, diffusion, release in free volumes and other main phenomena. More details can be found in [30]

- **Thermal expansion**

  The thermal strain rate tensor is proportional to the fuel temperature rate.

$$\frac{d\overline{\overline{\epsilon}}_{f,thermal}}{dt} = \overline{\overline{a}}_f\frac{T_f}{dt} \tag{1.35}$$

  Where $\overline{\overline{a}}_f$ is the diagonal tensor with elements the fuel dilatation coefficients for each direction.

For cladding constitutive stress-strain equation the strain is decomposed in viscoplastic, creep and thermal expansion contributions.

$$\frac{d\overline{\overline{\sigma}}_c}{dt} = \underline{\underline{C}}^c : \left[\frac{d\overline{\overline{\epsilon}}_{c,t}}{dt} - \frac{d\overline{\overline{\epsilon}}_{c,v}}{dt} - \frac{d\overline{\overline{\epsilon}}_{c,creep}}{dt} - \frac{d\overline{\overline{\epsilon}}_{c,thermal}}{dt}\right] \tag{1.36}$$

- **Viscoplastic**

  Using the Hill's quadrature yield criterion $\sigma^{eq}_{c,hill} = \sqrt{\overline{\overline{\sigma}}_c : \underline{\underline{H}}^c : \overline{\overline{\sigma}}_c}$, where $\underline{\underline{H}}^c$ is a 4th order tensor depending on cladding temperature and fast neutron flux, the viscoplastic strain rate is written as:

$$\frac{d\overline{\overline{\epsilon}}_{c,v}}{dt} = \frac{d\epsilon^{eq}_{c,v}}{dt}\underline{\underline{H}}^c : \frac{\overline{\overline{\sigma}}_c}{\sigma^{eq}_{c,hill}} \tag{1.37}$$

  Where $\frac{d\epsilon^{eq}_{c,v}}{dt}$ is the equivalent viscoplastic strain rate depending on cladding temperature, stress tensor and fast neutron flux. More details can be found in [31].

- **Creep**

  The cladding creep strain rate is modeled in a similar way with the fuel with the difference that the equivalent strain plastic deformation is a function of time t, cladding temperature T_c and fast neutron flux ϕ^p.

$$\frac{d\overline{\overline{\epsilon}}_{c,creep}}{dt} = \frac{3}{2}\frac{d\epsilon^{eq}_{c,creep}(\sigma_{c,eq}, \phi^p, T_c)}{dt}\frac{S_f}{\sigma_{c,eq}} \tag{1.38}$$

- **Thermal expansion**

  Similarly to fuel the thermal strain rate tensor is proportional to the cladding temperature rate.

$$\frac{d\overline{\overline{\epsilon}}_{c,thermal}}{dt} = \overline{\overline{a}}_c\frac{T_c}{dt} \tag{1.39}$$

  Where $\overline{\overline{a}}_c$ is the diagonal tensor with elements the cladding dilatation coefficients for each direction.

1.4.3.2 Thermal

The modeling of thermal heat equation is done by using laws for thermal conductivity and thermal capacity of cladding and fuel detailed in [32] and [26]. The fuel thermal conductivity is a function of burn-up, porosity and temperature $\lambda_f(BU, P, T_f)$. The cladding thermal conductivity $\lambda_c(T_c)$ and the specific heat capacities for both cladding and fuel are functions of temperature $c_{p,f}(T_f)$, $c_{p,c}(T_c)$. While now the heat equations can be solved in the fuel and cladding, the temperature difference in the gap must still be determined. This is done by a dedicated gap heat transfer model calculating the coefficient h_{gap} [33]. The temperature difference, with some simplifications, can be seen as $\Delta T_{gap} = \frac{q''_{gap}}{h_{gap}}$, where q''_{gap} is the thermal heat flux reaching the gap. The gap heat transfer model defines the h_{gap} as the sum of three heat transfer terms $h_{gap} = h_{rad} + h_{cond} + h_{cont}$. The radiation h_{rad}, conduction h_{cond} and contact h_{cont}.

- **Radiation**

  The radiative contribution is small during normal operation where the temperatures are low but under accidental situations it can potential have an important impact. It is described by the relation:

$$h_{rad} = \frac{C_s}{\frac{1}{e_f} + \frac{1}{e_c} - 1}\frac{T^4_{f,s} - T^4_{c,s}}{T_{f,s} - T_{c,s}} \tag{1.40}$$

  Where:

- C_s is the Stefan-Boltzmann constant.
- e_f and e_c are the fuel and cladding emissivities.
- $T_{f,s}$ and $T_{c,s}$ are the external fuel and internal cladding surface temperatures.

- **Conduction**

  The conduction heat transfer term can be seen as a series of thermal resistances in the gap and the fuel and cladding surfaces. With some simplification the conduction term can be written as:

$$h_{cond} = \frac{\lambda_{gap}}{s + \beta_2(\Delta R_f + \Delta R_c) + l_f + l_c} \tag{1.41}$$

  Where:

  - λ_{gap} is the gap thermal conductivity affected by the fission gas releases.
  - ΔR_f and ΔR_c are the arithmetic mean roughness for fuel and cladding surfaces.
  - s is the gap width and β_2 is a model parameter.
  - l_f and l_c are the gas extrapolation lengths for fuel and cladding surface. The extrapolation lengths allow to take into account the effective gap seen by the gas molecules. It is especially important when the gap width is small in comparison with the gas mean free path.

- **Contact**

  When there is contact between the fuel pellet and the cladding the heat transfer improves depending mainly on the contact pressure [34]. It is modeled by the contact heat transfer coefficient.

$$h_{cont} = \beta_5 \overline{\lambda} \Delta \overline{R} \left(\frac{P_c}{\Delta \overline{R}^2 \overline{\overline{\sigma}}_g} \right)^{\beta_6} \tag{1.42}$$

  Where:

  - P_c is the contact pressure.
  - β_5 and β_6 are model parameters.
  - $\overline{\lambda}$ and $\Delta \overline{R}$ are the mean conductivity and roughness of fuel and cladding.
  - $\overline{\overline{\sigma}}_g$ is the minimum between the fuel and cladding yield stress tensor.

It is important to notice that there are additional models for calculating the high burn up structure and cladding oxidation detailed in [26]. These models have a direct impact in reducing the conductivity of the fuel and the cladding. Indirectly they affect the fission gas releases in the gap and the cladding ductility. These aspects can have a very important role during accidents.

1.4.3.3 Boundary conditions

In order to solve the equations mechanical and thermal boundary conditions are needed. The mechanical ones are:

- The loading on the external surface of the cladding is the fluid pressure.
- There is no fluid penetration through the walls.
- Unilateral fuel pellet cladding contact
- Equal axial strains for fuel and cladding.

The thermal boundary conditions are related to the quantities provided by other codes or by integrated simplified models:

- The power generation in the fuel rod. Usually average values are given in the whole fuel pellet and the radial profile is reconstructed based on simplified neutronic models or empirical correlations.
- The cladding wall temperature.

1.4.3.4 Numerical discretization

In thermal-hydraulics we will see that different channels are defined (e.g. quarter of assembly). Usually for each channel one representative fuel pin is modeled by the fuel-thermomechanics code. The different fuel pins are treated independently and their modeling can be easily parallelized. For their space discretization finite elements are used. The fuel pin is discretized axially and radially in meshes as illustrated in figure 1.11.

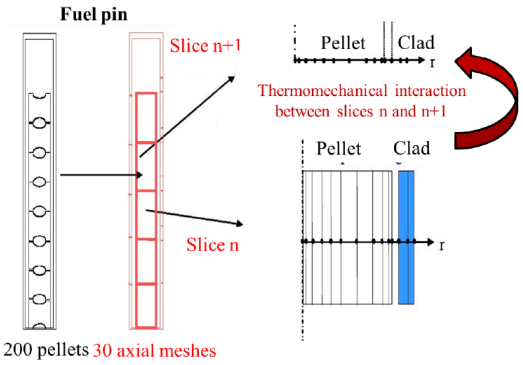

Figure 1.11: Axial and radial discretization of a fuel pin [1].

Each axial mesh is modeled using a 1D axisymmetric radial geometry with plane strain deformation. The axial stress is considered independent of the axial position and depends on the gap pressure creating a coupling between the slices. The mechanical equilibrium equation is integrated and the radial displacements u_r together with the axial strain ϵ_{zz} are calculated. The heat equation is solved and the temperatures are calculated on the defined radial grid for each slice. Concerning the time discretization, a Gauss-Seidel coupling between thermal and mechanical modeling is performed for each slice and time step. This is presented in figure 1.12. The iterations stop based on convergence criteria for radial temperature distribution, gap width and gas swelling [26].

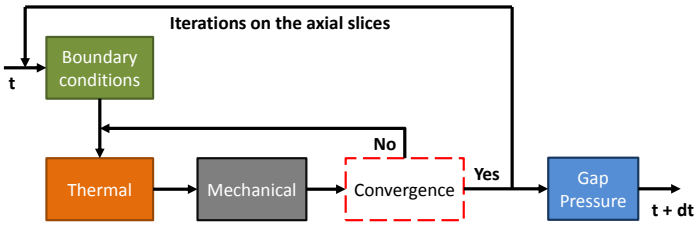

Figure 1.12: Thermal - Mechanical coupling scheme.

1.4.4 ALCYONE V1.4 code

ALCYONE V1.4 [35] is a 3D finite element code PWR fuel code developed by a common project between CEA, EDF and Framatome within the PLEIADES framework [36]. The CASTEM [37] finite elements code is used for space discretization in both the thermal and mechanical modeling. ALCYONE V1.4 [35] can treat the fuel rod evolution under both nominal and transients conditions. For the thesis purposes the 1D approach described in the Section 1.4.3.4 is used.

1.5 Thermal-hydraulics modeling

1.5.1 Basics

The field of thermal-hydraulics studies the coolant flow behavior in the different systems of the PWR from core to steam generator and condenser. In the context of the thesis we focus in the

core region where, at nominal conditions, liquid water is entering from the bottom of the fuel assemblies with an average mass flow rate of $18000kg/s$ at an average temperature $290°C$. It receives heat from the power generation along the core and exits from the top at an average temperature of $330°C$ under nominal pressure of 155 bars. The reactor conditions, the geometry and the power produced in the core have an important impact on the water flow. Before presenting the constitutive equations we introduce basic thermal-hydraulic phenomena occurring in a PWR and related quantities [25], [38].

1.5.1.1 Heat transfer

The heat generated in the core leads to temperature increase in the fuel and cladding. The liquid water flowing through the assemblies serves as a coolant and extracts the generated heat. This can result in the formation of vapor bubbles. Two-phase flow regimes are created with different mechanisms of heat transfer:

- **Single phase flow**: The cladding wall temperature is inferior to the saturation temperature of the liquid and thus the liquid temperature does not reach saturation. There is no vapor formation resulting in a single phase flow convective heat transfer.
- **Sub-cooled boiling**: In this case the cladding wall temperature is superior to the fluid saturation temperature but the fluid bulk temperature has not reach saturation yet. This is called sub-cooled boiling. At a first phase initiated at the Onset of Nucleate Boiling (ONB), small vapor bubbles are created near the cladding wall but cannot leave the wall because they instantly condensate. Both the liquid and wall temperature increase weakly in this phase. When the water temperature is high enough (Onset of Significant Void) the bubbles can leave the wall and transfer to the bulk of the water.
- **Vapor film boiling**: If the heat flux coming from the fuel is higher than a critical threshold called Critical Heat Flux (CHF) then the fluid around the cladding vaporizes enough creating a vapor film. The heat transfer reduces significantly leading to an instant increase of the cladding temperature. The phenomenon is called Departure from Nucleate Boiling (DNB) and is a crucial phenomenon for safety studies.

1.5.1.2 Mass transfer

During the axial flow, as we mentioned, vapor can be produced from sub-cooled boiling. Since the vapor bubbles are generated near the cladding surface where the temperature is higher can condense as they move towards the bulk of the water. There is thus a mass transfer between vapor and liquid.

1.5.1.3 Pressure drop

There is a pressure drop on the coolant along the axial flow due to three main effects: gravity, acceleration and friction. Friction is a result of the continuous along the flow wall friction and of the singular friction due to local obstacles like mixture grids. The presence of vapor affects the friction and thus must be taken into account. The acceleration pressure drop is related to the density decrease and is significant only when vapor appears due to the density differences between the two phases.

1.5.2 Balance equations

The behavior of the coolant flow in the core is described by a general set of local instantaneous balance equations of mass, momentum and energy on a constant control volume V (eulerian form). There is one set of equations for each field and one for the interface between two fields. Since we focus on liquid and vapor phases of water there are a total of 9 equations. For liquid and vapor phase $k = l, v$ the local mass balance equation and the balance at their interface are:

$$\frac{\partial \rho_k}{\partial t} + \vec{\nabla} \cdot (\rho_k \vec{v_k}) = 0 \tag{1.43a}$$

$$\rho_l(\vec{v_i} - \vec{v_l}) \cdot \vec{n_l} + \rho_v(\vec{v_i} - \vec{v_v}) \cdot \vec{n_v} = 0 \tag{1.43b}$$

Where:

- ρ_k and $\vec{v_k}$ are the phasic densities and velocities.
- $\vec{v_i}$ is the velocity of the interface between the two phases and $\vec{n_l} = -\vec{n_v}$ the normal vector on the interface.

The local momentum balance equation and the balance at their interface are:

$$\frac{\partial \rho_k \vec{v_k}}{\partial t} + \vec{\nabla} \cdot (\rho_k \vec{v_k} \otimes \vec{v_k}) = \rho_k \vec{g} + \vec{\nabla} \cdot (\overline{\overline{\tau}} - p\mathbb{I}) \tag{1.44a}$$

$$\rho_l (\vec{v_l} - \vec{v_i}) \cdot \vec{n_l} (\vec{v_l} - \vec{v_v}) = (\overline{\overline{\tau}} - p\mathbb{I})_l \cdot \vec{n_l} + (\overline{\overline{\tau}} - p\mathbb{I})_v \cdot \vec{n_v} \tag{1.44b}$$

Where:

- $\vec{g}$ is the gravity force per unit mass.
- $\overline{\overline{\tau}}$ is the shear stress tensor per unit area.
- p is the isotropic pressure and $\mathbb{I}$ the unitary tensor.

The local energy balance equation and the balance at their interface are:

$$\frac{\partial \rho_k u_k}{\partial t} + \vec{\nabla} \cdot \rho_k h_k \vec{u_k} = \rho_k \vec{g} \cdot \vec{u_k} + \vec{\nabla} \cdot (\overline{\overline{\tau}} \cdot \vec{v_k}) - \vec{\nabla} \cdot \vec{q_k}'' + q''' \tag{1.45a}$$

$$\rho_l (\vec{v_l} - \vec{v_i}) \cdot \vec{n_l} (u_l - u_v) = (\overline{\overline{\tau_l}} \cdot \vec{v_l} - \overline{\overline{\tau_v}} \cdot \vec{v_v}) \cdot \vec{n_l} - (p_l \cdot \vec{v_l} - p_v \cdot \vec{v_v}) \cdot \vec{n_l} - (\vec{q_l}'' - \vec{q_v}'') \cdot \vec{n_l} \tag{1.45b}$$

Where:

- $u_k = u^i + \frac{1}{2} v^2$ is the stagnation energy and $h_k = u_k - \frac{p}{\rho_k}$ its corresponding enthalpy.
- q''' expresses both the volumetric heat source due to the heat flux at the cladding external surface and the power density deposition in the fluid.
- $\vec{q_k}''$ is the heat flux induced by thermal conductivity and turbulent mixing.

All the above equations are derived without considering surface tension on the interface. If the surface tension is included additional terms are included in the interface equations to represent the resulting accumulation of mass, momentum and energy. More details can be found in [38].

The modeling of these equations in the reactor core has rapidly evolved the last decades with the increase of computational power. Computational Fluid Dynamics (CFD) codes have been developed for two-phase flow with various degrees of approximations. The different CFD currently available methods differ on the treatment of time and space linked to the turbulunces and two-phase interfaces. A state of the art of these methods can be found in [39] and [40] from local Direct Numerical Simulations (DNS) to open medium Large Eddy Simulations (LES), (U)RANS and porous medium approaches at an assembly channel or fuel rod/sub-channel scale. A qualitative representation of a quantity with the different methods is illustrated in figure 1.13.

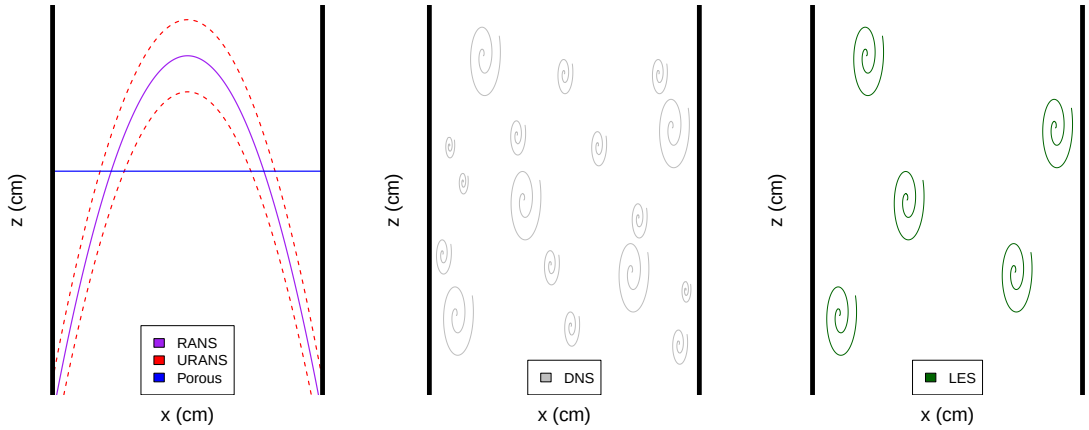

Figure 1.13: Modeling of a thermal-hydraulic quantity using DNS, LES, RANS, URANS and Porous methods.

In DNS the local instantaneous equations are solved directly taking into account all the turbulences and the two-phase interfaces. For this reason it is a computationally expensive method used for very local phenomena at the scale of μm. LES method can be a computationally more efficient alternative for larger scales of the order of mm. They are used for simulations inside an assembly. The interfaces are treated through space filtering where interfaces with length larger than the filter size are simulated directly while the ones with length smaller than the filter size are treated statistically. This method can be applied when the filter size is smaller than the turbulence scales. (U)RANS is a method using statistical time averaging for both the turbulences an the interfaces leading to average quantities such as the void fraction. For 3D core design and safety studies the computational cost of the previously mentioned methods is still prohibitive. Besides that, there is no need to go beyond the subchannel scale (cm), calculate the fine profiles of the important quantities (e.g. velocity) and track the exact evolution of the interfaces. For these reasons, porous medium methods are used to calculate the evolution of macroscopic quantities up to the subchannel scale. The physical quantities in the balance equations are both averaged spatially at this scale and in time using (U)RANS techniques. The time filter size must be large enough to average the high frequency turbulences but small enough for the transient evolution. Additionally, since in the subchannel scale there are solid structures, the equations have to be multiplied by a characteristic fluid/solid function representing the presence presence of fluid or solid in the considered volume respectively. The interfaces are treated statistically or implicitly by heat, mass and momentum transfer models.

The porous medium modeling with 4 equations is used in this thesis with the thermal-hydraulic code FLICA4. In the following Section the modeling aspects relevant to FLICA4 are presented.

1.5.3 Porous medium modeling with 4 equations

The balance equations for the two-phase mixture and the mass balance for the vapor consist a total of 4 equations to be solved [41]. The integration is performed on an elementary volume without explicit modeling of the fluid and solid structures and thus a characteristic function called porosity is applied to distinguish between fluid and solid. Besides that, for the two phases a space and time averaging of quantities governing the equation is applied. Finally closure laws are necessary to solve the equations together with boundary conditions and a numerical discretization.

1.5.3.1 Space averaging

In the elementary volume V, where both solid structures and fluid are present in the medium, the volumetric average of a quantity $w(\vec{r})$ with $\vec{r} \in V$ is defined as:

$$< w(t) >= \frac{1}{V} \int_V w(\vec{r}, t) dr \tag{1.46}$$

Considering V_f as the volume of the fluid in V and if we assume that the solid structures are immobile, the porosity of the medium can be defined as:

$$\phi \equiv < \chi_f(t) >= \frac{V_f}{V} \tag{1.47}$$

Where $\chi_f(\vec{r},t)$ is the local fluid/solid characteristic function. With this definition of the porosity we obtain the following equivalence for the fluid volumetric average of a quantity:

$$< w(t) >_f = \frac{< \chi_f(t) w(t) >}{< \chi_f(t) >} \tag{1.48}$$

1.5.3.2 Time averaging

The time is descritized for the solution of the equations and in each time step average quantities are computed:

$$\overline{w}(\vec{r}) = \frac{1}{\Delta T} \int_{\Delta T} w(\vec{r},t) dt \tag{1.49}$$

The ΔT size must be large enough to average high frequency two phase fluctuations but small enough compared to the evolution of transient phenomena that we want to study.

1.5.3.3 Phase function

The presence of phase $k = l, v$ is described by the phase characteristic function $\alpha_k(\vec{r},t)$ that equals 1 when phase k is present and 0 otherwise. This leads to the definition of void fraction as:

$$< \alpha >= \frac{1}{V} \int_V \alpha_v(\vec{r},t) dr = \frac{V_v}{V} \tag{1.50}$$

Where V_v is the volume occupied by the vapor in the volume V. This phase function is used together with the phasic densities to define the average phasic quantities:

$$\{w\}_f^k = \frac{< \overline{\alpha_k}\, \overline{\rho_k}\, \overline{w} >_f}{< \overline{\alpha_k}\, \overline{\rho_k} >_f} \tag{1.51}$$

Where $\alpha_v =< \alpha >$ and $\alpha_l = 1 - < \alpha >$. The mixture quantities are averaged with a similar ponderation:

$$\{w\}_f = \frac{< \overline{\rho_k}\, \overline{w} >_f}{< \overline{\rho_k} >_f} \tag{1.52}$$

1.5.3.4 Balance equations

There are a total of 4 equations: mixture mass balance (sum of liquid and vapor mass balance equations), vapor mass balance, mixture momentum balance and mixture energy balance. For each quantity of the two phase flow balance equations we will use its corresponding phasic or mixture average but we will keep the same notation as in the general previous framework by omitting the averaging symbols. The 4 equations are written as:

$$\phi \frac{\partial \rho}{\partial t} + \vec{\nabla} \cdot (\phi \rho \vec{v}) = 0 \tag{1.53a}$$

$$\phi \frac{\partial \rho c}{\partial t} + \vec{\nabla} \cdot (\phi \rho c \vec{v}) = -\vec{\nabla} \cdot \left[\phi \rho c (1-c) \vec{v_r}\right] + \vec{\nabla} \cdot K_T \vec{\nabla} c + \Gamma_v \tag{1.53b}$$

$$\phi \frac{\partial \rho \vec{v}}{\partial t} + \vec{\nabla} \cdot (\phi \rho \vec{v} \otimes \vec{v}) = -\vec{\nabla} \cdot \left[\phi \rho c (1-c) \vec{v_r} \otimes \vec{v_r}\right] + \phi \rho \vec{g} + \vec{\nabla} \cdot \phi (\overline{\overline{\tau}} - p \mathbb{I}) + \phi \tau_f \tag{1.53c}$$

$$\phi \frac{\partial \rho u}{\partial t} + \vec{\nabla} \cdot \phi \rho h \vec{v} = -\vec{\nabla} \cdot \left[\phi \rho c (1-c)(h_v - h_l) \vec{v_r}\right] + \phi \rho \vec{g} \cdot \vec{u} + \vec{\nabla} \cdot \phi (\overline{\overline{\tau}} \cdot \vec{u}) - \vec{\nabla} \cdot \phi \vec{q}'' + \phi q''' \tag{1.53d}$$

- Equation 1.53a is the mixture mass balance. The two terms correspond to the temporal and advective contributions with ρ and $\vec{v}$ the mixture density and velocity.

- Equation 1.53b is the vapor mass balance. The first two terms again correspond to the temporal and advective contribution with $c = \frac{\alpha_v \rho_v}{\rho}$ and $\vec{v_r} = \vec{v_v} - \vec{v_l}$ is the relative velocity. The third and forth are the dispersions average and turbulent contributions with K_T the turbulence diffusion coefficient. The fifth term Γ_v is the vapor mass production due to vaporization occuring in contact with the heating walls and due to mass exchange at the liquid-vapor interface.

- Equation 1.53c is the mixture momentum balance. The first three terms represent the temporal, advenction and average dispersion contributions. The forth and fifth are the gravity and stress contributions. The sixth is the friction force.

- Equation 1.53d is the mixture energy balance. The first three terms represent the temporal, advenction and average dispersion contributions. The forth and fifth are the gravity and stress contributions while the sixth and seventh are the wall heat flux and volumetric heat sources contributions.

Some of the main assumption made to derive these equations are:

1. The mixture is considered isobaric.

2. The vapor is considered to be at saturation.

The derived set of equations need some closure laws in order to be solved since terms like the relative velocity and the stress gradient must be modeled.

1.5.3.5 Closure laws

There are many options for each closure law. In the following we list the ones used in this thesis detailed in [42] and [43].

- **Equations of state:** The phasic properties (e.g. density, enthalpy, viscosity) are functions of pressure and temperature. We consider isobaric $p_l = p_v = p$ and isothermal $T_l = T_v = T$ conditions. Vapor is considered to be at saturation and thus the equations of state for densities and enthalpies reduce to:

$$\rho_l = \rho_l(p,T) \quad , \quad h_l = h_l(p,T) \quad , \quad \rho_v = \rho_v(p), \quad , \quad h_v = h_v(p) \tag{1.54}$$

  The mixture density and enthalpy are defined as $\rho = \alpha\rho_v + (1-a)\rho_l$ and $h = ch_v + (1-c)h_l$ respectively.

- **Relative velocity:** Drift flux models are used expressing the vapor velocity as:

$$v_v = C_0 J + v_{vj} \tag{1.55}$$

  Where:

  - J is the volumetric flux.
  - C_0 is a concentration parameter representing the global effects due to void and velocity profiles.
  - v_{vj} is the effective drift velocity and represents the local relative velocity effects.

  Ishii correlations are used for calculating C_0 and v_{vj}.

- **Heat transfer:** The temperature on the cladding wall T_w, the fluid temperature T_f and the wall heat flux Φ_w describe the three heat transfer modes presented in the thermo-hydraulics basics. They are modeled by different correlations and transitions conditions:

- Single phase flow: $T_w < T_{sat} + \Delta T_{sat}$, where T_{sat} is the saturation temperature and ΔT_{sat} is modeled by the Jens & Lottes correlation. The temperature difference is calculated by:

$$(T_w - T_l) = \frac{\Phi_w}{H_c} \tag{1.56}$$

  Where H_c is the convective heat transfer coefficient calculated by Dittus Boelter expression.

- Sub-cooled boiling: $T_w = T_{sat} + \Delta T_{sat}$ and $T_l < T_{sat}$. This heat transfer is characterized by a constant wall temperature. The thermal flux now is divided in two fractions, one that heats the sub-cooled water (moderate heat transfer) and one that creates the vaporization (very efficient heat transfer). The vaporization fraction increases as the fluid temperature increases. In PWR nominal operating conditions the saturation temperature is not reached and thus nucleate boiling does not occur.

- Vapor film boiling: It is initiated when $DNBR = \frac{\Phi_c}{\Phi_w} < 1.3$. $DNBR$ is the Departure From Nucleate Boiling Ratio. Φ_c is the CHF depending mainly on the pressure, mass flux and quality and is calculated by $W3$ correlation. The value 1.3 is a penalization taking into account the uncertainties of the CHF correlation. When this limit is reached a post-DNB vapor film heat transfer occurs described by:

$$(T_w - T_{film}) = \frac{\Phi_w}{H_{BST}} \tag{1.57}$$

  Where $T_{film} = 0.5(T_w + T_{sat})$ and H_{BST} is the heat transfer coefficient calculated by Bishop-Sandberg-Tong expression.

- **Mass transfer:** It models the vaporization of liquid that is divided in two parts $\Gamma_v = \Gamma_{v,w} + \Gamma_{v,I}$. The first term represents the vapor generation on a heating surface:

$$\Gamma_{v,w} = XS_h \frac{\Phi_w}{h_{v,sat} - h_{l,sat}} \tag{1.58}$$

  Where S_h is the heated surface in the elementary volume and X is a fraction representing the fraction of the heat flux used to vaporize the liquid. If $T_w < T_{sat} + \Delta T_{sat}$ there is single phase flow and $X = 0$ and if $T_l = T_{sat}$ there is nucleate saturated boiling and $X = 1$. Between the two conditions:

$$X = \frac{T_w - T_{sat} - \Delta T_{sat}}{T_w - T_l - \Delta T_{sat}} \tag{1.59}$$

  The second term represents the mass transfer at the interface (e.g. condensation) and it is calculated by:

$$\Gamma_{v,I} = \frac{\Phi_I}{h_{v,sat} - h_{l,sat}} \tag{1.60}$$

  Where Φ_I is the heat transfer at the interface calculated by a recondensation model.

- **Momentum transfer:** It is the modeling of friction and shear stress related contributions. Friction occurs with the solid structures in contact with the fluid flow. It is modeled by:

$$\tau_f = -\frac{1}{2}\rho\vec{v}\|\vec{v}\| \left(\frac{\overline{\overline{\Lambda_k}}}{D_h} + \overline{\overline{K_s}} \right) \tag{1.61}$$

  Where:

  - $D_h = \frac{4A}{P_w}$ is the hydraulic diameter with A the cross-section flow area and P_w and wetted perimeter.

- The tensor $\overline{\overline{\Lambda_k}}$ accounts for the continuous friction distributed along the wall and is calculated by a correlation based on an isothermal friction coefficient and corrections taking into account the heated wall and the two phase flow.
- The tensor $\overline{\overline{K_s}}$ accounts for singular pressure drops due to local obstacles (e.g. mixing grids) and is provided by the user when the geometry is defined.

The shear stress tensor is modeled by:

$$\tau_{ij}^k = \mu_k(1 + M_k^t)\left(\frac{\partial v_k^i}{x_j} + \frac{\partial v_k^j}{x_i}\right) \tag{1.62}$$

Where $\mu_k M_k^t$ is the turbulent viscosity for each phase k.

- **Thermal source:** They consist the two last terms in the mixture energy balance. The first one is the heat flux induced by thermal conductivity and turbulent mixing:

$$\vec{q}'' = \frac{\lambda_l}{c_{p,l}}(1 + K_T)\nabla h_{deb} \tag{1.63}$$

Where:

- λ_l and $c_{p,l}$ are the fluid conductivity and specific capacity.
- h_{deb} is the debiting enthalpy defined as $h_{deb} = \frac{G_v h_v + G_l h_l}{G}$ with G_k and G the phasic and mixture mass flow rates.

The second term accounts for the heat flux at the cladding external surface and the volumetric heat sources in the elementary volume mainly due to photon energy deposition.

$$q''' = Q_f + \frac{\Phi_w S_w}{V_f} \tag{1.64}$$

Where:

- S_w is the wall surface.
- V_f is the fluid volume.
- $Q_f = \gamma \frac{P_{tot}}{V_f}$ is the power density deposition in the fluid calculated as a small fraction $\gamma = 0.026$ of the total power P_{tot} produced in the core.

1.5.3.6 Boundary conditions

Two different categories of boundary conditions are necessary:

- **Thermal power conditions**: they require the computation of the heat sources. They are provided by solving the power generation (neutronics) and heat conduction equations (fuel thermomechanics). Different codes can be used to solve thoses equations.
- **Hydraulic flow conditions**: a selection of the mass flow, fluid enthalpy and pressure are given at the inlet and outlet of the geometry. For the 4 equation porous modeling in this thesis the mass flow and enthalpy are given at the inlet while the pressure is given at the outlet.

For REA calculations the thermal power boundary conditions vary in time.

1.5.3.7 Numerical Discretization

For space discretization finite volume method are used where the balance equations are integrated on a discretized mesh. In each mesh the solutions (ρ, ρc, ρv, ρu) are considered constant. The integration of the equations leads to the calculation of these quantities on the interface between the meshes. For the convective terms an approximate Riemann solver is used while for the diffusive a VF9 calculation scheme is adopted. For time discretization an implicit scheme solved by a Newton method is used where the Newton residual is calculated by a preconditioned conjugate gradient. More details can be found in [1] and [42].

1.5.4 FLICA4 code

The code used for the thermal-hydaulics modeling in this thesis is FLICA4 [44] [45], a 3D two-phase flow code specially devoted to reactor core and developed at CEA. It uses porous medium 4 equation modeling presented previously. Most of the types of reactors and experimental facilities can be modeled under both stationary and transient conditions. In the context of the thesis the radial discretization is one thermal-hydraulic channel per quarter of assembly and the axial is 30 meshes along the active fuel length. The reflector is not modeled. FLICA4 is used in a multi-1D axial modeling by considering the channels to be isolated.

1.6 Multi-physics Rod Ejection Accident (REA)

REA may occur in a nuclear reactor if there is an unwanted increase in fission rate and reactor power due to a control rod ejection that may damage the reactor. It is a design basis accident, classified as a category 4 event (i.e. with a frequency of occurrence evaluated at $10^{-4} - 10^{-6}$ per reactor, per year). A control rod is ejected after experiencing a mechanical failure of the driven mechanism resulting in a strong pressure difference between the internal (155bar) and the external (1bar) of the core. The ejection duration is very short (0.1s) due to this pressure difference. The control rod is made of neutrons absorbents to control the fission rates in the reactor and thus its fast removal will induce an insertion of positive reactivity in the core that will increase rapidly the fission rates and consequently the power. The radial map of the power is expected to be deformed leading to a high deformation factor around the area of the ejection as can be seen in figure 1.14.

The intensity of the transient will depend on the reactivity inserted ρ_{inj} and the effective delayed neutron fraction β_{eff}. If $\rho_{inj} > \beta_{eff}$ the transient evolution is governed by the prompt neutrons and thus is more violent (supercritical prompt transient). In REA studies two reactor initial conditions prior to the ejection are considered: Hot Full Power (HFP) when the reactor is at nominal power and temperature conditions and Hot Zero Power (HZP) when the reactor is shutdown but still with a reactor temperature of $290°C$. The latter leads to more violent transients and potentially prompt neutron driven because at HZP the control rods are inserted deeper in the core. This means that the control rod worth and thus the injected reactivity is larger. For this reason we consider HZP initial conditions. Three different phases can be identified during REA governed by different physical aspects:

1. The first phase, where the transient starts followed by rapid local increase in power due to the insertion of positive reactivity. The phenomenon is considered quasi-adiabatic because the temperatures of the cladding and coolant do not increase significantly due to thermal inertia of the fuel. This phase is governed mainly by neutronics.

2. The second phase, where the temperature of the fuel starts rapidly to increase leading to a Doppler feedback effect. As we have seen the increase of fuel temperature will lead to the broadening of the U-238 absorption resonances resulting in more neutrons absorptions and thus exerting a negative feedback effect on the reactivity and a corresponding decrease of power. It is important to notice that until the end of this phase the heat flux does not reach the coolant, and thus the coolant temperature and density are more or less constant at its initial value. This phase is governed mainly by neutronics strongly coupled with fuel-thermomechanics.

3. The third phase, where the heat is transferred to the coolant leading in a thermal-hydraulic evolution of the system. The cladding temperature increases during this phase and if DNB occurs it can exceed its melting point inducing a failure of the cladding. The coolant-moderator temperature is increasing and the density decreasing. This leads to a negative moderator feedback effect due to the less effective slowing down of neutrons (spectrum hardening). The Doppler combined now with the moderator feedback effect decrease the power even more. At the end of this phase the SCRAM safety system will react and insert the remaining control rods. The whole transient duration is of the order of 1-2 seconds. This phase is governed by strong coupling between neutronics, fuel-thermomechanics and thermal-hydraulics.

Under the REA three phases, fuel pellet and cladding experience different phenomena affecting their integrity and properties.

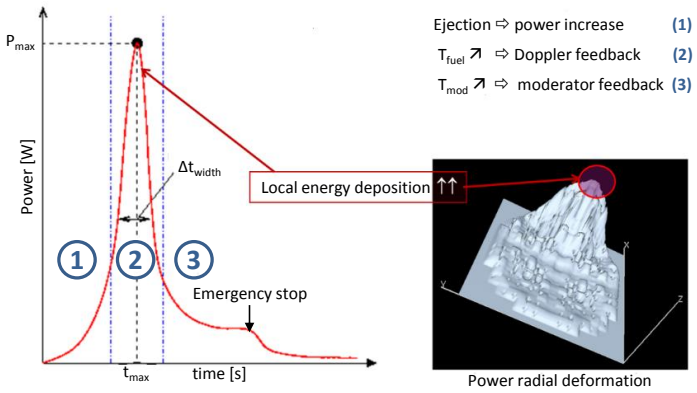

Figure 1.14: Power evolution during REA.

1.6.1 Fuel pellet behavior

The main phenomena occurring in UO_2 fuel pellets are: heat up, fragmentation, swelling and fission gas releases. Adiabatic heat up occurs in the initial phase and the radial temperature follows the radial power profile with peak at the periphery for irradiated fuel. In the later stages of the transient (phase 3) when the heat is conducted the temperature profile approaches its normal parabolic shape. This behavior can be seen in figure 1.15. For this reason the fuel melting, if it occurs in the first two phases of the transient, will happen close to the fuel pellet periphery. The local melting UO_2 temperature for un-irradiated fuel is $3120K$ and the associated enthalpy is $1150J/g$. For irradiated fuel these limits are reduced.

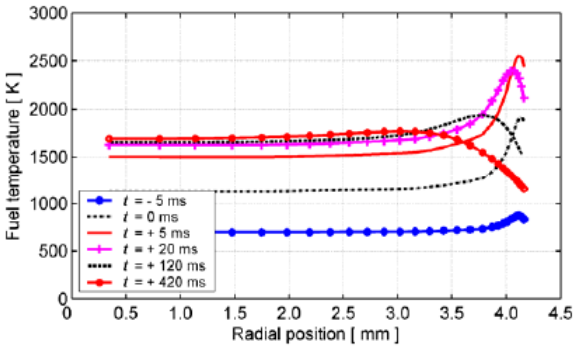

Figure 1.15: Radial fuel temperature distribution during a REA [6].

Circumferential cracks can occur in fuel pellets during the phase 1 and 2 due on the boundary of the high burn-up structure induced by tensile stresses. During the late stages of the transient radial cracks are created due to tensile hoop stresses. Additionally, retained fission gases are released in the gap and increase the internal gas pressure creating fine fragments. This is enhanced by the fuel cracks and the higher fuel temperature and gas concentration in the "rim" region that induce grain boundary decohesion. Fuel transient swelling by the growth of pores and bubbles is shown by experimental results to be less important than thermal expansion in their contribution to the gap closure. This can lead to a pellet cladding mechanical interaction (PCMI) during the initial phase of the transient.

1.6.2 Cladding behavior

The main phenomena occurring in the zircaloy IV cladding are: heat up, transient deformation, water corrosion and failure. The heat up occurs mainly by heat conduction from the fuel pellets in the third phase of REA and depends strongly on the width and condition of the gap (delayed heating). Besides that, heat up occurs also through gamma attenuation directly with the power

increase in the first two phases of the transient (prompt heating). Since heat up occurs mainly through conduction the cladding inner surface temperature is higher than the outer one inducing thermal stresses and affecting the local ductility. In the third phase the heat extracted by the coolant can lead to DNB resulting in a rapid increase in cladding temperature. The local melting temperature for the cladding is 2035K.

Thermal expansion, pressure difference and the potential PCMI lead to cladding deformation during the transient. In the first phase of the transient PCMI may have a big impact whereas pressure difference on the later phase.

High cladding temperatures occurring in post-DNB conditions accelerates cladding corrosion through oxidation with UO_2 fragments in the inner surface and with coolant water on the outer surface. This causes embrittlement and decrease of ductility that can lead to failure during the last phase of the transient. Besides that, hydrogen is also produced and diffuses to the cold surface of the cladding. When its local concentration exceeds the maximum solid solubility zirconium hydrides precipitations occur further reducing the ductility of the cladding.

Failure of the cladding causes fuel dispersion in the coolant generating pressure pulses that induce mechanical damages in the nearby components such as the fuel assemblies and the pressure vessel. There are three main failure modes.

- PCMI occurring in the first and second phase of the transient when the fuel pellet heats up mainly due to expansion. The cladding is at low temperature with low ductility increasing the probability of failure. This mode depends strongly on the initial conditions of the fuel rod.

- Cladding ballooning and burst under high temperatures due to post-DNB conditions.

- Cladding disruption under quenching from post-DNB high temperatures during the third phase of the transient. It occurs due to cladding embrittlement by the enhanced oxidation under high temperatures.

For HZP initial conditions and prompt driven power pulses the first mechanism is more prominent for high burn-up fuel rods while the other two are more probable for low burn-up rods. A simplified synthetic overview of the different phenomena and the resulting failure mechanisms is provided in figure 1.16.

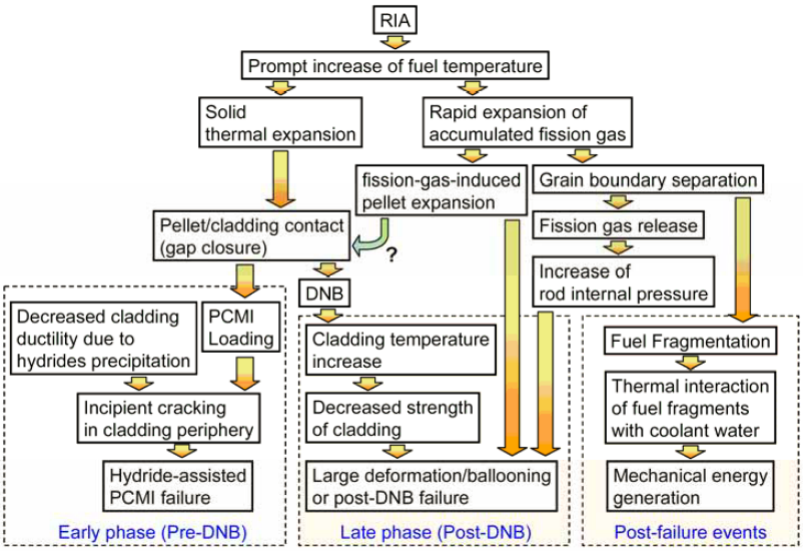

Figure 1.16: Main phenomena occuring during REA [6].

1.6.3 Safety

The important quantities determining the general fuel rod behavior under REA are the power pulse characteristics (peak, width), the coolant conditions (pressure, temperature, flow rate), the burn-up state (gap width, cladding corrosion, internal pressure, radial power distribution) and the fuel rod design (initial geometries, fuel composition, fill gas pressure). For ensuring the safety of the reactor during REA, meaning that no failure will occur, limits are being imposed on different quantities. The limits vary in different countries. We present the main ones based on [46] and [47]:

- Enthalpy limit of the fuel (radial average) in relation with the mechanical stress exerted by the fuel to the cladding: Deposed enthalpy $837J/g$ for irradiated fuel and $942J/g$ for fresh (Fuel dispersion) $\rightarrow$ PCMI effect.
- Limit on the cladding maximum temperature due to embrittlement and oxidation: $T_c^{max} < 1482°C$ (Cladding fragmentation risk) $\rightarrow$ above this temperature uncontrolled hydrogen production (exothermic reaction) that can lead to explosion.
- Additional limits: Fuel melt volume $< 10\%$ of the total (core melt risk), number of pins with Boiling crisis $< 10\%$ of the total.

1.7 Coupling framework

Multi-physics coupling modeling for PWR transients has been the subject of research across the world with undergoing projects such as CASL [48] [49] and NEAMS [50] in USA and NURESAFE [51] in Europe. At CEA, CORPUS project [52] based on SALOME [53] open source software was developed and recently has been extended to treat REA with neutronics, fuel-thermomechanics and thermal-hydraulcis [1] BE and Best Effort coupling capabilities. BE is a coupling representing the most important phenomena with reasonable accuracy and an optimized computational cost. Best Effort is a time consuming coupling with each physic being detailed with few assumptions in order to model as good as possible the phenomena of interest.

In this thesis the Best Effort coupling is established between APOLLO3®, FLICA4 and ALCYONE V1.4 codes respectively as seen in figure 1.17. The coupling scheme starting from HZP initial core conditions involves, at each time step, an initial ALCYONE1 calculations alimenting FLICA4 with the resulting cladding wall heat flux Φ_{wall}. This together with the previous step APOLLO3® results allows FLICA to calculate the cladding wall temperature and coolant density. The cladding wall temperature is given to ALCYONE1 for a second more accurate calculation and the resulting effective fuel temperature calculated by *Rowlands* formula is provided to APOLLO3® together with the coolant density from FLICA4. A new neutronic calculation is performed and the iterations continue until a user defined threshold. All the exchange quantities are spatial fields. The Best Effort coupling scheme is illustrated in figure 1.18.

The BE coupling is between APOLLO3® and FLICA4. The simplified thermal module of FLICA4 is used without mechanical consideration. It is an explicit coupling starting from HZP initial core condition. At first a FLICA4 calculations is performed using the previous step APOLLO3® results for the power injected in the fuel and the fluid. FLICA4 then calculates the temperature distribution in the fuel and the corresponding *Rowlands* effective fuel temperature. It also computes internally the cladding wall heat flux in order to solve the thermal-hydraulics equations and calculate the moderator temperature and density. These results are given APOLLO3® to update the neutronic results before advancing to the new time step. The iterations continue until a user defined threshold is reached. This coupling can be seen in figure 1.19. As in the Best Effort coupling all the exchange quantities are spatial fields.

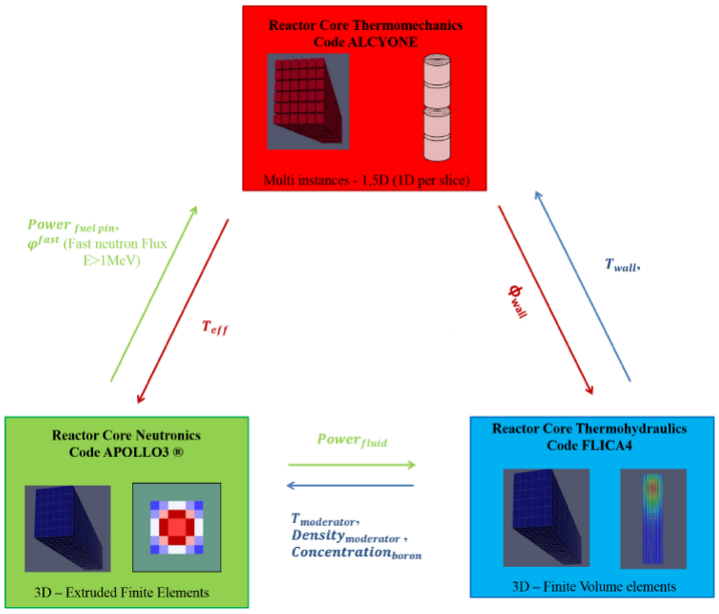

Figure 1.17: CORPUS coupling framework.

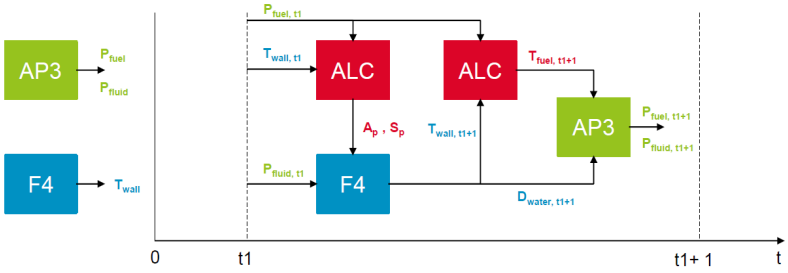

Figure 1.18: Best Effort coupling scheme.

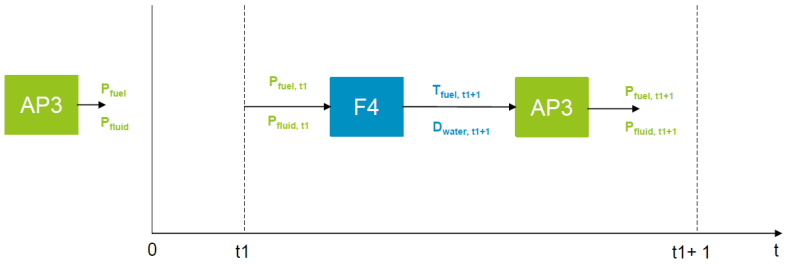

Figure 1.19: BE coupling scheme.

1.8 Best Estimate Plus Uncertainties (BEPU)

BEPU is a systematic approach where calculations taking into account the most important physical phenomena with reasonable approximations and estimation of their respected uncertainties are used for licensing and safety evaluations. The phenomena are usually identified by PIRT[7] approaches. BEPU is a step forward from conservative approaches permitting to reduce the margins in safety criteria as illustrated in figure 1.20. The goal is not to eliminate completely conservatism but

[7] Phenomena Identification and Ranking Table it is an approach applied to different safety scenario. The most important phenomena are identified together with their degree of knowledge or uncertainty.

to minimize it based on our current state of knowledge. It is based on the ALARA (As low as reasonable achievable) principle concerning the radiation risks for human beings and it is a very complex approach evolving in time. Historically the BEPU concept is around for the last 30 years with various documents released by NRC, IAEA and other institutions shaping its form. BEPU has been used in the licensing of two reactors so far: the Angra-2 (Brazil) and the Atucha-2 (Argentina) [54].

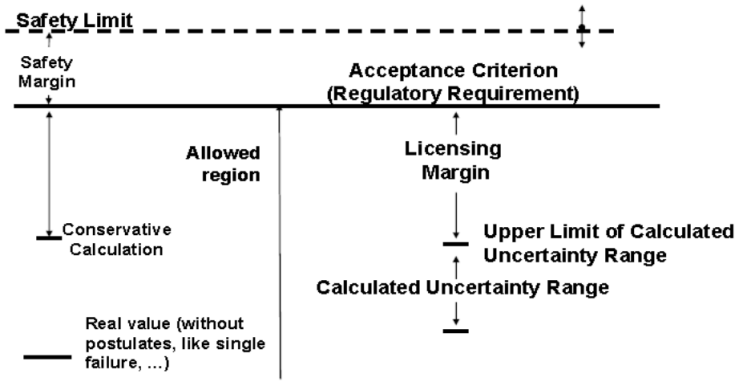

Figure 1.20: Safety margins and acceptance licensing criteria [7].

1.8.1 BEPU short history

The rapid increase of nuclear reactors size in USA (60s) lead to the need of new requirements for safety regulations because the ones applied on smaller scale reactors could not be extrapolated on the new reactors. Based on the principle of defense in depth the US NRC adopted a conservatism approach by the release of 10 CFR 50.46b document and some guidance rules in its appendix-K (70s). In this approach penalized safety acceptance criteria were identified for important quantities of the reactor and basic guidelines for the modeling of important underlying physical phenomena were provided.

The increase in the development of Best Estimate codes (mainly concerning Thermal-Hydraulics) in the 80s highlighted the large margins in the safety calculations. US NRC in 1987 allowed the use of Best Estimate codes together with a validated uncertainty evaluation methodology for safety calculations. This lead to a rapid increase in BEPU research in 90s and the release of CSAU: Code scaling, applicability and uncertainty, a roadmap with 14 general steps that need to be followed for safety calculations. These steps treated aspects of code validation and verification, applicability, scaling distortions, nodalization optimization, uncertainty evaluation and many other. A variation of CSAU with clearer steps was EMDAP: Evaluation model development and assessment process. Both of these were not complete methodologies but roadmaps that the proposed methodologies will need to follow. Since then in USA and Europe a big effort was made to develop consistent BEPU methodologies in the following years. In order to apply and compare the different methodologies international projects like UMS [55] and BEMUSE [56] were created. The results of these projects highlighted the importance of the input uncertainty quantification and the user and code effect. This lead to the PREMIUM benchmark [57] focusing mainly on the input uncertainty quantification of the physical models and comparing the results between the existing methodologies. The results were not satisfactory and the conclusion was that a more systematic approach needed to be defined. This systematic approach was called SAPIUM [58] and is currently under development. Additionally, UAM benchmark [59] was launched and is currently ongoing concerning multiscale and multi-physics uncertainty analysis. Different exercises from separate physics at pin scale to coupled multi-physics at the core scale for both steady state and transient scenarios are included. More details about BEPU evolution are provided in [60].

1.8.2 BEPU types methodologies

Various BEPU methodologies were developed so far across USA and Europe from both industry and research institutions [61], [62]. Most of them follow the CSAU roadmap and can be grouped

in three categories depending on the method used to evaluate the uncertainties: the stochastic propagation of inputs uncertainties (SPIU), the extrapolation of output uncertainty (EOU) also called "propagation of output uncertainties") and the deterministic uncertainty estimation (DUE) [63].

1.8.2.1 Stochastic propagation of input uncertainties

The inputs are treated as uncertain quantities with assigned probability density functions (pdf). Their uncertainties are propagated to the output quantities of interest using the code. Two different general approaches exist. In the first one Monte Carlo sampling is used to approximate the output's pdf by the empirical measure of the output sample. This empirical estimation of expectations or probabilities converge slowly with the sample size[8]. For this reason the usually time consuming code is used to explore the inputs domain and then approximated by a surrogate model that can generate enough evaluations. The empirical measure can then be used to estimate the desired quantile by the empirical quantile. In the second one the non-parametric Wilk's method is applied to get a conservative quantile estimation. More exactly the number of simulations needed to estimate the quantile of interest with a given tolerance is evaluated and the Wilks quantile is then defined as the maximum of the output sample (typically 95% quantile with 95% tolerance is used in nuclear safety studies). This method uses directly the code for the uncertainty propagation. The first approach was used initially in CSAU while later BEPU methodologies like: GRS, IRSN and ENUSA used the second one.

1.8.2.2 Extrapolation of output uncertainty

This method consists in identifying Separate Effect Test (SET) and Integral Test Facilities (ITF) relevant to the under study nuclear power plant and extract experimental data. The code calculation is run on this reduced scale facilities and its discrepancy with the available data is used to quantify the uncertainty in the reduced scale and then extrapolate it to the reactor scale. An emphasis is given on minimizing the user effect on nodalization and on the scalability of the extrapolated uncertainties. UMAE and CIAU are examples of this approach.

1.8.2.3 Deterministic uncertainty evaluation

In this method the code is used to calculate the sensitivity of the inputs on the output and then using the "sandwich rule" estimate the first and second moment of the output. The "sandwich rule" is presented in the following Chapter. The most efficient method uses only two code evaluations, the forward and the adjoint solutions to estimate the sensitivities. This method is well adapted for cases of large systems with many inputs. The Adjoint Sensitivity Analysis Procedure (ASAP) calculates the local sensitivities assuming linear relationship between inputs and output. The Global Adjoint Sensitivity Analysis Procedure (GASAP) generalizes ASAP for critical points in the inputs-output phase-space. Data adjustment and assimilation (DAA) can be used to include knowledge from experimental measurements in a Bayesian framework. CASUALIDAD [64], [65] is an approach that includes ASAP/GASAP and DAA in their uncertainty estimation.

1.8.2.4 Synthetic comparison

Each BEPU methodology for estimating the uncertainty of the safety quantities of interest has advantages and drawbacks. The stochastic propagation of input uncertainties with surrogate models (SPIU-SM) can estimate the complete output's pdf. However, it introduces an additional approximation error due to the use of surrogate models and it depends on the inputs assigned pdf. Besides that, a limited number of inptus must be selected. Stochastic propagation of inputs uncertainties using Wilk's formula (SPIU-WF) does not have the limitation on input's size, does not introduce an additional error and is using an optimal number of code calculations but it is limited to estimate the quantile of an output and it assumes that the inputs' pdf are true. The extrapolation of output uncertainty needs only one core calculation and does not make any assumption on inputs uncertainty but it needs experimental dataset relevant to the safety analysis and the demonstration of scaling. The deterministic uncertainty evaluation needs two code evaluations and thus is well adapted for large scale calculations with many inputs. It can assimilate experimental data to

[8] For a sample size N the empirical mean converges in $1/\sqrt{N}$.

improve the initial input uncertainty quantification. However, it makes assumptions of linearity between inputs and outputs, although for critical points this can be overcome. It requires the codes capabilities of calculating adjoint solutions, something difficult to be implemented in multi-physics transient calculations using coupling of different codes. A synthetic comparison of the methods related to the inputs and outputs uncertainty quantification, the number of code calculations, the possibility of integrating experimental data and their practical implementation is given in table 1.2. A more detailed comparison is provided in [66].

Table 1.2: Comparison of different types of BEPU methodologies

	Inputs	**Outputs**	**Code calculations**	**Experimental data**	**Implementation**
SPIU-SM	pdf	pdf	many	no	easy
SPIU-WF	pdf	quantile	few	no	easy
EOU	none	standard deviation	one	yes	medium
DUE	covariance	covariance	two	potentially	difficult

1.8.3 Sources of uncertainties

In a full core PWR transient analysis there are many sources of uncertainties [67]. The main ones can be grouped in the following categories:

- Modeling: The theoretical equations describing a phenomenon include some assumptions and simplifications. Besides that physical models and correlations induce further errors.
- Input data: Physical (e.g. cross-sections) and technological (e.g. geometries) quantities in the physical models and equations are uncertain. Additionally, boundary and initial conditions are also uncertain. Experimental measurements are usually used to quantify the above mentioned sources of uncertainties introducing potential correlations.
- Nodalization: It involves the different steps for solving a specified modeling introducing errors and uncertainties. The phase space of the equations is discretized and the geometry is homogenized. Sometimes a smaller scale geometry is employed inducing scaling effects. Numerical algorithms are used to solve the equations on the selected discretization. These algorithms converge to approximate solutions.

It is important to highlight that the user effect can have a great impact on the sources of uncertainties (mainly on the modeling and nodalization) due to discrepancies in data interpretation and lack of experience. However, this effect is difficult to quantify.

1.8.4 BEPU research

The continuous development and improvement of BE codes together with increasing BEPU safety needs motivates the currently ongoing research for applying and improving the current methodologies. Some examples of recent works are following. In [68] improvements in thermohydraulic LWR code assessment and validation and in the input uncertainty quantification of the code inputs are presented. FFTB method is used to define the variation ranges of each input. In [69] GRS method is applied for neutronic lattice and core BWR steady state calculations. This method is also applied on PWR transient control rod drop focusing on thermal-hydraulics inputs. In [70] they explore different non-parametric methods alternative to Wilks' formula in a PWR Large-Break LOCA transient. In [71] a BEPU methodology is extended to include knowledge from probabilistic safety analysis and is applied on a PWR "Loss of feed Water" scenario. In [72] a neutronics, fuel-thermomechanics, thermal-hydraulics multi-physics BEPU analysis for PWR Large-Break LOCA transient is performed.

1.9 Motivation and challenges

We saw that in REA strong multi-physics interactions occur between neutronics, fuel-thermomechanics and thermal-hydraulics that need to be modeled in order to predict accurately the transient evolution. We also presented the different state of the art codes, their modeling and the different

available coupling schemes developed at CEA. The motivation of this thesis is to use these modeling advancements in an uncertainty quantification framework. This creates many challenges related to the high computational cost, the large input and output dimensions, dependencies and interactions between inputs and potential non-linearities and discontinuities in the multi-physics transient calculations.

In the previously presented BEPU framework it is clear that there is an effort to develop methodologies for uncertainty analysis with industrial applications that can integrate the modeling advancements of state of the art codes. In this thesis the objective is to explore different statistical tools and different multi-physics coupling schemes to develop an uncertainty quantification methodology (UQM) that could address the challenges facing the REA modeling.

There are three different levels of homogenization for multi-physics transient modeling: the fuel pin, the fuel assembly and the whole core. In an equivalent way we can identify three different levels of uncertainty quantification modeling. These two aspects are used as axes in figure 1.21 where their different possible combinations are illustrated. In order to better illustrate this categorization we focus on the neutronics modeling only.

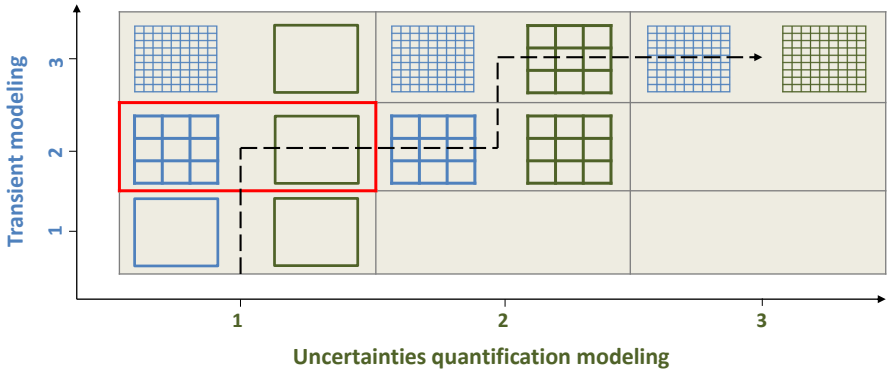

(1, 1)	Point kinetics with uncertainties on the core effective quantities (control rod worth, Doppler coefficient, etc.).
(1, 2)	Assembly level of homogenization with uncertainties on macroscopic cross-section applied homogeneously in the whole core.
(1, 3)	Pin by Pin level of homogenization with uncertainties on macroscopic cross-section applied homogeneously in the whole core.
(2, 2)	Assembly level of homogenization with uncertainties on macroscopic cross-section taking into account spatial correlations.
(2, 3)	Pin by Pin level of homogenization with uncertainties on macroscopic cross-section taking into account spatial correlations.
(3, 3)	Pin by Pin level of homogenization with uncertainties on microscopic cross-sections.

Figure 1.21: Different levels of possible transient (blue) and uncertainty quantification (green) modeling with examples for neutronics. With red borders we highlight the levels used in this thesis.

The first level for transient modeling is the homegenization of the whole core as used in point kinetics. This leads to globally averaged physical quantities. The corresponding level for uncertainty modeling would be the homogeneous application of inputs uncertainties in the whole core. It can be seen as considering the uncertainties spatially fully correlated. The second level for transient modeling is the assembly scale homogenization as presented in the three step deterministic approach of figure 1.7. This creates 3D physical quantities averaged in each assembly. The equivalent uncertainty modeling level would be to consider spatial correlations for the inputs. For example the uncertainty propagation of microscopic cross-sections in lattice calculations can provide estimate of the correlations between macroscopic cross-sections of each assembly. The third level for the transient modeling is the homogenization at a pin scale allowing the representation of

local heterogeneities inside the assembly. This level for uncertainty modeling would be the uncertainty propagation directly from microscopic physical quantities (e.g. microscopic cross-sections in neutronics). The dashed arrow indicates the potential evolution of the transient and uncertainty modeling since we consider that there is no interest for the other modeling combinations. Using this categorization, the REA study of this thesis is situated in the (1, 2) level. We use an assembly scale of homogenization for the transient modeling and we apply the uncertainties homogeneously in the whole core.

Chapter 2

Overview of Uncertainty Quantification Methods

2.1 Introduction

The complexity of Best Estimate (BE) codes increases as we take into account more phenomena. While this results in an improvement of their accuracy, their predictions will still exhibit uncertainties. This is attributed to various reasons among which the main are: physical quantities, technological data, physical modeling and phase space discretization. Moreover, in cases of strong multi-physics coupling interdisciplinary interactions can occur rendering the uncertainty analysis quite challenging. Large input and output dimensions with dependencies and interactions between inputs and non-linear inputs-outputs relationships are some of the main challenges. This highlights the necessity to consider an adequate uncertainty quantification framework, especially for safety calculations. In such a framework different statistical tools are used in order to take into account the input uncertainties, propagate them through the codes to outputs of interest and calculate important statistical quantities. A typical framework for uncertainty quantification is presented in figure 2.1.

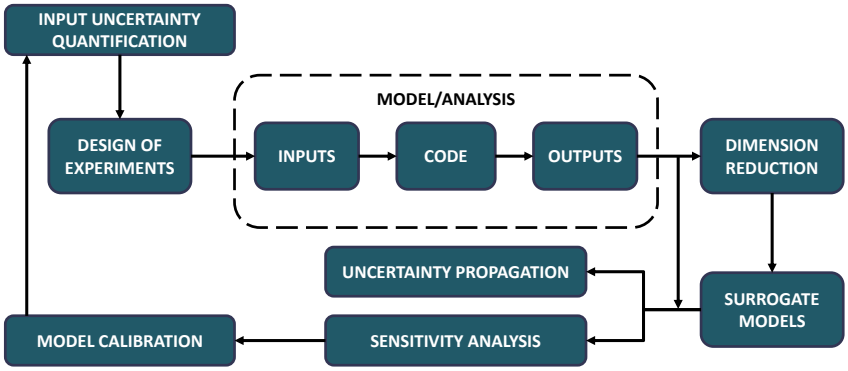

Figure 2.1: Typical uncertainty quantification framework.

The framework consists of different steps that will be detailed in dedicated Sections. The first and central step is the selection of the **Model/Analysis**. The scenario to be studied is defined and the codes that will model it together with their different options and nodalization. The inputs - outputs of interest and the statistical quantities to be studied are identified. This step was mainly discussed in the Chapter 1. For presenting the rest of the steps it is easier to start from the end goals: **Uncertainty Propagation** and **Sensitivity Analysis** discussed in Section 2.3 and Section 2.7 respectively. In the latter the qualitatively or quantitatively outputs sensitivity to each input is estimated while in the former the inputs uncertainties are propagated to the outputs. In order to achieve those goals many code evaluations are needed, something that in most of the cases is prohibitive due to the computational cost of each evaluation. This issue is overcome by using **Surrogate Models** to approximate the underlying function between inputs and outputs. They are detailed in Section 2.5. The design and training of surrogate models can be difficult when the inputs and outputs dimensions are large. To this purpose the **Dimension Reduction** step presented in Section 2.4 aims at identifying a reduced effective input subspace. Code evaluations are needed for the training of the surrogate models. The selection of the inputs points on which the code will be evaluated is called **Design of Experiments (DOE)** and consist the subject of Section 2.6. There are different ways to create DOE but in general it is required that they explore the input space as good as possible. These DOE are called space-filling designs. The inputs probabilistic space from which the DOE will be created is defined in the **Input Uncertainty Quantification** step. Different methods exist that are detailed in Section 2.2. In this thesis we deal with continuous input variables so that their joint distribution is characterized by a joint probability density function (pdf). **Model calibration** discussed in Section 2.8 can be used in order to improve the initial uncertainty quantification of the inputs based on observed data coming from either measurements or from higher fidelity codes. Finally, in the last Section 2.9 of this Chapter we give an overview of some state of the art research related to all these steps of the uncertainty quantification framework.

Before detailing each step we will introduce basic notations and statistical attributes that will be

used in the whole Chapter. We consider the code to be a function between the random input variables $X \in \mathbb{R}^d$ and random output variables $Y \in \mathbb{R}^q$.

$$Y = F(X) : \mathbb{R}^d \to \mathbb{R}^q \tag{2.1}$$

Depending on the case the variables could be scalar ($d, q = 1$) or functional ($d, q >> 1$). Often a dataset of code evaluations will be required to estimate different quantities. We will consider the dataset of size N denoted by $\mathbf{D}_N = \left[\mathbf{X}_n, \mathbf{Y}_n = F(\mathbf{X}_n)\right]_{n=1}^N$. The nth realization of ith input is the scalar X_n^i. The matrix (vector) containing the observations of functional (scalar) input is defined as $\mathbf{X}_{D_N}$ with elements $X_{D_N}^{ij} = X_i^j$ for $i = 1 \dots N$, $j = 1 \dots d$. The functional (scalar) nth realization of the inputs is a vector (scalar) $\mathbf{X_n} = (X_n^i)_{i=1}^d$ of size d while $\mathbf{X}^i = (X_n^i)_{n=1}^N$ is the vector of size N containing the evaluations of the ith scalar variable. Equivalent definitions are considered for the outputs. The pdf of the inputs is denoted by p_X.

Now we will define some basic statistical attributes. We will consider the case of scalar input and output X, Y ($d = q = 1$). The random variable X has mean value μ_X and variance σ_X^2 defined in equations 2.2a and 2.2b together with their empirical estimators $\hat{\mu}_X$, $\hat{\sigma}_X^2$ based on the observed dataset. The former is the expected value of the random variable while the latter is a measure of spreading around its mean value.

$$\mu_X = E[X] = \int X p_X(X) dX, \quad \hat{\mu}_X = \frac{1}{N} \sum_{i=1}^N X_i \tag{2.2a}$$

$$\sigma_X^2 = Var(X) = E[(X - E[X])^2] = \int (X - \mu_X)^2 p_X(X) dX, \quad \hat{\sigma}_X^2 = \frac{1}{N-1} \sum_{i=1}^N (X_i - \hat{\mu}_X)^2 \tag{2.2b}$$

The covariance c_{XY} between the two random variables X, Y is defined in equation 2.3a and its empirical estimator $\hat{c}_{XY}$ in equation 2.3b.

$$c_{XY} = Cov(X, Y) = E[(X - E[X])(Y - E[Y])] \tag{2.3a}$$

$$\hat{c}_{XY} = \frac{1}{N-1} \sum_{i=1}^N (X_i - \hat{\mu}_X)(Y_i - \hat{\mu}_Y) \tag{2.3b}$$

The covariance can be normalized between -1 and 1 in what it is called the correlation coefficient ρ_{XY} defined in equation 2.4 together with its empirical estimator. A value of zero indicates no correlation. The correlation increases as the absolute value of the coefficient increases towards 1. It is important to notice that uncorrelated variables do not imply that they are independent while independent variables are necessary uncorrelated.

$$\rho_{XY} = \frac{c_{XY}}{\sigma_X \sigma_Y}, \qquad \hat{\rho}_{XY} = \frac{\hat{c}_{XY}}{\hat{\sigma}_X \hat{\sigma}_Y} \tag{2.4}$$

Another statistical quantity of the random variable X is the quantile x_a, which is defined as the value of the random variable for which $P(X \leq x_a) = a$. For example if $a = 95\%$ then x_{95} is the quantile and the random variable has 95% of being less than this value.

$$P(X \leq x_{95}) = 0.95 \tag{2.5}$$

Finally, the notion of confidence intervals is related to an empirical estimation of a statistical quantity (e.g. mean, variance, quantile). It is independent of the quantity to be estimated and depends only on the sample used for the estimation. For example a 95% confidence interval for the mean value μ_X based on the dataset will be $[\hat{a}^N, \hat{b}^N]$, where the $\hat{a}^N$ and $\hat{b}^N$ depend only on the dataset, is such that:

$$P(\mu_X \in [\hat{a}^N, \hat{b}^N]) \geq 0.95 \tag{2.6}$$

2.2 Input uncertainty quantification

There are various sources of uncertainties in the inputs variables of a physical phenomenon modeling. In general two broad types are distinguished:

- **Stochastic (aleatoric) uncertainty:** concerning variables that show natural variability. This means that for the same physical phenomenon and conditions these variables will vary stochastically (e.g. temperature of a room).
- **Epistemic uncertainty:** related to variables that have an uncertainty due to lack of knowledge (e.g. constant variable in a physical law). This uncertainty is reducible by acquiring more observations and insights about the physical phenomenon.

The first step of the uncertainty analysis is the quantification of the input uncertainties. In literature [73] different approaches exist based on the prior available knowledge and on the nature of the uncertain variables.

2.2.1 Experts judgment

If not much is known for the uncertainty of a variable and no experimental observations are available then the uncertainty can be quantified from experts based on experience and intuition. If some information is known about the behavior of the uncertainty (e.g. moments, positiveness, bounds) then the principle of maximum entropy can be used to assess the most appropriate pdf. The differential entropy for the scalar variable X with pdf p_X is defined in equation 2.7.

$$H(X) = -\int_{-\infty}^{\infty} p_X(X) \log\left(p_X(X)\right) dX \tag{2.7}$$

For example in the case where we know that the variable is centered around a mean value μ_X with variance σ_X^2 and that there are no bounds the equation 2.7 is maximized with the following constraints:

$$\int_{-\infty}^{\infty} p_X(X)dX = 1, \quad \int_{-\infty}^{\infty} X p_X(X)dX = \mu_X, \quad \int_{-\infty}^{\infty} (X-\mu_X)^2 p_X(X)dX = \sigma_X^2$$

The Lagrange multipliers method can be used to maximize the entropy under these equality constraints. The objective function for the optimization J and its derivative with respect to p_X are shown in equations 2.8a and 2.8b.

$$\begin{aligned} J(p_X) = &-\int_{-\infty}^{\infty} p_X(X) \log\left(p_X(X)\right) dX + \lambda_0 \left(\int_{-\infty}^{\infty} p_X(X)dX - 1\right) \\ &+ \lambda_1 \left(\int_{-\infty}^{\infty} X p_X(X)dX - \mu_X\right) + \lambda_2 \left(\int_{-\infty}^{\infty} (X-\mu_X)^2 p_X(X)dX - \sigma_X^2\right) \end{aligned} \tag{2.8a}$$

$$\frac{\partial J(p_X)}{\partial p_X dX} = -\log\left(p_X(X)\right) - 1 + \lambda_0 + \lambda_1 X + \lambda_2 (X-\mu_X)^2 \tag{2.8b}$$

By taking $\frac{\partial J(p_X)}{\partial p_X} = 0$ the pdf that maximizes the entropy takes the form of equation 2.9.

$$p_X(X) = e^{\lambda_0 - 1 + \lambda_1 X + \lambda_2 (X-\mu_X)^2} \tag{2.9}$$

The pdf is replaced in the equality constraints in order to calculate the Lagrange multipliers. This results in the values $\lambda_0 - 1 = log(\frac{1}{\sqrt{2\pi}\sigma_X})$, $\lambda_1 = 0$, $\lambda_2 = -\frac{1}{2\sigma_X^2}$. The obtained pdf is the normal distribution $\mathcal{N}(\mu_X, \sigma_X^2)$ with mean μ_X and variance σ_X^2.

$$p_X(X) = \frac{1}{\sqrt{2\pi}\sigma_X} e^{-\frac{(X-\mu_X)^2}{2\sigma_X^2}} \tag{2.10}$$

In a similar way the pdf maximizing the entropy with other information can be derived. For example if the distribution is bounded in $[a, b]$ then the maximum entropy pdf is the uniform distribution in this bounds $\mathcal{U}(a, b)$.

2.2.2 Statistical inference

In the case where enough observations exist the pdf can be inferred through parametric and non-parametric methods. The parametric methods assume the pdf of the random scalar variable X to belong to a family of pdfs $p_X(X, \boldsymbol{\theta})$ with hyperparameters $\boldsymbol{\theta}$ that are usually estimated by two possible methods. The first one is the **Method of Moments** where $\boldsymbol{\theta}$ is estimated by equating the moments of the analytic distributions with the empirically estimated moments (equations 2.2a and 2.2b). The second one is the **Maximum Likelihood**. The observations are considered independent and identically distributed (i.i.d) and thus the likelihood of obtaining them is:

$$L(\boldsymbol{\theta}, \mathbf{X}_{D_N}) = \prod_{i=1}^{N} p_X(X_i, \boldsymbol{\theta}) \tag{2.11}$$

The $\boldsymbol{\theta}$ is estimated by maximizing this likelihood function. Usually the log likelihood is used because it is easier to maximize:

$$\hat{\boldsymbol{\theta}}^{ML} = \underset{\boldsymbol{\theta} \in \Theta}{\operatorname{argmax}} \left(\sum_{i=1}^{N} \log \left(p_X(X_i, \boldsymbol{\theta}) \right) \right) \tag{2.12}$$

The non-parametric methods do not assume that the pdf belongs to some predefined family of distributions but instead estimates it directly from the observations. Their main drawback is that they need many observations for the estimation to converge. The **Histogram** is an example of such method, where the variable domain is divided into bins and the probability of each bin is estimated by counting the percentage of the observations falling into this bin. A better method is the **Kernel Smoothing** where the pdf is estimated through a kernel function. For a function k_X to be used as kernel it needs to be positive and normalized to $\int_{-\infty}^{\infty} k_X(X) dX = 1$. The pdf estimation using a Gaussian kernel of isotropic variance σ_h^2 is expressed as:

$$\hat{p}_X = \frac{1}{Nh} \sum_{i=1}^{N} \left(\frac{1}{\sqrt{2\pi}\sigma_h} e^{-\frac{(X - X_i)^2}{2\sigma_h^2}} \right) \tag{2.13}$$

2.2.3 Bayesian inference

This method uses observations of the random variable to improve prior knowledge about its pdf. The posterior pdf is calculated based on the Bayes' rule. For example let us assume that the variable pdf as previously belongs to a specific pdf family $p_X(X, \boldsymbol{\theta})$ with hyperparameters $\boldsymbol{\theta}$. In addition, we assume that the prior knowledge for $\boldsymbol{\theta}$ is described by its corresponding pdf $p_\theta(\boldsymbol{\theta})$. The posterior pdf of $\boldsymbol{\theta}$ (i.e. the pdf of the distribution of the hyperparameters given the data) then is described by:

$$p_\theta^{post}(\boldsymbol{\theta}) = \frac{L(\boldsymbol{\theta}, \mathbf{X}_{D_N}) p_\theta(\boldsymbol{\theta})}{\int_{-\infty}^{\infty} L(\boldsymbol{\theta}', \mathbf{X}_{D_N}) p_\theta(\boldsymbol{\theta}') d\boldsymbol{\theta}'} \tag{2.14}$$

The likelihood L is the same as the one defined in the Section 2.2.2. The posterior distribution of X can be integrated then through $p_X^{post}(X) = \int_{-\infty}^{\infty} p_X(X, \boldsymbol{\theta}) p_\theta^{post}(\boldsymbol{\theta}) d\boldsymbol{\theta}$. Usually this is not done but instead an estimator $\hat{\boldsymbol{\theta}}$ is used e.g. maximum a posteriori (MAP).

2.2.4 Stochastic inverse

In some cases it is very difficult to obtain observations for an input variable or even impossible (e.g. empirical correlations uncertainties) but it can be easy to obtain observations for some outputs. Thus through inverse uncertainty propagation the input variables pdf can be estimated. It is used often in model calibration which we will detail in Section 2.8. Bayesian approaches are used as previously with the difference that the likelihood now is described by the model relating the inputs to the outputs. Usually instead of using the integrals for the calculation of the posterior distribution it is sampled using Markov Chain Monte Carlo techniques (MCMC).

2.3 Uncertainty propagation

In this section we are interested in studying the model of equation 2.1 behavior with regards to uncertainty. We already saw that the input of the model X can be uncertain. The model's output Y, considered scalar, is a random quantity due to the propagation of uncertainty from the inputs through the code and to the output. The goal of the uncertainty propagation is to estimate the pdf of the output p_Y or some quantities of interest (e.g. mean, variance). Based on this, uncertainty propagation methods can be clustered in the following categories:

- **Statistical moments analysis:** the goal is to calculate or estimate the statistical moments of the output (usually mean and variance). Different methods exist based on quadrature, Monte Carlo simulations or Taylor expansions.
- **Reliability analysis:** the aim is to calculate the probability of Y exceeding a threshold. Usually it is a rare event corresponding to the tail of p_Y.
- **Probability density function analysis:** here the goal is to estimate the whole pdf of the output. It is evident that this case encompasses the two previous ones. Monte Carlo simulations are used to estimate this pdf.

2.3.1 Monte Carlo simulation

Random sampling of inputs and outputs are evaluated and gathered in the previously defined dataset of size N. The output's mean μ_Y and variance σ_Y^2 can be estimated through equations 2.2a and 2.2b. It is important to note that this method does not require any regularity on F and that the convergence is independent of the dimension of X but slow ($1/\sqrt{N}$ for any empirical estimator). For each estimated statistical quantity confidence intervals can be computed using the Central Limit Theorem (CLT) [74]. We assume that the output is i.i.d and thus the variance of the mean estimator becomes:

$$Var(\hat{\mu}_Y) = Var\left(\frac{1}{N}\sum_{n=1}^{N} Y_n\right) = \frac{1}{N^2}\sum_{n=1}^{N} Var(Y_n) = \frac{1}{N^2} N\sigma_Y^2 = \frac{\sigma_Y^2}{N} \tag{2.15}$$

The CLT states that the sum of i.i.d variables, as is the case $\hat{\mu}_Y$, follows a normal distribution described by equation 2.16.

$$\frac{\sqrt{N}(\hat{\mu}_Y - \mu_Y)}{\sigma_Y} \sim \mathcal{N}(0,1) \tag{2.16}$$

We know from the law of large numbers that $\hat{\sigma}_Y/\sigma_Y \to 1$ and with the use of Slutsky's theorem we obtain:

$$\frac{\sqrt{N}(\hat{\mu}_Y - \mu_Y)}{\hat{\sigma}_Y} \sim \mathcal{N}(0,1)$$

This allows us to calculate confidence intervals for the mean value. For example the 95% confidence interval will be:

$$P(\mu_Y \in [\hat{\mu}_Y - 1.96\frac{\hat{\sigma}_Y}{\sqrt{N}}, \hat{\mu}_Y + 1.96\frac{\hat{\sigma}_Y}{\sqrt{N}}]) \simeq 0.95$$

The variance estimator $\hat{\sigma}_Y^2$ distribution is more complicate to calculate and it depends on the kurtosis (fourth statistical moment). For the specific case of normal distribution for Y and with large N the distribution can be approximated by:

$$\hat{\sigma}_Y^2 \approx \mathcal{N}(\sigma_Y^2, \frac{2\sigma_Y^4}{N-1})$$

The complete pdf of Y can be estimated as well through statistical inference and the cumulative distribution function (CDF) can be computed easily in order to calculate quantiles.

2.3.2 Integration methods

In this method the moments are estimated by the evaluation of the integrals. For the mean and variance it is the integrals of equations 2.2a and 2.2b. In rare cases of the integrals can be computed analytically. In most cases this is impossible and thus quadrature is used to approximate the integral through a sum of weighted code evaluations. If the input variables are i.i.d, the weighted sums are shown in equations 2.17a and 2.17b with w_i and X_i the corresponding weights and quadrature points. The weights and points depend on the marginal input pdfs and in these equations identical pdf are considered.

$$\tilde{\mu}_Y = \sum_{i_1=1}^{N} \cdots \sum_{i_d=1}^{N} w_{i_1} \dots w_{i_d} F(X_{i_1}^1, \dots, X_{i_d}^d) \tag{2.17a}$$

$$\tilde{\sigma}_Y^2 = \sum_{i_1=1}^{N} \cdots \sum_{i_d=1}^{N} w_{i_1} \dots w_{i_d} \left(F(X_{i_1}^1, \dots, X_{i_d}^d) - \tilde{\mu}_Y\right)^2 \tag{2.17b}$$

This method requires some regularity conditions on the underlying function to be integrated and it can be applied in cases of low dimensionality due to the numerous model evaluations needed. Sparse quadratures are used to in order to alleviate the last drawback.

2.3.3 Perturbation methods

If the model is close to linear it can be written as linear combination of the inputs with weights their partial derivatives. This method requires the calculations of all the partial derivatives of the model $\frac{\partial F}{\partial X^i}$ and the evaluation of the model on the mean input vector μ_X. If the covariance matrix of the inputs is C_X, and the vector of size d containing the partial derivatives evaluated at μ_X is S_X then the estimators for the mean and variance of the output are the following:

$$\hat{\mu}_Y = F(\mu_X) \tag{2.18}$$

$$\hat{\sigma}_Y^2 = S_X^T C_X S_X \tag{2.19}$$

$$S_X = \begin{bmatrix} \frac{\partial F}{\partial X_1}(\mu_X) \\ \frac{\partial F}{\partial X_2}(\mu_X) \\ \vdots \\ \frac{\partial F}{\partial X_d}(\mu_X) \end{bmatrix} \tag{2.20}$$

The estimator of the variance in equation 2.19 is also called "*Sandwich rule*". Usually the derivatives of the model are approximated by a first order Taylor expansion or by adjoint calculations based on generalized perturbation theory. This method is fast because it needs only $d+1$ model evaluations (in the case of adjoint only 2) and it can calculate the first and second moments. It has the constraint of the model to be linear or at least to be linearized.

2.3.4 Reliability methods

To compute rare events or failure probabilities can be quite costly for Monte Carlo methods due to slow convergence. In this case First and Second order of Reliability Methods (FORM/SORM) [73] give an approximation of those probabilities with reduced computational cost. These methods are based on a transformation of the input parameters in the standard normal space followed by an approximation of the failure domain by a domain whose boundary is a hyperplane (FORM) or a quadratic surface (SORM). Then the probability can be evaluated with integration on the standard normal space.

2.4 Dimension reduction

Many statistical analyses suffer from the "curse of dimensionality". When the inputs or outputs are functional quantities then there is a strong interest in dimension reduction techniques. Such techniques aim at reducing the effective dimensions of the functional quantity. With the term effective we mean either by restricting the dimension reduction on the variables of interest or by transformation to variables where dimension reduction is more efficient. There are two broad categories of dimension reduction techniques. The first one is based on screening and the sensitivity between inputs and outputs are qualitatively estimated to discarding the non important inputs. In this Section we focus on the second one which is better adapted for functional quantities. It is called feature selection and we will detail two methods that use information from potential correlations which is often the case for spatial or temporal quantities. The Principal Component Analysis (PCA) that can be applied independently to inputs or outputs. It identifies hyperplanes of maximum variance in the functional space. For a specific reduction size the PCA is the method that explains better the approximated functional quantity in terms of mean square error. The Partial Least Square (PLS), proposed by [75], is a method that finds a linear regression between projections of inputs and outputs that maximize their cross-covariance. Synthetically we can say that PCA reduces the functional dimension in an optimal way with respect to the functional variance while PLS reduces dimension by taking into account the relationship between inputs and outputs and assuming it is linear.

2.4.1 Principal Components Analysis (PCA)

It is a method closely linked with Karhunen-Loève (KL) decomposition [76], where a stochastic process is represented by a linear combination of infinite orthogonal basis functions. The basis functions are not predefined but depend on the stochastic process itself. They are the eigenfunctions corresponding to the covariance function of the stochastic process. PCA can be seen as the discretized version of KL [77]. We consider the functional output Y, which means that it is $\mathbb{R}^q$-valued with $q >> 1$, as a discretized stochastic field. PCA is applied, without loss of generality, on centered processes. To this purpose, from the collected N evaluations $\mathbf{Y}_{D_N}$ in a $N \times q$ matrix the empirical mean vector is estimated $\hat{\boldsymbol{\mu}}_{\boldsymbol{Y}}$ and extracted to create the centered around zero matrix $\mathbf{Y}_{c,N}$. PCA finds the orthogonal linear projection of $\mathbf{Y}_{c,N}$ where the basis vector are called principal components and express the functional variance in a descending order. These basis vectors are the eigenvectors of $\mathbf{Y}_{c,N}$ covariance matrix. If $\mathbf{Y}_{c,N}$ has strong correlations the number of principal components needed to represent most of the variance can be quite small. This is carried out by first computing the empirical covariance matrix and its eigenvalue decomposition. The $q \times q$ matrix $\mathbf{W}$ contains the eigenvectors, with ith eigenvector at the ith column, and the $q \times q$ diagonal matrix $\mathbf{\Lambda}$ contains the eigenvalues with the ith one on Λ^{ii}. The eigenvalues represent the variance explained by each eigenvector/principal component and are in a descending order. The transformed coordinates of the original quantity in the projected space $\mathbf{T}$ are called scores.

$$\mathbf{C} = \frac{\mathbf{Y}_{c,N}^T \mathbf{Y}_{c,N}}{N}, \quad \mathbf{C} = \mathbf{W}\mathbf{\Lambda}\mathbf{W}^{-1}, \quad \mathbf{T} = \mathbf{Y}_{c,N}\,\mathbf{W} \tag{2.21}$$

Using predefined variance explanation threshold (e.g. 99%) the $l << q$ first eigenvectors needed for this variance representation are kept only. This can result in a significantly reduced projected space $(N \times l)$. An approximation of the original observations $\tilde{\mathbf{Y}}_{D_N}$ can be calculated by the truncated matrices $\mathbf{T_l}$ $(N \times l)$, $\mathbf{W_l}$ $(q \times l)$ and the extracted mean vector through equation 2.22. $\mathbf{M_Y}$ is the matrix of size $N \times q$ with each row containing the mean vector $\hat{\boldsymbol{\mu}}_{\boldsymbol{Y}}$.

$$\tilde{\mathbf{Y}}_{D_N} = \mathbf{T_L}\mathbf{W_L}^T + \mathbf{M_Y} \tag{2.22}$$

The truncated eigenvectors matrix is stored and the functional quantity can be reduced to few scalar quantities represented by the scores. For example if a prediction at a new point $\mathbf{X}_{new}$ is sought then it suffices to construct a surrogate model to approximate the underlying function between the inputs and the scores. This will allow to predict the corresponding scores for the new point and calculate the predicted $\tilde{\mathbf{Y}}_{new}$ from equation 2.22.

2.4.2 Partial Least Squares (PLS)

PLS shares some similarities with PCA in the sense that it finds as well linear projections of the functional quantities. The difference is that it does not aim at finding the projections representing the maximum variance of a functional quantity but instead aims at taking into account the relation between two functional quantities by finding their projections that maximize the cross-covariance. It is essentially a linear regression in the projected input and output spaces. We consider X and Y as both functional inputs and outputs ($d >> 1, q >> 1$). PLS decomposes them through equations 2.23a and 2.23b with a predefined dimension reduction size set to l.

$$\mathbf{X} = \mathbf{T_X}\mathbf{P_X^T} + \mathbf{E_X} \tag{2.23a}$$

$$\mathbf{Y} = \mathbf{T_Y}\mathbf{P_Y^T} + \mathbf{E_Y} \tag{2.23b}$$

Where $\mathbf{T_X}$ and $\mathbf{T_Y}$ are matrices of size $N \times l$ representing the coordinates of X and Y in their projected reduced spaces of dimension $l << d, q$. $\mathbf{P_X^T}$ and $\mathbf{P_Y^T}$ are the orthogonal matrices of size $d \times l$ containing the projection basis vectors. $\mathbf{E_X}$ and $\mathbf{E_Y}$ are the residual errors assumed i.i.d. normal variables. The decomposition is perform in such a way that maximizes the cross-covariance between $\mathbf{T_X}$ and $\mathbf{T_Y}$. Different iterative algorithms exist for the computation of $\mathbf{T_X}$, $\mathbf{T_Y}$, $\mathbf{P_X^T}$ and $\mathbf{P_Y^T}$ [78].

2.4.3 Stochastic warping

PCA and PLS are simple and powerful techniques to reduce dimensions. Nevertheless, in some cases they might require many scores that can have complicated relationships with the inputs. This creates difficulties in their approximation by surrogate models and increases the prediction error. To overcome this a stochastic warping can be applied. This method for temporal functional quantities is used and detailed in [79]. It consists in applying a translation and scaling of the observations prior to the dimension reduction. This is performed by a change of variable. Considering the functional output $Y(u, \omega)$ as a stochastic process with u the variable of the field of size q (e.g. time, space) and ω the sample space. $Y(u, \omega_n) = \mathbf{Y}_n$ is the nth stochastic functional realization and $Y(u_i, \omega) = Y^i$ is the scalar ith random variable. The change of variable is seen in equations 2.24a and 2.24b, where the variable u is replaced by v a linear function of u and ω.

$$\tilde{Y}(v, \omega) = Y(u, \omega) \tag{2.24a}$$

$$v(u, \omega) = Q_\omega u + D_\omega \tag{2.24b}$$

For the thesis purposes we will focus only in the case of translation, meaning that $Q_\omega = 1$, reducing the unknown to only D_ω. This translation is a random variable and must be computed for each sample. There are various methods to do so and we will limit to presenting the two most relevant for the thesis. In the first method a weighted average field value is calculated for each sample of the dataset $\mathbf{Y}_{D_N}$ through equation 2.25.

$$u_{m,\omega} = \frac{\sum_{i=1}^{q} u_i Y(u_i, \omega)^2}{\sum_{i=1}^{q} Y(u_i, \omega)^2} \tag{2.25}$$

Then a reference field u_r is selected as the empirical mean of $u_{m,\omega}$ and the translation D_ω is defined as the difference of each sample's averaged field value to the reference one.

$$D_\omega = u_{m,\omega} - u_r \quad , \quad u_r = \frac{1}{N}\sum_{n=1}^{N} u_{m,\omega_n} \tag{2.26}$$

In the second method the translation is the result of an optimization process. The function to be optimized is a function of similarity c of each sample to a reference one. The empirical mean of Y denoted by $\hat{\mu_Y}(u)$ is used as the reference function. D_ω is the the optimal value D that maximizes the function c.

$$c(D) = \frac{\sum_{i=1}^{q} Y(u_i + D, \omega)\hat{\mu}_Y(u_i)}{\sqrt{\sum_{i=1}^{q} Y(u_i + D, \omega)^2}\sqrt{\hat{\mu}_Y(u_i)^2}} \tag{2.27}$$

$$D_\omega = \underset{D}{\operatorname{argmax}}\, c(D)$$

Once the values of D_ω are computed, with one of the two methods, the translation in equations 2.24a and 2.24b is performed. The stochastic process now is centered and dimension reduction can be applied on $\tilde{Y}$ more efficiently. In order to make predictions for new input design points an additional surrogate model must be constructed between the model inputs X and the field translation values D_ω. The prediction for a new input value $\mathbf{X}_{new}$ will give a predicted field translation D_{new} that will be applied on the predicted centered field $\tilde{\mathbf{Y}}_{new}$ using the scores of the dimension reduction method. Finally the inverse translation is applied to retrieve the original functional output $\mathbf{Y}_{new}$ through equation 2.28.

$$\mathbf{Y}_{new}(u) = \tilde{\mathbf{Y}}_{new}(\upsilon - D_{new}) \tag{2.28}$$

In the process of the translation in the discrete case it is clear that depending on the translation, field values will be missing from the beginning or the end of the field space. To overcome this the last value is extended until the start or the end of the field limits.

2.5 Surrogate models

The code usually is based on a set of discretized equations in space (3D) and time. In order to solve them, various numerical methods are applied that can become very time consuming. This acts as a budget constraint for analyses that require numerous code evaluations like Monte Carlo uncertainty propagation or sensitivity analysis. Surrogate models are used to alleviate this budgetary constraint by approximating the inputs-outputs underlying function. They are constructed based on a inputs-outputs dataset, usually obtained from specific DOE that are detailed in the Section 2.6. The code is considered as a black-box and the surrogate models are simple analytic functions (e.g. polynomials) permitting very fast evaluations of new points. There are plenty of possible models. We will focus on four of them: generalized linear models [80], polynomial chaos expansion (PCE) [73] [81] [82], kriging [83] [84] and artificial neural networks (ANN) [80]. Before presenting the different surrogate models it is important to highlight that the approximation induces an error that must be estimated. We will detail different ways to estimate this error. For the whole Section a scalar output is considered $Y = F(X)$ and the surrogate model is denoted by $\tilde{F}(X)$ constructed on the dataset $\mathbf{D}_N$ of size N.

2.5.1 Error evaluation

The induced approximation error by the surrogate model is defined as:

$$\varepsilon(X) = F(X) - \tilde{F}(X) \tag{2.29}$$

Three different error estimators are considered. The first one is the interpolation error. It is the mean square error on the dataset used for the surrogate model construction and is estimated empirically through the following equation:

$$\varepsilon_{int} = \frac{1}{N}\sum_{n=1}^{N}(F(\mathbf{X}_n) - \tilde{F}(\mathbf{X}_n))^2 \tag{2.30}$$

The error is usually normalized to the output's variance empirical estimator $\hat{\sigma}_Y^2$. The R_{int}^2 quantity representing the percentage of the output's variance represented by the surrogate model is computed as well.

$$R_{int}^2 = 1 - \frac{\varepsilon_{int}}{\hat{\sigma}_Y^2} \tag{2.31}$$

A value close to 1 indicates indicates how well the surrogate model interpolates on the dataset. It is a cheap estimator because it does not need any other code evaluations but it does not quantify well the predictive capability of the surrogate model on new input points due to the overfitting.

The second error estimator is the prediction error. It is the mean square error on a new dataset $D'_M = \left[\mathbf{X}'_m, \mathbf{Y}'_m = F(\mathbf{X}'_m)\right]_{m=1}^{M}$ of size M not seen by the surrogate model. It is exactly the same equations as the interpolation error but on this new dataset.

$$\varepsilon_{pred} = \frac{1}{M}\sum_{m=1}^{M}(F(\mathbf{X}'_m) - \tilde{F}(\mathbf{X}'_m))^2 \tag{2.32}$$

$$R^2_{pred} = 1 - \frac{\varepsilon_{pred}}{\hat{\sigma}^2_Y} \tag{2.33}$$

The prediction error is a good estimator of the surrogate model's predictive capability but requires code evaluations on a new dataset, something time consuming and in some cases even not feasible.

Finally, the third error estimator used in the thesis is the Leave-One-Out (LOO), where for each point i of the original dataset of size N the surrogate model is constructed based on all the points except i. The response of this model is called $\tilde{F}^{\sim i}(X)$ and the error on the prediction of the ith point is calculated. The mean square error for all i leads to the LOO error estimator of equation 2.34 and its corresponding R^2_{loo} quantity in equation 2.35.

$$\varepsilon_{loo} = \frac{1}{N}\sum_{i=1}^{N}(F(\mathbf{X}_i) - \tilde{F}^{\sim i}(\mathbf{X}_i))^2 \tag{2.34}$$

$$R^2_{loo} = 1 - \frac{\varepsilon_{loo}}{\hat{\sigma}^2_Y} \tag{2.35}$$

This estimator is a compromise between the two previous ones. It has better predictive capabilities than the empirical error but not as good as the prediction error. It does not require new code evaluations but N surrogate models must be constructed. Depending on the surrogate model used there are analytic equations to compute it directly.

2.5.2 Generalized Linear Models (GLM)

This methods considers that $Y = F(X)$ can be approximated by a linear combinations of p predefined functions $[h_i(X)]_{i=0}^{p}$. The first function is assumed to be the constant $h_0(X) = 1$. The output can be expressed by:

$$Y = \tilde{F}(X) + \varepsilon = \sum_{i=1}^{p}\beta_i h_i(X) + \varepsilon \tag{2.36}$$

Where β_i is the unknown coefficients associated to each function and ε the residual error. Using now the dataset $\mathbf{D}_N$ we define $\mathbf{H}$ the matrix of size $N \times p$ containing the function evaluations on this dataset $H^{ij} = h_j(\mathbf{X}_i)$. The unknown coefficients vector of size p is denoted by $\boldsymbol{\beta}$ while the residual error vector by $\boldsymbol{E} = (\varepsilon_i)_{i=1}^{N}$.

$$\mathbf{Y_{D_N}} = \mathbf{H}\boldsymbol{\beta} + \boldsymbol{E} \tag{2.37}$$

The most used estimator of the coefficients is the least squares one, where the residual sum of square errors $\sum_{i=1}^{N}\varepsilon_i^2$ is minimized. The resulting estimator is described in equation 2.38.

$$\hat{\boldsymbol{\beta}} = (\mathbf{H}^T\mathbf{H})^{-1}\mathbf{H}^T\mathbf{Y_{D_N}} \tag{2.38}$$

If the model of equation 2.36 is correct with normal residual error $\varepsilon \sim \mathcal{N}(0, \sigma^2)$ then the coefficients estimator is also a normal random variable $\hat{\boldsymbol{\beta}} \sim \mathcal{N}(\boldsymbol{\beta}, (\mathbf{H}^T\mathbf{H})^{-1}\sigma^2)$. The Gauss-Markov theorem shows that the least square estimator of the coefficients is the Best Linear Unbiased Estimator (BLUE). Nevertheless, by using other biased estimator like Ridge regression or Lasso smaller residual errors can be achieved. More details about those estimators can be found in [80].

2.5.3 Polynomial Chaos Expansion (PCE)

PCE belongs to the general category of spectral representation methods. The random response Y is expanded through equation 2.39, where ϕ_α are the basis functions spanning the Hilbert functional subspace L^2 with measure density equal to the joint pdf of X.

$$Y = \tilde{F}(X) + \varepsilon = \sum_{\alpha \in \mathbb{N}^d} w_\alpha \phi_\alpha(X) + \varepsilon \tag{2.39}$$

The output is considered a scalar second-order random quantity satisfying $E[Y^2] < \infty$. For independent inputs $X^i, i = 1 \dots d$ their multivariate pdf $p_X(X)$ can be written as products of the marginals pdf p_{X^i}:

$$p_X(X) = \prod_{i=1}^{d} p_{X^i}(X^i) \tag{2.40}$$

In the marginal Hilbert functional subspace L_i^2 with measure density equal to the marginal pdf p_{X^i} we assume ϕ_j^i a complete family of orthonormal basis functions with $j \in \mathbb{N}$:

$$< \phi_s^i, \phi_t^i >_H = \int_{\mathbb{R}} \phi_s^i(X_i) \phi_t^i(X_i) p_{X^i}(X^i) dX^i = \delta_{st} \tag{2.41}$$

It can be shown that the tensor product of these marginals bases is a basis of the original Hilbert space and thus:

$$\phi_\alpha(X) = \prod_{i=1}^{d} \phi_{\alpha_i}(X^i) \tag{2.42}$$

where $\alpha = (\alpha_1, \dots, \alpha_d) \in \mathbb{N}^d$ is a vector index of the corresponding univariate bases indices $\alpha_i = j$ of ϕ_j^i. The output then has the spectral decomposition of equation 2.39.

Having made those assumptions the univariate functions are selected as orthonormal polynomials that can be derived from the marginals pdf of the inputs. If the input are independent with Gaussian distribution then the obtained polynomials are the Hermite polynomials visualized in figure 2.2 and the expansion of the output Y is called polynomial chaos expansion.

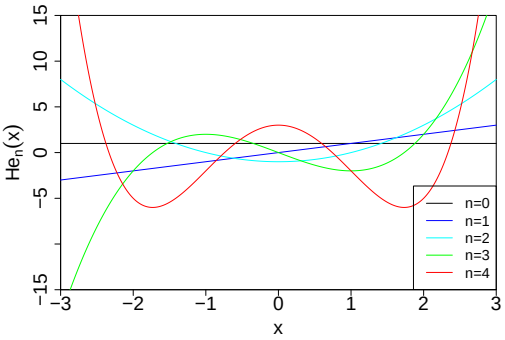

Figure 2.2: hermite polynomials $He_n(x)$ up to fourth order ($n = 4$).

In the case of dependent parameters either a transformation is performed to render them independent similar to the PCA projection or different marginal basis functions have to be calculated that are no longer polynomials. The next step to build the PCE is to truncate the expansion in order to get a tractable form for the surrogate model (with a finite number of coefficients to estimate). A usual truncation law is:

$$A_q^{d,p} = \{ \quad \boldsymbol{\alpha} \in \mathbb{N}^d : \left(\sum_{i=1}^{d} \alpha_i^q \right)^{1/q} \leq p \quad \}$$

Where p is the maximum total degree of the multivariate polynomial basis and $q \in [0, \infty]$ is the index of isotropic reduction. For $q = 1$ the total number of polynomials to be evaluated is $(d+p)!/d!p!$. The final formulation of the truncated PCE is:

$$Y = \tilde{F}_t(X) + \varepsilon = \sum_{\alpha \in A_q^{d,p}} w_\alpha \phi_\alpha(X) + \varepsilon \tag{2.43}$$

Having selected the basis functions the w_α coefficients remain to be calculated. There are two general methods to calculate them: the intrusive and the non intrusive methods. Since we consider our code as black-box we are going to present the latter methods for whom only model evaluations are needed without demanding modifications in the code. There are two different non intrusive methods: the projection and the regression. In the projection method due to the orthonormality the PCE coefficients are estimated through equation 2.44 either by MC (or quasi MC) simulations either by quadrature methods.

$$w_\alpha = E[Y \phi_\alpha(\mathbf{X})] = \int_{\mathbb{R}^d} F(\mathbf{X}) \phi_\alpha(X) p_X(X) dX \tag{2.44}$$

In the regression method the vector of coefficients $\mathbf{w} = (w_i)_{i=0}^{k-1}$ of size k are calculated by minimizing the squared least squares residual error based on the dataset of size N.

$$\mathbf{w} = \text{argmin} \frac{1}{N} \sum_{n=1}^{N} (\mathbf{w}^T \mathbf{\Phi}(\mathbf{X_n}) - F(\mathbf{X_n}))^2 \tag{2.45}$$

Where $\mathbf{\Phi}(\mathbf{X}_n)$ is a k dimensional vector of the multivariate polynomials evaluations,with k the cardinality of $A_q^{d,p}$. Finally, if we define $\mathbf{H}$ as the (N x k) matrix of the evaluations of the multivariate polynomials for all the realizations the solution of the minimization problem is the same with the GLM:

$$\mathbf{w} = (\mathbf{H}^T \mathbf{H})^{-1} \mathbf{H}^T \mathbf{Y}_N \tag{2.46}$$

The regression problem for PCE is much better conditioned than for GLM. Once the coefficients are computed then the PCE is fully defined. In order to assess the quality of the PCE approximation the different error estimations can be computed. Concerning the LOO error and if the coefficients of the PCE are computed by regression there is an analytic expression for its calculation:

$$\varepsilon_{loo} = \frac{1}{N} \sum_{n=1}^{N} \left(\frac{\mathbf{w}^T \mathbf{\Phi}(\mathbf{X_n}) - F(\mathbf{X_n})}{1 - \theta_n} \right)^2 \quad , \quad \theta_n = \left(\mathbf{H} (\mathbf{H}^T \mathbf{H})^{-1} \mathbf{H}^T \right)_{nn} \tag{2.47}$$

A big advantage of PCE is that the statistical moments and the sensitivity analysis can be derived directly as a post-processing of the PCE coefficients. For a specific set of input indices α the weight w_α is the value in the estimated weight vector $\mathbf{w}$ corresponding to the ϕ_α. The mean value and the variance of the output are given directly from:

$$\tilde{\mu}_Y = w_0 \tag{2.48}$$

$$\tilde{\sigma}_Y^2 = \sum_{A^{\sim 0}} w_a^2 \tag{2.49}$$

Where $A^{\sim 0}$ are all the indices except the zero one. The higher order moments can be calculated as well. Concerning now the sensitivity analysis the Sobol indices (see Section 2.7.4.1), that demand a lot of evaluations, can be estimated directly. We define the set of indices D_i containing only the variable i as:

$$D_i = \{ \boldsymbol{\alpha} : \quad \alpha_j > 0, j = i \quad and \quad \alpha_j = 0, j \neq i \}$$

Then the first order Sobol index of parameter X^i is estimated by:

$$\hat{S}_i = \sum_{D_i \cap A} w_\alpha^2 \quad / \quad \tilde{\sigma}_Y^2 \tag{2.50}$$

If we define the set D_i^T then total Sobol index of parameter X^i can be estimated in the same way:

$$D_i^T = \{\boldsymbol{\alpha} : \quad \alpha_j > 0, j = i\}$$

$$\hat{S}_i^T = \sum_{D_i^T \cap A} w_\alpha^2 \quad / \quad \tilde{\sigma}_Y^2 \tag{2.51}$$

The PCE is well adapted for smooth models but can face difficulties when dealing with discontinuities. The generalization to other input distributions can be performed with the use of different polynomials. As we said the main advantage is the direct computation of sensitivity indices from the coefficients and the easy explicit form of the surrogate model. The main disadvantage is the error induced from the truncation, that is difficult to assess and that this method is not well adapted for high dimensional inputs or dependent inputs.

2.5.4 Kriging

This surrogate model is constructed with the use of Gaussian processes. At first we should define the concept of Gaussian vectors. A vector is considered Gaussian when all the possible linear combinations of the components are random variables with Gaussian distributions. The distribution of a Gaussian vector is defined by its mean vector and its variance-covariance matrix. We define $y_1 \in \mathbb{R}^{d_1}$ as a Gaussian vector of size d_1 with mean vector μ_{y_1} and variance-covariance matrix $\mathbf{K_{y_1}}$.

$$y_1 \sim N(\mu_{\mathbf{y_1}}, \mathbf{K_{y_1}})$$

Having define the Gaussian vector we can introduce the theorem of Gaussian conditioning states that if we have two Gaussian vectors $y_1 \in \mathbb{R}^{d_1}$ and $y_2 \in \mathbb{R}^{d_2}$ and the vector $(y_1, y_2)^T \in \mathbb{R}^d$ with $d = d_1 + d_2$ is a Gaussian vector as well:

$$\begin{bmatrix} y_1 \\ y_2 \end{bmatrix} \sim N\left(\begin{bmatrix} \mu_{\mathbf{y_1}} \\ \mu_{\mathbf{y_2}} \end{bmatrix}, \begin{bmatrix} \mathbf{K_{y_1}} & \mathbf{K_{y_1 y_2}} \\ \mathbf{K_{y_2 y_1}} & \mathbf{K_{y_2}} \end{bmatrix} \right)$$

Where $\mathbf{K_{y_1}}$ and $\mathbf{K_{y_2}}$ are the covariance matrices of size $d_1 \times d_1$ and $d_2 \times d_2$ respectively. $\mathbf{K_{y_1 y_2}}$ and $\mathbf{K_{y_2 y_1}}$ are the cross-covariance matrices of size $d_1 \times d_2$ and $d_2 \times d_1$ with $\mathbf{K_{y_1 y_2}} = \mathbf{K_{y_2 y_1}}^T$. In this case there is an analytic expression for the distribution of y_2 conditioned to y_1. The conditioned distribution is Gaussian with mean and covariance described by:

$$E[y_2|y_1] = \mu_{y_2} + \mathbf{K_{y_2 y_1}} \mathbf{K_{y_1}^{-1}} (y_1 - \mu_{y_1}) \tag{2.52a}$$

$$Var(y_2|y_1) = \mathbf{K_{y_2}} - \mathbf{K_{y_2 y_1}} \mathbf{K_{y_1}^{-1}} \mathbf{K_{y_1 y_2}} \tag{2.52b}$$

The equations 2.52a and 2.52b state that we can adjust the expectation and the variance of a part of a Gaussian vector conditioned that we have observations of the rest of the vector. Now we can define the continuous Gaussian process as a family $y(x)$ of random variables defined over $x \in \mathcal{X}$ such that any linear combination is Gaussian distributed. Its distribution can be characterized by a mean function $\mu_y(x) : \mathcal{X} \to \mathbb{R}$ and a covariance function $k(x, x') : \mathcal{X} \times \mathcal{X} \to \mathbb{R}$.

$$y(x) \sim GP(\mu_y(x), k(x, x')) \tag{2.53}$$

If the covariance and mean functions are known and we have a deterministic data set of observations $\mathbf{x_{obs}} = (x_i)_{i=1}^N, \mathbf{y_{obs}} = (y(x_i))_{i=1}^N$ of size N then we can use the Gaussian conditioning to predict the value at a new point $y(x_0)$.

$$E[y(x_0)|\mathbf{y_{obs}}] = \hat{y}(x_0) = \mu_y(x_0) + \mathbf{k}^T(x_0) \mathbf{K}^{-1} (\mathbf{y_{obs}} - \boldsymbol{\mu_{obs}}) \tag{2.54}$$

$$Var[y(x_0)|\mathbf{y_{obs}}] = \hat{\sigma}^2(x_0) = k(x_0, x_0) - \mathbf{k}^T(x_0) \mathbf{K}^{-1} \mathbf{k}(x_0) \tag{2.55}$$

Where $\mathbf{k}(x_0) = (k(x_0, x_i))_{i=1}^N$ is a vector of size N. $\mathbf{K}$ is a matrix of size $N \times N$ corresponding to the covariance matrix of the observations and thus $K_{ij} = k(x_i, x_j)$, $i = 1, \ldots, N$, $j = 1, \ldots, N$. $\boldsymbol{\mu_{obs}} = (\mu_y(x_i))_{i=1}^N$ is the vector of size N created by the evaluations of the mean function on the data set and $k(x_0, x_0)$ corresponds to the unconditioned variance of $Y(x_0)$. The Gaussian process passes exactly through the points of the data set (perfect interpolation). It is also interesting that

beyond the expected value the process also predicts the variance and thus can create confidence intervals. An illustration for $d = 1$ and $N = 7$ is presented in figure 2.3.

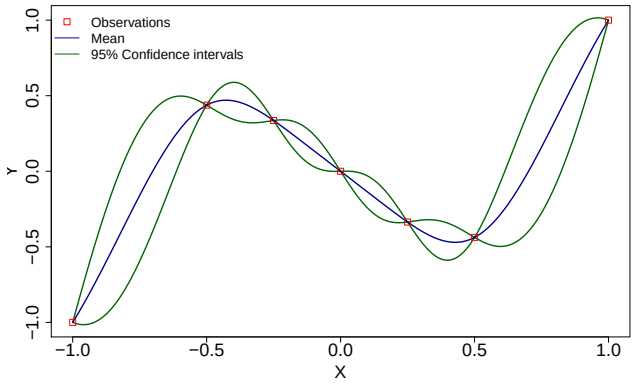

Figure 2.3: Typical Gaussian process predictions.

The Kriging surrogate model considers the input-output input-output function $Y = F(X) : \mathbb{R}^d \to \mathbb{R}$ to be a Gaussian processes, where the output is considered a scalar. The output then can be expressed as:

$$Y = \tilde{F}(X) + \varepsilon = \mu(X) + Z(X) \tag{2.56}$$

Where $\mu(X) : \mathbb{R}^d \to \mathbb{R}$ is a mean function and $Z(X)$ is a centered Gaussian process ($E[Z(X)] = 0$) with isotropic stationary covariance function $k(X, X') : \mathbb{R}^d \times \mathbb{R}^d \to \mathbb{R}$. The concept of isotropic stationarity for a covariance function means that it depends only on the distance between the points:

$$k(X, X') = k(|X - X'|)$$

The covariance function is chosen to be a positive definite function and usually is selected from specific families of parametric functions (e.g. Exponential, Matérn). In the thesis we used the Matérn 5/2 function. The function is parametric, meaning that it contains parameters that must be estimated. The vector of parameters of the function $\boldsymbol{\theta}$ are called hyper-parameters and they can be estimated through Maximum Likelihood , Restricted Maximum Likelihood and Cross Validation [83]. The stationarity implies that the variance of the Gaussian process is the same for all Y since $k(|X - X|) = k(0) = \sigma^2$. The variance σ^2 is usually unknown and is added the hyper-parameters that must be estimated. The mean function can be of any form but in general two cases are studied. The first one is the case of linear combination of known basis functions and unknown coefficients called Universal Kriging:

$$\mu(X) = \sum_{i=1}^{p} h_i(X)\beta_i = \mathbf{h}(X)^T\boldsymbol{\beta} \tag{2.57}$$

The second one is the case of Simple Kriging where the mean function is assumed to be known (equivalent to known $\boldsymbol{\beta}$). There can be different combinations of known and unknown parameters but we will focus on the Universal Kriging with unknown variance and hyper-parameters. In this case the unknown vector of coefficients $\boldsymbol{\beta}$ of size p (the number of basis functions) must be estimated as well. We can see that the total parameters that must be estimated in order to have a well defined Kriging model are: $(\boldsymbol{\theta}, \sigma, \boldsymbol{\beta})$. We mentioned that the covariance function depends on the hyper-parameters $\boldsymbol{\theta}$ and that is why we will change its notation to $k_\theta(X, X')$. Using the dataset $\mathbf{D}_N$ the prediction of a new point $Y(\mathbf{X}_{new})$ for its expected value[1] and variance is given by the following equations:

$$\hat{Y}(\mathbf{X}_{new}) = \mathbf{h}(\mathbf{X}_{new})^T\hat{\boldsymbol{\beta}} + \mathbf{k}_{\hat{\theta}}(\mathbf{X}_{new})^T\mathbf{K}_{\hat{\theta}}^{-1}(\mathbf{Y}_{\mathbf{D_N}} - \mathbf{H}\hat{\boldsymbol{\beta}}) \tag{2.58}$$

[1] It is the Best Linear Unbiased Predictor

$$\hat{\sigma}^2(\mathbf{X}_{new}) = \hat{\sigma}^2 - \mathbf{k}_{\hat{\theta}}(\mathbf{X}_{new})^T \mathbf{K}_{\hat{\theta}}^{-1} \mathbf{k}_{\hat{\theta}}(\mathbf{X}_{new}) + \mathbf{B}^T \left(\mathbf{H}^T \mathbf{K}_{\hat{\theta}}^{-1} \mathbf{H}\right)^{-1} \mathbf{B} \tag{2.59}$$

In the equations above $\mathbf{B} = \mathbf{h}(\mathbf{X}_{new}) - \mathbf{H}^T \mathbf{K}_{\hat{\theta}}^{-1} \mathbf{k}_{\hat{\theta}}(\mathbf{X}_{new})$ and $\mathbf{h}(\mathbf{X}_{new})$ is a vector of size p of the evaluations of the mean function basis functions. The estimated parameters are $\hat{\boldsymbol{\beta}}$, $\hat{\boldsymbol{\theta}}$, $\hat{\sigma}$ and $\mathbf{k}_{\hat{\theta}}(\mathbf{X}_{new})$ and $\mathbf{K}_{\hat{\theta}}$ are defined similar to equation 2.54. $\mathbf{H}$ with $H^{ij} = h_j(\mathbf{X}_i)$ for $i = 1 \dots N$ $j = 1 \dots p$ is the matrix of size $N \times p$ containing all the evaluations of the basis functions on the complete dataset. We can see that in equation 2.59 a term is added in comparison to equation 2.55. This term is non-negative and is coming from the uncertainty propagation of the $\hat{\boldsymbol{\beta}}$ estimation. There is no uncertainty propagation of parameters $(\hat{\sigma}, \hat{\boldsymbol{\theta}})$[2]. When the uncertainty of those parameters is taken into account the method is called full Bayesian.

Once the equations 2.58 and 2.55 are constructed the only thing remaining is the estimation of the parameters. We present the Maximum Likelihood Estimator. If we decompose the covariance function in $k_\theta(X, X') = \sigma^2 r_\theta(X, X')$ then the covariance matrix becomes $\mathbf{K}_{\hat{\theta}} = \hat{\sigma}^2(\hat{\boldsymbol{\theta}}) \mathbf{R}_{\hat{\theta}}$. The likelihood is not maximized directly but instead the likelihood criterion of equation 2.60 is minimized. The criterion is derived by a monotonic transformation of the likelihood [83].

$$L(\boldsymbol{\theta}) = \frac{1}{N} \log(|\hat{\sigma}^2(\boldsymbol{\theta}) \mathbf{R}_{\hat{\theta}}|) + \frac{1}{N \hat{\sigma}^2(\boldsymbol{\theta})} \left(\mathbf{Y}_{\mathbf{D_N}} - \mathbf{H}\hat{\boldsymbol{\beta}}(\boldsymbol{\theta})\right)^T \mathbf{R}_{\hat{\theta}}{}^{-1} \left(\mathbf{Y}_{\mathbf{D_N}} - \mathbf{H}\hat{\boldsymbol{\beta}}(\boldsymbol{\theta})\right) \tag{2.60}$$

$$\hat{\boldsymbol{\theta}} = \underset{\boldsymbol{\theta} \in \boldsymbol{\Theta}}{\operatorname{argmin}} \, L(\boldsymbol{\theta})$$

The estimator of $\hat{\sigma}^2$ and $\hat{\boldsymbol{\beta}}$ are presented in equations 2.61 and 2.62

$$\hat{\sigma}^2(\hat{\boldsymbol{\theta}}) = \frac{1}{N} \left(\mathbf{Y}_{\mathbf{D_N}} - \mathbf{H}\hat{\boldsymbol{\beta}}(\hat{\boldsymbol{\theta}})\right)^T \mathbf{R}_{\hat{\theta}}^{-1} \left(\mathbf{Y}_{\mathbf{D_N}} - \mathbf{H}\hat{\boldsymbol{\beta}}(\hat{\boldsymbol{\theta}})\right) \tag{2.61}$$

$$\hat{\boldsymbol{\beta}}(\hat{\boldsymbol{\theta}}) = \left(\mathbf{H}^T \mathbf{R}_{\hat{\theta}}^{-1} \mathbf{H}\right)^{-1} \mathbf{H}^T \mathbf{R}_{\hat{\theta}}^{-1} \mathbf{Y}_{\mathbf{D_N}} \tag{2.62}$$

This estimation is unbiased with covariance matrix which corresponds to the term added in equation 2.55:

$$\mathbf{Q}_{\hat{\beta}} = \left(\mathbf{H}^T \mathbf{K}_{\hat{\theta}}^{-1} \mathbf{H}\right)^{-1} \tag{2.63}$$

In the Bayesian case a prior distribution is assigned $\boldsymbol{\beta} \sim \mathcal{N}(\boldsymbol{\beta}_{prior}, \mathbf{Q}_{\mathbf{prior}})$ and the posterior expected value and covariance matrix are estimated by:

$$\hat{\boldsymbol{\beta}}_{post} = \boldsymbol{\beta}_{prior} + \left(\mathbf{Q}_{\mathbf{prior}}^{-1} + \mathbf{H}^T \mathbf{K}_{\hat{\theta}}^{-1} \mathbf{H}\right)^{-1} \mathbf{H}^T \mathbf{K}_{\hat{\theta}}^{-1} (\mathbf{Y}_{\mathbf{D_N}} - \mathbf{H}\boldsymbol{\beta}_{prior}) \tag{2.64}$$

$$\mathbf{Q}_{\mathbf{post}} = \left(\mathbf{Q}_{\mathbf{prior}}^{-1} + \mathbf{H}^T \mathbf{K}_{\hat{\theta}}^{-1} \mathbf{H}\right)^{-1} \tag{2.65}$$

We can now use this posterior distribution of $\boldsymbol{\beta}$ to calculate the posterior distribution of $Y(\mathbf{X}_{new})$:

$$\hat{Y}(\mathbf{X}_{new}) = \mathbf{h}(\mathbf{X}_{new})^T \hat{\boldsymbol{\beta}}_{post} + \mathbf{k}_{\hat{\theta}}(\mathbf{X}_{new})^T \mathbf{K}_{\hat{\theta}}^{-1} (\mathbf{Y}_{\mathbf{D_N}} - \mathbf{H}\hat{\boldsymbol{\beta}}_{post}) \tag{2.66}$$

$$\hat{\sigma}^2(\mathbf{X}_{new}) = \hat{\sigma}^2 - \mathbf{k}_{\hat{\theta}}(\mathbf{X}_{new})^T \mathbf{K}_{\hat{\theta}}^{-1} \mathbf{k}_{\hat{\theta}}(\mathbf{X}_{new}) + \mathbf{B}^T \mathbf{Q}_{\mathbf{post}} \mathbf{B} \tag{2.67}$$

If we assume that the observations of the Gaussian process have noise then the Kriging model becomes:

$$\tilde{F}(X) = \mu(X) + Z(X) + \epsilon(X) \tag{2.68}$$

Usually the errors on the observations $\boldsymbol{\epsilon} = (\epsilon_1, \dots, \epsilon_n)$ is considered a centered Gaussian vector of size N with covariance matrix $\mathbf{K}_\epsilon$. To estimate now the parameters and to predict the value $Y(\mathbf{X}_{new})$ the same equations that we saw in the case without the noise can be used with only difference that now the covariance matrix of the observations becomes: $\mathbf{K}'_{\hat{\theta}} = \mathbf{K}_{\hat{\theta}} + \mathbf{K}_\epsilon$. In the

[2] Plugin method

case where the noises of the observation are considered i.i.d with the variance σ_ϵ^2 the covariance matrix of the observations becomes: $\mathbf{K}'_{\hat{\theta}} = \mathbf{K}_{\hat{\theta}} + \sigma_\epsilon^2 \mathbf{I}$.

Finally, to assess if the Kriging model representing the model is a good approximation the typical error estimators for the empirical error and the prediction error can be used. For the Leave-One-Out error there is an analytic expression for its calculation:

$$\epsilon_{LOO} = \frac{1}{N} \sum_{i=1}^{N} \left(\frac{(\tilde{\mathbf{K}}_{\hat{\theta}} \mathbf{Y})_i}{(\tilde{\mathbf{K}}_{\hat{\theta}})_{i,i}} \right)^2 \tag{2.69}$$

where $\tilde{\mathbf{K}}_{\hat{\theta}} = \mathbf{K}_{\hat{\theta}}^{-1} - \mathbf{K}_{\hat{\theta}}^{-1} \mathbf{H} (\mathbf{H}^t \mathbf{K}_{\hat{\theta}}^{-1} \mathbf{H})^{-1} \mathbf{H}^t \mathbf{K}_{\hat{\theta}}^{-1}$ for the universal kriging.

The main advantage of Kriging is that it has an explicit formulation for the Best Linear Unbiased Predictor (BLUP) and it can estimate its variance. Besides that, it can treat noisy cases or models that are not so regular. The main disadvantage is that it cannot be used in cases of high input dimensions and can become time consuming if the dataset of observations increases a lot.

2.5.5 Artificial Neural Networks (ANN)

ANN is a surrogate model inspired from the biological neural networks of the brain. It is constructed from a collection of neurons divided in hidden layers. Each neuron is a non linear function g. The neurons of the first layer has as input a linear combination of the input variables and as output the non linear transformation through an activation function g as shown in figure 2.4. If more layers exist then the input of a hidden layer neuron will be a linear combination of the output's of the previous hidden layer's neurons. More information about the motivation behind ANN can be found in [80].

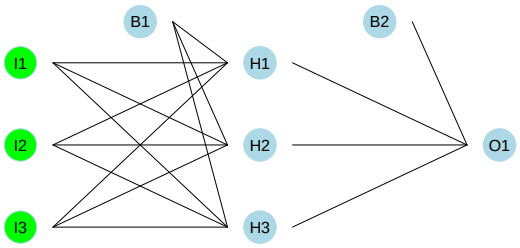

Figure 2.4: An example of an ANN with 1 hidden layer and 3 inputs.

In the case where we want to replace the model: $Y = F(X) : \mathbb{R}^d \to \mathbb{R}$ we have d inputs. If we select $M = d$ neurons for one hidden layer (options used in this thesis) and we define the weight of an input i for a neuron j as w_{ij} and the weight of the neuron's output as w_j the ANN output's function will be:

$$Y = \tilde{F}(X) + \varepsilon = \sum_{j=1}^{M} w_j g \left(\sum_{i=1}^{d} w_{ij} X^i + w_{j0} \right) + w_0 + \varepsilon \tag{2.70}$$

with w_{j0} and w_0 the bias weight on each neuron and the output.

For this ANN model the only thing that remains in order to be complete is to estimate the weights and select the activation function. We have a total of $N(d+2)+1$ weights to be estimated. The activation function usually used is the sigmoid:

$$g(u) = \frac{1}{1 + e^{-u}} \tag{2.71}$$

The weights of the ANN are estimated through a procedure called learning of the ANN. In general a cost or error function c is defined and the weights are the result of minimizing the cost function (or at least close to minimum). For our case where we have the dataset D_N of size N and the ANN goal is to approximate as best as possible the underlying function between X and Y and we

are in the supervised learning category. In the supervised learning the cost function usually used is the mean squared error:

$$c(\mathbf{w}) = \frac{1}{N}\sum_{i=1}^{N} |F(\mathbf{X_i}) - \tilde{F}(\mathbf{X_i})|^2 = \frac{1}{N}\sum_{i=1}^{N} |\varepsilon_i|^2 \tag{2.72}$$

Having defined the cost function the weights are calculated through the following general algorithm:

- In the first iteration only, the weights are initialized.
- The $\tilde{Y}_{i,\mathbf{w}} = \tilde{F}(\mathbf{X_i}, \mathbf{w})$ are computed with forward propagation through the ANN and the cost is evaluated.
- Calculate the gradient of the weights vector: $\frac{\partial c}{\partial \mathbf{w}}$.
- Update the weights vector as stochastic gradient descent.

Different algorithms of backpropagation exist [85] but we will not look into it because it is not in the scope of the thesis. Once the ANN model is constructed and the supervised learning is performed the surrogate model is validated through the typical error estimators. The main advantage of ANN is that they can treat high input dimensions but they might need a very large training set for the supervised learning. The optimization method can lead to local minima far from the global and that's why different initialization weights must be considered.

2.6 Design of Experiments

The Design of Experiments (DOE) is the selected code evaluations on the inputs X space to create the dataset $\mathbf{D}_N$. This design will be mainly used to construct the surrogate models and the goal is to explore as much as possible the inputs space $\mathbb{R}^d$ in order to capture potential non-linearities. Such DOE are called space-filling designs [86]. The most popular methods for constructing DOE are the following:

- **Full Factorial designs**: Each input variable is discretized separately. The result is a full tensorized grid of points that can be symmetric or asymmetric (size of discretization can vary among the variables). It suffers from the "curse of dimensionality" since the number of design points increase exponentially.
- **Sparse Factorial designs**: They are used to alleviate the limited use of full factorial designs in high input dimensions. These designs discard some of the tensorized grid points and create a sparse grid based on some rules [87].
- **Random Sampling**: It is a simple Monte Carlo sampling where the input variables are sampled randomly from their joint pdf. These designs do not suffer from the "curse of dimensionality" since the sample size is independent of the input dimensions. Nevertheless, as the dimension increases the input space increases as well and for a constant sample size the space will be explored poorly.
- **Latin Hypercube Sampling (LHS)**: The previous poor exploratory properties of random sampling in high dimensions can be overcome using the LHS designs. We consider uniform inputs distribution. For a predefined sample size N the marginal input space is uniformly divided in N intervals creating N^d hypercubes. From these hypercubes N are selected and a sample is generated in each one. The hypercubes selection has to preserve the Latin Hypercube property of each sample being the only one in each axis-aligned hyperplane containing it [86]. An optimization process is applied on the generated samples in order to cover the input space as good as possible. LHS are mainly used in this thesis for the surrogate model construction and will be detailed in the Sections 2.6.1 -2.6.2 discussing particularly the case of arbitrary input distribution with independent coordinates.
- **Quasi Monte Carlo Sampling**: This method is based on algorithms that produce low discrepancy sequences (e.g. Halton sequence) that try to fill as much as possible the input space.

Typical designs generated by these methods are illustrated in the following figure.

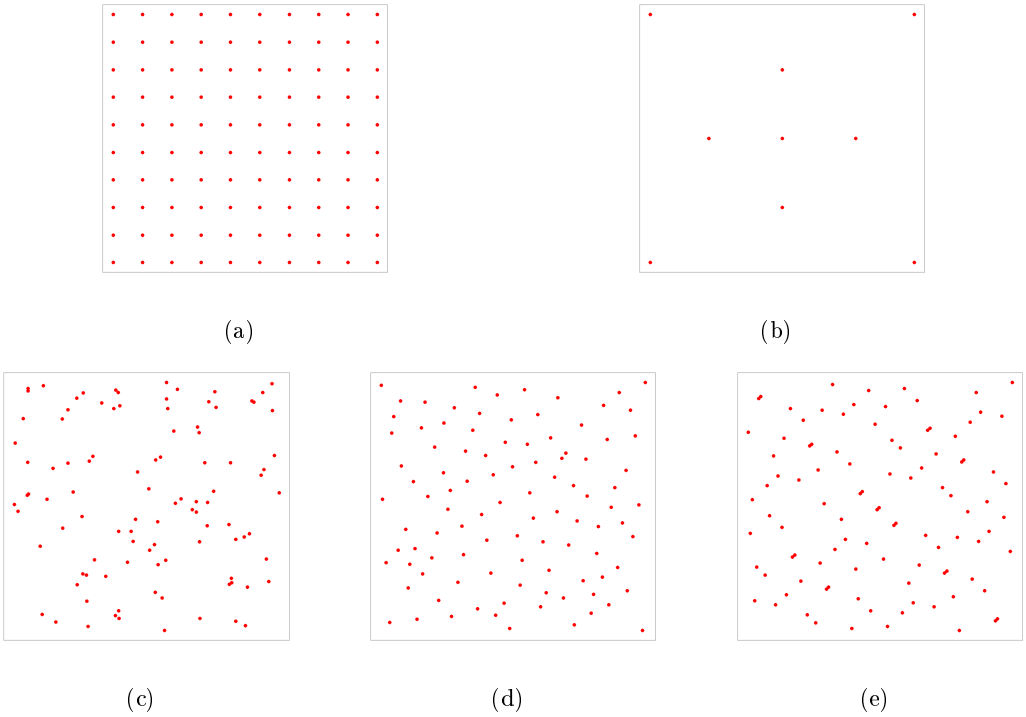

(a) (b)

(c) (d) (e)

Figure 2.5: Examples of DOE: Full Factoral (a), Sparse Factorial (b), Random Sampling (c), LHS (d) and Quasi Monte Carlo Sampling (e).

2.6.1 Latin Hypercube Sampling (LHS) presentation

LHS as mentioned are DOE with space-filling properties. We consider the construction of a size N LHS like the case of $\mathbf{D}_N$ in the input space of $X \in \mathbb{R}^d$. The LHS is initially constructed for the independent variables $Z \in \mathbb{R}^d$ in the domain of their cumulative distribution function (cdf) $F_Z(Z)$ which is $[0,1]^d$. The marginal domain of each input variable Z^i is divided into N uniform intervals. The combination of all this intervals creates N^d hypercubes. From these hypercubes N are selected in such a way that the projections of the centers of the hypercubes on the axis of each variable is uniformly distributed. This is achieved by selecting d permutations of $1 \dots N$. In a $2D$ design with $N = 5$ it means that there cannot be two samples in the same row or column as illustrated in the left of figure 2.6. In this example the corresponding permutations are $\pi_1 = (3;1;4;5;2)$ and $\pi_2 = (2;5;1;3;4)$. In each selected hypercube one sample is drawn randomly. The projection of the sample n on each variable is denoted by u_n^i and the transformation to the Z variables space is performed through the inverse transform of the cdf $Z_n^i = F^{-1}(u_n^i)$. Using the previous example the transformation process is seen in the right part of figure 2.6.

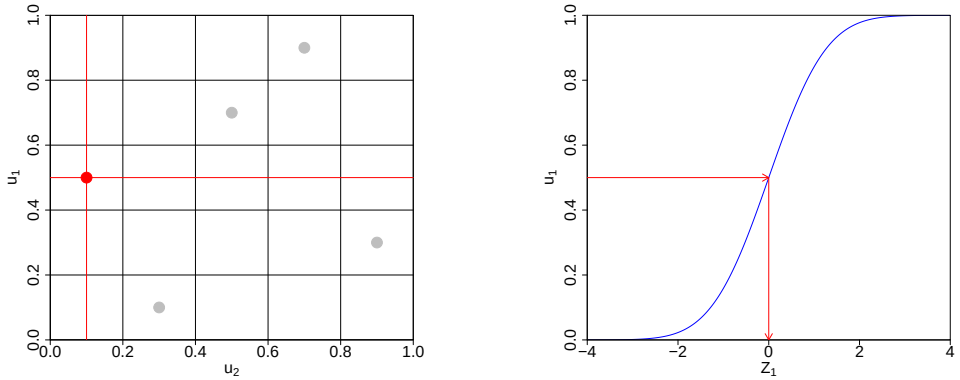

(a) (b)

Figure 2.6: LHS marginal projection property (a) and inverse transformation using the cdf (b).

Although the nature of LHS assures that marginally the points are well distributed this is not necessarily the case for the points in the input space. The resulting LHS can have good or bad space-filling properties as it can be seen in figure 2.7. To this purpose an optimization of the LHS with respect to some criteria that quantify the space-filling quality is applied. The different optimization methods are detailed in Section 2.6.2.

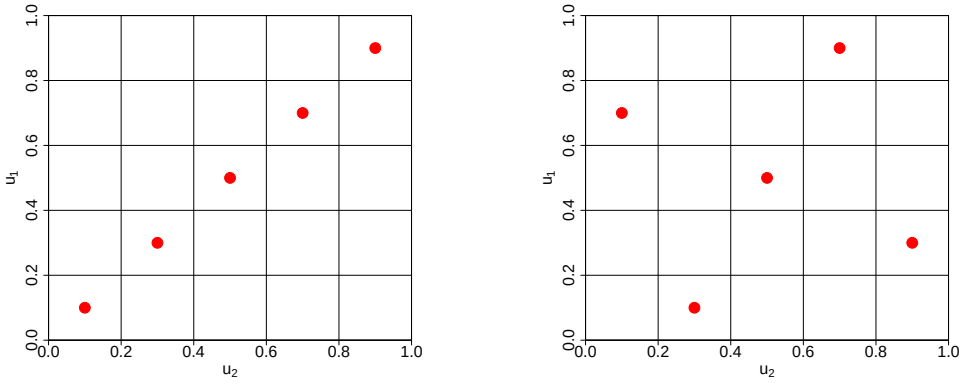

(a) (b)

Figure 2.7: LHS with bad (a) and good (b) space-filling properties.

We consider now our input X as multivariate normal $\mathcal{N}(\mu_X, C_X)$ with mean μ_X and covariance C_X. We define Z as standard normal variables $\mathcal{N}(0,1)$. The LHS in the X space is expressed by equation 2.73, where $\mathbf{Z}$ is the previously obtained dataset of size $N \times d$ with $Z^{ij} = Z_i^j$ for $i = 1 \dots N$, $j = 1 \dots d$ and $\mathbf{M}_X$ the matrix of size $N \times d$ containing μ_X at each row. $\sqrt{C_X}$ is the matrix square root of the covariance matrix (positive semidefinite).

$$\mathbf{X_{D_N}} = \mathbf{M}_X + \sqrt{C_X}\mathbf{Z} \tag{2.73}$$

2.6.2 LHS optimization

As we observed previously, some LHS can have poor space-filling properties in the input space. This means that in this space some points can be close to each other and thus this reduces the amount of information gained by evaluating those points by the code. Different optimal criteria are used in order to avoid such designs and enhance the LHS by ensuring the spreading of the points in the space. A good overview of the developed criteria is given in [88]. We will present some of the most used criteria on the $u_n \in [0,1]^d$ uniform variables for the design $\mathbf{D_N}$.

- **Geometric criteria**: They are based on the euclidean distances between the DOE points $d_{ij} = \|u_i - u_j\|_2$. Two main criteria exist. The first one is called *"minimax"* and aims at minimizing the maximum distance of any point in $[0,1]^d$ to its nearest design point. This is equivalent to minimizing the criterion:

$$\phi_{mM}(\mathbf{D_N}) = \max_{u \in [0,1]^d} \min_{i=1\dots N} \|u - u_i\|_2 \tag{2.74}$$

  The second one is called *"maximin"* and aims at maximizing the minimum distance between the design points. This is equivalent to maximizing the criterion:

$$\phi_{Mm}(\mathbf{D_N}) = \min_{\substack{i,j=1\dots N \\ i \neq j}} d_{ij} \tag{2.75}$$

  The minimax criterion is more attractive for surrogate model construction, since it takes into account the whole domain. Its computation is, however, infeasible for dimensions larger than 4 or 5 [89]. On the other hand the *maximin* is much easier to compute but is difficult to optimize. For this reason a new criterion ϕ_p more efficient to optimized can be used.

$$\phi_p(\mathbf{D_N}) = \Big[\sum_{\substack{j,k \leq N \\ j<k}} d_{jk}^{-p} \Big]^{\frac{1}{p}} \tag{2.76}$$

The asymptotic equivalence between minimizing ϕ_p and maximizing ϕ_{Mm} is shown in [89]. In practice a value of $p = 50$ can be used as proposed by [90].

- **Uniformity criteria**: They are based on discrepancy measures evaluating how close the DOE is to a uniform design. Discrepancy is defined as the difference between the uniform cdf $U(\mathbf{u})$ and the empirical cdf of the DOE $U_N(\mathbf{u})$.

$$D^*(\mathbf{D_N}) = \max_{\mathbf{u} \in [0,1]^d} |U_N(\mathbf{u}) - U(\mathbf{u})| \tag{2.77}$$

By minimizing this discrepancy the LHS is optimized. Discrepancy measures are constructed based on the L^2-norm discrepancy, an alternative to D^* [91]. From the many existing measures two prominent ones are the centered C^2 and wrap-around W^2 discrepancies.

$$\begin{aligned} C^2(\mathbf{D}_N) = &\left(\frac{13}{12}\right)^d - \frac{2}{N} \sum_{n=1}^{N} \prod_{i=1}^{d} \left(1 + \frac{1}{2}|u_n^i - 0.5| - \frac{1}{2}|u_n^i - 0.5|^2\right) \\ &+ \frac{1}{N^2} \sum_{n,k=1}^{N} \prod_{i=1}^{d} \left(1 + \frac{1}{2}|u_n^i - 0.5| + \frac{1}{2}|u_k^i - 0.5| - \frac{1}{2}|u_n^i - u_k^i|\right) \end{aligned} \tag{2.78a}$$

$$W^2(\mathbf{D}_N) = \left(\frac{4}{3}\right)^d + \frac{1}{N^2} \sum_{n,k=1}^{N} \prod_{i=1}^{d} \left(\frac{3}{2} - |u_n^i - u_k^i|(1 - |u_n^i - u_k^i|)\right) \tag{2.78b}$$

- **Minimum Spanning Tree (MST) criteria**: They were recently developed [88] and build trees by connecting with edges all the DOE points. The MST is the tree with minimum sum of edge lengths. The mean m_{MST} and standard deviation σ_{MST} of the edge lengths can be estimated for each DOE. Designs with large m_{MST} and small σ_{MST} have good space-filling properties.

When the dimensions and size of the LHS are small all the possible LHS can be compared based on the selected criterion. This is not possible in large dimensions and sample sizes. Optimization iterative methods are used in order to find an approximation of the best LHS. We will present two main methods applied to the minimization of ϕ_p criterion:

- **Simulated Annealing (SA)**: It is a metaheuristic global optimization method [91]. Starting from a random initial LHS an iterative process is conducted where at each iteration an elementary permutation by random permutation of two coordinates in the LHS is performed. The designs that improve ϕ_p are always accepted, while the ones that do not improve can be accepted with a probability that depends on the increment of ϕ_p (between the original design and the transformed one) and a temperature parameter T. This is done in order to avoid getting stuck in a local minimum. The temperature is progressively decreased from an initial temperature T_0 so as to decrease the probability to accept a worse design. The optimization stops when the selected number of iterations is reached. The quantities that need to be initialized are: the temperature T_0, the number of iterations, the selection of the temperature decrease method and its parameters. The selected profile for the temperature evolution along the iterations is the geometric profile $T = cT$ [92], with c that must be defined in order to get extensive exploration of possible designs and fast minimization of ϕ_p. The pseudo algorithm of one of the possible implementations of this method for optimizing an initial design $\mathbf{D}_0$ of size N in $\mathbb{R}^d$ with initial temperature T_0, profile parameter $0 < c < 1$ and number of iterations N_i is:

SA pseudo algorithm

$D_{best} = \mathbf{D}_0$, $C_{best} = \phi_p(\mathbf{D}_0)$, $T = T_0$: initialization of the best design, best criterion and temperature
for $(i = 1, i \leq N_i, i++)$ **do**
    Create new design $\mathbf{D}_i$ by elementary permutation and evaluate $C_i = \phi_p(\mathbf{D}_i)$
    $a = \min(exp(\frac{C_{best} - C_i}{T}), 1)$
    Sample b from bernoulli distribution with parameter a
    if $(b == 1)$ **then**
        $D_{best} = \mathbf{D}_i$ and $C_{best} = C_i$
    end if
    $T = cT$
end for

- **Enhanced Stochastic Evolutionary algorithm (ESE)**: It is a stochastic optimization method sharing many similarities with SA [93]. It consists of two nested iteration loops. In the inner one J LHS are created by random elementary permutations and among them the one with the minimum ϕ_p is selected. The acceptance/rejection of the design is based on a temperature T parameter, similar to SA, where large values indicate more bad designs being accepted. At the end of each step of the inner iterations the acceptance ratio is calculated and the temperature is adjusted accordingly. If the ratio is smaller than a threshold (< 0.1) then the temperature is increased, otherwise is decreased. The pseudo algorithm of one possible implementation of this method for optimizing an initial design $\mathbf{D}_0$ of size N in $\mathbb{R}^d$ with initial temperature T_0, number of random LHS J and number of inner and outer iterations N_o, N_i is:

ESE pseudo algorithm

$D_{best} = \mathbf{D}_0$, $C_{best} = C_c = \phi_p(\mathbf{D}_0)$, $T = T_0$: initialization of the best design, best and comparison criterion and temperature
for $(o = 1, o \leq N_o, o++)$ **do**
    $D^o_{best} = D_{best}$, $C^o_{best} = C_{best}$
    for $(i = 1, i \leq N_i, i++)$ **do**
        Create J LHS by random elementary permutations
        Select the design D^i_{best} with minimum $C^i_{best} = \phi_p(\mathbf{D^i_{best}})$
        $\Delta C = C^i_{best} - C_c$, $u = Uniform(0, 1)$
        if $(\Delta C \leq Tu)$ **then**
            $C_c = C^i_{best}$
            if $(C^i_{best} \leq C^o_{best})$ **then**
                $D_{best} = D^i_{best}$, $C_{best} = C^i_{best}$
            end if
        end if
    end for
    Compute the ratio of accepted designs τ_a
    if $(C_{best} < C^o_{best})$ **then**
        $T :\searrow$ $(\tau_a > 0.1)$ or $T :\searrow$ $(\tau_a \leq 0.1)$
    else
        $T :\nearrow$ $(\tau_a \leq 0.1)$ or $T :\searrow$ $(\tau_a > 0.1)$
    end if
end for

2.7 Sensitivity analysis

In our model $Y = F(X)$ the output is a random quantity due to the uncertainty propagation of the inputs. Sensitivity analysis goal is to identify which input variables have an impact on the output's uncertainty (qualitative) and then quantify this impact (quantitative). This can be used subsequently to reduce the dimensions of the input space. The methods that give a

qualitative information on the inputs are called screening methods. The quantitative methods focus on explaining the part of the output's uncertainty that belongs to each input variable or combination of variables. The sensitivity analysis methods can also be divided in local and global depending on if they concentrate on the local impact of the input parameters or on the whole domain of variation. Besides that, one might be interested in the sensitivities of different statistical quantities of the output, from its variance to quantiles and even the whole distribution. An overview of the main methods for sensitivity analysis will be presented [94]. In general scalar output is considered except in the dedicated Section 2.7.6 to the functional output sensitivity analysis.

2.7.1 Screening

This category is about methods that are based on partial derivatives, increments of the inputs around some reference value or some empirical correlation estimation. They are usually used for screening of independent inputs by allowing an initial fast estimation of the inputs importance.

2.7.1.1 One factor at a Time (OAT)

OAT is a simple local method where the derivatives of each variable evaluated at the mean value μ_X are used as sensitivity indices. For the ith variable X^i it is expressed by:

$$S^i_{OAT} = \frac{\partial}{\delta X^i}(\mu_X) \tag{2.79}$$

The derivatives can be estimated either by finite differences or by adjoint methods. In the thesis context with coupled multi-physics transient calculations the former one can be only used. The derivatives are thus estimated by small perturbation $\delta h > 0$ around the mean value.

$$\hat{S}^i_{OAT} = \frac{F(\mu_X + \delta h \mathbf{e^i}) - F(\mu_\mathbf{X})}{\delta h} \tag{2.80}$$

Where $\mathbf{e^i}$ is the standard basis vector. The OAT index is the absolute value $|\hat{S}^i_{OAT}|$. The sensitivity depends on the choice of the reference value and cannot capture non-linear or interaction effects

2.7.1.2 Morris method

Morris method can be seen as a global OAT method for screening. M reference values $\mathbf{X}_m$ are sampled and for each value the OAT sensitivity index $\hat{S}^i_{m,OAT}$ is calculated for all the variables. Using these sensitivity indices the mean and variance of the Morris method are defined and estimated through equations 2.81a and 2.81b.

$$\mu^i_M = E[|S^i_{OAT}|], \quad \hat{\mu}^i_M = \frac{1}{N}\sum_{m=1}^{M} |\hat{S}^i_{m,OAT}| \tag{2.81a}$$

$$V^i_M = E[(S^i_{OAT} - E[S^i_{OAT}])^2], \quad \hat{V}^i_M = \frac{1}{M-1}\sum_{m=1}^{M} (\hat{S}^i_{m,OAT} - \frac{1}{M}\sum_{m'=1}^{M} \hat{S}^i_{m',OAT})^2 \tag{2.81b}$$

The mean Morris index $\hat{\mu}^i_M$ represents the direct sensitivity of the input parameters to the output. The variance Morris index $\hat{V}^i_M$ captures the sensitivity through interactions with the rest of the inputs and the non-linearities between the inputs and the output. These two effects cannot be separated. Usually the result of Morris method is plotted as in figure 2.8, where 10 inputs are considered.

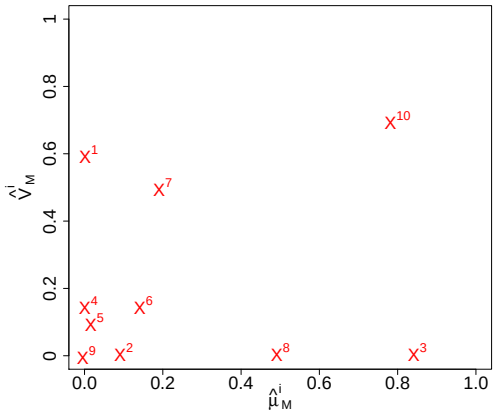

Figure 2.8: A typical Morris plot for 10 inputs.

This method allows to neglect directly some inputs with small computational cost (the ones close to the origin of the plot: X^2, X^4, X^5, X^6, X^9). The remaining inputs can be separated in parameters with linear effects (close to the $\hat{\mu}^i_M$ axis: X^3, X^6), with non-linear or interaction effects (X^1,X^7) and with both (X^{10}) depending on their place in the Morris plot. The method does not make any hypothesis on the model but it is more efficient if there is some regularity.

2.7.2 Correlation based indices

2.7.2.1 Pearson Coefficient (PC)

Pearson coefficient S^i_{PC} is a measure of linear correlation between output Y and each input X^i. With σ_Y, σ_{X^i} the corresponding standard deviations and c_{X^iY} the input-output covariance PC is defined as:

$$S^i_{PC} = \frac{c_{X^iY}}{\sigma_{X^i}\sigma_Y} \tag{2.82}$$

It is bounded in $[-1, 1]$. A value of 0 indicates that Y and X^i are uncorrelated while a value of 1 (-1) indicates full positive (negative) linear correlation. We remind that uncorrelated variables does not imply independent variables while independent variables are necessary uncorrelated. The empirical estimator of PC is:

$$\hat{S}^i_{PC} = \frac{\sum_{n=1}^{N}(X^i_n - \hat{\mu}_{X^i})(Y_n - \hat{\mu}_Y)}{\sqrt{\sum_{n=1}^{N}(X^i_n - \hat{\mu}_{X^i})^2}\sqrt{\sum_{n=1}^{N}(Y_n - \hat{\mu}_Y)^2}} \tag{2.83}$$

Where $\hat{\mu}_{X^i}$ and $\hat{\mu}_Y$ are the mean empirical estimators of X^i and Y.

2.7.2.2 Standardized Regression Coefficient (SRC)

The SRC is derived from the standardized[3] linear regression between Y and X^i, which are considered independent. SRC score is defined based on the regression coefficients α_i:

$$SRC_i = \alpha_i \frac{\sigma_{X^i}}{\sigma_Y} \tag{2.84}$$

The estimator $\widehat{SRC}_i$ of the SRC score can be obtained from the empirical estimators $\hat{\alpha}_i$, $\hat{\sigma}_{X^i}$ and $\hat{\sigma}_Y$ based on the dataset $\mathbf{D}_N$. The SRC sensitivity index is defined as $S^i_{SRC} = (SRC_i)^2$ and estimated by $\hat{S}^i_{SRC} = (\widehat{SRC}_i)^2$. If the linearity is valid then the variance of the output is decomposed to combinations of the input variables variances in equation 2.85.

$$Var(Y) = \sum_{i=1}^{d} \alpha_i^2 Var(X^i) \tag{2.85}$$

[3]Standardized in the sense that from the variables the mean is extracted and the standard deviation is divided in order to render them standard normal.

S^i_{SRC} is then bounded in $[0,1]$ with $\sum_{i=1}^{d} S^i_{SRC} = 1$. In this case $\hat{S}^i_{PC}$ and $\widehat{SRC}_i$ are identical with $\hat{c}_{X^iY} = \alpha_i \hat{\sigma}_{X^i}$. If for the uncertainty propagation the perturbation method is used then the partial derivatives of the inputs are equal to α_i and the SRC can be calculated directly from equation 2.84 using the results of the "*Sandwich rule*".

2.7.2.3 Partial Correlation Coefficient (PCC)

When a controlling variable Z is affecting both X^i and Y the result of PC coefficient can be misleading. To this purpose PCC removes the effect of Z focusing on the intrinsic correlation between X^i and Y. It is the correlation coefficient conditioned on the different values of Z. The controlling variables can be other inputs correlated to X^i. In that sense PCC can detect redundancies between inputs, the situation when two inputs are highly correlated but only one of them is important for the output. The PC for both of them will have similar values while PCC will identify the input impacting the output and the PCC of the other input will have an estimated value close to zero. The PCC sensitivity index S^i_{PCC} can be defined in relation to the PC coefficients of $X^i - Y$ ($S^{X^iY}_{PC}$), of $X^i - Z$ ($S^{X^i,Z}_{PC}$) and of $Y - Z$ (S^{YZ}_{PC}) :

$$S^i_{PCC} = \frac{S^{X^iY}_{PC} - S^{X^iZ}_{PC}\, S^{YZ}_{PC}}{\sqrt{1-(S^{X^iZ}_{PC})^2}\sqrt{1-(S^{YZ}_{PC})^2}} \tag{2.86}$$

The PCC can be then estimated empirically by the PC empirical estimators:

$$\hat{S}^i_{PCC} = \frac{\hat{S}^{X^iY}_{PC} - \hat{S}^{X^iZ}_{PC}\, \hat{S}^{YZ}_{PC}}{\sqrt{1-(\hat{S}^{X^iZ}_{PC})^2}\sqrt{1-(\hat{S}^{YZ}_{PC})^2}} \tag{2.87}$$

2.7.3 Monotonic model coefficients

When the model is non-linear SRC, PC and PCC fail to correctly estimate the output's sensitivities to the inputs. This limitation can be alleviated for monotonic models. The dataset $\mathbf{D}_N = \left[\mathbf{X}_n, \mathrm{Y_n}\right]_{n=1}^{N}$ is replaced by $\mathbf{D^R_N} = \left[\mathbf{Rx}_n, \mathrm{Ry_n}\right]_{n=1}^{N}$ with $\mathbf{Rx}_n$ and $\mathrm{Ry_n}$ the rank of each sample in the dataset. The estimation of the previous coefficients on this dataset gives rise to the Standardized Rank Regression Coefficient (SRRC), Spearman coefficient (SC) and the Partial Rank Correlation Coefficient (PRCC)

2.7.4 Analysis of Variance (ANOVA) indices

Analysis of variance (ANOVA) is called the decomposition of the output's variance on the different inputs. For the case of linear model and independent inputs the SRC can be seen as ANOVA indices. In this Section we present two indices that go beyond these constraints. The Sobol indices [95] that do not make any assumption on the model but are applied on independent inputs. The Shapley indices [96] that like Sobol do not make any model assumption but can treat dependent inputs. Both Sobol and Shapley indices are methods of Global Sensitivity Analysis (GSA).

2.7.4.1 Sobol

It is the main global sensitivity analysis method. No hypothesis is made on the model $Y = F(X)$. The main hypothesis is made on the inputs parameters which should be independent. The goal is to define indices by decomposing the variance of Y (ANOVA). In order to perform this decomposition Y must be square integrable. This is achieved by decomposing the model in sum of subfunctions:

$$Y = f_0 + \sum_{i=1}^{d} f_i(X^i) + \sum_{1\le i<j\le d} f_{ij}(X^i, X^j) + \cdots + f_{1\ldots d}(X^1, \ldots, X^d) \tag{2.88}$$

Where the subfunctions are defined by:

$$
\begin{aligned}
f_0 &= E[Y] \\
f_i(X^i) &= E[Y|X^i] - f_0 \\
f_{ij}(X^i, X^j) &= E[Y|X^i, X^j] - f_i(X^i) - f_j(X^j) - f_0 \\
&\vdots
\end{aligned}
$$

which are such that f_0 is constant and the rest of the subfunctions are orthogonal to each other. If we apply the ANOVA on this decomposition we obtain:

$$
Var(Y) = \sum_{i=1}^{d} D_i + \sum_{1 \le i < j \le d} D_{ij} + \cdots + D_{1\ldots d} \tag{2.89}
$$

with

$$
\begin{aligned}
D &= Var(Y) \\
D_i &= Var(E[Y|X^i]) \\
D_{ij} &= Var(E[Y|X^i, X^j] - E[Y|X^i] - E[Y|X^j]) \\
&\vdots
\end{aligned}
$$

The D_i explains the part of the output's variance directly from the parameter X^i while the D_{ij} explains the part of the output's variance due to the interaction between parameter X^i and X^j. We define the set A_i containing all the possible combinations of indices containing i. Based on these quantities the following Sobol indices are defined [97]:

$$
S_i = \frac{D_i}{D} \quad , \quad S_{ij} = \frac{D_{ij}}{D} \quad , \quad S_{T_i} = \sum_{\alpha_i \in A_i} S_{\alpha_i}
$$

with the following properties:

$$
S_i \ge 0, \quad S_{ij} \ge 0, \qquad \sum_{i=1}^{d} S_i + \sum_{1 \le i < j \le d} S_{ij} + \cdots + S_{1\ldots d} = 1
$$

The S_i is called the 1st order Sobol index and represents the direct effect of parameter X^i on the outputs variance . The S_{ij} is called the 2nd order Sobol index and represents the effect of the interaction between parameters X^i and X^j. The S_{T_i} is called the total Sobol index and represents the total effect of parameter X^i, directly and through all its possible interactions with the other parameters. It is obvious that if the inputs dimension is large the number of sensitivity indices to be computed increases rapidly. That is why usually we calculate only the first order and total Sobol indices. In order to estimate those indices large sample size are needed[4] and they are usually obtained by using surrogate models. To this purpose, we consider 2 large input samples of size M are generated $\mathbf{X}_{(m,1)}$ and $\mathbf{X}_{(m,2)}$ with $m = 1 \ldots M$. The typical estimators for f_0 and D are:

$$
\hat{f}_0 = \frac{1}{M} \sum_{m=1}^{M} F(X^1_{(m,1)}, \ldots, X^i_{(m,1)}, \ldots, X^d_{(m,1)}) \tag{2.90}
$$

$$
\hat{D} = \frac{1}{M} \sum_{m=1}^{M} F(X^1_{(m,1)}, \ldots, X^i_{(m,1)}, \ldots, X^d_{(m,1)})^2 - \hat{f}_0^2 \tag{2.91}
$$

To estimate the S_i index the D_i is estimated through:

$$
\hat{D}_i = \frac{1}{M} \sum_{m=1}^{M} F(X^1_{(m,1)}, \ldots, X^i_{(m,1)}, \ldots, X^d_{(m,1)}) F(X^1_{(m,2)}, \ldots, X^i_{(m,1)}, \ldots, X^d_{(m,2)}) - \tilde{f}_0^2 \tag{2.92}
$$

[4] At the order of 10^5

Where $\tilde{f}_0^2$ is a better adapted estimator of f_0^2 than the previous one for the 1st order index estimation [97]:

$$\tilde{f}_0^2 = \frac{1}{M}\sum_{m=1}^{M} F(X^1_{(m,1)},\ldots,X^i_{(m,1)},\ldots,X^d_{(m,1)})F(X^1_{(m,2)},\ldots,X^i_{(m,2)},\ldots,X^d_{(m,2)}) \tag{2.93}$$

The 1st order Sobol indice is estimated then by:

$$\hat{S}_i = \frac{\hat{D}_i}{\hat{D}} \tag{2.94}$$

For the total index the notion of $D_{\sim i}$ is introduced as the complement quantity of D_i and $X^{\sim i} = (X^j)_{j\in A\setminus i}$ as the complement of X^i, where $A = \{1\ldots d\}$.

$$D_{\sim i} = Var(E[Y|X^{\sim i}])$$

Then $D_{\sim i}$ is estimated from equation 2.95 and the corresponding total Sobol index from equation 2.96.

$$\hat{D}_{\sim i} = \frac{1}{M}\sum_{m=1}^{M} F(X^1_{(m,1)},\ldots,X^i_{(m,1)},\ldots,X^d_{(m,1)})F(X^1_{(m,1)},\ldots,X^i_{(m,2)},\ldots,X^d_{(m,1)}) - \hat{f}_0^2 \tag{2.95}$$

$$\hat{S}_{T_i} = 1 - \frac{\hat{D}_{\sim i}}{\hat{D}} \tag{2.96}$$

For this estimation of the whole Sobol indices $N(2d+2)$ model calls are necessary.

2.7.4.2 Shapley indices

This method is starting to be used quite recently and is a generalization of Sobol indices that can treat dependent input parameters. It is based on the Shapley values used in game theory. The main idea is to calculate the impact of an input on the output at all its possible combinations with the other inputs. If we could calculate all the Sobol indices we could also calculate the Shapley indices as well. To do so is very time consuming and it suffers from the "curse of dimensionality". The Shapley indices offer an approximate evaluation much less time consuming and independent of the inputs dimensions. In order to estimate the Shapley indices we will introduce some definitions. For the inputs $X \in \mathbb{R}^d$ we define $K = \{1, 2, \ldots, d\}$ the set containing all the indices of the parameters, π a permutation of the indices in K and $P_i(\pi)$ as the set that includes all parameters preceding index i in π. For example if $d = 6$ then $K = \{1, 2, 3, 4, 5, 6\}$, π could be $\{3, 6, 2, 1, 5, 4\}$ and then $P_1(\pi) = \{3, 6, 2\}$. The next step now is to define a cost function that relates a set of parameters to a value. In the context of global sensitivity the possible cost functions are:

$$\tilde{c}(J) = Var(Y) - E[Var(Y|X^J)] \tag{2.97}$$

$$c(J) = E[Var(Y|X^{\sim J})] \tag{2.98}$$

with $J \subseteq K$ and $X^{\sim J} = (X^i)_{i\in K\setminus J}$ complement of X^J

The $\tilde{c}(J)$ cost function is interpreted as the expected reduction in the outputs variance when the values of the parameters X^J are known. The $c(J)$ cost function is interpreted as the expected remaining outputs variance if all the parameters except J are known. The function $c(J)$ is used and if we define $\Pi(K)$ the set of all possible perturbations of K then the exact Shapley index for parameter X^i is:

$$Sh_i = \sum_{\pi\in\Pi(K)} \frac{1}{d!}(c(P_i(\pi)\cup\{i\}) - c(P_i(\pi))) \tag{2.99}$$

The cost function can be estimated by two loop Monte Carlo simulations [98] and the corresponding estimation of the Shapley index is:

$$\widehat{Sh}_i = \sum_{\pi \in \Pi(K)} \frac{1}{d!} (\hat{c}(P_i(\pi) \cup \{i\}) - \hat{c}(P_i(\pi))) \tag{2.100}$$

The number of possible permutations of d inputs is $d!$ and increases factorialy with the dimension of the input vector. To overcome this limitation N random permutations π_r are generated and an approximate Shapley index is calculated by:

$$\widehat{Sh}_i^{rand} = \frac{1}{N} \sum_{r=1}^{N} (\hat{c}(P_i(\pi_r) \cup \{i\}) - \hat{c}(P_i(\pi_r))) \tag{2.101}$$

2.7.5 Dependence measures

The dependence measures [99] can be used to overcome some limitations of ANOVA indices. The first one is that they estimate the impact of each input on the output's variance only, while dependence measures can estimate the impact on the whole output's distribution. The second one is that they are used only for quantitative analysis and cannot be used for screening purposes based on a selected sample while dependence measure can be used for both. The third and last one is that ANOVA indices cannot adapt easily to functional outputs. We will see in Section 2.7.6 that they can still be used in conjunction with PCA. Dependence measures can be used straightforward for functional outputs. We remind that we consider the model $Y = F(X) : \mathbb{R}^d \to \mathbb{R}$. Dependence measures are based on estimating the statistical dependence between Y and X^i with zero value indicating independent variables. Different approaches exist and we will detail some of the main ones.

2.7.5.1 Mutual information

Mutual information I dependence measure is based on the entropy H defined in equation 2.7 of X^i, Y and of joint (Y, X^i). The sensitivity index is expressed as:

$$S_{MI}^i = I(X^i; Y) = H(X^i) + H(Y) - H(X, Y) = \int p_{X^iY}(X^i, Y) \ln \left(\frac{p_{X^iY}(X^i, Y)}{p_{X^i}(X^i) p_Y(Y)} \right) dX^i dY \tag{2.102}$$

This index is always positive and zero in case of independent variables ($p_{X^iY} = p_{X^i} p_Y$).

2.7.5.2 Distance correlation

Distance correlation [100] is based on the notion of distance covariance $d_{cov}(X^i, Y)$. It is the distance between the joint characteristic function of (X^i, Y) denoted by ϕ_{X^iY} and the product of their marginals ϕ_{X^i} and ϕ_Y. The characteristic function for a random variable Z is the Fourier transform of its pdf and is defined as $\phi_Z(t) = E[e^{itZ}]$. The distance covariance is expressed through equation 2.103, where w is a positive weighting function defined in [100]. The weight function ensures that the distance covariance is 0 when the variables are independent and positive when they are dependent.

$$d_{cov}^2(X^i, Y) = \|\phi_{X^iY} - \phi_{X^i}\phi_Y\|_w^2 = \int |\phi_{X^iY}(X^i, Y) - \phi_{X^i}(X^i)\phi_Y(Y)|^2 w(X^i, Y) dX^i dY \tag{2.103}$$

The distance correlation sensitivity index is defined as:

$$S_{dcor}^i = \frac{d_{cov}(X^i, Y)}{\sqrt{d_{cov}(X^i, X^i)\, d_{cov}(Y, Y)}} \tag{2.104}$$

2.7.5.3 Hilbert-Schmidt Independence Criterion (HSIC) indices

HSIC indices were proposed by [101] for the detection of non-linear dependencies between two random variables. This is achieved by computing the cross-covariance between non-linear transformations of the variables. We consider the scalar input $X \in \mathcal{X}$ and the scalar output $Y \in \mathcal{Y}$.

The main motivation to derive the HSIC indices is based on searching an independence criterion C_{XY} with the property: *" If (X, Y) are independent if and only if $C_{XY} = 0$ "*.

We introduce the notion of the Reproducing Kernel Hilbert-Schmidt (RKHS) function space $\mathcal{F}$ from $\mathcal{X}$ to $\mathbb{R}$. It is a Hilbert space of functions $f : \mathcal{X} \to \mathbb{R}$ for which the application $f \to f(x)$ is continuous for all $x \in \mathcal{X}$. The Riesz theorem [102] states that for any $x \in \mathcal{X}$ there exists a unique evaluation function $\phi_x \in \mathcal{F}$ with the following reproducing property for all $f \in \mathcal{F}$:

$$f(x) =< f, \phi_x > \tag{2.105}$$

This evaluation function defines the reproducing kernel $k_X : \mathcal{X} \times \mathcal{X} \to \mathbb{R}$ for $\mathcal{F}$ as:

$$k_X(x, x') = \phi_x(x') =< \phi_x, \phi_{x'} > \tag{2.106}$$

The Moore-Aronszanj theorem [103] states that if $k_X : \mathcal{X} \times \mathcal{X} \to \mathbb{R}$ is a symmetric and positive definite kernel then there is a unique RKHS on $\mathcal{X}$ for which k_X is the reproducing kernel.

We introduce $\mathcal{G}$ a second RKHS of functions g from $\mathcal{Y}$ to $\mathbb{R}$ with reproducing kernel k_Y. The cross-covariance operator C_{XY} between X and Y is the linear operator $\mathcal{G} \to \mathcal{F}$ defined by:

$$< f, C_{XY} g >= E_{X,Y}[f(X)g(Y)] - E_X[f(X)]E_Y[g(Y)] \tag{2.107}$$

for $f \in \mathcal{F}$, $g \in \mathcal{G}$.

The Hilbert-Schmidt Independence Criterion (HSIC) is defined as $S_{HSIC} = \|C_{XY}\|^2_{HS}$ and can be expressed using the reproducing kernels [101] by:

$$\begin{aligned} S_{HSIC} = \|C_{XY}\|^2_{HS} = & \, E_{X,X',Y,Y'}[k_X(X, X')\, k_Y(Y, Y')] \\ & + E_{X,X'}[k_X(X, X')]\, E_{Y,Y'}[k_Y(Y, Y')] \\ & - 2\, E_{X,Y}[E_{X'}[k_X(X, X')]\, E_{Y'}[k_Y(Y, Y')]] \end{aligned} \tag{2.108}$$

In [101] the HSIC indices are estimated empirically through:

$$\hat{S}_{HSIC} = \frac{Tr(\mathbf{K}_X\, \mathbf{H}\, \mathbf{K}_Y\, \mathbf{H})}{N^2} \tag{2.109}$$

Where:

- $\mathbf{K}_X$ and $\mathbf{K}_Y$ are the Gram matrices of the kernel functions defined as $K^{jk}_{\mathcal{X}} = k_X(X_j, X_k)$ and $K^{jk}_Y = k_{\mathcal{Y}}(Y_j, Y_k)$ for $j \leq N, k \leq N$.
- $\mathbf{H}$ is a centering matrix with elements $H^{jk} = \delta_{jk} - \frac{1}{N}$ for $j \leq N, k \leq N$.

The important propery of HSIC indices is the following: "*If k_X and k_Y are universal and $\mathcal{X}$ and $\mathcal{Y}$ are compact then $S_{HSIC} = 0$ if and only if X and Y are independent.*". The universal property means that the corresponding RKHS function spaces $\mathcal{F}$ and $\mathcal{G}$ are dense in the space of continuous functions on $\mathcal{X}$ and $\mathcal{Y}$ with respect to the infinity norm [104]. There is no clear way for the selection of the kernel functions. In this thesis we use Gaussian kernels (satisfying the universal property).

2.7.5.4 HSIC statistical significance test

While the HSIC indices measure non-linear dependencies between X^i and Y they are not robust enough to be used directly for screening. It is preferable that they are used in statistical significance tests. The non-asymptotic significant test based on resampling presented in [105] can be used for screening purposes. The null hypothesis "H_0 : X^i and Y are independent" is adopted with a significance level $\alpha = 0.05$. The following procedure is applied for each input to identify which of them are important.

HSIC significance test

Initialize $\alpha = 0.05$, B bootstrap (with replacement) size and $p = 0$
Compute $\widehat{S}^i_{HSIC}$ for (X^i, Y)
Realize B bootstrap (with replacement) samples Y^b of Y
for $(b = 1, b \leq B, b++)$ **do**
    Compute HSIC indice between X^i and Y^b: $\widehat{S}^{i,b}_{HSIC}$ for (X^i, Y^b)
    $p = p + \frac{1}{B} 1_{\widehat{S}^{i,b}_{HSIC} > \widehat{S}^i_{HSIC}}$
end for
If $p < \alpha$ the H_0 is rejected and the variable X^i is considered important for Y

2.7.6 Functional sensitivity indices

So far the sensitivity indices were calculated for scalar outputs. In the case of functional ones $\mathbf{Y} \in \mathbb{R}^q$ different approaches have been proposed recently.

2.7.6.1 ANOVA aggregated indices

ANOVA indices decompose the variance of a scalar output on each input. For functional outputs PCA can be used to reduce the output's dimension to few scalar scores using equation 2.21. Based on a DOE surrogate models are used to approximate the underlying functions between the scalar PCA scores and the inputs. The surrogate models are used to perform the needed evaluations in order to estimate the Sobol or Shapley indices. An aggregate index is computed through equation 2.110 weighted by the scores variance representation $V^l = \frac{\Lambda_{ll}}{Tr(\mathbf{\Lambda})}$ over the total variance of the functional output. For the Sobol indices this method was introduced by [106]. We present the equivalent expression for the aggregated Shapley index in equation 2.110, where $\widehat{Sh}^i_l$ is the Shapley index between the input X^i and the output PCA score T_l.

$$\widehat{Sh}^i_{agg} = \sum_{l=1}^{L} \widehat{Sh}^i_l V^l \tag{2.110}$$

2.7.6.2 Dependence measures

For mutual information and distance covariance the extension to both functional inputs and outputs is straightforward for $X \in \mathbb{R}^d$ and $Y \in \mathbb{R}^q$. For HSIC indices it is more complicated since the kernel is applied on a metric for functional variables. For such kernels the universal property is not guaranteed [99]. As a consequence the independence detection cannot be guaranteed. However, approaches based on PCA have been presented for temporal and spatial outputs in [107] and [108]. The intuition behind these approaches is to define a distance metric in the functional space based on the scores of the PCA. The distance between each pair of functional realizations is calculated and the kernel function is applied on these distances.

2.8 Model calibration

Physical phenomena are often quite complex and in order to describe them simplified models are used. Often these models apart from the input variables contain also unknown parameters to be determined in order to enhance the model prediction capabilities. We consider a model $G(X, \boldsymbol{\theta})$, with unknown parameters $\boldsymbol{\theta}$, aiming at replacing the scalar underlying function $Y = F(X)$. In this example we use the input-outputs general notations but any intermediate inputs or outputs quantities can be used as well.

$$Y = G(X, \boldsymbol{\theta}) + \varepsilon \tag{2.111}$$

Model calibration consists of the estimation of $\boldsymbol{\theta}$, with ε the calibration error. Various approaches exist based on an obtained dataset $\mathbf{D}_N$. This dataset can be the result of experimental measurements or of a higher fidelity model. We are going to detail two approaches. Mean square error minimization, where $\boldsymbol{\theta}$ is estimated by minimizing $E[\varepsilon^2]$. Bayesian calibration, where a prior estimate of $\boldsymbol{\theta}$ is updated through the likelihood of observing $\mathbf{D}_N$. The calibration model for the

obtained dataset is expressed in equation 2.112, with $\mathbf{E}_{D_N}$ the vector of size N of the calibration errors $(\varepsilon_i)_{i=1}^N$.

$$Y_{D_N} = G(\mathbf{X}_{D_N}, \boldsymbol{\theta}) + \mathbf{E}_{D_N} \tag{2.112}$$

2.8.1 Mean Square Error minimization

The calibration parameters $\boldsymbol{\theta}$ are estimated by minimizing the mean square error of the calibration model:

$$\hat{\boldsymbol{\theta}} = \underset{\boldsymbol{\theta}\in\boldsymbol{\Theta}}{\operatorname{argmin}} \frac{1}{N}\sum_{i=1}^{N}(Y_i - G(\mathbf{X}_i, \boldsymbol{\theta}))^2 \tag{2.113}$$

Different optimization methods can be used to find this minimum. This approach aims at finding the best fitting of the model on the dataset.

2.8.2 Bayesian calibration

The previous method is very limited since it cannot include model inadequacy, observation errors and other sources of uncertainties. Bayesian calibration is a more mathematically rigorous approach since it defines a statistical framework. It updates a prior knowledge of $\boldsymbol{\theta}$ by conditioning on the observed dataset. The posterior pdf of $\boldsymbol{\theta}$ can take into account various sources of uncertainties (e.g. observation uncertainties) and allow to include the calibration parameters uncertainty. The general statistical framework is described by equation 2.114, where ε_i are N realizations of i.i.d., the error related to the observations $\varepsilon \sim \mathcal{N}(0, \sigma_\varepsilon^2)$.

$$Y_i = F(\mathbf{X_i}) + \varepsilon_i \tag{2.114}$$

The Bayes rule as we saw in Bayesian inference (Section 2.2.3) need the definition of the likelihood function of observing the dataset. This likelihood function depends on both the model and error definitions and assumptions. In [109] an overview on the different statistical frameworks is presented. The deterministic calibration model G is either computationally cheap and can be used directly or it is computational expensive and is approximated by a Gaussian process similar to the one presented for Kriging in Section 2.5.4. Besides that, the model can be considered as representing exactly the undergoing physical phenomena or as introducing a model discrepancy. The combination of these modeling and error options create 4 different frameworks M_1, M_2, M_3, M_4 of increasing complexity:

1. **Cheap code without discrepancy (M_1)**: The code model is fast enough to be used directly and is assumed to completely replace the physical phenomena. This results in the M_1 framework described by:

$$Y_i = G(\mathbf{X_i}, \boldsymbol{\theta}) + \varepsilon_i \tag{2.115}$$

2. **Expensive code without discrepancy (M_2)**: The code model is computationally expensive and thus a Gaussian process is used to replace it. The Gaussian process as in Kriging is constructed on the joint domain $(X, \boldsymbol{\theta})$ by a dedicated DOE of size M $\mathbf{D}_M^F = \left[(\mathbf{X}_m, \boldsymbol{\theta}_m), \mathbf{Y}_m\right]_{m=1}^M$. It is defined by its mean $\mu_F(X, \boldsymbol{\theta})$ and covariance function $c_F((X, \boldsymbol{\theta}), (X', \boldsymbol{\theta}'))$. As in Kriging the mean function is usually is a linear combination of predefined functions $\mu_F(X, \boldsymbol{\theta}) = h_F(X, \boldsymbol{\theta})\boldsymbol{\beta}_F$ and the covariance function is selected from a family of kernel functions with hyperparameters $(\sigma_F, \boldsymbol{\psi_F})$. No discrepancy is considered between the Gaussian process and the physical phenomena. This results in the M_2 framework described by:

$$Y_i = GP(\mu_F, c_F)_i + \varepsilon_i \tag{2.116}$$

   Together with $\boldsymbol{\theta}$ the Gaussian process parameters $(\boldsymbol{\beta}_F, \sigma_F, \boldsymbol{\psi_F})$ must be estimated as well.

3. **Cheap code with discrepancy (M_3)**: The code model is computationally fast and is used directly. The discrepancy between the model and the physical phenomena $\delta(\mathbf{X_i}) = F(\mathbf{X_i}) - G(\mathbf{X_i}, \boldsymbol{\theta})$ is modeled by a Gaussian process. It is defined by its mean function $\mu_d(X) = h_d(X)\boldsymbol{\beta}_d$ and covariance function $c_d(X, X')$ with hyperparameters $(\sigma_d, \boldsymbol{\psi_d})$. This results in the M_3 framework described by:

$$Y_i = G(\mathbf{X_i}, \boldsymbol{\theta}) + GP(\mu_d, c_d)_i + \varepsilon_i \tag{2.117}$$

Together with $\boldsymbol{\theta}$ the Gaussian process parameters $(\boldsymbol{\beta}_d, \sigma_d, \boldsymbol{\psi_d})$ must be estimated as well. There is an identifiability issue arising from the fact that multiple pairs of $(\boldsymbol{\theta}, \delta(X))$ can verify the discrepancy definition. This can be solved by setting the mean function $\mu_d = 0$ [110].

4. **Expensive code without discrepancy (M_4)**:The code model is computationally expensive and thus a Gaussian process is used to replace it as in M_2. The discrepancy is modeled by a Gaussian process as in M_3. The resulting framework M_4 introduced in the seminal work [110] is described by:

$$Y_i = GP(\mu_F, c_F)_i + GP(\mu_d, c_d)_i + \varepsilon_i \tag{2.118}$$

Together with $\boldsymbol{\theta}$ the two Gaussian process parameters $(\boldsymbol{\beta}_F, \sigma_F, \boldsymbol{\psi_F})$ and $(\boldsymbol{\beta}_d, \sigma_F d\boldsymbol{\psi_d})$ must be estimated as well.

For each model the likelihood must be defined prior to the estimation of the parameters. The parameters are usually grouped in two categories: the calibration parameters $\boldsymbol{\theta}$ common for all the statistical frameworks and the rest called nuance parameters depending on the framework. Once the framework is selected and its corresponding likelihood defined the estimation of the parameters can be performed either through Maximum Likelihood Estimation (MLE) or Bayesian Estimation. In MLE the parameters that maximize the likelihood are estimated either altogether in what is called full MLE or in separate steps (for M_2 and M_4). In the M_2 first the model Gaussian process hyperparameters are estimated through MLE on their partial likelihood and then plugged into the full likelihood. Secondly, $\boldsymbol{\theta}$ are estimated by maximizing this modified likelihood. For M_4 the $\boldsymbol{\theta}$ are estimated by mean square error minimization and then plugged into the calibration model to estimate the discrepancy by non-parametric regression on $(\mathbf{X}_{D_N}, Y_{D_N} - G(\mathbf{X}_{D_N}, \hat{\boldsymbol{\theta}})$. In Bayesian Estimation a prior is assigned to all the parameters to be estimated. Usually Jeffreys priors are used [111]. In full Bayesian Estimation the joint posterior of the outputs is estimated. This means that the nuance parameters must be integrated in order to estimate the marginal posterior pdf of $\boldsymbol{\theta}$. This approach is difficult due to the large number of nuance parameters. To this purpose [110] and [112] used an approach in separate steps called Modular Bayesian Estimation similar to the one in MLE. The difference is that the posterior pdf is sampled using Monte Carlo Markov Chains (MCMC) methods.

2.9 State of the art research

Most of the above mentioned topics are of high interest in research and development. We present some recent works on statistics and on application of these or similar methods in nuclear engineering.

2.9.1 Research in Statistics

With the rise of machine learning and data science an emphasis is given in feature selection methods that can be seen as methods for dimension reduction either on the inputs or outputs. The best representation of high dimensional non-linear data is sought. In [113] two methods based on HSIC indices are proposed to deal with interactions and redudancies between inputs in high dimensional spaces. Both methods use $sup - HSIC$ measure wich can be seen as the maximum HSIC value among different kernel functions. In [114] a novel method is proposed for feature selection based on HSIC indices and Lasso regularization which penalizes for large input sets. The method is applied to millions of inputs with very promising results. An interesting method for feature selection is presented in [115] where the conditional covariance is used as a metric of conditional dependence.

The input subset is calculated by minimizing the conditional covariance that is estimated using kernel functions. Another promising method gaining popularity for dimension reduction is the autoencoders, which consists of specific types of neural networks where their outputs are their inputs. This means that they find a representation that is as close as possible to the original inputs. Autoencoders are used in [116].

Uncertainty analysis in presence of functional inputs and outputs is a very challenging field of ongoing research. In [78] a methodology based on PCA and PLS is used for uncertainty propagation in the presence of both scalar and functional dependent inputs. An advanced uncertainty analysis methodology based on HSIC indices for screening and kriging for surrogate model was developed recently in [117]. In [118] and [119] PLS and PCA are combined with kriging for constructing surrogate models in high dimensional input spaces. Non linear PCA in conjuction with kriging and chaos polynomials are used for constructing surrogate models in high dimensional input spaces in [120].

Design of experiments research focus mainly on developing DOE adapted for specific purposes (e.g. failure probability estimation). In [88] different space-filling designs are studied and new ones are proposed. In [89] the applicability of different space-filling designs is studied and the need to consider non space-filling designs for specific cases is highlighted. In [121] sequential designs are presented for failure probability uncertainty estimation in a multifidelity framework. The high and low fidelity codes are modeled by two kriging models. In [122] an adaptive design construction for calibration purposes is studied. Kriging models are used to replace the actual code and the design is sequentially constructed based on Expected Improvement criterion in order to reduce the calibration error.

Sensitivity analysis is a field of constant research undergoing a lot of evolution in recent years. In [123] a generalization of Sobol indices for dependent variables is presented. A new sensitivity index called RDC measuring the non-linear dependency between two random variables is proposed in [124]. It is based on random non-linear copula projections of the variables, it is computationally cheaper than HSIC indices and it is possible to adapt it to functional random variables. Various sensitivity indices based on dependence measures are introduced in [99]. Besides that, their use in feature selection for large dimensions is evaluated. Johnson indices where used for high dimensional dependent inputs for linear model in [125]. In [126] the concept of goal oriented sensitivity indices was introduced based on contrast functions. An example of these goal oriented sensitivity indices is the quantile sensitivity indices studied in [127]. Besides that, sensitivity indices evaluating the sensitivity on the uncertainty of the inputs probability density function are developed in [128].

2.9.2 Research in Nuclear Engineering

Statistical state of the art methods are starting to being used in nuclear applications. In fuel-thermal, [129] used URANIE platform for uncertainty analysis of PWR fuel under irradiation modeled using METEOR code. Monte Carlo uncertainty propagation and sensitivity analysis by estimating Sobol indices were performed. The results are compared to experimental measurements. In [130] BISON code and the DAKOTA platform were used for fission gas sensitivity analysis based on a similar approach to Morris method. In [131] FRAPCON a comparative sensitivity analysis using Pearson correlations and Sobol indices highlight the necessity of using sensitivity indices that capture interactions between inputs on the outputs. An interesting approach is carried out in [132] for a thermal-hydraulic modeling of a conceptual reactor design. Adjoint sensitivity analysis showed the need to calculate second order sensitivities due to non-linearities. In neutronics [133] applied an uncertainty propagation and sensitivity analysis (Sobol indices) for functional outputs on a neutronic transient modeled by point kinetics. Kriging and PCE were used in conjuction with PCA for dimension reduction. An interesting approach is presented in [134]. A methodology for dimension reduction using of linear projections similar to PCA, including calculation of bounds for the reduction error, is used to replace neutronic/fuel-thermal coupled codes. A lot of research is done for cross-sections uncertainty analysis in large cores. In [135] assembly depletion in lattice calcualtions is studied while in [21] full detailed PWR core static uncertainty analysis using adjoint solutions. In [136] the differences between core assembly and pin by pin homegenization level is highlighted in an uncertainty analysis using COBAYA code. Both Monte Carlo and adjoint approaches were applied.

Chapter 3

Development and Testing of an Uncertainty Quantification Methodology

3.1 Introduction

Pressurize Water Reactors (PWR) computational modeling evolves with the available computational power. The complexity of Best Estimate (BE) codes increases and coupling frameworks are developed in order to simulate strong multi-physics transients. An example of such transient is the Rod Ejection Accident (REA) detailed in Section 1.6. In Chapter 1 we saw that three different disciplines or 'physics' are identified as important for REA. The first one is neutronics modeling the power generation by calculating the neutrons' distribution in the core. The second one is fuel-thermomechanics modeling the heat distribution inside the fuel pin induced by the power generation. Mechanical and temperature evolution are computed from the fuel pellet center until the cladding external surface. The third one is thermal-hydraulics modeling the heat extraction by the coolant. The temperature, density and other thermal-hydraulics quantities are calculated as the coolant circulates in the pressurized core.

In a multi-physics coupling framework the different neutronic, fuel-thermomechanic and thermal-hydraulic BE codes are coupled in order to improve the transient modeling. In this thesis we use the coupling framework developed at CEA for the REA modeling. It is based on CORPUS tool for the coupling of APOLLO3 ® (neutronics), FLICA4 (thermal-hydraulics) and ALCYONE V1.4 (fuel-thermomechanics). As discussed in Section 1.7 two couplings are available. The BE coupling of APOLLO3 ® - FLICA4 and the Best Effort coupling of APOLLO3 ® - FLICA4 - ALCYONE V1.4.

Driven by the need of improving the safety margins uncertainty analyses are carried out and Best Estimate Plus Uncertainty (BEPU) methods are developed with industrial applications. In Chapter 2 we saw an overview of statistical tools that could be used in an uncertainty quantification methodology (UQM). The use of the CORPUS coupling framework to develop an UQM for a REA creates many challenges:

- Computationally expensive modeling not allowing many code evaluations.
- Large input and output dimensions that can create difficulties for the application of the different statistical tools.
- Input dependencies that can lead to redundant inputs. This is the case when two inputs are strongly dependent and one is very important for an output while the other one is not. Most of the sensitivity methods will detect both of the inputs as very important.
- Interaction between inputs on the outputs variance. This can occur when one input is not directly significant to an output but only in conjunction with another input.
- Non-linear output behavior. It is not always easy for the surrogate model to correctly approximate a non-linear function, especially where there are discontinuities.

The objective is to explore the different statistical tools to address some of these challenges in the UQM.

In this Chapter we present the development and testing of the UQM on a small scale core called MiniCore that is representative of a PWR core behavior. In Section 3.2 we detail the MiniCore geometry with all its modeling aspects (e.g. discretization) the initial state and the reference characteristics of the REA. In Section 3.3 we identify the inputs and outputs for the UQM and discuss the inputs uncertainty quantification. In Section 3.4 we perform preliminary decoupled stand-alone uncertainty analysis studies for each code. Depending on the nature of the inputs and outputs relevant statistical tools are tested.

In Section 3.5, we study the multi-physics APOLLO3® - FLICA4 BE coupling scheme with all the identified inputs and outputs. An input dimension reduction method is developed to identify important input subspaces. Additionally, an adaptation of the simulated annealing LHS optimization algorithm is developed to guarantee good space-filling properties in both the original input space and the identified important input subspace. Both methods and relevant statistical tools are

tested on the BE coupling scheme. The conclusions drawn from the preliminary decoupled and multi-physics coupled studies are used to develop the UQM step by step scheme.

In Section 3.6, the case of the gap heat transfer (H_{gap}) is studied in order to improve the multi-physics BE modeling used in Section 3.5. Since the inclusion of ALCYONE V1.4 increases dramatically the computational cost there is a strong interest in trying to extract knowledge from decoupled ALCYONE V1.4 analyses. We present a methodology to calibrate a simplified H_{gap} model and to quantify its uncertainty. The calibrated model is introduced then in the BE coupling scheme creating an improved BE modeling. The originality of the proposed H_{gap} model is that its uncertainty can be quantified and propagated through the APOLLO3 ® - FLICA4 coupling. The UQM is tested again on this improved coupling and for selected design points comparisons are made with APOLLO3® - FLICA4 - ALCYONE V1.4 Best Effort coupling scheme. The Chapter ends with some general conclusions in Section 3.7.

In general the pre-treatment, the calculations and the post-treatment of the results are performed with Python language scripts. For testing the different statistical tools and developing the UQM R statistics language is used. The Best Effort calculations were carried out on the new TGCC Joliot-Curie cluster.

3.2 REA modeling and description

3.2.1 Core design

The REA is studied in a small scale core geometry called MiniCore for the test and development phase of the UQM. The MiniCore is representative of a PWR core behavior and was used as a proof of concept in [1]. The small size allows to test different coupling levels and statistical tools in order to develop the UQM in an environment relatively close to a PWR. The geometry is presented in figure 3.1 and consists of a 5×5 assembly lattice. The 3×3 inner lattice are fuel assemblies with three different burn-ups: 0, 15 and 30 GWd/t while the outer assemblies are water reflector assemblies. The fuel has a typical UO_2 composition except the central assembly where it has a mixture composition of $UO_2 - GdO_3$. The total height of the core is 468.72 cm with a bottom and top reflector of 21 cm leading to a fuel active height of 426.72 cm. The assemblies are a 17×17 lattice of fuel pins as typical PWR assemblies with pitch 21.504 cm. The control rod at the initial core state is injected from the top in the central assembly and is covering 82 cm of the active fuel height.

Pin pitch (cm)	1.26
Assembly pitch (cm)	21.504
Active height (cm)	426.72
Full height (cm)	468.72
Control rod cover rate	$\frac{82}{426.72}$

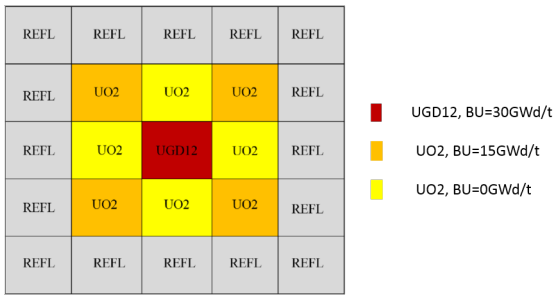

Figure 3.1: MiniCore geometry and characteristic dimensions.

3.2.2 Modeling

The REA in the MiniCore geometry is modeled by the CORPUS coupling framework presented in Section 1.6 that includes the codes: APOLLO3 ® for neutronics , FLICA4 for thermal-hydraulics and ALCYONE V1.4 for fuel-thermomechanics. Two multi-physics couplings exist: the APOLLO3 ® - FLICA4 BE coupling and the APOLLO3 ® - FLICA4 - ALCYONE V1.4 Best Effort coupling. Besides that, each code includes simplified modelings of the other branches of physics allowing computationally cheap stand-alone simulator modeling of REA. The phase space of the equations

of each code are discretized and boundary conditions are applied in order to establish the modeling of the REA.

In APOLLO3 ® a two group Diffusion approximation (equations 1.21a and 1.21b) is used with void boundary conditions on the neutron current (Section 1.3.3). The geometry is discretized radially at the level of quarter of assembly and axially in 34 axial meshes of which 30 are dividing the active fuel height and 4 are used for bottom and top reflector. A total number of 3400 meshes is used. The interaction with other disciplines arises from the multiparametric macroscopic cross-sections. More precisely, the parameters of fuel temperature and moderator density are the ones estimated by fuel-thermomechanics and thermal-hydraulics respectively.

In FLICA4 the 4 equations porous modeling is used with a multi-1D axial flow approximation (Section 1.5.3). The porous modeling consists in averaging the thermal-hydraulic quantities in both time and space. The presence of coolant and solid structures is taken into account through the calculated effective porosity of the medium. The coolant is treated as a mixture of vapor and liquid. A system of 4 equation is solved (equations 1.53a - 1.53d): mixture mass balance, vapor mass balance, mixture momentum balance and mixture energy balance. The boundary conditions consist in determining the inlet mass flow and enthalpy and the outlet pressure. One thermal-hydraulic channel is used for each quarter of assembly in accordance with the neutronics discretization and only the fuel active part is modeled. A total number of 1080 meshes is used. The interactions with neutronics comes from the power directly injected in the coolant by gamma emission and with fuel-thermomechanics by the heat flux reaching the coolant due to head diffusion in the fuel.

Both APOLLO3 ® and FLICA4 spatial discretizations are illustrated in figure 3.2. The green border indicates the complete geometry modeled by APOLLO3 ®. The blue border the fuel active geometry part modeled by FLICA4 excluding thus the reflector assemblies.

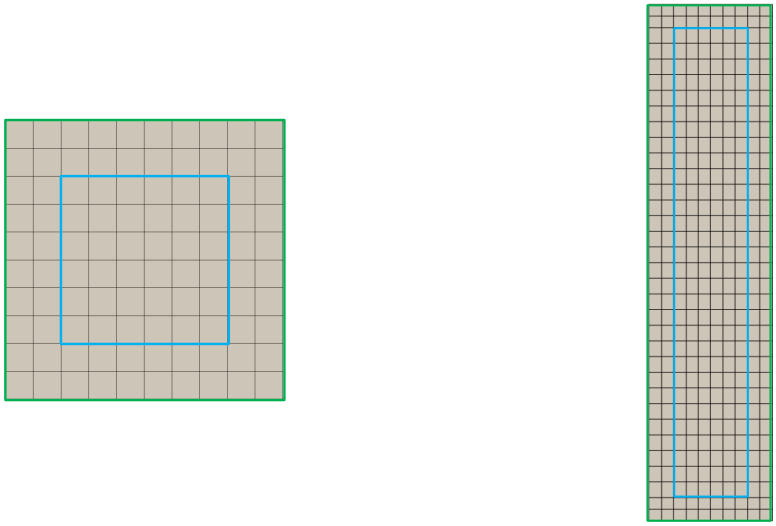

Figure 3.2: APOLLO3 ® and FLICA4 radial (left) and axial discretization (right). The green borders indicate the part of the geometry modeled by APOLLO3 ® and the blue borders the part of the geometry modeled by FLICA4.

In ALCYONE V1.4 a 1D radial approximation is used for solving the fuel-thermomechanics equations as described in Section 1.4.3. The boundary conditions consist in determining the loadings such as the external pressure on the fuel pin and by determining the power generated in the fuel and the cladding external wall temperature. The two last ones are the interactions with neutronics and thermal-hydraulics respectively. One average fuel pin is used for each thermal-hydraulic channel with the same axial discretization of 30 meshes in accordance with both neutronics and thermal-hydraulics modeling. For the radial discretization the fuel is divided into 25 regions with finer discretization at the external part. The power distribution inside a fuel pin is not uniform and changes with its burn-up (Section 1.4.1.1). During the fuel evolution in the core the U-238 at

external part interacts with the epithermal neutrons producing Pu-239 that has high probability to exhibit fission. This creates an external fuel zone with higher power and thus higher burn-up. Beyond $40GWd/t$ this zone restructures to what is called the high burn-up structure with increased porosity. That is why a finer discretization needs to be used at the fuel periphery. The cladding is divide into 3 regions. At this point is important to mention the simplified thermal model of FLICA4 because it is the one used for the UQM development. In FLICA4 a 1D radial fuel thermal modeling is available with a discretization of 7 regions in the fuel and 3 regions in the cladding. The thermal equations are solved in the fuel and the cladding are linked through the gap heat transfer that is modeled by a constant value. The two radial fuel pin discretizations of FLICA4 and ALCYONE V1.4 are presented together in figure 3.3.

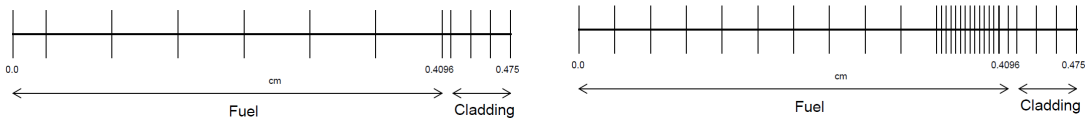

Figure 3.3: Fuel thermal radial discretization in FLICA4 (left) and ALCYONE V1.4 (right) for the MiniCore geometry.

The time discretization for the REA is the same for all the codes for each coupling or stand-alone modeling. A total transient duration of $0.4\,s$ is considered with a constant incremental time step of $0.001\,s$. The control rod is ejected in $0.1\,s$.

The two group macroscopic cross-sections are generated for each assembly by APOLLO2 lattice calculations. They are the same cross-sections used in [1] and are parameterized in burn-up, boron concentration, moderator density and fuel temperature. More information about the range of the cross-section parametrization can be found in Appendix A. For the isotopic composition of the fuel in ALCYONE V1.4 a typical PWR power evolution is applied. The core is set at a Hot Zero Power (HZP) condition, meaning that the temperature is around $290°C$ and the power negligible.

For the REA study in this core an important aspect is the xenon ($Xe-135$) distribution since it can radically alter the control rod worth and consequently the transient evolution. To this purpose a $Xe-135$ axial profile is applied in all the fuel assemblies. The profile is the result of a xenon transient calculation with APOLLO3 ®. The profile leading to higher control rod worth is selected and applied homogeneously in all the fuel assemblies. This is done in order to simplify the MiniCore modeling. The selected $Xe-135$ axial profile is visualized in figure 3.4.

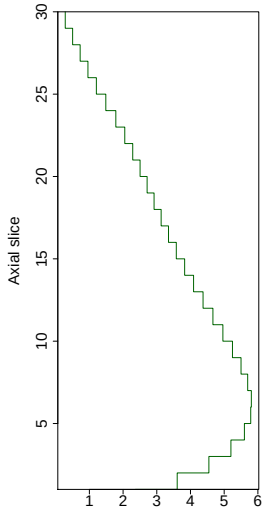

Figure 3.4: $Xe-135$ concentration in $10^{15}\,atoms/cm^3$ axial profile applied homegenously in all the fuel assemblies of the MiniCore.

We observe that the maximum is located towards the bottom of the fuel assembly. This pushes

more neutrons to the top of the assembly where the control rod is located. The effective absorption of the control rod thus increases resulting in a higher control rod worth and thus a more violent transient.

3.2.3 Initial state and reference transient

The MiniCore, as mentioned, is at a HZP conditions with the control rod inserted in the top part of the central assembly. The core is critical and the initial negligible power distribution is illustrated in figure 3.5, where we can see the peaked towards the top power exactly under the control rod position. In table 3.1 some characteristic core conditions are given. The initial core power is $0.11\,W$ and the fuel and moderator temperatures are both at $290°C$.

The reference (without uncertainties) REA characteristics obtained by an APOLLO3 ® - FLICA4 modeling are presented in table 3.2 and figure 3.6. The control rod worth is $\rho_{\text{worth}} = 1.7\,\$$ indicating a strongly prompt driven transient. It is the injected reactivity in the core due to the control rod extraction as defined in Section 1.3.1.3. In the figure on the right we can observe the created power pulse of width $\Gamma = 17\,ms$ with a maximum power of $\mathrm{P}_{\text{core}}^{\text{max}} = 60\mathrm{P}_{\text{nom}}$ at instant $\mathrm{t}^{\text{max}} = 160\,ms$. Where P_{nom} is the MiniCore nominal power. The power at the end of the transient reduces to $\mathrm{P}_{\text{core}}^{\text{end}} = 0.72\mathrm{P}_{\text{nom}}$. The deformation factor F_{xyz} is defined as the ratio between the maximum local power and the average local power. The F_{xyz} in time is plotted starting from 3.5 and reaching up to 4.1 when the control rod is fully ejected $(0.1\,s)$.

Table 3.1: Characteristic conditions of the MiniCore initial state.

Initial core power	$\mathbf{P}_{\mathbf{core}}^{\mathbf{init}}$ **(W)**	0.11
Moderator density	$\mathbf{D_{mod}}$ **(g/cm^3)**	0.745
Pressure	**P (bar)**	155
Volumetric flow rate	**Q** (m^3/h)	4241
Fuel temperature	$\mathbf{T_f}$ **(°C)**	290
Moderator temperature	$\mathbf{T_m}$ **(°C)**	290
Boron concentration	$\mathbf{C_{bor}}$ **(ppm)**	694

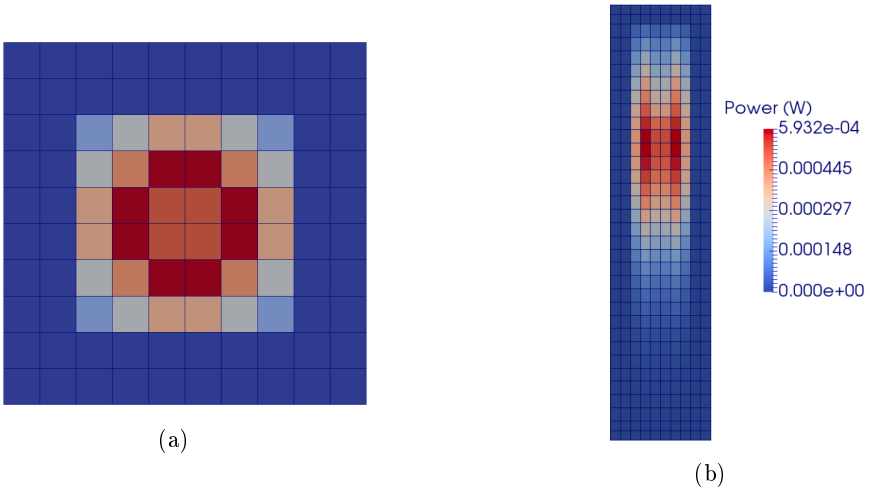

(a) (b)

Figure 3.5: Initial power distribution in the MiniCore for the radial (a) and axial (b) cross-sections at the center.

Table 3.2: Characteristic quantities for the reference REA in the MiniCore.

Effective delayed neutron fraction	$\beta_{\mathbf{eff}}$ **(pcm)**	569
Control rod worth	$\rho_{\mathbf{worth}}$ **(\$)**	1.7
Maximum core power	$\mathbf{P}^{\mathbf{max}}_{\mathbf{core}}$	$60\mathrm{P}_{\mathrm{nom}}$
Final core power	$\mathbf{P}^{\mathbf{end}}_{\mathbf{core}}$	$0.72\mathrm{P}_{\mathrm{nom}}$
Power pulse width	$\mathbf{\Gamma}$ **(ms)**	17
Time of maximum core power	$\mathbf{t}^{\mathbf{max}}$ **(ms)**	160
Maximum $3D$ **deformation factor**	$\mathbf{F}^{\mathbf{max}}_{\mathbf{xyz}}$	4.1

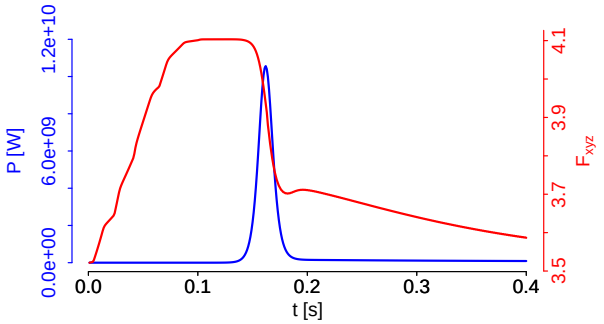

Figure 3.6: Integral power and F_{xyz} deformation factor evolution for the reference REA in the MiniCore.

3.3 Input uncertainties modeling

Before testing different statistical tools and developing the UQM it is important to identify the uncertain inputs and outputs of interest for the REA. Additionally, the input uncertainties must be quantified prior to the different uncertainty studies.

3.3.1 Inputs-Outputs identification

The inputs and outputs were identified based on PIRT approaches and expert opinions. We remind that PIRT (Phenomena Identification and Ranking Table) is an approach applied to different safety scenarios where the most important phenomena are identified together with their degree of knowledge or uncertainty. A total of 22 scalar inputs and 4 outputs (three scalars and one functional) were selected spanning the different interacting physics and are presented in table 3.3.

For the inputs, in neutronics we identified the different macroscopic cross-sections and kinetic parameters. The considered two group macroscopic cross-sections are the disappearance cross-section[1] TD_1 and TD_2, $\nu \times fission$ cross-section NF_1 and NF_2, diffusion coefficient D_1 and D_2 and scattering cross-section from energy group 1 (fast) to 2 (thermal) $S_{1\to 2}$. The kinetic parameters are the effective delayed neutron fraction β_{eff}, the effective decay constant λ_{eff} and the group inverse velocities IV_1 and IV_2.

In fuel-thermomechanics the materials laws of thermal conductivity and specific heat capacity for the fuel and the cladding are considered (λ_f, λ_c, Cp_f, Cp_c). Additionally, the gap heat transfer H_{gap}, the Rowlands temperature T_R used as the effective Doppler temperature and the power radial profile P_r were also taken into account. As discussed in Section 1.3.3.7, since in neutronics there is no fine description of the fuel pin temperature compared to fuel-thermomechanics an effective temperature must be used for the Doppler effect taking into account the radial variation. In our case we use the Rowlands temperature as the effective Doppler temperature. Concerning

[1] Defined as the total cross-section minus the self-scattering

P_r, as mentioned in Section 1.4.1, with the fuel evolution in the core the power is peaked towards the periphery. This radial profile is modeled by a parametric function described in [137] and the uncertainty is considered on the fuel external surface power.

In thermal-hydraulics different models were identified as important: the convective heat transfer H_c, the recondensation K_{v0}, the threshold R_{crit} determining when the DNB is reached and the post-DNB heat transfer H_{dnb} beyond this threshold. All these models are discussed in Section 1.5.3.5.

Table 3.3: Inputs and outputs uncertain quantities in **neutronics** , **thermal-hydraulics** and **fuel thermal**.

Inputs (22 scalars)			
$\mathbf{TD_g(2)}$	Disappearance cross-section of group g	$\mathbf{NF_g(2)}$	$\nu \times$ fission cross-section of group g
$\mathbf{D_g(2)}$	Diffusion coefficient of group g	$\mathbf{S_{1\to 2}}$	Scattering cross-section of group 1 to 2
$\mathbf{IV_g(2)}$	Inverse velocity of group g	$\beta_{\mathbf{eff}}$	Effective delayed neutrons
$\lambda_{\mathbf{eff}}$	Effective decay constant		
$\lambda_{\mathbf{f}}$	Fuel thermal conductivity	$\lambda_{\mathbf{c}}$	Cladding thermal conductivity
$\mathbf{Cp_f}$	Fuel specific heat capacity	$\mathbf{Cp_c}$	Cladding specific heat capacity
$\mathbf{H_{gap}}$	Fuel-cladding gap heat transfer	$\mathbf{T_R}$	Rowland temperature
$\mathbf{P_r}$	Power radial profile		
$\mathbf{H_c}$	Convective heat transfer	$\mathbf{R_{crit}}$	Criterion for post-DNB heat transfer
$\mathbf{K_{v0}}$	Recondensation	$\mathbf{H_{dnb}}$	Post-DNB heat transfer
Outputs (3 scalars + 1 functional)			
$\mathbf{P_{lin}^{max}}$	Local linear power (max in time)	$\mathbf{P_{lin}^{2D}(x,y)}$	Radial distribution of
$\mathbf{H_f^{max}}$	Fuel stored enthalpy (max in time)		linear power at the time and
$\mathbf{DNB^{min}}$	Distance from $\mathbf{R_{crit}}$ (min in time)		axial position of $\mathbf{P_{lin}^{max}}$

For the outputs, in neutronics we consider the maximum local linear power during the REA P_{lin}^{max} and the radial linear power distribution P_{lin}^{2D} at the time and radial plane of P_{lin}^{max}. In fuel-thermomechanics we selected the maximum local stored enthalpy H_f^{max} while in thermal-hydraulics the minimum distance to DNB DNB^{min}. The latter output is defined as the difference between the DNBR (Section 1.5.3.5) and the DNB threshold R_{crit}.

The identified inputs and outputs will be used for the application of the UQM. For the testing of different statistical tools in order to derive the UQM more outputs will be studied related to each analysis. This will allow to highlight advantages and disadvantages of some methods and to avoid the applicability restriction of the UQM only on the identified inputs and outputs.

3.3.2 Input uncertainty quantification

In Section 2.2 we saw that there are different methods for the uncertainty quantification from expert judgment to statistical or Bayesian inference. In this thesis for the identified inputs we use the UAM recommendations where they are available and expert opinions for the rest. More details about the quantification of the input uncertainties can be found in Appendix B. We remind that UAM is an international uncertainty analysis benchmark [59]. The resulting pdf for the inputs are presented in table 3.4.

For the neutronic inputs, the two group macroscopic cross-sections and the kinetic parameters, a multivariate normal distribution is used based on statistical inference. The mean vector of the pdf is the reference cross-sections produced in CEA $\boldsymbol{\Sigma_{CEA}}$ and the covariance matrix $\mathbf{C_{UAM}}$ empirically estimated by the results of UAM. The UAM provided a dataset of two group macroscopic cross-sections resulting from neutronic lattice uncertainty propagation. This dataset of 100 realizations was adapted for the cross-sections used by APOLLO3 ® by assuming:

1. Negligible uncertainties on the up-scattering cross-section $S_{2\to1}$.

2. Negligible $n-2n, n-3n\ldots$ cross-sections uncertainties.

The adapted macroscopic cross-sections dataset was used to estimate the correlation matrix and the relative standard deviations of the cross-sections. Finally, $\mathbf{C_{UAM}}$ is calculated using the correlation matrix, the relative standard deviations and the reference CEA cross-sections. The correlation matrix for the neutronic inputs is illustrated in figure 3.7, where we can see large positive and negative correlations. The TD_1 is strongly positively correlated with $S_{1\to2}$ and IV_1 and negatively with D_1. The β_{eff} is strongly positively correlated with λ_{eff} and both are in general uncorrelated to the other neutronic inputs.

Table 3.4: Inputs uncertainty quantification results.

Neutronics		Fuel-thermomechanics	
$\mathbf{TD_g}$, $\mathbf{NF_g}$, $\mathbf{D_g}$, $\mathbf{S_{1\to2}}$, $\mathbf{IV_g}$, $\beta_{\mathbf{eff}}$, $\lambda_{\mathbf{eff}}$	$\mathcal{N}(\boldsymbol{\Sigma_{CEA}}, \mathbf{C_{UAM}})$	$\lambda_\mathbf{f}$	$\mathcal{N}(1, 0.05)$
Thermal-hydraulics		$\lambda_\mathbf{c}$	$\mathcal{N}(1, 0.05)$
$\mathbf{H_c}$	$\mathcal{N}(1, 0.15)$	$\mathbf{Cp_f}$	$\mathcal{N}(1, 0.015)$
$\mathbf{R_{crit}}$	$\mathcal{N}(1, 0.15)$	$\mathbf{Cp_c}$	$\mathcal{N}(1, 0.015)$
$\mathbf{K_{v0}}$	$\mathcal{N}(1, 0.125)$	$\mathbf{H_{gap}}$	$\mathcal{U}(2000, 50000)$
$\mathbf{H_{dnb}}$	$\mathcal{U}(0.8, 1.2)$	$\mathbf{P_r}$	$\mathcal{U}(1, 1.08) + \mathcal{N}(0, 0.0175)$
		$\mathbf{T_R}$	$\mathcal{U}(0, 1)$

The rest of the inputs are considered independent of the neutronic inputs and between them. The thermal-hydraulic input distributions are mainly based on CEA experts opinions and are applied as random multiplication coefficients with mean 1 on the different models. The R_{crit} usually is penalized to 1.3 and in this thesis we considered this value as the 95% upper quantile of a normal distribution with mean value 1. For H_{DNB} a uniform distribution is used reflecting the limited current knowledge about this phenomenon.

In fuel-thermomechanics inputs and more specifically for the thermal conductivities and specific heat capacities the UAM recommendations were used. For the Rowlands temperature a uniform distribution was considered on the weight fraction of the fuel centerline temperature. In the reference situation (equation 1.20) the Rowlands temperature has a 4/9 weight on the fuel centerline temperature and 5/9 on the fuel external surface temperature. By using an uncertain multiplication factor with $\mathcal{U}(0,1)$ distribution on the centerline temperature weight we consider that it can only decrease uniformly between 4/9 and zero with a corresponding increase in the external surface temperature weight. The H_{gap} is a particular input quantity since in the BE coupling H_{gap} is an uncertain constant in FLICA4 with uniform pdf bounded by its value for a complete open gap ($2e^3\,Wm^{-2}K^{-1}$) and for a pellet-cladding contact ($5e^4\,Wm^{-2}K^{-1}$). In the Best Effort coupling H_{gap} becomes a result of ALCYONE V1.4 and thus is not considered. We will see that a part of the thesis work is dedicated to calibrating a H_{gap} model in order to introduce it in the BE coupling and improve its modeling without increasing its computational cost. The uncertainties of the calibrated model will be estimated as well and added to the uncertain inputs. Finally, the power radial profile uncertainty is modeled by a multiplication factor on the fuel external surface power with a pdf resulting from the convolution of a normal and an uniform distribution. The power radial profile is peaked towards the periphery for the high burn-up fuel pins as was described in Section 1.4.1. The deformation is increasing with burn-up and to model it an explicit function of burn-up is used [137]. The uncertainty results from two independent effects and is modeled by the sum of two independent variables: the uncertainty of the function used is modeled by a random variable with distribution $\mathcal{N}(0, 0.0175)$ and the uncertainty due to the presence or not of a guide tube near the fuel pin is modeled by a random variable with distribution $\mathcal{U}(1, 1.08)$.

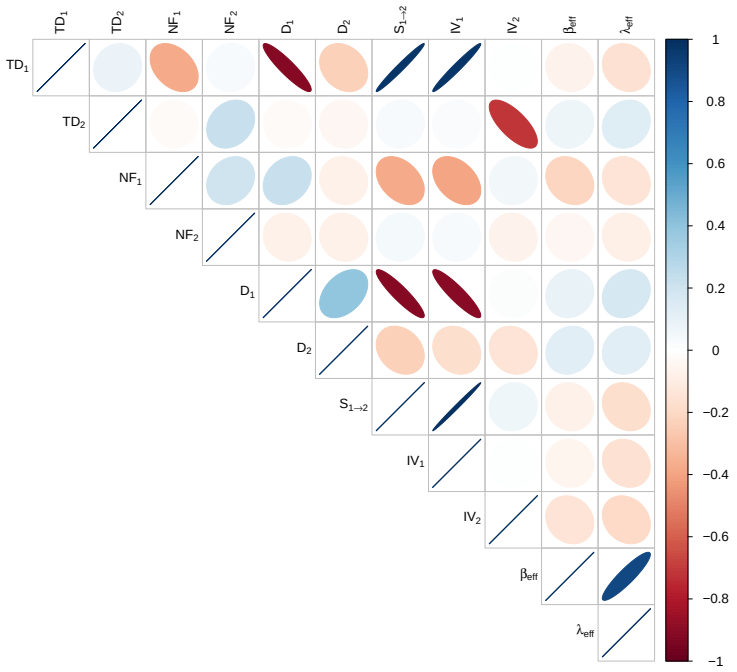

Figure 3.7: Correlation matrix for neutronic inputs.

3.4 Preliminary stand-alone studies

3.4.1 Introduction

Some of the different available uncertainty analysis tools from Chapter 2 are tested initially in cheap stand-alone calculations. This will allow to evaluate their efficiency in an environment relatively close to the BE coupling on which the UQM will be developed. The tools that do not perform well will be rejected. Besides that, it is interesting to start from separate physics analyses and progressively add more layers of coupling rendering the REA modeling more complex. It is important to remember that with the MiniCore geometry we cannot extract physical conclusions and thus we focus mainly on the conclusions drawn for each statistical tool. We perform three different analyses, one for each code:

- **Neutronics stand-alone**: Two different analyses are carried out using only APOLLO3 ®. The first is for the static initial state where only the macroscopic cross-sections are uncertain. The second is for the REA transient using an adiabatic fuel thermal treatment in order to model the Doppler feedback. Both analyses include inputs with strong dependencies and thus the performance of the different global sensitivity methods for dependent inputs will be tested. From the ones presented in Section 2.7 we focus on the ANOVA indices (Section 2.7.4) that decompose the variance of the output on each input. Shapley indices are compared to the Sobol indices. The former are estimated without using the "pick-freeze" method, as presented in Section 2.7.4.2. The latter are estimated by the "pick-freeze" method of Section 2.7.4.1. This method is not adapted for dependent inputs but it is used throughout the thesis since we focus on the more robust Shapley indices for the dependent inputs. There are methods for estimating Sobol indices that are better adapted for dependent inputs such as in the work of T. A. Mara [138], but we consider that they are not of interest in the context of the thesis. Additionally, we test the performance of the HSIC indices. They belong to the dependence measures (Section 2.7.5) that estimate the sensitivity on the whole output pdf and not only its variance. The HSIC screening capabilities in statistical significance tests are evaluated, as defined in Section 2.7.5.4. These tests verify the null hypothesis that the input and output are independent. If the hypothesis is rejected the input is considered as significant. Uncertainty propagation is carried out and the complete outputs histograms are estimated. For testing all the previous statistical tools surrogate models must be trained.

The behavior of three different surrogate models of Section 2.5 is evaluated: linear, kriging and artificial neural networks (ANN). The transient analysis gives the opportunity to test functional outputs using Principal Components Analysis (PCA). This method was described in Section 2.4.1 and essentially derives basis functions adapted for the best representation of each functional output. In cases that PCA might not be enough it can be enhanced by stochastic warping (Section 2.4.3) which aims at translating the output observations in order to render them as similar as possible. The functional output sensitivity is estimated using aggregate Shapley indices defined in equation 2.110 of Section 2.7.6.1.

- **Thermal-hydraulics stand-alone**: The reference power pulse from the APOLLO3 ® stand-alone study is used as an imposed power evolution in FLICA4. The uncertainty of both fuel-thermal and fuel-thermomechanics is considered as described in table 3.4. The performances of the previously mentioned sensitivity methods are evaluated for independent inputs with various pdfs.

- **Fuel-thermomechanics stand-alone**: The reference power pulse from APOLLO3 ® stand-alone study and the corresponding cladding wall temperature evolution from FLICA4 are applied in ALCYONE V1.4. For testing purposes the modeling is restricted to the axial slice where the maximum linear power occurs. In this analysis only the four fuel and cladding thermal laws will be considered as uncertain. This study allows us to test the performance of the sensitivity methods and surrogate models on different outputs than the ones accessible to the BE coupling that will be used for the UQM development. An example is the detailed radial evolution of the fuel temperature or the H_{gap} evolution with time. This will increase our confidence that the tools could be used also in a Best Effort coupling where the computational cost is too high to perform these tests.

3.4.2 Neutronics stand-alone studies

APOLLO3 ® stand-alone modeling is used for two uncertainty studies. The first is for the static initial state and the second one is for the REA using an adiabatic fuel thermal treatment.

3.4.2.1 Static

For this study an the macroscopic cross-sections are the uncertain inputs. Since at its reference state the core is critical, for each cross-section sampling the core has to be rendered critical. There are three methods that can be used to do so: fission adjustment, boron concentration adjustment or leakage adjustment. Each method can have an impact on the uncertainty analysis. We selected boron concentration adjustment since it is the one that is the closest to the real operation of the core.

In the study [139] that part of it can also be found in the Appendix C the criticality method was found to have a sensitivity up to 20%. Three criticality methods were studied: fission adjustment, boron concentration adjustment and leakage adjustment. An additional uncertain input was considered corresponding to the criticality option with probability 1/3 for each option. The sensitivity on the maximum local linear power for an APOLLO3 ® stand-alone REA modeling was studied. The result is the variance represented by the Shapley indice of this new input for the control rod worth.

In this study for each cross-section perturbation a first static calculation computes the multiplication factor k_{eff}. The boron concentration C_{bor} is then adjusted in order to render the core critical. This criticality method will be used for the rest of the studies. Finally a second static calculation is performed with the control rod extracted in order to compute the control rod worth ρ_{worth} and the deformation factor when the control rod is ejected F^{ej}_{xyz}. The computational time needed for one code evaluation is 15 seconds. The inputs, outputs and statistical methods tested are the following:

- **Inputs:** TD_1, TD_2, NF_1, NF_2, D_1, D_2, $S_{1\to2}$.
- **Outputs:** k_{eff}, ρ_{worth}, C_{bor} and F^{ej}_{xyz}.
- **Statistical tools:**

- **Surrogate models:** Linear, kriging and ANN. They are trained on a learning DOE and their prediction error is estimated using a second DOE.
- **Uncertainty propagation:** Brute Monte Carlo method using different surrogate models for histogram empirical estimation.
- **Global sensitivity analysis:** Shapley and Sobol indices using surrogate models and HSIC indices estimated directly from the obtained code evaluations.
- **Screening method:** HSIC statistical significance tests directly from the obtained code evaluations.

A LHS of size 150 is created in order to train the different surrogate models for each output. The prediction error of each surrogate is estimated based on a second LHS of size 75. The results for the interpolation and prediction errors are presented in table 3.5. It is clear that all the outputs have a linear relationship with the inputs and consequently all the surrogate models have very small errors. The kriging interpolation errors are zero since by its definition (Section 2.5.4) it passes from all the design points.

Table 3.5: Surrogate models interpolation and prediction errors for neutronics stand-alone static study in the MiniCore.

	Linear		**Kriging**		**ANN**	
	ε_{int} (%)	ε_{pred} (%)	ε_{int} (%)	ε_{pred} (%)	ε_{int} (%)	ε_{pred} (%)
$\mathbf{k_{eff}}$	$2.36e^{-3}$	$2.15e^{-3}$	0.00	$1.56e^{-4}$	$1.96e^{-3}$	$1.69e^{-2}$
$\mathbf{C_{bor}}$	$2.33e^{-3}$	$2.36e^{-3}$	0.00	$2.14e^{-4}$	$1.26e^{-3}$	$2.90e^{-2}$
$\boldsymbol{\rho_{worth}}$	$7.09e^{-2}$	$7.60e^{-2}$	0.00	$8.24e^{-2}$	$4.84e^{-2}$	$1.68e^{-1}$
$\mathbf{F^{ej}_{xyz}}$	$9.94e^{-3}$	$1.52e^{-2}$	0.00	$5.75e^{-4}$	$1.55e^{-3}$	$1.87e^{-2}$

Having trained the surrogate models we use the linear one to propagate the uncertainties to the outputs and estimate empirically their histograms. Brute Monte Carlo is used with $1e^5$ samples and in figure 3.8 we can see the obtained histograms together with the estimated first two moments.

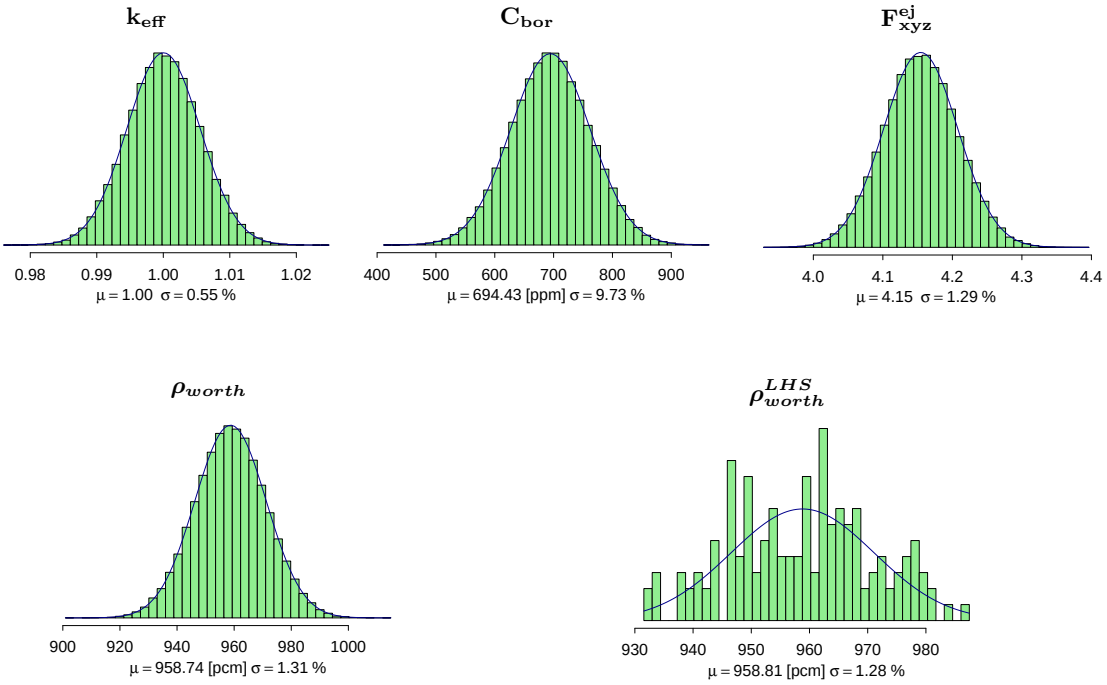

Figure 3.8: Outputs histograms estimation for neutronics stand-alone static study in the MiniCore.

We observe that since the inputs are multivariate normal and the underlying function is linear then all the outputs have also a normal pdf. For highlighting the need of surrogate models to correctly

estimate the histograms we provide the histogram estimated directly with the code evaluations for ρ_{worth}. It is the histogram indicated by ρ^{LHS}_{worth}. It is clear that it is not converged although the dataset is large enough for the estimation of the first two moments.

For the quantification of the outputs sensitivity to each input Shapley and Sobol indices are estimated using the linear model. Both of these indices analyze the sensitivity on the outputs variance (second moment). Additionally we estimate also the HSIC sensitivity indices that capture the sensitivity on the whole pdf of the output. We present the results for k_{eff}, F^{ej}_{xyz} and ρ_{worth} in figures 3.9 - 3.11 respectively. The sensitivities for C_{bor} are similar with k_{eff} and are not shown. For Shapley indices $1e^4$ output evaluations were used while for Sobol $1e^5$. These will be the sampling size for each of their estimation in the following studies as well. What we clearly observe is that the Sobol indices fail to provide sensitivity indices that can be meaningfully interpreted with large negative indices. This is something expected since the inputs have strong correlations. This is especially the case for the TD_1, D_1 and $S_{1\to2}$ cross-sections as we can see in figure 3.7. A second observation that can be drawn is the fact that the HSIC indices do not add up to 1 always, something also expected by their definition in Section 2.7.5.3. However, this does not impact their use as screening method since we can see that they manage to correctly identify which inputs are the most important.

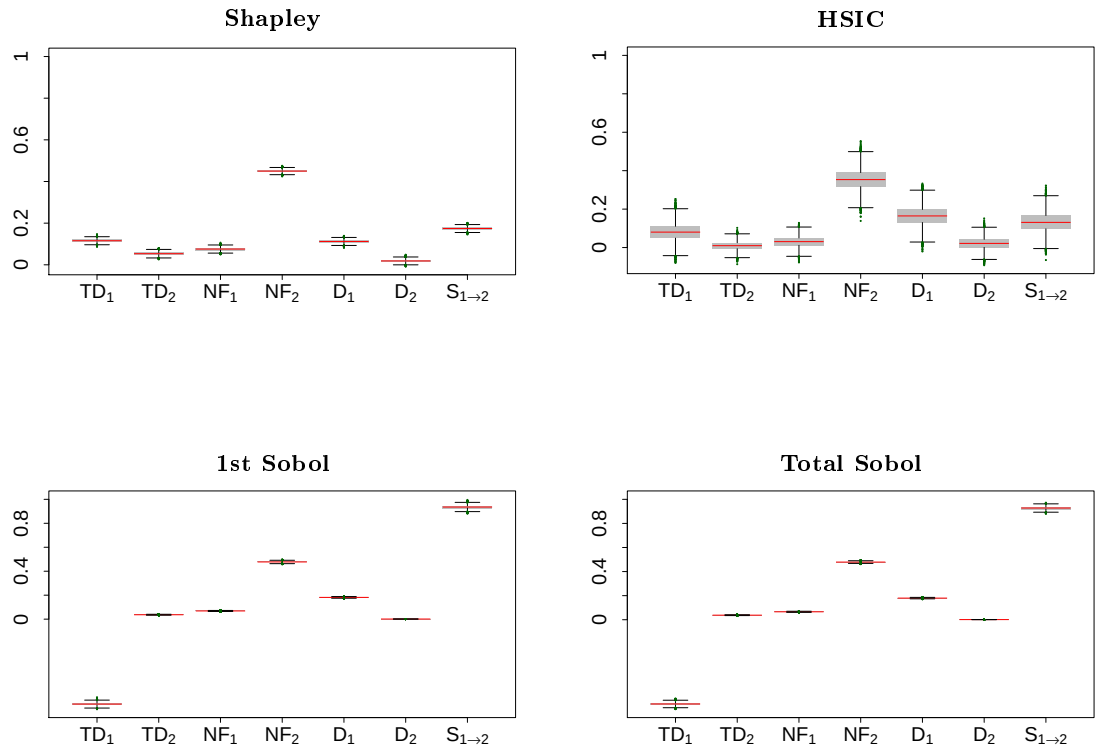

Figure 3.9: k_{eff} sensitivity analysis results for neutronics stand-alone static study in the MiniCore.

The HSIC indices are not so robust since they use a small dataset for their estimation. To this purpose statistical significance tests are used based on bootstrap resampling as described in Section 2.7.5.4. The result of these tests is a rejection or not of the null hypothesis that each output and input are independent. The rejected inputs are considered the statistically significant ones. A bootstrap size of 200 was used with an alpha value of 0.05. These options will be used in all the following studies. The results are gathered in table 3.6. We conclude that all the inputs with non-zero Shapley indices are selected as statistically significant something that shows that this method can be used for screening of inputs with strong correlations.

Table 3.6: HSIC statistical significance test results for neutronics stand-alone static study in the MiniCore.

	Statistical significant inputs
$\mathbf{k_{eff}}$	TD_1, NF_1, NF_2, D_1, $S_{1\to2}$
$\boldsymbol{\rho_{worth}}$	TD_1, NF_1, NF_2, D_1, $S_{1\to2}$
$\mathbf{F^{ej}_{xyz}}$	TD_1, NF_1, D_1, D_2, $S_{1\to2}$

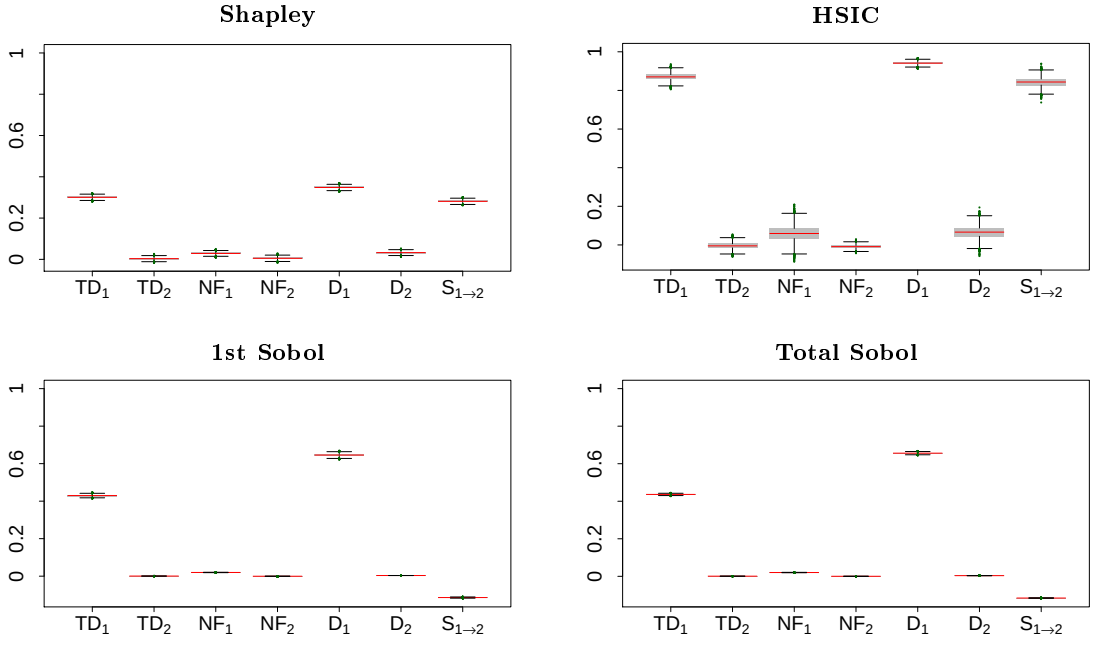

Figure 3.10: F^{ej}_{xyz} sensitivity analysis results for neutronics stand-alone static study in the MiniCore.

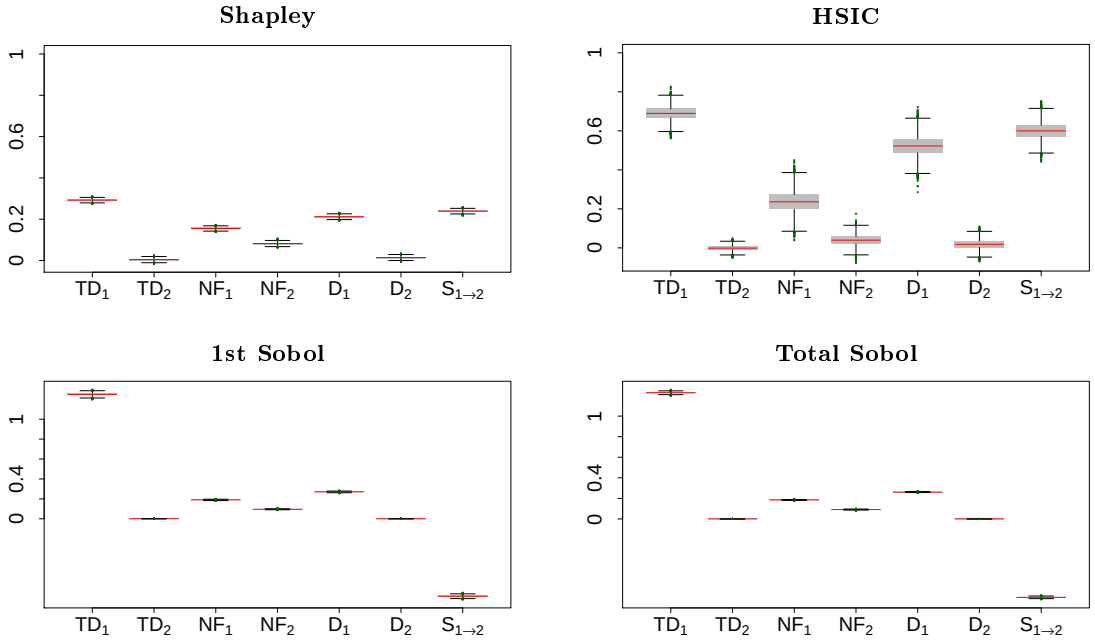

Figure 3.11: ρ_{worth} sensitivity analysis results for neutronics stand-alone static study in the MiniCore.

3.4.2.2 Transient

For this study the macroscopic cross-sections and the kinetic parameters are the uncertain inputs. Starting from a critical state the control rod is ejected in $0.1s$ and the fuel thermal is considered adiabatic with constant specific heat capacity. This essentially means that all the power is stored in the fuel and the temperature follows the power increase without any heat conduction. The Doppler negative feedback is thus obtained creating the power pulse. During the transient we follow the evolution in time of the maximum local linear power P^t_{lin}, compute its maximum value P^{max}_{lin} and the radial linear power P^{2D}_{lin} at the time and axial slice of the maximum. Additionally, the pulse width Γ is also calculated. The computational time needed for one code evaluation is 1.5 minutes. The inputs, outputs and statistical methods tested are the following:

- **Inputs:** TD_1, TD_2, NF_1, NF_2, D_1, D_2, $S_{1\to2}$, IV_1, IV_2, β_{eff}, λ_{eff} .
- **Outputs:** P^{max}_{lin} (scalar), Γ (scalar), P^t_{lin} (functional in time) and P^{2D}_{lin} (functional in space).
- **Statistical tools:**
  - **Surrogate models:** Linear, kriging and ANN. They are trained on a learning DOE and their prediction error is estimated using a second DOE.
  - **Uncertainty propagation:** Brute Monte Carlo method using different surrogate models for histogram empirical estimation.
  - **Global sensitivity analysis:** Shapley and Sobol indices using surrogate models and HSIC indices estimated directly from the obtained code evaluations.
  - **Screening method:** HSIC statistical significance tests directly from the obtained code evaluations.
  - **Functional outputs:** PCA is used to reduce the functional output dimensions. The principal components needed to represent 95% of the variance are retained and used for functional uncertainty propagation and global sensitivity analysis by aggregate Shapley indices.

A LHS of size 150 is created in order to train the different surrogate models for each output. In this study, since we already saw the application of the statistical methods on scalar outputs in Section 3.4.2.1, we focus mainly on the functional outputs. For P^{2D}_{lin} there is not need of stochastic warping, meaning that there is no radial translation of the linear power among the pulses. The two first principal components $P^{2D}_{lin,pc1}$, $P^{2D}_{lin,pc2}$ are kept. For P^t_{lin} stochastic warping improves considerably the dimension reduction from 11 principal components to 2 ($P^t_{lin,pc1}$, $P^t_{lin,pc2}$) adding also the translation time $P^t_{lin,dt}$ as a third uncertain variable needed for the reconstruction of P^t_{lin}. We note that it is easy to approximate the weights of the first principal components by surrogate models but it becomes increasingly difficult to do so for high-order principal components. The stochastic warping is performed with a comparison to reference pulse selected as the empirical mean. In figures 3.12 - 3.13 we can see on the former the original maximum linear power pulses of the training LHS and on the latter the translated pulses due to the stochastic warping. For the warped P^t_{lin} and the P^{2D}_{lin} we plot the eigenfuctions of the first two principal components in figure 3.14. We can see that higher eigenfunctions include higher frequencies of variation.

A second LHS of size 75 was used to estimate the approximation error of each surrogate model. The result for the interpolation and prediction errors are presented in table 3.7. For the functional outputs their first principal components and the shift time are treated as scalar outputs and the errors of the surrogate models are presented as well. The kriging surrogate models behave significantly better in most of the cases and especially for the approximation of the principal components. For this reason it will be the model used in the uncertainty propagation and sensitivity analysis. The maximum predictive error of kriging is 4% for the Γ while for the rest outputs it has an error of less than 1%.

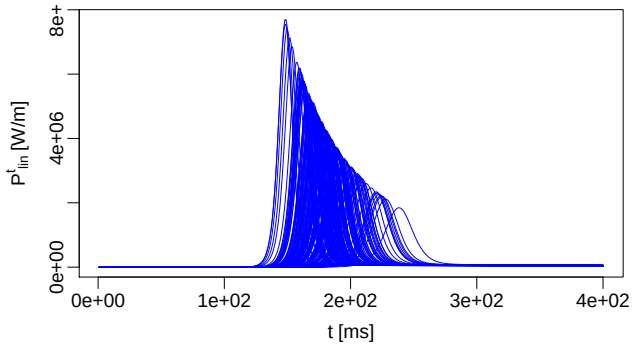

Figure 3.12: All the maximum linear power power pulses of the training LHS for neutronics stand-alone REA study in the MiniCore.

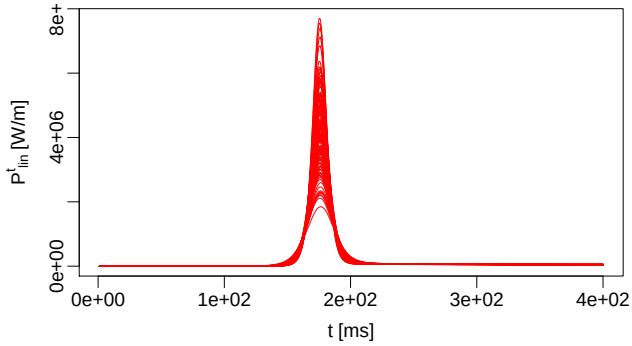

Figure 3.13: Stochastic warping results of the maximum linear power pulses of the training LHS for neutronics stand-alone REA study in the MiniCore.

Table 3.7: Surrogate models interpolation and prediction errors for neutronics stand-alone REA study in the MiniCore.

	Linear		**Kriging**		**ANN**	
	ε_{int} (%)	ε_{pred} (%)	ε_{int} (%)	ε_{pred} (%)	ε_{int} (%)	ε_{pred} (%)
$\mathbf{P^{max}_{lin}}$	1.20	1.45	0.00	$6.06e^{-2}$	$2.80e^{-3}$	$2.42e^{-1}$
$\mathbf{\Gamma}$	4.73	6.26	0.00	4.3	$1.61e^{-2}$	$1.60e^{+1}$
$\mathbf{P^{2D}_{lin,pc1}}$	1.19	1.48	0.00	$8.57e^{-2}$	$3.35e^{-3}$	$4.10e^{-1}$
$\mathbf{P^{2D}_{lin,pc2}}$	5.96	5.93	0.00	$9.39e^{-1}$	$9.54e^{-3}$	1.37
$\mathbf{P^{t}_{lin,pc1}}$	$4.43e^{-1}$	$5.04e^{-1}$	0.00	$3.70e^{-2}$	$4.86e^{-3}$	$3.52e^{-1}$
$\mathbf{P^{t}_{lin,pc2}}$	1.25	1.69	0.00	$7.94e^{-1}$	$2.13e^{-2}$	3.08
$\mathbf{P^{t}_{lin,dt}}$	2.13	2.37	0.00	$4.28e^{-1}$	$4.36e^{-3}$	1.14

Brute Monte Carlo is used for uncertainty propagation with $1e^5$ samples for each output. The obtained histograms for the scalar outputs and the relative standard deviations for the functional ones are presented in figures 3.15 - 3.16. The P^{max}_{lin} and Γ histograms show a non normal pdf. For the former one a comparison with a point kinetics analytical uncertainty analysis is performed in Appendix D. The relative standard deviation of P^{2D}_{lin} does not vary radially while for P^{t}_{lin} strong variations occur mainly around the time of the power peak.

The Shapley, Sobol and HSIC indices for P^{max}_{lin} are illustrated in figure 3.17. All the indices are similar for Γ. In figure 3.18 we present the aggregated Shapley indices for P^{2D}_{lin} and P^{t}_{lin}. As in the static study we see that the Sobol indices are not well adapted for inputs with strong correlations. The β_{eff} and λ_{eff} are the dominant variables based on both HSIC and Shapley indices for P^{max}_{lin}, P^{2D}_{lin} and P^{t}_{lin}.

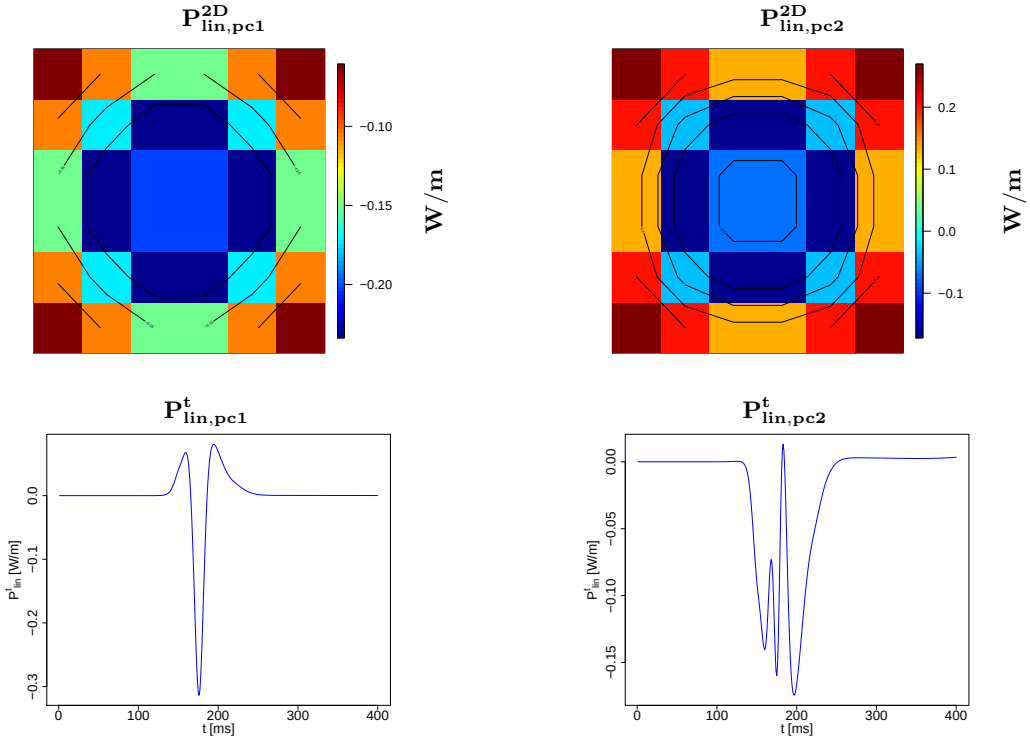

Figure 3.14: P^{2D}_{lin} and P^{t}_{lin} 1st and 2nd principal components for neutronics stand-alone REA study in the MiniCore.

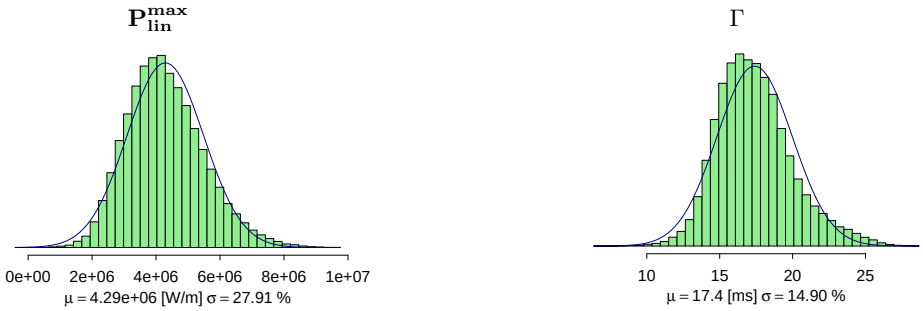

Figure 3.15: P^{max}_{lin} and Γ histograms for neutronics stand-alone REA study in the MiniCore.

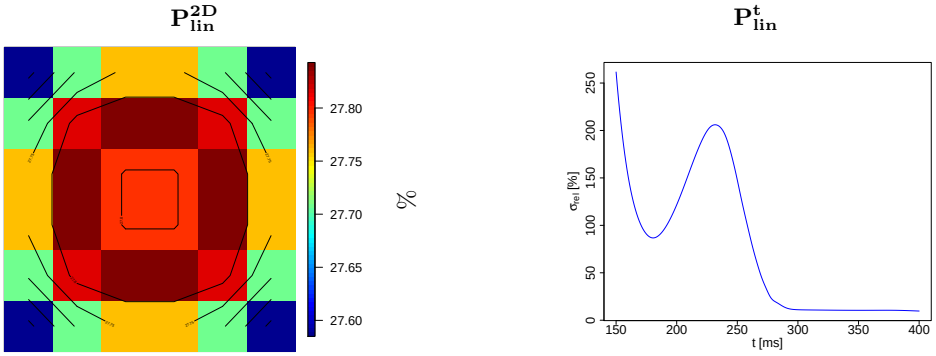

Figure 3.16: P^{2D}_{lin} and P^{t}_{lin} relative standard deviation distribution for neutronics stand-alone REA study in the MiniCore.

It is important to notice that there is a strong correlation between β_{eff} and λ_{eff}, meaning that one of them could have an important sensitivity index just through their correlation and not by their impact on output. This is called redundancy and cannot be detected by the sensitivity methods.

We will try to address this effect in the screening process, where the goal will be to select the least number of inputs that represent most of the output variation.

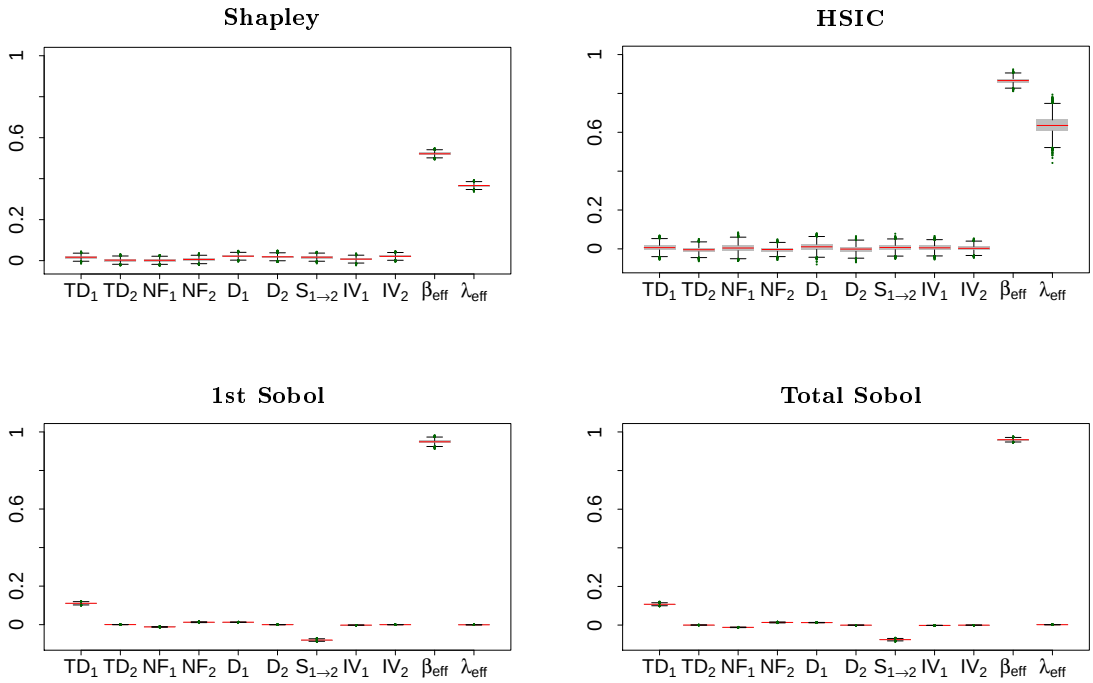

Figure 3.17: P_{lin}^{max} sensitivity analysis results for neutronics stand-alone REA study in the Mini-Core.

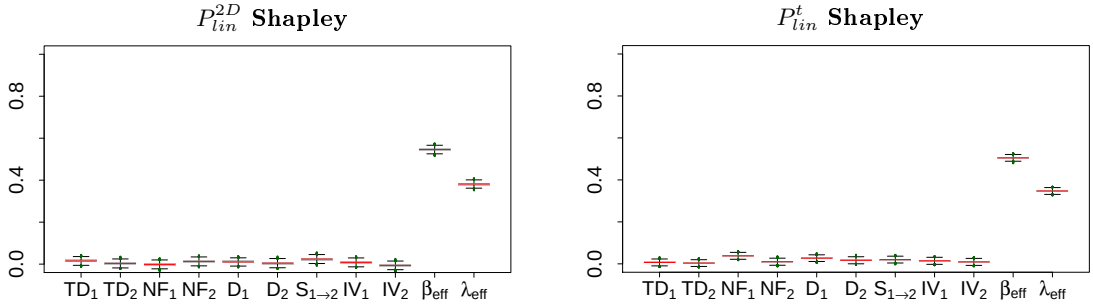

Figure 3.18: P_{lin}^{2D} and P_{lin}^{t} aggregate Shapley indices for neutronics stand-alone REA study in the MiniCore.

The HSIC statistical significance tests results are presented in table 3.8. For all the considered outputs, including the principal components of the functional ones, the selected inputs are the dominant ones based on the Shapley indices. The inputs with large sensitivities are always selected and sometimes even inputs with very small sensitivities.

Table 3.8: HSIC statistical significance test results for neutronics stand-alone REA study in the MiniCore.

	Statistical significant inputs
$\mathbf{P_{lin}^{max}}$	TD_1, D_1, $S_{1\to2}$, β_{eff}, λ_{eff}
$\mathbf{P_{lin,pc1}^{2D}}$	D_1, β_{eff}, λ_{eff}
$\mathbf{P_{lin,pc2}^{2D}}$	TD_1, NF_1, D_1, D_2, $S_{1\to2}$, IV_1, β_{eff}, λ_{eff}
$\mathbf{P_{lin,pc1}^{t}}$	TD_1, D_1, $S_{1\to2}$, β_{eff}, λ_{eff}
$\mathbf{P_{lin,pc2}^{t}}$	TD_1, D_1, β_{eff}, λ_{eff}
$\mathbf{P_{lin,dt}^{t}}$	TD_1, D_1, $S_{1\to2}$, β_{eff}, λ_{eff}

3.4.3 Thermal-hydraulics stand-alone study

The reference REA pulse from the previous study is applied in FLICA4. The fuel-thermomechanics and the thermal-hydraulics inputs from table 3.4 are considered for this study. For these physics their identified outputs of interest in table 3.3 are calculated. The interest in this study lies in evaluating that the statistical tools perform well also for independent inputs with various pdf. The computational time needed for one code evaluation is 4.5 minutes. The inputs, outputs and statistical methods tested are the following:

- **Inputs:** λ_f, λ_c, Cp_f, Cp_c, H_{gap}, P_r, T_R, H_c, R_{crit}, R_{v0}, H_{dnb}.
- **Outputs:** H_f^{max}, DNB^{min}.
- **Statistical tools:**
  - **Surrogate models:** Linear, kriging and ANN. They are trained on a learning DOE and their prediction error is estimated using a second DOE.
  - **Uncertainty propagation:** Brute Monte Carlo method using different surrogate models for histogram empirical estimation.
  - **Global sensitivity analysis:** Shapley and Sobol indices using surrogate models and HSIC indices estimated directly from the obtained code evaluations.
  - **Screening method:** HSIC statistical significance tests directly from the obtained code evaluations.

A LHS of size 150 is created in order to train the different surrogate models for each output. The results of the surrogate models training are gathered in table 3.9. The outputs behavior are strongly non-linear and that is why the linear model shows large errors. The ANN has a low interpolation error, however, it has a very large prediction error indicating a strong overfitting. Only the kriging model shows satisfactory approximation errors and for this reason it will be used for the rest of the analyses in this study.

Table 3.9: Surrogate models interpolation and prediction errors for thermal-hydraulics stand-alone study in the MiniCore.

	Linear		**Kriging**		**ANN**	
	$\boldsymbol{\varepsilon_{int}}$ (%)	$\boldsymbol{\varepsilon_{pred}}$ (%)	$\boldsymbol{\varepsilon_{int}}$ (%)	$\boldsymbol{\varepsilon_{pred}}$ (%)	$\boldsymbol{\varepsilon_{int}}$ (%)	$\boldsymbol{\varepsilon_{pred}}$ (%)
$\mathbf{H_f^{max}}$	$2.50e^{+1}$	$2.74e^{+1}$	0.00	$4.38e^{-2}$	$3.30e^{-3}$	$7.12e^{+1}$
$\mathbf{DNB^{min}}$	$3.95e^{+1}$	$4.02e^{+1}$	0.00	$1.27e^{-1}$	$2.87e^{-2}$	$6.93e^{+1}$

Brute Monte Carlo is used for uncertainty propagation with $1e^5$ samples for each output. The obtained histograms are drawn in figure 3.19. The sensitivity indices are similar for both outputs and are shown in in figure 3.20. A first observation is the agreement between Shapley and Sobol indices in the case of independent inputs. It is clear that H_{gap} is the only dominant parameter due

to its large range of variation. Additionally, we observe that the distance to boiling crisis shows variation of 77% with very small probability around 0.002% of reaching it ($DNB^{min} < 0$).

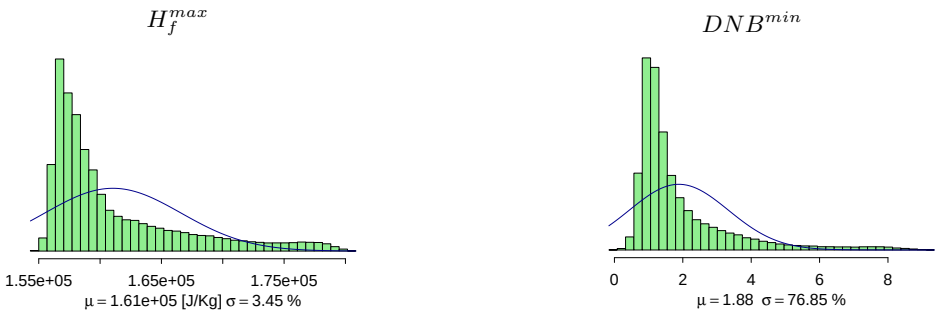

Figure 3.19: H_f^{max} and DNB^{min} histograms for thermal-hydraulics stand-alone study in the MiniCore.

Finally, the results of HSIC statisical significance tests are shown in table 3.10. The H_{gap} is selected for both of the outputs as expected from the Shapley indices and additionally for DNB^{min} the R_{crit} is also selected even if it had a negligible Shapley index. This is not strange since it appears explicitly in the DNB^{min} computation: $DNB = DNBR - R_{crit}$.

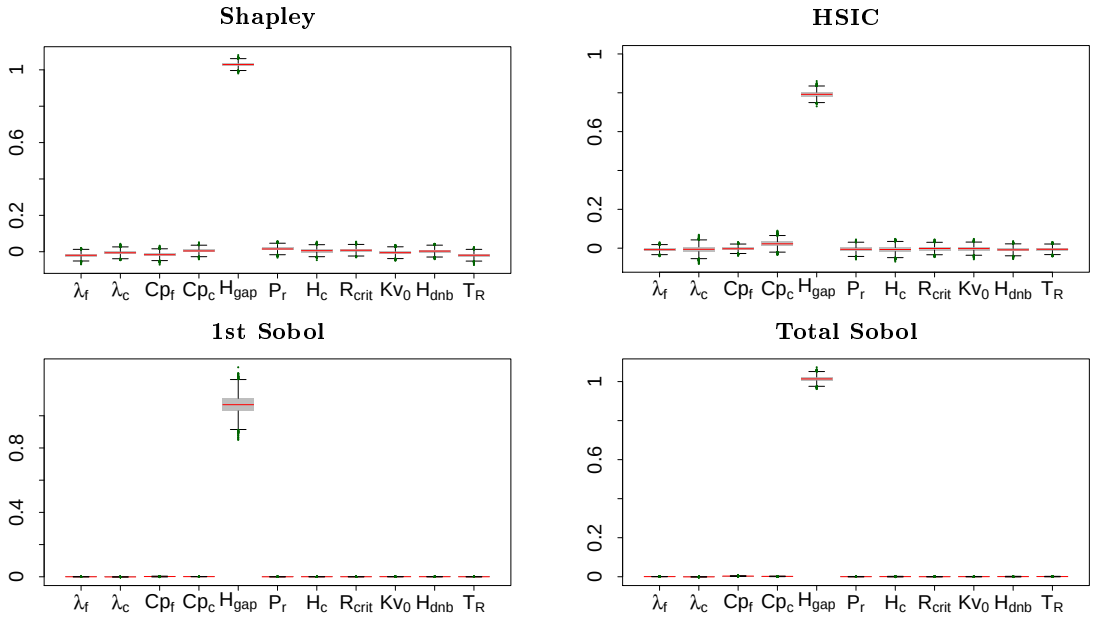

Figure 3.20: H_f^{max} and DNB^{min} sensitivity results for thermal-hydraulics stand-alone study in the MiniCore.

Table 3.10: HSIC statistical significance test results for thermal-hydraulics stand-alone study in the MiniCore.

	Statistical significant inputs
$\mathbf{H_f^{max}}$	H_{gap}
$\mathbf{DNB^{min}}$	H_{gap}, R_{crit}

3.4.4 Fuel-thermomechanics stand-alone study

The reference REA power pulse from the APOLLO3 ® study and the corresponding cladding wall temperature from FLICA4 are imposed as boundary conditions in ALCYONE V1.4. Only the

axial slice with the maximum linear power is modeled. This axial slice is located in the assembly of 0 burn-up. The fuel and cladding material laws are consider as uncertain inputs, since H_{gap} now is an output and the other fuel-thermomechanics inputs cannot be used in ALCYONE V1.4. In this study the goal will be to focus mainly on outputs that are not available in a Best Estimate coupling and verify that the statistical tools perform well for those as well. For this purpose we will focus on the maximum gap heat transfer during the REA H_{gap}^{max} and two functional outputs, the temporal evolution of the cladding internal surface temperature T_{ci}^{t} and the radial distribution of the fuel pin temperature at the end of the transient $T_{0.4}^{r}$. The computational time needed for one code evaluation is 6 minutes. The inputs, outputs and statistical methods tested are the following:

- **Inputs:** λ_f, λ_c, Cp_f, Cp_c.
- **Outputs:** H_{gap}^{max}, T_{ci}^{t}, $T_{0.4}^{r}$.
- **Statistical tools:**
  - **Surrogate models:** Linear, kriging and ANN. They are trained on a learning DOE and their prediction error is estimated using a second DOE.
  - **Uncertainty propagation:** Brute Monte Carlo method using different surrogate models for histogram empirical estimation.
  - **Global sensitivity analysis:** Shapley and Sobol indices using surrogate models and HSIC indices estimated directly from the obtained code evaluations.
  - **Screening method:** HSIC statistical significance tests directly from the obtained code evaluations.
  - **Functional outputs:** PCA is used to reduce the functional output dimensions. The principal components needed to represent 95% of the variance are retained and used for functional uncertainty propagation and global sensitivity analysis by aggregate Shapley indices.

A LHS of size 80 is created in order to train the different surrogate models for each output. Smaller size LHS is used compared to the previous studies because the input dimension is significantly smaller. For both functional outputs 2 principal components are needed ($T_{ci,pc1}^{t}$, $T_{ci,pc2}^{t}$,$T_{0.4,pc1}^{r}$, $T_{0.4,pc2}^{r}$) for representing 95% of the variance and are plotted in figure 3.21. There was no need of stochastic warping.

The prediction error of each surrogate was estimated based on a second LHS of size 40. The results of the surrogate models training are gathered in table 3.11. All the models have satisfactory errors with kriging showing slightly better results. For this reason it will be used for the uncertainty propagation and sensitivity analysis.

Brute Monte Carlo is used for uncertainty propagation with $1e^5$ samples for each output. The obtained histograms of H_{gap} and the relative standard deviation for T_{ci}^{t} and $T_{0.4}^{r}$ are presented in figure 3.22. We see that in general there are very small variations around the mean values.

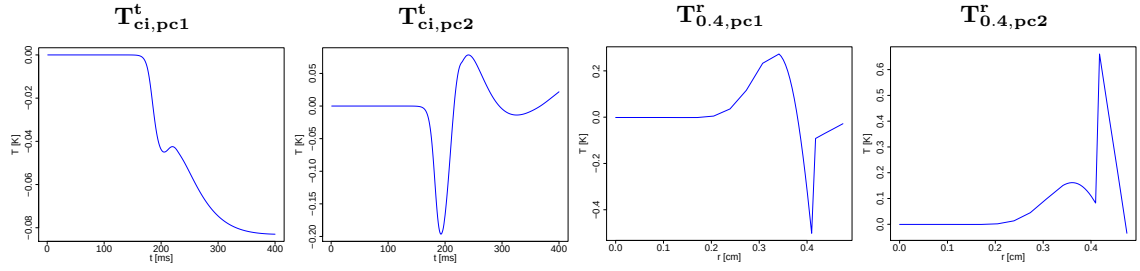

Figure 3.21: T_{ci}^{t} and $T_{0.4}^{r}$ 1st and 2nd principal components for fuel-thermomechanics stand-alone study in the MiniCore.

Table 3.11: Surrogate models interpolation and prediction errors for fuel-thermomechanics stand-alone study in the MiniCore.

	Linear		Kriging		ANN	
	ε_{int} (%)	ε_{pred} (%)	ε_{int} (%)	ε_{pred} (%)	ε_{int} (%)	ε_{pred} (%)
$\mathbf{H^{max}_{gap}}$	$3.55e^{-1}$	$3.62e^{-1}$	0.00	$1.32e^{-4}$	$2.37e^{-3}$	$5.05e^{-3}$
$\mathbf{T^{t}_{ci,pc1}}$	$5.14e^{-1}$	$5.92e^{-1}$	0.00	$1.02e^{-2}$	$8.99e^{-3}$	$1.95e^{-2}$
$\mathbf{T^{t}_{ci,pc2}}$	$2.48e^{-1}$	1.85	0.00	1.65	$1.17e^{-2}$	1.62
$\mathbf{T^{r}_{0.4,pc1}}$	$1.96e^{-1}$	$3.42e^{-1}$	0.00	$1.92e^{-1}$	$1.36e^{-3}$	$1.95e^{-1}$
$\mathbf{T^{r}_{0.4,pc2}}$	$5.78e^{-1}$	5.24	0.00	4.74	$6.53e^{-2}$	4.78

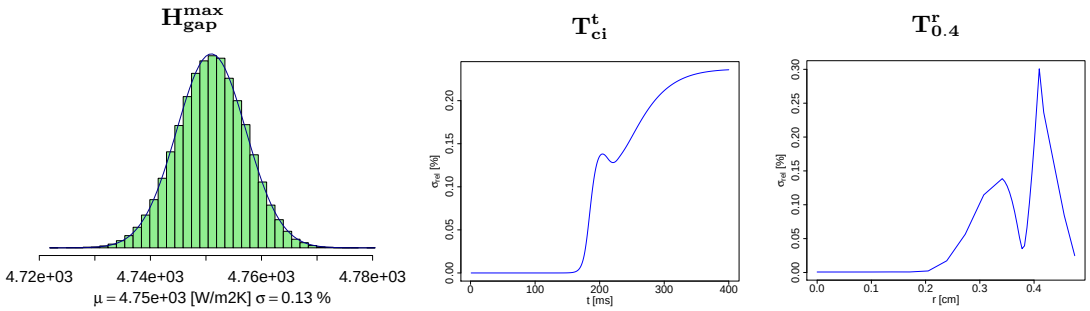

Figure 3.22: H^{max}_{gap} histogram and T^{t}_{ci} and $T^{r}_{0.04}$ relative standard deviation evolution for fuel-thermomechanics stand-alone study in the MiniCore.

The Shapley, Sobol and HSIC indices for H^{max}_{gap} are presented in figure 3.23. There is an agreement among all the indices, something expected since the inputs are independent. The most important input is the λ_f responsible for 70% of H^{max}_{gap} variance while λ_c is responsible for the rest 30%. The aggregated Shapley indices for the two functional outputs can be seen in figure 3.24. For T^{t}_{ci} the λ_c is more important while for $T^{r}_{0.4}$ the λ_f.

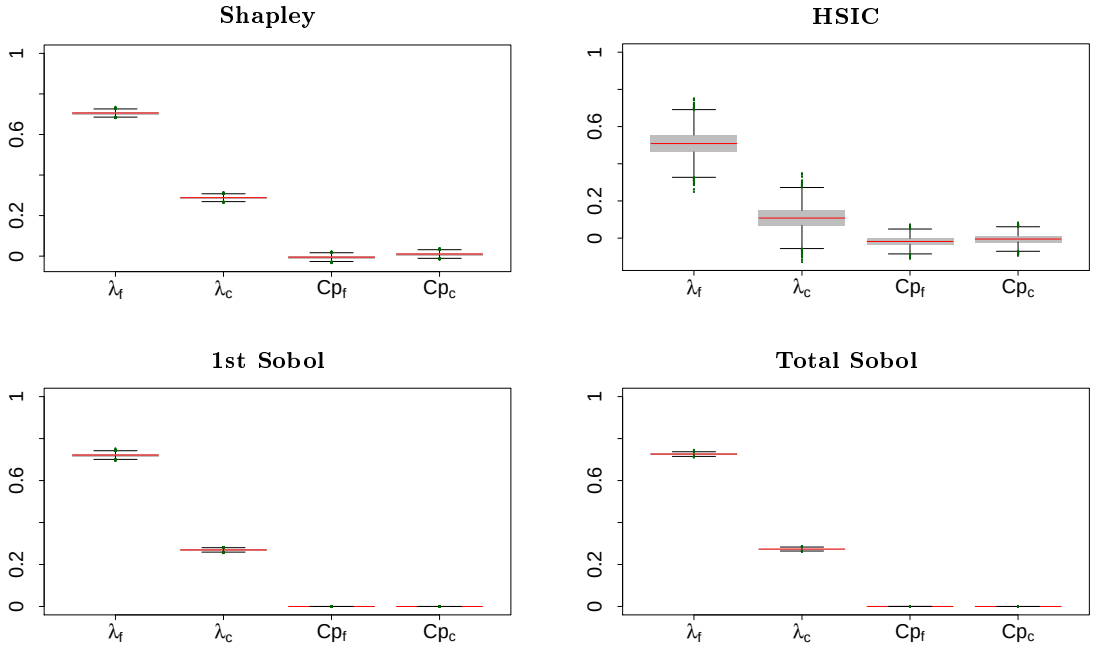

Figure 3.23: H^{max}_{gap} sensitivity results for for fuel-thermomechanics stand-alone study in the MiniCore.

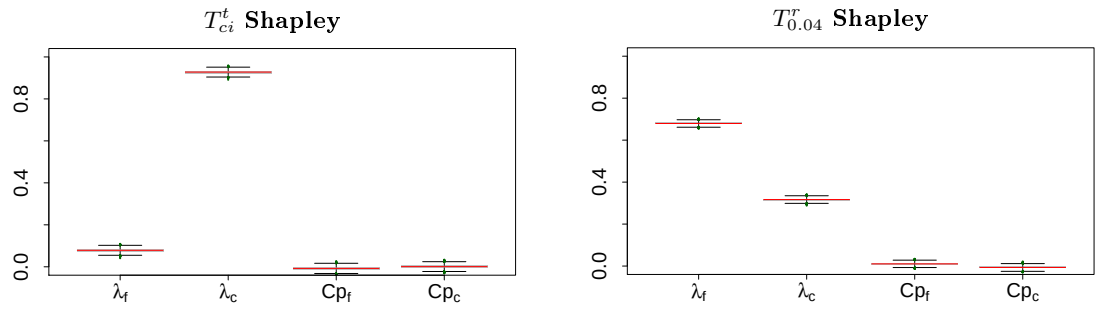

Figure 3.24: T^t_{ci} and $T^r_{0.04}$ aggregate Shapley indices for fuel-thermomechanics stand-alone study in the MiniCore.

The results for HSIC statistical significance tests are presented in table 3.12. For all the considered outputs, including the principal components of the functional ones, the selected inputs are the dominant ones based on the Shapley indices. An interesting observation is the selection of λ_f for $T^r_{0.04,pc1}$ and λ_c for $T^r_{0.04,pc2}$. This can be explained by the corresponding eigenfunctions of figure 3.21. For $T^r_{0.04,pc1}$ the main variations are located in the fuel region (1-26) and thus λ_f is more important. However, for $T^r_{0.04,pc2}$ the main variations are located in the cladding region (27-30) and thus λ_c is more important.

Table 3.12: HSIC statistical significance test results for fuel-thermomechanics stand-alone study in the MiniCore.

	Statistical significant inputs
$\mathbf{H^{max}_{gap}}$	λ_f, λ_c
$\mathbf{T^t_{ci,pc1}}$	λ_c
$\mathbf{T^t_{ci,pc2}}$	λ_f, λ_c
$\mathbf{T^r_{0.04,pc1}}$	λ_f
$\mathbf{T^r_{0.04,pc2}}$	λ_c

3.4.5 Conclusions

The stand-alone preliminary analysis for each code allowed to test and evaluate the performances of different statistical tools under different conditions. In APOLLO3 ® we studied their behavior for inputs with strong correlations and for different outputs from scalar up to $2D$ functional fields. Most of the outputs were not far from having a linear behavior and that is why all the surrogate models show relatively small prediction errors with kriging performing slightly better, especially for the principal components of the functional outputs. We saw that Sobol indices cannot give meaningful sensitivities due to the inputs correlations, while the Shapley indices are well adapted. In FLICA4 the statistical tools performance was evaluated for independent inputs. There were strong non-linearities and only the kriging showed satisfactory prediction errors. As expected from there definitions there was an agreement between Shapley and Sobol indices. In ALCYONE V1.4 we focused mainly on outputs that could be accessible only in a Best Effort coupling. An emphasis was given in functional quantities such as the radial temperature distribution. All the statistical tools performed well in this study. For all the above mentioned studies HSIC indices showed that they can be very useful in the screening process. Particularly their use in statistical significance tests managed to identify for all the outputs the relevant subset of inputs. Finally, the conclusions concerning the UQM that can be drawn from these studies are:

- Kriging models will be used as surrogate models
- Shapley indices will be used for both dependent and independent inputs as the global sensitivity indices.

- HSIC indices and their use in statistical significance tests are promising for screening or dimension reduction process.

- Functional outputs will be analyzed using PCA. The stochastic warping is necessary mainly for translated outputs such as the maximum linear power evolution in time. Aggregated Shapley indices are used as sensitivity indices for the whole functional output.

3.5 Development of Uncertainty Quantification Methodology (UQM)

3.5.1 Introduction

From the preliminary studies we concluded that kriging surrogate models will be used in UQM in conjunction with PCA for functional outputs. Shapley indices and aggregated Shapley indices will be used for scalar and functional outputs respectively. HSIC indices can be used in statistical significance tests to identify a small subset of important inputs just by using a dataset of code evaluations. In this subsection we are going to use these conclusions in a multi-physics BE APOLLO3 ® - FLICA4 coupling. The goal is to use this modeling to develop the UQM that will be applied to a large scale PWR core.

While in the preliminary studies the inputs dimension was relatively low, in this multi-physics modeling we use all the identified inputs from table 3.3. The kriging models face difficulties when they are trained in large inputs dimension and thus there is a strong interest in identifying effective input subspaces with reduced dimension. We have also to keep in mind that the derived UQM must be also extendable to a larger input dimension. To this purpose we develop two methodologies in order to address the potential large inputs dimension. The first consist in identifying a subset of important inputs based on the HSIC statistical significance tests. This aims at addressing the challenges of dependent inputs, with potential interactions and redundancies. The second is related to the training of the kriging models. The optimization of a LHS in the original input space does not guarantee good space-filling properties in the important input subspaces. Besides that, the use of LHS optimized only in the subspace for the kriging training leads to an unquantified error due to the dimension reduction. What we propose is a method that optimizes the LHS in both the original input space and the identified important input subspaces. This allows an efficient surrogate model construction with an error estimation that includes the dimension reduction error. For the description of the two methods we define the function $\mathbf{Y} = F(\mathbf{X}) : \mathbb{R}^d \rightarrow \mathbb{R}$ to be the underlying function between the random inputs of dimension d and a random scalar output[2].

Both of these methods will be first presented and then tested on the APOLLO3 ® - FLICA4 multi-physics BE coupling together with the statistical tools selected from the preliminary studies. At the end of this subsection we will combine the conclusion drawn from this study to develop the UQM scheme.

3.5.2 Input Dimension Reduction Method (IDRM)

The dimension of the input space is large and potentially only a small subspace is important for a scalar output Y. The goal of this method is to identify this important input subspace. We denote by $\mathcal{S}_d$ the set of size (cardinal) d containing the inputs indices and $\mathbf{X}_d$ the corresponding inputs. There are many challenges related to the dependencies between inputs, potential interactions, redundancies and the non-linear behaviors between inputs and outputs. There is no methodology that can deal efficiently with all of these constraints.

In this work we use the HSIC significance tests, as used in the preliminary studies, to treat dependencies, non-linearities and interactions. The result is an initial subset of inputs considered as important ($\mathcal{S}_{d0}$, $\mathbf{X}_{d0}$). Using $\mathcal{S}_{d0}$ a kriging model (Kr) is trained and its leave-one-out (LOO) error is estimated (ϵ_{LOO}). If the error is not satisfactory, inputs are sequentially added until the user decides to stop or until all the inputs are included ($\mathcal{S}_{d1}$, $\mathbf{X}_{d1}$). This is applicable to our case of

[2]For functional outputs the methods are applied on the selected scalar scores of the principal components

22 inputs but it could also be extended to larger dimension. For larger dimension it can become prohibitive.

Finally, in order to treat the redundancies, the resulting subspace defined by the set $\mathcal{S}_{d1}$ from the previous step is subjected to a sequential extraction of one input at a time and the corresponding LOO error is computed. If the error stays close to constant within a small $\delta\varepsilon$ when the input is extracted then the input is rejected from the subspace. After applying this to all inputs of $\mathcal{S}_{d1}$ the final subspace defined by the set $\mathcal{S}_{d2}$ and corresponding to $\mathbf{X}_{d2}$ inputs is identified. This step has to be used with caution, it can reduce the effective inputs subspace in term of representation but still the correlated rejected inputs should be mentioned. This input dimension reduction method is carried out with an initial random DOE. The following procedure details the input dimension reduction method. The inputs $\mathbf{X}_{di}$ are defined by the set of indices $\mathcal{S}_{di}$.

IDRM process

Code evaluations on initial random DOE.
HSIC significance test $\rightarrow$ initial important subspace $\mathcal{S}_{d0}$ and $\mathbf{X}_{d0} \in \mathbb{R}^{d0}$
Compute ϵ_{LOO} for $\mathrm{Kr}(\mathbf{X}_{d0}, Y)$, set $\mathcal{S}_{r0}$ as the rejected inputs subspace of dimension $r0 = d - d0$ and $\mathcal{S}_{d1} = \mathcal{S}_{d0}$
while User decision based on error evolution **do**
    for $(i = 1, i \leq r0, i++)$ **do**
        Compute ϵ^i_{LOO} for $\mathrm{Kr}(\mathbf{X}_{d1} \cup X^i_{r0}, Y)$
    end for
    Selection of X^i_{r0} and its corresponding index S^i_{r0} with minimum ϵ^i_{LOO}
    Update $\mathcal{S}_{d1} = \mathcal{S}_{d1} \cup \mathcal{S}^i_{r0}$
end while
Set $\mathcal{S}_{d2} = \mathcal{S}_{d1}$, update ϵ_{LOO} for $\mathrm{Kr}(\mathbf{X}_{d1}, Y)$ and define error threshold $\delta\epsilon$
for $(i = 1, i \leq d2, i++)$ **do**
    Compute ϵ^i_{LOO} for $\mathrm{Kr}(\mathbf{X}_{d2,i}, Y)$ with $\mathbf{X}_{d2,i}$ the inputs corresponding to $\mathcal{S}_{d2,i} = \mathcal{S}_{d2} \setminus \mathcal{S}^i_{d2}$
    if $(\epsilon^i_{LOO} - \epsilon_{LOO} < \delta\epsilon\ )$ **then**
        $\mathcal{S}_{d2} = \mathcal{S}_{d2,i}$
    end if
end for
Set of reduced inputs subspaces S_{d2} and the corresponding inputs $X_{d2} \in \mathbb{R}^{d2}$

The proposed IDRM was tested on the famous Morris function $Y = F_{morris}(X, k)$ [140] used in sensitivity studies. The function has a fixed parameter k determining how many of the inputs will be significant.

$$F_{morris}(X, k) = \alpha \sum_{i=1}^{k} \left(X^i + \beta \sum_{i<j=2}^{k} X^i X^j \right) \tag{3.1}$$

Where:

- $\alpha = \sqrt{12} - 6\sqrt{0.1(k-1)}$
- $\beta = 12\sqrt{0.1(k-1)}$

For the testing purposes we used 22 inputs, as the dimension of the inputs in the UQM. Each input is independent and has $\mathcal{U}(0, 1)$ pdf. A sampling of 100 (X, Y) realizations is used with parameter $k = 10$, meaning that only $(X^i)_{i \leq 10}$ are significant. In order to test the redundancy capability the last variable while not used in the function has a strong correlation of 0.9 with X^{10}. The input dimension reduction method was tested and the results for the selected input sets at the different steps (S_{d0}, S_{d1}, S_{d2}) are gathered in the table 3.13. The method in the initial step identifies all the significant inputs together with one non-significant (X^{11}) and the correlated output that we added (X^{22}). In the second step no other input is added since the kriging error is already low. Finally on the third step the redundant variable and the non-significant one are rejected and thus the optimal dimension reduction is achieved.

Table 3.13: Input dimension reduction method result on Morris function

	Selected inputs
$\mathbf{S_{d0}}$	X^1, X^2, X^3, X^4, X^5, X^6, X^7, X^8, X^9, X^{10}, X^{11}, X^{22}
$\mathbf{S_{d1}}$	X^1, X^2, X^3, X^4, X^5, X^6, X^7, X^8, X^9, X^{10}, X^{11}, X^{22}
$\mathbf{S_{d2}}$	X^1, X^2, X^3, X^4, X^5, X^6, X^7, X^8, X^9, X^{10}

3.5.3 Latin Hypercube Sampling subspaces optimization

The kriging models for each output are constructed on space-filling LHS. The training of these models is more efficient in a reduced input space responsible for most of the output variation. The identification of this subspace of the original input space is achieved through the previously described IDRM. The construction of LHS in the original input space does not guarantee good space-filling properties in the identified input subspaces. Besides that, the construction of a LHS only in these subspaces creates an unquantified dimension reduction error.

To this purpose we adapted the Simulated Annealing (SA) optimization algorithm of the LHS to improve the ϕ_p space-filling criterion also in the specified subspaces of interest. The minimization of ϕ_p leads to designs with better space-filling properties. The SA is described in Section 2.6.2 and consist in applying random permutations of two design points. Starting from an initial random LHS many iteration of such permutations are performed and the ϕ_p criterion is evaluated. The permutations that improve the criterion are kept. In order to avoid to get stuck in local minima a trade-of is used between exploring and improving the LHS. This means that with some probability worse LHS might be kept in order to explore better the space of available LHS. If we denote with I_{prj} the identified inputs subspaces of dimension d_p and with $\mathbf{D}[I_{prj}]$ the projections of a LHS design D the modified algorithm is:

SA improved subspaces pseudo algorithm

$D_{best} = \mathbf{D}_0$, $C_{best} = \phi_p(\mathbf{D}_0)$, $\mathbf{C}_{p,best} = \boldsymbol{\phi}_p^{prj}(\mathbf{D}_0[I_{prj}])$, $T = T_0$: initialization of the best design, best criterion and temperature
for $(i = 1, i \leq N_i, i++)$ **do**
    Create new design $\mathbf{D}_i$ by elementary permutation and evaluate $C_i = \phi_p(\mathbf{D}_i)$ and $\mathbf{C}_{p,i} = \boldsymbol{\phi}_p^{prj}(\mathbf{D}_i[I_{prj}])$
    $a = \min(exp(\frac{C_{best}-C_i}{C_{best}T} + \sum_j^{d_p} \frac{C^j_{p,best}-C^j_{p,i}}{C^j_{p,best}T}), 1)$
    Sample b from bernoulli distribution with parameter a
    if $(b == 1)$ **then**
        $D_{best} = \mathbf{D}_i$, $C_{best} = C_i$ and $\mathbf{C}_{p,best} = \mathbf{C}_{p,i}$
    end if
    $T = cT$
end for

We can see that compared to the SA algorithm in Section 2.6.2 we modified only the α variable. This quantity is above 1 when the LHS is improved and below 1 when is worsened. In our modified algorithm we added the ϕ_p criterion in the desired subspaces. When ϕ_p is improved in the complete space and all the important subspaces the value is above 1. When ϕ_p is worsened in the complete space and all the important subspaces the value is below 1. In the intermediate cases depending on the relative improve in each space it can be above or below 1.

It is important to notice that as the number of subspaces increase the optimization becomes less effective. In the case where a large number of subspaces must be optimized, maximum projections can be used, developed recently by [141], where all the input subspaces are optimized based on a modified version of ϕ_p criterion. For testing purposes we use a design of size $N = 50$ in $d = 5$ dimension with two subspaces of importance $I_1 = \{1, 2\}$, $I_2 = \{3, 4, 5\}$. The ϕ_p criterion evolution results can be seen in figure 3.25.

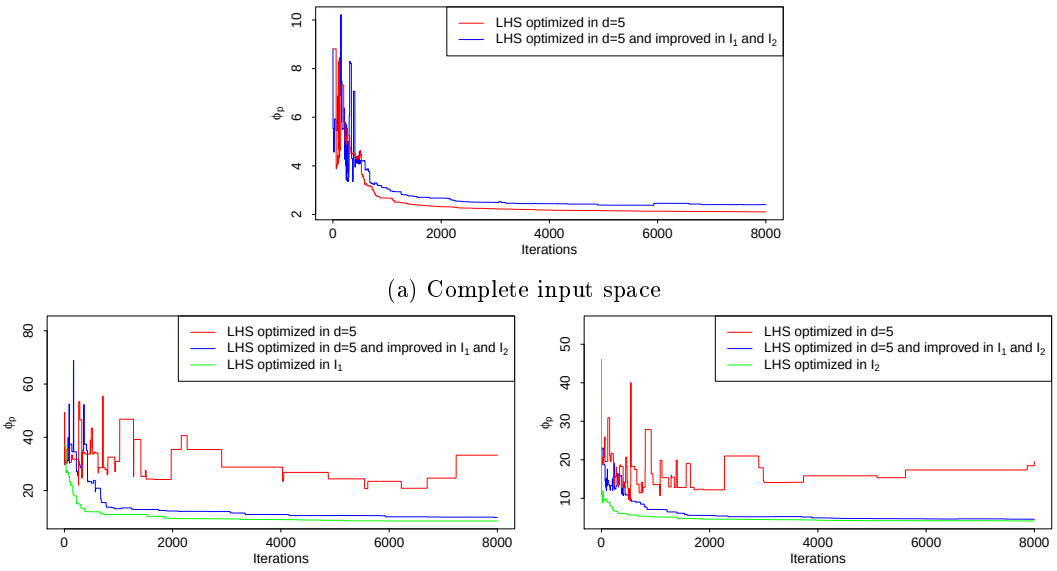

(a) Complete input space

(b) I_1 subspace

(c) I_2 subspace

Figure 3.25: Comparison of an optimized LHS in $d = 5$ and an improved one in the two subspaces with indices I_1 and I_2 in the complete input space (a), the I_1 subspace (b) and the I_2 subspace (c).

We compare the criterion in the original space with a LHS only optimized in this space and we observe that they are quite close for both designs. In the subspaces we compare the criterion with two LHS, one optimized only in the original input space and one optimized only in the subspace. The two LHS with which we compare our optimized LHS can be seen as limiting cases. We observe a significant gain in the criterion with a converging behavior. In contrast, the LHS optimized only in the original input space the criterion behavior is random. The obtained ϕ_p value at the end of the iterations is close to the value of the LHS only optimized in each subspace, a very promising result.

3.5.4 Multi-physics Best Estimate (BE) coupling study

The APOLLO3 ® - FLICA4 multi-physics BE coupling will be used to test and develop the UQM. We remind that it is an explicit coupling with $0.001s$ incremental time step for a total REA duration of $0.4s$. The complete inputs and outputs identified in table 3.3 will be studied. An emphasis will given in testing the IDRM and the LHS subspace optimization. The computational time needed for one code evaluation is 6 minutes. The inputs, outputs and statistical methods that will be tested are summarized:

- **Inputs:** TD_1, TD_2, NF_1, NF_2, D_1, D_2, $S_{1\to2}$, IV_1, IV_2, β_{eff}, λ_{eff}, λ_f, λ_c, Cp_f, Cp_c, H_{gap}, P_r, T_R, H_c, R_{crit}, R_{v0}, H_{dnb}.
- **Outputs:** P_{lin}^{max}, P_{lin}^{2D} (functional), H_f^{max}, DNB^{min}.
- **Statistical tools:**
  - **IDRM:** Identification of an effective reduced input space.
  - **LHS subspaces optimization:** Construction of LHS with good space-filling properties in both the original input space and the subspaces identified by IDRM.
  - **Uncertainty propagation:** Brute Monte Carlo method using kriging surrogate models for histogram empirical estimation.
  - **Global sensitivity analysis:** Shapley indices estimated using kriging models.
  - **Functional outputs:** PCA is used to reduce the functional output dimension. The principal components needed to represent 95% of the variance are retained and used for functional uncertainty propagation and global sensitivity analysis (aggregated Shapley indices).

An initial random sampling of size 125 is used as DOE for the IDRM. The result for each output including the first two principal components of P_{lin}^{2D} retained by the PCA are presented in table 3.14. We can observe that the λ_{eff} while having large sensitivities indices in the preliminary studies was rejected by the IDRM. This is due to its high correlation with β_{eff} but eventually its direct effect is negligible. The identified subspaces can be grouped in two: $I_1 = (TD_1, NF_1, NF_2, D_1, S_{1\to2}, \beta_{eff}, Cp_f, H_{gap}, T_R)$ and $I_2 = (\beta_{eff}, Cp_c, H_{gap}, R_{crit})$.

Table 3.14: Input dimension reduction method result for multi-physics BE coupling study in the MiniCore.

	Selected inputs
$\mathbf{P_{lin}^{max}}$	TD_1, NF_1, NF_2, D_1, $S_{1\to2}$, β_{eff}, Cp_f, H_{gap}, T_R
$\mathbf{P_{lin,pc1}^{2D}}$	TD_1, NF_1, NF_2, D_1, $S_{1\to2}$, β_{eff}, Cp_f, H_{gap}, T_R
$\mathbf{P_{lin,pc2}^{2D}}$	TD_1, NF_1, NF_2, D_1, β_{eff}
$\mathbf{H_f^{max}}$	TD_1, NF_1, NF_2, β_{eff}, Cp_f, H_{gap}
$\mathbf{DNB^{min}}$	β_{eff}, Cp_c, H_{gap}, R_{crit}

For the training of the kriging models a learning LHS of size 250 with optimized subspaces I_1 and I_2 was constructed. The comparative results for the ϕ_p criterion are presented in figure 3.26. We can see the significant gain in the criterion optimization with an obtained value close to the LHS optimized only in the subspaces.

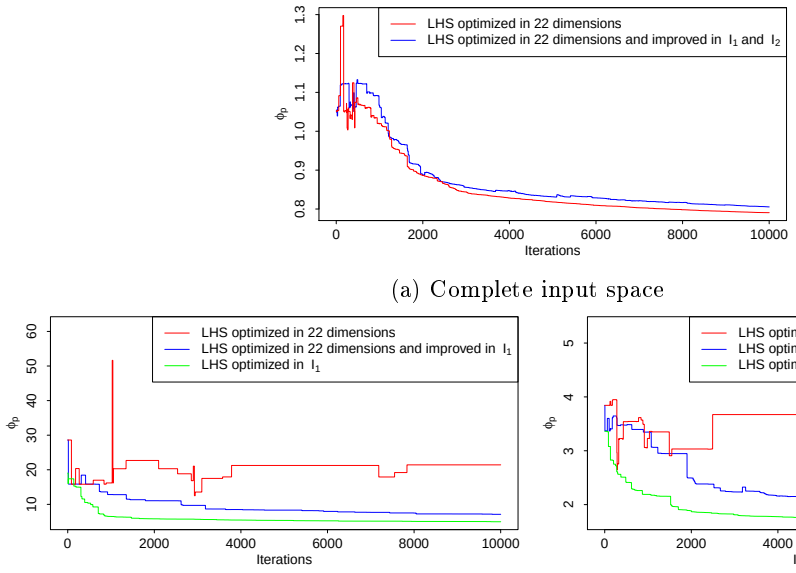

(a) Complete input space

(b) I_1 subspace

(c) I_2 subspace

Figure 3.26: Comparison of an optimized LHS in $d = 22$ and an improved one in the two subspaces with indices I_1 and I_2 in the complete input space (a), the I_1 subspace (b) and the I_2 subspace (c).

The kriging models are trained on the identified input subspaces. The leave-one-out error is directly estimated while the prediction error is estimated using a second LHS of size 125 optimized in the original input space. The result for the interpolation, leave-one-out and prediction error are presented in table 3.15. For all the outputs the prediction errors are small with maximum value 1.46% for DNB^{min}.

Table 3.15: Kriging model interpolation, leave-one-out and prediction errors for multi-physics BE coupling study in the MiniCore.

	Kriging		
	$\boldsymbol{\varepsilon_{int}}$ (%)	$\boldsymbol{\varepsilon_{loo}}$ (%)	$\boldsymbol{\varepsilon_{pred}}$ (%)
$\mathbf{P_{lin}^{max}}$	0.00	$8.21e^{-2}$	$1.07e^{-1}$
$\mathbf{P_{lin,pc1}^{2D}}$	0.00	$8.2557e^{-2}$	$1.11e^{-1}$
$\mathbf{P_{lin,pc2}^{2D}}$	0.00	$5.79e^{-1}$	$5.92e^{-1}$
$\mathbf{H_f^{max}}$	0.00	$1.436e^{-1}$	$1.61e^{-1}$
$\mathbf{DNB^{min}}$	0.00	1.82	1.46

Brute Monte Carlo is used for uncertainty propagation with $1e^5$ samples for each output. The obtained histograms for the scalar outputs and the relative standard deviation for the functional one are presented in figure 3.27. We observe a normal pdf for H_f^{max}, a close to normal for P_{lin}^{max} and a strongly non-normal pdf for DNB^{min}. The relative standard deviations of the radial variation for P_{lin}^{2D}, as in the APOLLO3 ® stand-alone study, is very small. For DNB^{min} we observe a very large relative standard deviation of 76% with a probability of 0.02% to reach boiling crisis.

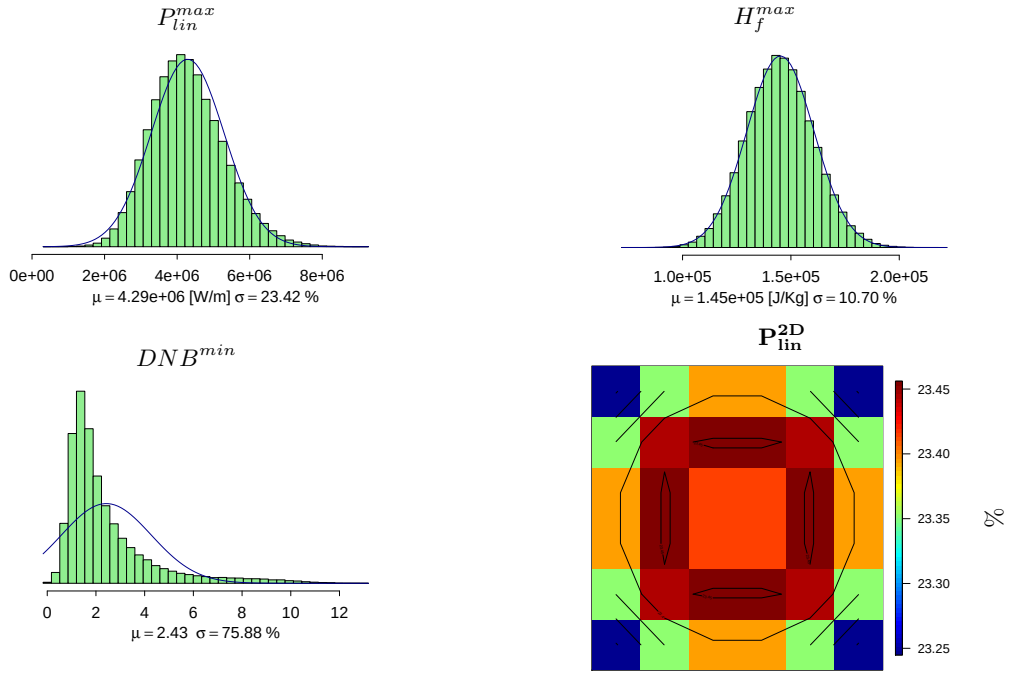

Figure 3.27: P_{lin}^{max}, H_f^{max} and DNB^{min} histograms and P_{lin}^{2D} relative standard deviation distribution for multi-physics BE coupling study in the MiniCore.

Concerning the global sensitivity analysis, for each scalar output the Shapley indices are estimated while for the functional output the aggregate Shapley indices are estimated. The results are shown in figure 3.28. The β_{eff} is the dominant input for P_{lin}^{max}, P_{lin}^{2D} and H_f^{max} responsible for more than 80% of their variations. For DNB^{min} the dominant input is H_{gap} responsible for 90% of the variation. This is attributed to the large uncertainty range of H_{gap} and thus there is an increased motivation to improve its modeling. This will be addressed in the following subsection.

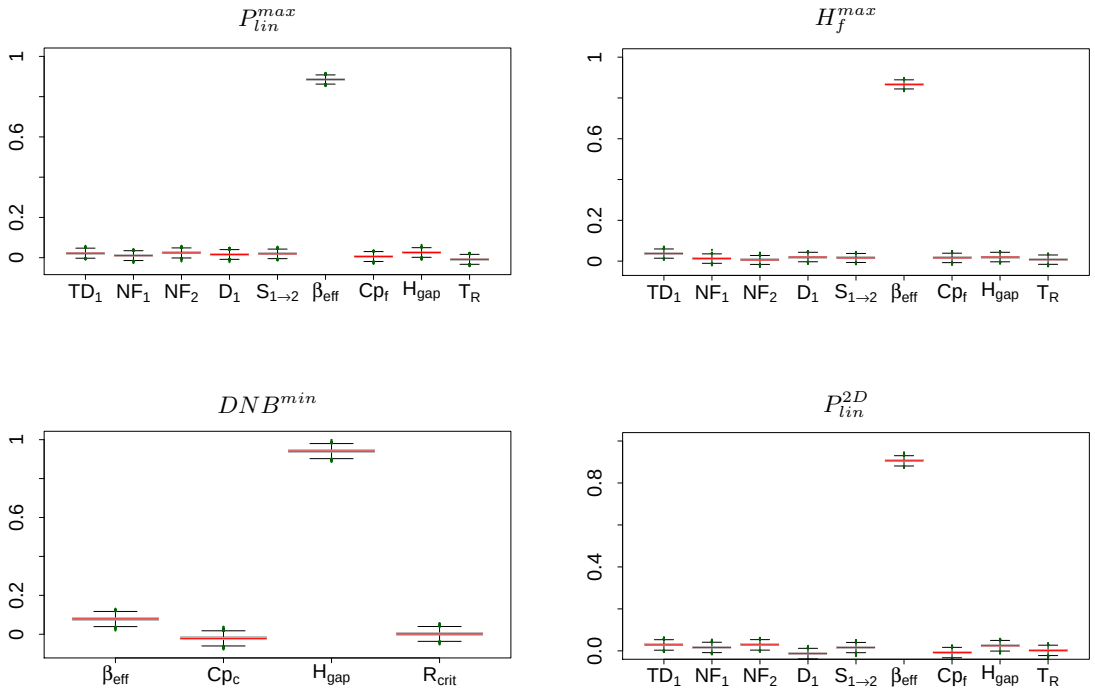

Figure 3.28: P_{lin}^{max}, H_f^{max} and DNB^{min} Shapley indices and P_{lin}^{2D} aggregate Shapley indices for multi-physics BE coupling study in the MiniCore.

3.5.5 Conclusions - UQM scheme

The APOLLO3 ® - FLICA4 multi-physics BE coupling was used to develop and test the input dimension reduction method and the optimization of LHS in both original input space and the identified subspaces. Both of the methods showed very compelling results allowing to treat potential large inputs dimension and addressing dependencies, interactions, redundancies and non-linearities. Additionally, the prediction errors of the kriging models include the dimension reduction errors adding more confidence for the following analyses. The trained surrogate models are used for uncertainty propagation and global sensitivity analysis. Both scalar and functional outputs are considered. Based on all these conclusions we derive the Uncertainty Quantification Methodology (UQM) for REA. In Chapter 4 we apply this methodology in a large scale PWR core. The UQM consist of four main steps and is illustrated in figure 3.29.

The initial step 0 is the definition of the case study with the desired uncertain inputs and outputs and the input uncertainty quantification. Since we assume that in the general case the input dimension can be large the step 1 consists in identifying the important input subspaces using IDRM for both scalar and functional outputs. This step is based on an initial random sampling.

The step 2 is the training of the kriging models for each output on the identified subspaces. The training LHS is constructed with good space-filling properties in both the original input space and the important subspaces. For the functional outputs the kriging models are constructed for the first principal components that represent 95% of the outputs variance. The prediction errors of the kriging models are estimated using an independent LHS.

The step 3 is the brute force Monte Carlo uncertainty propagation with the empirical estimations of the first two statistical moments and the histogram. Finally, in step 4 the global sensitivity analysis is performed using Shapley indices for scalar outputs and aggregated Shapley indices for functional ones.

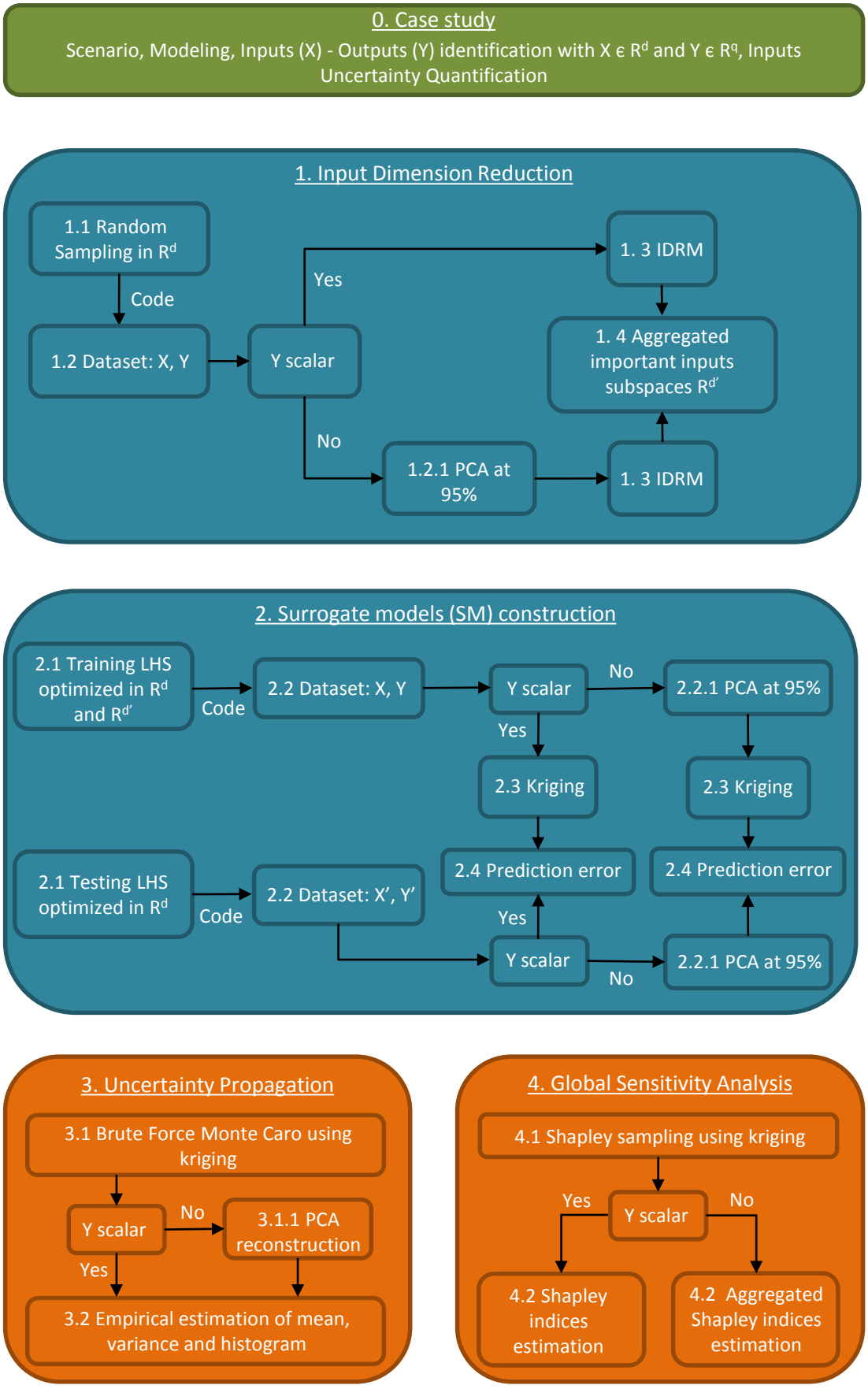

Figure 3.29: Uncertainty Quantification Methodology scheme

3.6 Improving the gap heat transfer modeling

3.6.1 Introduction

The gap heat transfer (H_{gap}) modeling so far in the BE coupling was done using a constant value during the REA with a uniform distribution over a large interval. This is one of the most important modeling differences between Best Effort and BE coupling. There is a strong interest thus to improve the H_{gap} modeling and introducing it in the previous coupling. In this subsection we address this challenge by calibrating a simplified H_{gap} model that is based on fuel thermal expansion. We consider that this model is adequate for the REA and especially for the gap closing phase. The calibration is performed through decoupled ALCYONE V1.4 calculations with imposed power evolution. We first detail the model with its calibration parameters. Afterwards, we present the calibration methodology where we discuss issues such as how the power pulses are selected, how many H_{gap} models will be created for the different fuel assemblies etc. Finally, we introduce the model in the BE coupling, apply the previously developed UQM and compare some selected design points with the results of the Best Effort APOLLO3 ® - FLICA4 - ALCYONE V1.4 coupling.

3.6.2 Gap heat transfer simplified model

The sharp power increase in the REA leads to a corresponding sharp fuel temperature increase. We assume that the H_{gap} evolution is driven by the gap closing due to fuel thermal expansion and by the gas conductivity evolution in the gap. This is used to derive the simplified formulation for H_{gap} defined by equations 3.2a - 3.2c.

$$H_{gap} = \frac{\lambda_g(T_g, E_f)}{e(T_f)} \tag{3.2a}$$

$$\lambda_g = \lambda_{g,init}\left(1 + \theta_1 \frac{T_g - T_{g,init}}{T_{g,init}} + \theta_2 E_f\right) \tag{3.2b}$$

$$e(T_f) = r_{c,init} - r_f(T_f) \tag{3.2c}$$

Where:

- λ_g is the gas conductivity in the gap and $\lambda_{g,init} = \frac{H_{gap}^{init}}{e_{init}}$ its initial value prior to the REA. The latter is calculated by the initial gap heat transfer H_{gap}^{init} and initial gap width e_{init}.
- T_g is the gas temperature and $T_{g,init}$ the initial gas temperature prior to the REA.
- E_f is the energy stored in the fuel during the REA.
- θ_1 and θ_2 are two calibration parameters that have to be estimated.
- e is the pellet-cladding gap width. It is assumed that only the fuel expansion is responsible for the gap evolution.
- $r_{c,init}$ is the initial internal cladding radius prior to the REA.
- $r_f = r_{f,init}\alpha_f(T_f)$ is the fuel external radius. The fuel expansion is modeled using the fuel expansion coefficient $\alpha_f(T_f)$ in [26] which is a cubic function of the fuel temperature T_f.

The H_{gap} predicted by the proposed simplified model is based on fuel thermal expansion and depends on the evolution of the λ_g and e. The λ_g is considered a linear function of T_g and E_f. The latter allows to include a historical effect on the conductivity. The two calibration parameters to be determined θ_1 and θ_2 are the coefficients of T_g and E_f respectively. The e evolution is assumed to depend only on the fuel thermal expansion while the cladding radius remains constant. For the modeling of the gas temperature T_g the average between the external fuel temperature and the internal cladding temperature is proposed. It is a strong assumption since the gradient in the gap is important but for the purpose of this simplified model we consider that it is justified.

3.6.3 Development of gap heat transfer calibration methodology

Having defined the simplified H_{gap} model the next step is to calibrate it. A calibration methodology was developed in this thesis illustrated in figure 3.30.

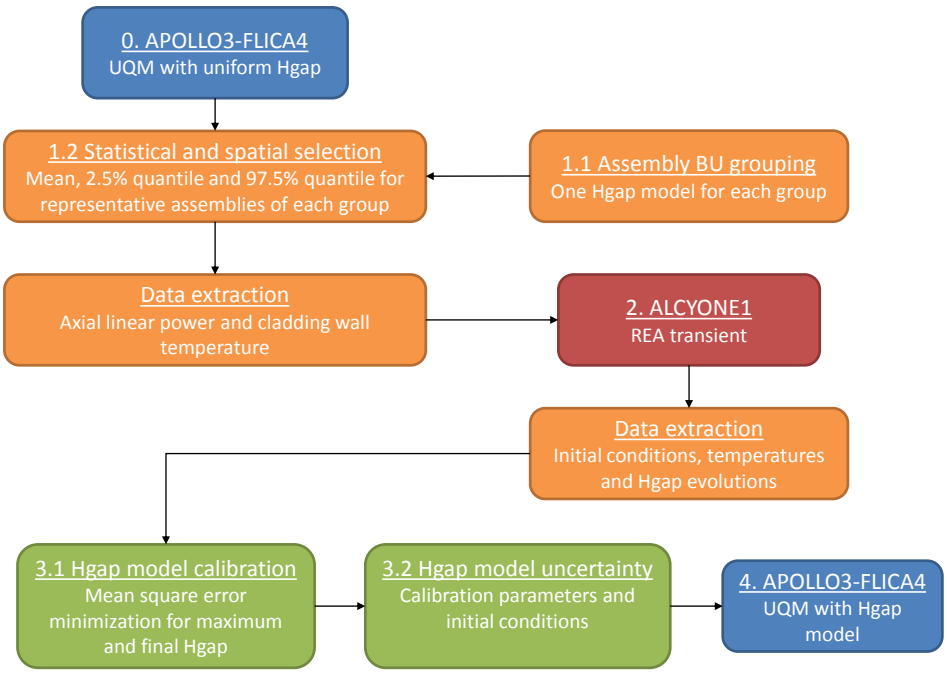

Figure 3.30: Gap heat transfer model calibration methodology scheme.

The starting point is the UQM application in the BE coupling of Section 3.5.4. The temperature evolution in the fuel depends on the fuel assembly burn-up and the power seen by this assembly in its position in the core. Since we need to build a H_{gap} model for every fuel spatial mesh (1080 meshes) a grouping is necessary. In step 1.1 we group the assemblies by similar radial average burn-up. This means that we will construct one H_{gap} model for every identified group. In the MiniCore case it is relatively straightforward to group the assemblies leading to three burn-up groups: 0, 15 and $30\,GWd/t$. It is important to notice that while there are only three models the initial conditions are different for each fuel pin leading to a radial and axial H_{gap} profile during REA.

The next step 1.2 consists in selecting representative pulses from the APOLLO3 ® - FLICA4 uncertainty analysis. The pulses must cover most of the possible H_{gap} variations inside the group due to both statistical and spatial aspects. For the statistical aspect three pulses are extracted: the mean and the 95% upper and lower quantiles of P_{lin}^{max}. For the spatial aspects, when the mean and the upper 95% quantile are imposed then the quarter assembly seeing the maximum power is selected. Correspondingly, when the lower quantile is imposed the quarter assembly seeing the lowest power is selected. This creates for each model three representative axial and temporal profiles of linear power and external cladding temperature.

In step 2 the selected profiles are extracted and imposed in a decoupled ALCYONE V1.4 REA transient calculation. One representative fuel pin is modeled. The resulting temperature and gap heat transfer profiles from ALCYONE V1.4 are extracted and used for the H_{gap} model calibration.

The calibration is carried out in step 3.1 by finding the parameters that minimize the mean square error on the H_{gap} maximum and final value during the REA for each axial slice. Once the parameters are estimated the final step 3.2 is to quantify the calibrated model uncertainty. The two main sources of uncertainties are the initial conditions and the calibrated parameters. The former one is quantified as two mutliplication coefficients on the initial gap width and the initial

H_{gap} with pdf $\mathcal{N}(1.0, 0.1)$. This is a result of a previous uncertainty analysis for fuel evolution calculations with ALCYONE V.1.4. The results also showed that the initial gap width and H_{gap} are fully negatively correlated. This leads to consider the two coefficients as fully negatively correlated ($\rho = -1$) rendering thus one effective uncertain quantity for the initial conditions $H_{g,i}$. The latter uncertainty source is the calibrated parameters. They are considered as fully positively correlated ($\rho = 1$) with uniform distributions. The bounds of the distributions are calculated in order to account for the calibration error. The effective uncertain input representing the calibration uncertainty is $H_{g,m}$. More details about how this is implemented are provided in the Section 3.6.4.

Finally, the model of equations equations 3.2a - 3.2c, including its two effective uncertain parameters, is introduced in the multi-physics coupling creating an Improved Best Estimate (IBE) modeling. It can be seen as an intermediate modeling between the BE and Best Effort modelings. The computational cost of IBE is similar to BE.

3.6.4 Test of gap heat transfer calibration methodology

Each step of the H_{gap} model calibration methodology is tested on the MiniCore in order to evaluate its performance. For the initial step 0 a multi-physics BE uncertainty propagation study must be performed. In our case we use the study of Section 6.5.4 where we tested the UQM on the APOLLO3 ® - FLICA4 BE coupling. The grouping of assemblies in step 1.1 for the MiniCore geometry (figure 3.1) as mentioned is rather straightforward since there are three discrete groups of burn-up. We consider one H_{gap} model for each burn-up resulting in a total of three models. From the results of the UQM for P_{lin}^{max} we select the mean, the upper and lower 95% quantile. From the identified design points and for each model in step 1.2 representative quarter of assemblies are identified and the results are presented in figure 3.31. The green circles indicate the selection of the mean and upper quantile and the yellow indicates the selection for the lower quantile. Following the defined procedure and due to the MiniCore symmetry for the $30\,GWd/t$ burn-up group there is only one possible choice for all three design points. For the $15\,GWd/t$ burn-up there are three possible choices, from which we select the quarter of assembly closer to the control rod ejection location for the mean and the upper quantile. This is because it is the one with the maximum linear power. For the lower quantile, the quarter assembly the farthest from the center is selected as it is the one with the minimum linear power. We follow the same reasoning for the $0\,GWd/t$ burn-up quarter assembly selection.

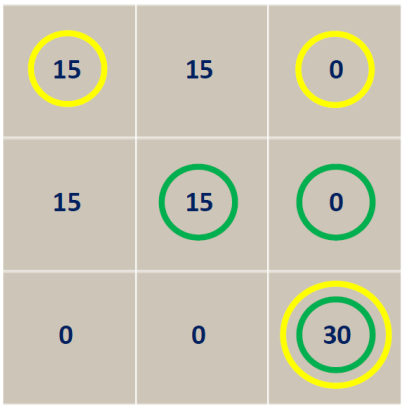

Figure 3.31: Selected representative quarter of assemblies for each H_{gap} model group on the symmetric 1/4 MiniCore geometry of figure 3.1.

At the end of this step for each design point there is a corresponding quarter of assembly for each group. In this quarter of assembly the axial and temporal profiles of the linear power and cladding wall temperature are extracted and applied in the decoupled ALCYONE V1.4 calculation. A representative fuel pin for each selected quarter of assembly in each sampling is modeled. The axial and temporal evolutions of the Hgap and radial temperature are calculated during the REA. These results together with the stored fuel energy are extracted. Only the values corresponding to the time of the maximum and final value of H_{gap} during the REA for all the axial slices are kept for the calibration in order to simplify the optimization. This creates a total dataset of $30 \times 3 \times 2 = 180$

results on which the simplified H_{gap} model is calibrated. The calibration parameters are optimized by minimizing the mean square error (Section 2.8.1) on this dataset. The resulting calibration error for the three different models are presented in figure 3.32 and the estimated calibration parameters in table 3.16.

Table 3.16: MiniCore H_{gap} model calibration parameters estimation

	0	**15**	**30**
$\boldsymbol{\theta_1}$	$2.18e^{-1}$	$7.90e^{-2}$	$-1.36e^{-1}$
$\boldsymbol{\theta_2}$ $[\mathbf{J^{-1}}]$	$1.13e^{-5}$	$1.63e^{-5}$	$2.02e^{-5}$

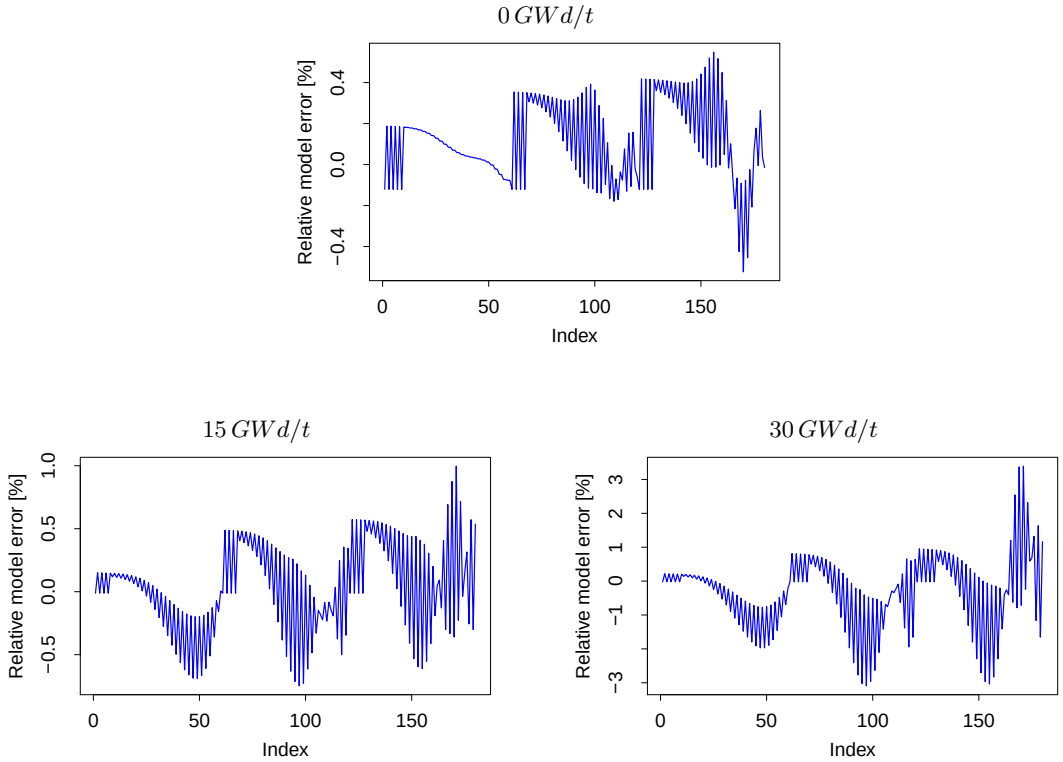

Figure 3.32: H_{gap} model calibration errors for the MiniCore assembly groups at $0\,GWd/t$, $15\,GWd/t$ and $30\,GWd/t$.

The next step in the methodology is to quantify the calibration parameters uncertainty. To this purpose we calculate a map by perturbating both inputs and estimating the maximum calibration error on the dataset. The result for the $30GWd/t$ group is illustrated in figure 3.33. We can observe the following facts: if both parameters increase, then the error decreases; if both parameters decrease, then the error increases. Based on this we use the assumption that the parameters are fully positively correlated in order to cover the maximum calibration error. This essentially means that the parameters can only vary on the diagonal. By deciding the upper and lower bounds of the (signed) error that we want to cover we obtain the bounds for each parameter as is shown in figure 3.33. For the other groups the result of the error evolution has similar behavior just with different bounds. At this point we make a second assumption that all the groups have parameters that are fully positively correlated. This is done in order to both simplify our uncertainty quantification and to be consistent with the uncertainty quantification of the rest inputs. For the all the other inputs the uncertainties are applied homogeneously on the whole core as depicted in figure 1.21. We observe that the calibration error increases with burn-up, meaning that the corresponding calibration parameters will have a larger range in their uniform pdf. This means that larger uncertainty will be propagated by the model for higher burn-ups. The results for the estimated ranges for each parameter are shown in table 3.17.

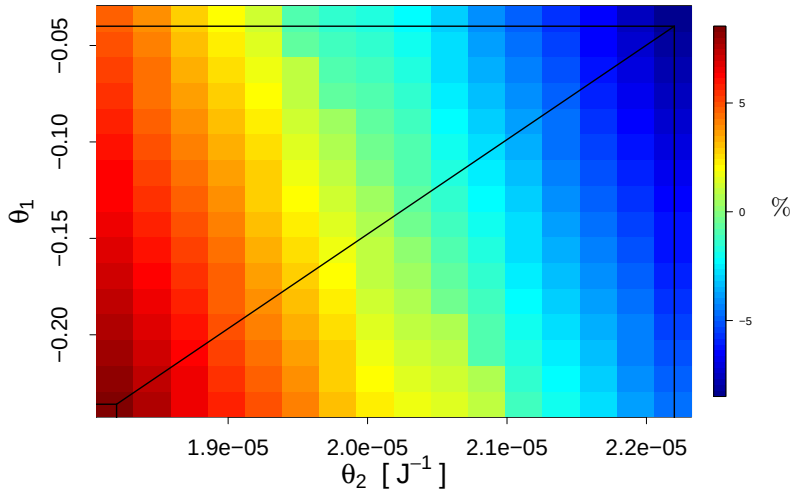

Figure 3.33: Maximum calibration error evolution with the calibration parameters for MiniCore $30GWd/t$ group.

Table 3.17: MiniCore H_{gap} model calibration parameters pdf estimation.

	0	**15**	**30**
$\boldsymbol{\theta_1}$	$\mathcal{U}(2.04e^{-1}, 2.334e^{-2})$	$\mathcal{U}(2.90e^{-2}, 1.29e^{-1})$	$\mathcal{U}(-2.36e^{-1}, -3.60e^{-2})$
$\boldsymbol{\theta_2}$ $[\mathbf{J^{-1}}]$	$\mathcal{U}(1.04e^{-5}, 1.24e^{-5})$	$\mathcal{U}(1.53e^{-5}, 1.73e^{-5})$	$\mathcal{U}(1.82e^{-5}, 2.22e^{-5})$

Using these bounds the prediction of the H_{gap} temporal evolution by the calibrated model is compared to the ALCYONE V1.4 calculation. The results at the axial slice with the maximum H_{gap} value for each model and design point are presented in figures 3.34 - 3.36.

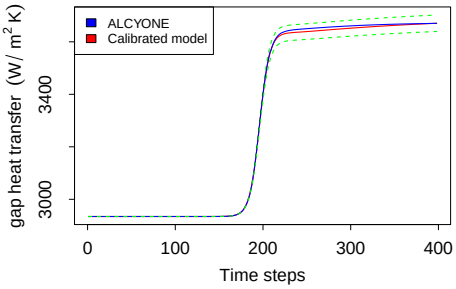

(a) Lower 95% Quantile

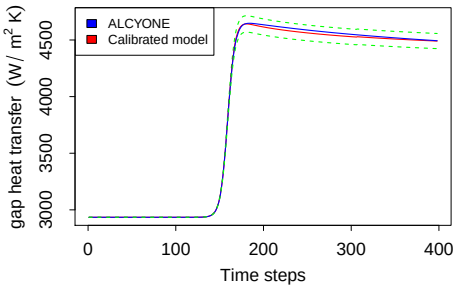

(b) Mean

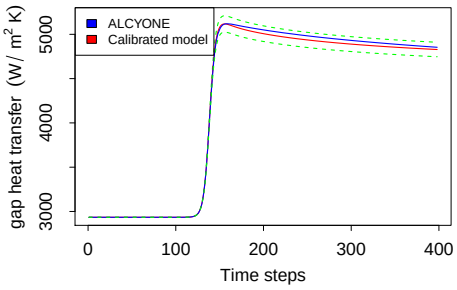

(c) Upper 95% Quantile

Figure 3.34: MiniCore $0GWd/t$ group calibration results including the uncertainty bounds (green).

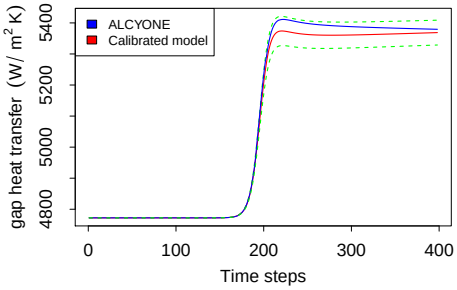

(a) Lower 95% Quantile

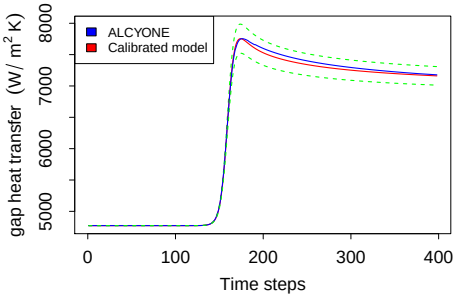

(b) Mean

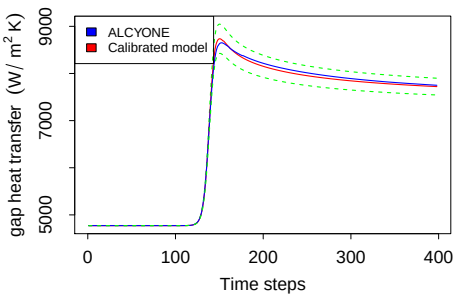

(c) Upper 95% Quantile

Figure 3.35: MiniCore $15GWd/t$ group calibration results including the uncertainty bounds (green).

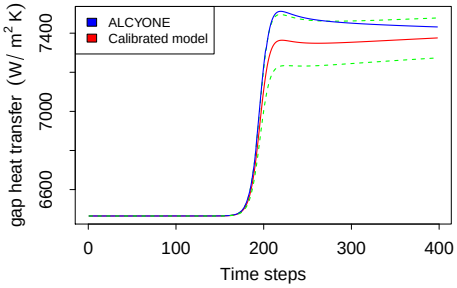

(a) Lower 95% Quantile

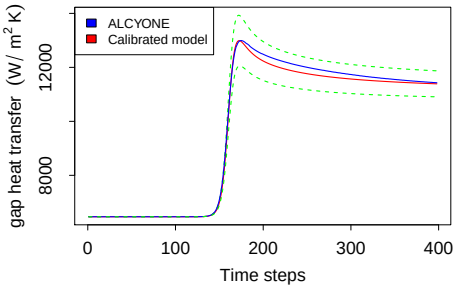

(b) Mean

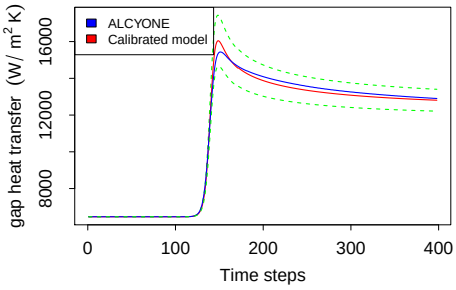

(c) Upper 95% Quantile

Figure 3.36: MiniCore $30GWd/t$ group calibration results including the uncertainty bounds (green).

The plotted H_{gap} predictions are also the ones with the larger errors and we can see that in all the predictions the ALCYONE V1.4 calculation is inside the uncertainty bounds created by the uncertain calibration parameters.

3.6.5 UQM tested on Improved Best Estimate (IBE) coupling

The calibrated H_{gap} models are introduced in the BE coupling to create the intermediate APOLLO3 ® - FLICA4 - HGAP multi-physics coupling. The complete UQM is applied on this modeling. The uncertain inputs and outputs of table 3.3 are used with the replacement of the constant H_{gap} uncertain input by the H_{gap} simplified model uncertainties. We defined two uncertain parameters, one related to the initial conditions of the model $H_{g,i}$ and one related to the calibration parameters uncertainty $H_{g,m}$. We remind that it is an explicit coupling with $0.001s$ incremental time step for a total REA duration of $0.4s$. The computational cost of this modeling is similar to the APOLLO3 ® - FLICA4 modeling (about 6 minutes).

For the step 1 of the UQM a random sampling of size 125 is used as DOE for the input dimension reduction. The result for the identified subspaces are gathered in table 3.18 and can be grouped in two: $I_1 = (TD_1, NF_1, NF_2, D_1, S_{1\to2}, \beta_{eff}, Cp_f, H_{g,i}, T_R)$ and $I_2 = (TD_1, NF_2, \beta_{eff}, H_{g,i}, H_c, R_{crit}, T_R)$. In step 2 of the UQM a learning LHS of size 250 with optimized subspaces I_1 and I_2 was constructed for the training of the kriging models. The kriging models are trained on the identified input subspaces. The result for the interpolation, leave-one-out and prediction errors are presented in table 3.19. The prediction errors are estimated on a second LHS of size 125. For all the outputs the prediction errors are small with larger errors for DNB^{min} (2%) and the second principal component of P_{lin}^{2D} (5.5%).

Table 3.18: UQM step 1 results for IBE coupling study in the MiniCore.

	Selected inputs
$\mathbf{P_{lin}^{max}}$	TD_1, NF_1, NF_2, $S_{1\to2}$, β_{eff}, Cp_f, T_R
$\mathbf{P_{lin,pc1}^{2D}}$	TD_1, NF_1, NF_2, $S_{1\to2}$, β_{eff}, Cp_f, T_R
$\mathbf{P_{lin,pc2}^{2D}}$	TD_1, D_1, β_{eff}
$\mathbf{H_f^{max}}$	TD_1, NF_1, NF_2, $S_{1\to2}$, β_{eff}, Cp_f, $H_{g,i}$
$\mathbf{DNB^{min}}$	TD_1, NF_2, β_{eff}, $H_{g,i}$, H_c, R_{crit}, T_R

Table 3.19: UQM step2 results for IBE coupling study in the MiniCore.

	ϵ_{int} (%)	ϵ_{loo} (%)	ϵ_{pred} (%)
$\mathbf{P_{lin}^{max}}$	0.00	$1.15e^{-1}$	$9.98e^{-2}$
$\mathbf{P_{lin,pc1}^{2D}}$	0.00	1.16^{-1}	$1.01e^{-1}$
$\mathbf{P_{lin,pc2}^{2D}}$	0.00	$6.16e^{-1}$	5.53
$\mathbf{H_f^{max}}$	0.00	$1.62e^{-1}$	$1.73e^{-1}$
$\mathbf{DNB^{min}}$	0.00	2.10	2.03

In step 3 of the UQM brute force Monte Carlo is used for uncertainty propagation with $1e^5$ samples for each output. The results are presented in figure 3.37. The obtained histogram for H_f^{max} and the relative standard deviation of P_{lin}^{2D} are similar to the APOLLO3 ® - FLICA4 study. For P_{lin}^{max} a shift towards to a lower mean value is observed with similar relative standard deviation. The histogram of DNB^{min} is the most impacted by the introduction of H_{gap} model, something expected from the previous sensitivities. The mean value is further from the boiling crisis and the relative standard deviation decreases from 76% to 26%. The histogram now has a close to normal distribution. This change is attributed to the more realistic modeling of H_{gap} leading to in average less heat transfer. The coolant extracts less heat and larger values for DNB^{min} are obtained. The probability now for reaching boiling crisis has decreased to 0.002% an order of magnitude of difference.

The final step 4 of the UQM is performed and the Shapley indices are estimated for all the outputs. The results are presented in figure 3.38. For P_{lin}^{max}, P_{lin}^{2D} and H_f^{max} as in the previous APOLLO3

® - FLICA4 study the only dominant input is β_{eff} responsible for more than 80% of the outputs variance. A significant difference in observed for the DNB^{min} sensitivities. The gap heat transfer is not any more the dominant input, instead the β_{eff} accounts for 70% of the outputs variance. The H_{gap} initial conditions are responsible for 20% while the rest 10% is divided among the other inputs.

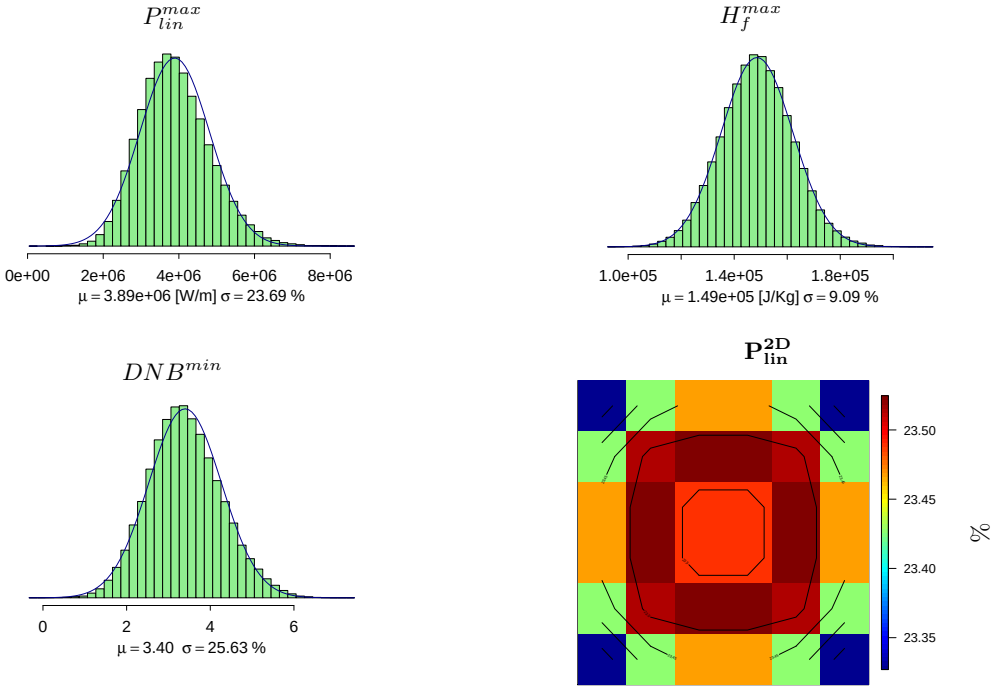

Figure 3.37: P_{lin}^{max}, H_f^{max} and DNB^{min} histograms and P_{lin}^{2D} relative standard deviation distribution for IBE coupling study in the MiniCore.

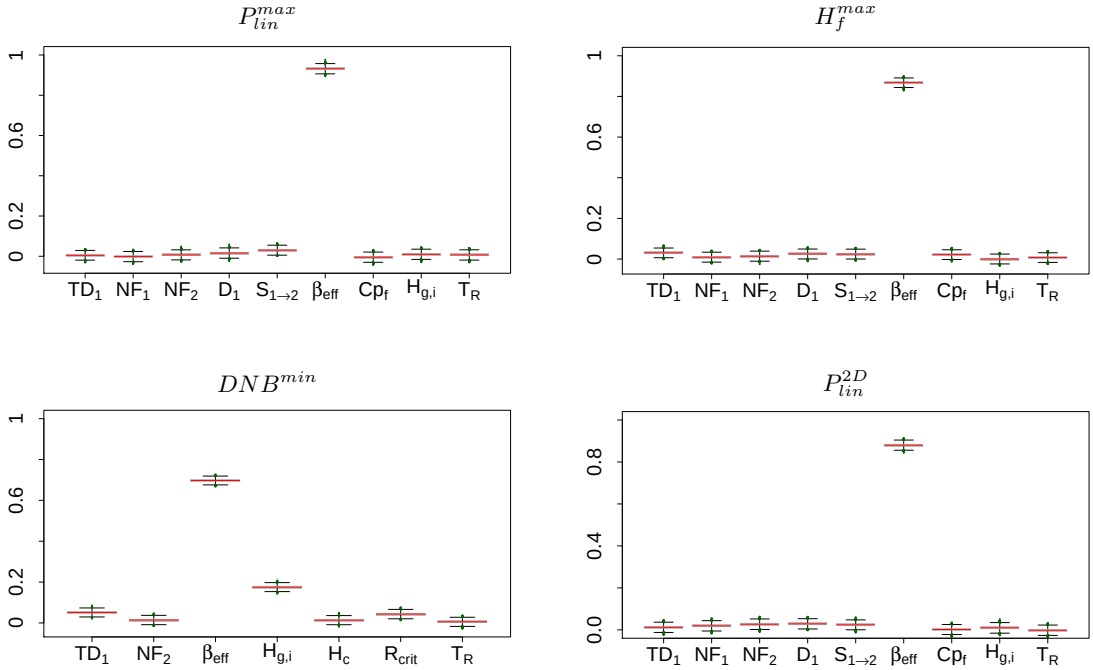

Figure 3.38: P_{lin}^{max}, H_f^{max} and DNB^{min} Shapley indices and P_{lin}^{2D} aggregate Shapley indices for IBE coupling study in the MiniCore.

3.6.6 Comparison with Best Effort coupling

By introducing the H_{gap} calibrated model to the BE coupling we improved its REA modeling. The new IBE coupling has an H_{gap} modeling much closer to the reality than the constant value used in the BE coupling. Additionally, the computational cost does not increase and remains around 6 minutes for one code evaluation. While the calibrated models have a small calibration error, it is important to compare the H_{gap} predicted evolution in REA with the Best Effort APOLLO3 ® - FLICA4 - ALCYONE V1.4 modeling. The introduction of ALCYONE V1.4 increases the computational cost for one code evaluation to 4 hours rendering a complete UQM prohibitive. For this reason three samples from the previous UQM were selected in order to compare the Best Effort and the IBE modelings. Since the H_{gap} variations in the $0\,GWd/t$ burn-up fuel is small only the results for the $15\,GWd/t$ and $30\,GWd/t$ are presented. We focus on the temporal H_{gap} evolution at the location of the maximum H_{gap}. The results for the $15GWd/t$ fuel are illustrated in figure 3.39. We observe an underestimation of 13% for the maximum and final value of the H_{gap} during REA. The results for the $30GWd/t$ fuel are illustrated in figure 3.40. There is a very good agreement for the maximum H_{gap} but there is an under-estimation for the last value of 17%.

The reasons for these underestimations can be multiple, from the simplistic nature of the model to the different temperature predictions in the two modelings. We remind that in FLICA4 the thermomechanics are not considered and that the radial discretization in ALCYONE V1.4 is much finer. This leads to different fuel temperatures that are an important aspect for the model. Additionally, in the model we use an effective gas temperature calculated as an average between the fuel external and cladding internal temperatures. This is a strong assumption that can explain part of this underestimation.

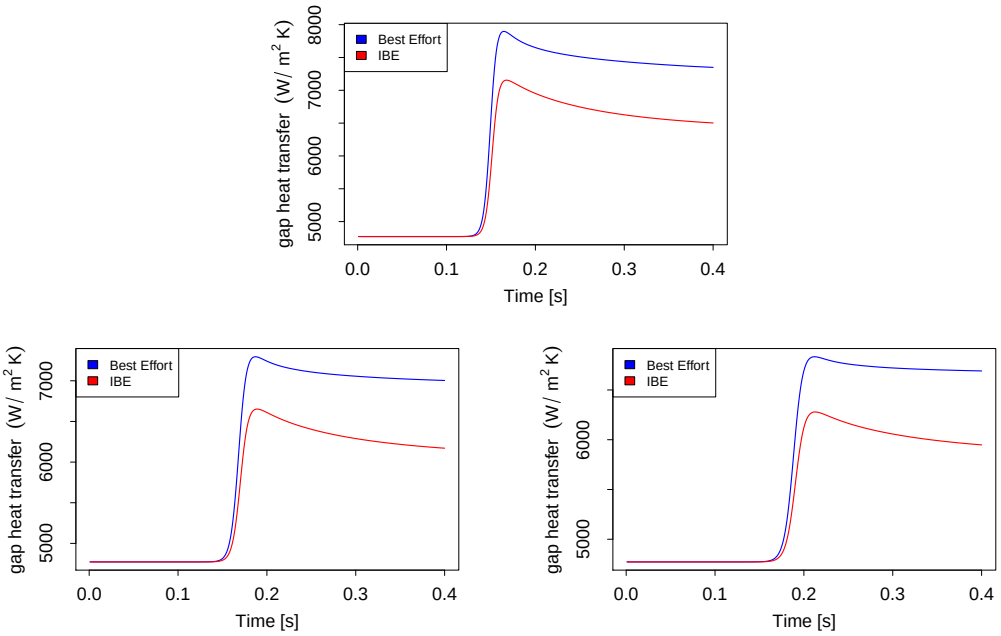

Figure 3.39: H_{gap} comparison for $15GWd/t$ burn-up fuel between IBE and Best Effort coupling. Three different samples are compared at the location of maximum H_{gap}.

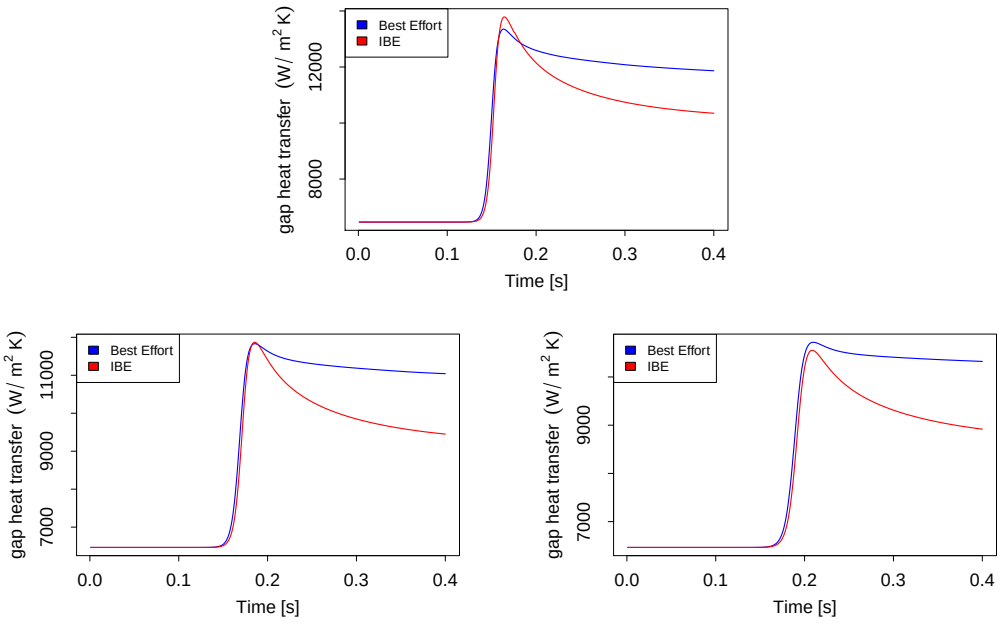

Figure 3.40: H_{gap} comparison for $30GWd/t$ burn-up fuel between IBE and Best Effort coupling. Three different samples are compared at the location of maximum H_{gap}.

3.6.7 Conclusions

In this subsection we developed and tested the methodology for calibrating a simplified H_{gap} model that is based on thermal expansion. We presented the different steps of the methodology from the selection of the imposed boundary conditions in the ALCYONE V1.4 REA decoupled calculations to the model calibration by mean square error minimization and the quantification of the model uncertainty. The methodology was tested on the MiniCore geometry and resulted in very satisfactory results concerning the calibration error. The defined uncertainty ranges of the calibration parameters covered in all the cases the predicted H_{gap} evolution during the REA by ALCYONE V1.4.

The H_{gap} model was introduced then in the APOLLO3 ® - FLICA4 BE coupling. This lead to IBE coupling, a significantly more realistic modeling of the REA with no increase on the computational cost. The UQM was tested on this improved modeling affecting mainly the margin to boiling crisis uncertainty quantification. The sensitivity of the H_{gap} decreased significantly due to its better modeling.

Finally, the IBE modeling was compared to the Best Effort modeling on three different samples in terms of the H_{gap} temporal prediction at the location of the maximum H_{gap}. The resulting comparison showed an underestimation of the H_{gap} between $13\% - 17\%$. This is attributed to the many assumptions of the calibrated model and to the differences of the fuel-thermomechanics modeling in FLICA4 and ALCYONE V1.4. This means that the developed IBE modeling cannot replace the Best Effort modeling but it can be used as a cheap realistic estimation in cases where the latter is unfeasible. This is usually the case in the uncertainty quantification since many code evaluations are needed and especially in the large scale PWR core study carried out in Chapter 4.

3.7 Conclusions

The goal in this Chapter was to develop and test an uncertainty quantification methodology (UQM) for a multi-physics REA modeled by an APOLLO3 ® - FLICA4 BE coupling. In Chapter 2 we discussed the different available statistical tools that could be included in the UQM.

Initially we started with preliminary stand-alone decoupled calculations for each code of the COR-

PUS coupling framework presented in Section 1.7. These studies allowed to select and validate the adequacy of some statistical tools. More specifically, the kriging models showed better performance with small prediction error for all the output quantities that were studied and for this reason they were selected. Concerning the global sensitivity analysis the Shapley and Sobol indices were studied. The former ones were selected due to the fact that they are well adapted for dependent inputs. The HSIC statisical significance test screening capabilities were also found to be very promising since they manage to identify for each output at least all the relevant inputs. Various functional outputs up to 2D fields were treated using PCA with 95% of variance with compelling results that increased our confidence for their modeling in the UQM.

With the insights gained from the preliminary studies the UQM was developed on an APOLLO3 ® - FLICA4 coupling. All the identified inputs and outputs were included in this study. Two methods were developed and tested. The first one is the input dimension reduction method (IDRM) based on HSIC statistical significance tests and showed very good results on the Morris function. The second one is an adaptation of the Simulated Annealing LHS optimization algorithm to improve the good space-filling properties in the identified input subspaces by IDRM. The maximin criterion is optimized by minimizing the ϕ_p criterion (Section 2.6.2) in both the complete inputs space and the identified subspaces. It was tested on 5 inputs dimension with very compelling results. Both methods were used then in the APOLLO3 ® - FLICA4 coupling validating their previous testing. The kriging models and Shapley indices were also tested in this coupling with similar results with the preliminary studies. The conclusions drawn from all these studies resulted in the development of the UQM scheme consisting of four steps. The first one is the identification of the important input subspaces. In the second step the kriging models are trained on LHS optimized in these subspaces and their prediction errors are estimated based on a second LHS. The third step uses these kriging models for brute force Monte Carlo uncertainty propagation. Finally, in the fourth step global sensitivity analysis is performed using the kriging models to estimate the Shapley indices for scalar outputs and the aggregated Shapley indices for the functional ones.

The BE coupling in the UQM development included many modeling simplifications. The main one was the use of a constant uncertain value for the H_{gap}, something that was reflected in the global sensitivity analysis. To improve this modeling, a simplified H_{gap} model based on thermal expansion was calibrated. The calibration methodology was developed including three main steps. In these steps the assemblies were grouped by burn-up with one model for each group. Boundary conditions were imposed in ALCYONE V1.4 REA decoupled calculations covering most of the H_{gap} variations. On the obtained results the H_{gap} models were calibrated by mean square error minimization. Additionally, the uncertainty of the models was quantified through two effective parameters. The methodology was tested on the MiniCore geometry with very promising results. Small calibration errors were observed and the defined uncertainty ranges of the calibration parameters covered in all the cases the predicted by ALCYONE V1.4 H_{gap} evolution during the REA. The calibrated H_{gap} model was then included in the BE coupling creating the IBE modeling without any impact on the computational cost. The UQM was tested on this improved modeling affecting mainly the margin to boiling crisis uncertainty quantification. The sensitivity of the H_{gap} decreased significantly due to its better modeling. Finally, the IBE modeling was compared to the Best Effort modeling on three different design points in terms of the H_{gap} prediction. The resulting comparison showed an underestimation of the H_{gap} between $13\% - 17\%$. This is attributed to the many assumptions of the calibrated model and to the differences of the fuel-thermomechanics modeling in FLICA4 and ALCYONE V1.4. However, we can conclude that we developed an improvement of the BE coupling without an increase in the computational cost that is much closer to the Best Effort coupling as far as the H_{gap} is concerned. This coupling cannot replace the Best Effort since there are many limiting assumptions but it can be used for a more realistic UQM on the large scale PWR core, where the Best Effort coupling is unfeasible.

Chapter 4

Application of the Uncertainty Quantification Methodology on PWR core

4.1 Introduction

Large scale PWR core transient simulations with a Best Estimate (BE) modeling have high computational cost, especially in the case of Rod Ejection Accident (REA) where a multi-physics modeling is necessary as discussed in Section 1.6. Furthermore, this budget limitation has even more constraints if an uncertainty quantification is performed for a REA. Many challenges such as the potential large input and output dimensions, input dependencies and non-linearities of the outputs accentuate the complexity.

In Section 3.5 we developed and tested an Uncertainty Quantification Methodology (UQM) that can address some of these challenges and tested it on a small scale core (MiniCore) representative of a Pressurized Water Reactor (PWR) behavior. REA was studied using the BE APOLLO3 ® - FLICA4 modeling of the CORPUS coupling framework presented in Section 1.7. The methodology includes two main steps. The first one is the identification of important input subspaces with regards to each output of interest. It is detailed in Section 3.5.2 and allows an input dimension reduction that facilitates the construction of surrogate kriging models. Statistical significance tests based on HSIC (Section 2.7.5.4) are used to this purpose. The second step detailed in Section 3.5.3 is the training of the kriging models on LHS optimized in both the complete input space and the identified subspaces. The kriging is trained only on these subspaces with a prediction error that includes the dimension reduction error. Finally, uncertainty propagation by brute Monte Carlo and global sensitivity analysis by estimating Shapley indices (Section 2.7.4.2) are carried out using the trained kriging models. The derived UQM can treat both scalar and functional outputs. For the latter Principal Components Analysis (PCA) is used by keeping the first principal components responsible for 95% of the outputs variance. PCA was discussed in Secton 2.4.1. For the global sensitivity analysis aggregate Shapley indices are estimated as defined in Section 2.7.6.1.

Another important methodological aspect studied in Section 3.6 was the improvement of the fuel thermal modeling in the BE coupling for a REA. One of the most important limitations of the BE coupling is the use of a constant gap heat transfer value (H_{gap}). A methodology was developed and tested to calibrate a simplified H_{gap} model based on thermal expansions. The fuel assemblies of the core are grouped by their burn-up. One model is used for each group but with different initial conditions that vary spatially. The calibration is performed on a dataset of H_{gap} and radial fuel temperatures evolution during REA created by decoupled ALCYONE V1.4 REA calculations. The uncertainty of the H_{gap} model was estimated due to both calibration and initial conditions. The former one is modeled by the attribution of uniform pdf on the calibration parameters with ranges that cover the calibration error. The latter is quantified as a multiplication coefficient on the initial H_{gap} and the pellet-cladding gap width by uncertainty propagation in the evolution calculations. Finally, the H_{gap} model is introduced in the BE coupling. This allows an uncertainty quantification for a REA with a good compromise between computational cost and physical modeling.

In this Chapter we apply these two methodologies on a large scale PWR core. The core and its modeling together with the initial state and characteristics of the reference transient are presented in Section 4.2. Since the REA modeling and its characteristics in the PWR core are different from the MiniCore, a preliminary static uncertainty quantification is performed in Section 4.4 in order to gain some basic insights. Quantities such as the multiplication factor and the control rod worth are studied. In the following Section 4.5 we apply the UQM on the APOLLO3 ® - FLICA4 BE coupling. The results are used in Section 4.6 to calibrate the H_{gap} models for different groups of fuel assemblies and creating thus an Improved Best Estimate (IBE) modeling. The UQM is then applied again on this modeling. Finally, in Section 4.7 we use the improved Best Estimate coupling to perform two uncertainty quantification studies. This time instead of focusing on the methodology we are mainly interested in the physical modeling options. In the first study we analyze the impact of a 3D thermal-hydraulics modeling instead of a multi-1D modeling where the thermal-hydraulic channels are considered as closed without transverse flows. In the second study, we analyze the impact of using finer thermal-hydraulic channels modeling.

4.2 REA modeling and description

4.2.1 Core design

The REA is studied in a large scale PWR core that was used in a previous work [46]. The geometry has an 1/8 symmetry presented in figure 4.1. It consists of 193 fuel assemblies with UO_2 and $UO_2 - GdO_3$ fuel compositions. Two different types of control rods are inserted at different depths. The black rods (B) with high neutrons absorption that are typically used for the shutdown of the reactor and the grey rods with less neutrons absorption that are used in the day to day reactivity control. The core is at HZP conditions at the end of the cycle as will described later. Around the fuel assemblies there is one ring of water reflector assemblies creating a total 17×17 lattice. The total height of the core is $468.72\,cm$ with a bottom and top reflector of $21\,cm$ leading to a fuel active height of $426.72\,cm$. Each assembly is a 17×17 lattice of fuel pins with pitch $21.504\,cm$. The control rod that will be ejected initiating the REA is located on the periphery as highlighted in figure 4.1. It is inserted $97\,cm$ from the top into the fuel active region as can be seen by the control rod cover rate. Due to the extraction of the control rod there is 1/2 symmetry for the REA. More details about the core can be found in [142]. This geometry will be used for all the studies of this Chapter.

Pin pitch (cm)	1.26
Assembly pitch (cm)	21.504
Active height (cm)	426.72
Full height (cm)	468.72
Control rod cover rate	$\frac{97}{426.72}$

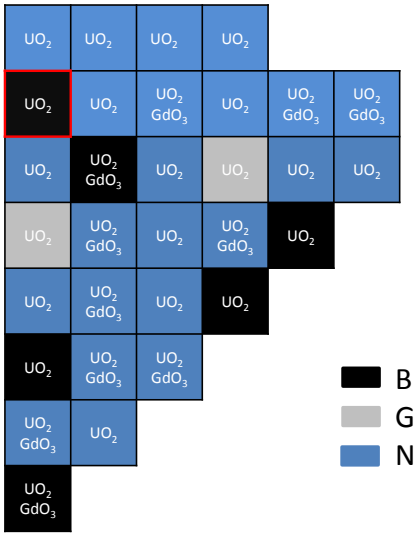

Figure 4.1: PWR 1/8 core geometry and characteristic dimensions. B indicates assemblies with black control rods, G with grey control rods and N with no control rods. The ejected control rod location is highlighted with red borders.

4.2.2 Modeling

The REA in the PWR core geometry is modeled using the BE modeling of the CORPUS coupling framework presented in Section 1.7. APOLLO3 ® for neutronics and FLICA4 for thermal-hydraulic are coupled as in the MiniCore case. The Best Effort modeling of the CORPUS framework including ALCYONE V1.4 for fuel-thermomechani is currently under development for this core and thus only the BE can be used for the UQM.

In APOLLO3 ® the same modeling options as in the MiniCore are selected. Two group Diffusion approximation (quations 1.21a and 1.21b) is used for energy and angle discretization with void boundary conditions on the neutron current. The radial discretization is at the level of the quarter of assembly creating 772 meshes. For the axial discretization 34 meshes are used of which 30 are for the fuel active height and the rest for the top and bottom reflector. This creates a total of 26248 meshes.

In FLICA4 the 4 equations porous modeling is used with a multi-1D axial flow approximation (Section 1.5.3). A system of 4 equation is solved (1.53a - 1.53d): mixture mass balance, vapor

mass balance, mixture momentum balance and mixture energy balance. The boundary conditions consist in determining the inlet mass flow and enthalpy and the outlet pressure. For the radial discretization one thermal-hydraulic channel is used for each assembly. In Section 4.7 an investigation of the radial discretization is performed by using one channel per quarter of assembly. For the axial discretization only the fuel active part is modeled using 30 meshes in accordance to APOLLO3 ® modeling. Both APOLLO3 ® and FLICA4 spatial discretizations are illustrated in figure 4.2. The fuel pin discretization in FLICA4 is finer than the one used for the MiniCore with 25 regions for the fuel part and 3 for the cladding. For the time discretization of the REA an adaptive end time is adopted based on the integral power evolution. For each transient when the power surpasses half its nominal value then a SCRAM signal is sent. It is considered that from this time on $0.6\,s$ are needed in order for the SCRAM to take place and end the modeling of the transient. The incremental time step is constant $0.001\,s$. The control rod is ejected in $0.1\,s$.

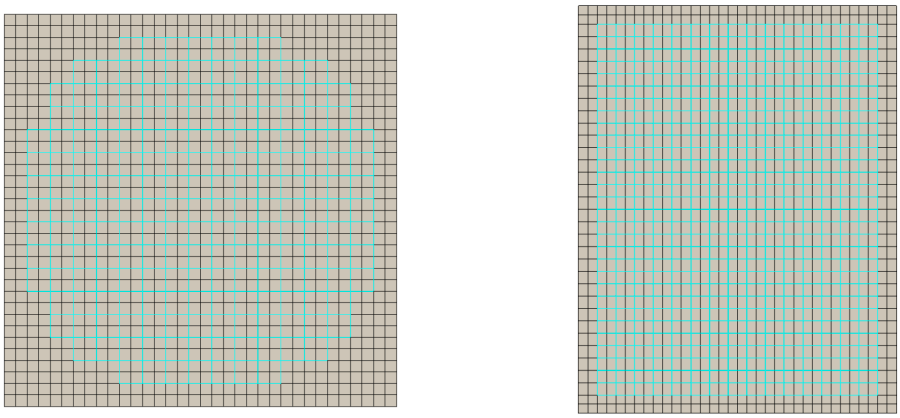

(a) Radial

(b) Axial

Figure 4.2: APOLLO3 ® radial and axial discretization with FLICA4 discretization superimposed (blue) for the PWR core.

The same two group macroscopic cross-sections as in the MiniCore are used parameterized in burn-up, boron concentration, moderator density and fuel temperature. The same material laws, power radial deformation function and thermal-hydraulics model options are used as well.

4.2.3 Initial state and reference transient

The PWR core is critical at the end of the cycle with Hot Zero Power (HZP) condition, meaning that the temperature is around $290°C$ and the power negligible ($3.8W$). There is a burn-up distribution resulting from core evolution calculation as described in [142]. The evolution is carried out by decoupled neutronic, fuel-thermomechanic, thermal-hydraulic modeling in 4 different steps:

1. Cycle evolution calculation using APOLLO3 ® with its internal multi-1D thermal-hydraulics model. This results in a burn-up distribution in the core.

2. Extraction of the linear power history for one average fuel pin for each fuel assembly. ALCYONE V1.4 evolution calculation using this linear power history. The results are the detailed thermomechanical and physico-chemical initial conditions of each fuel pin. These conditions will be used in the gap heat transfer model calibration in section 4.6.

3. FLICA4 static calculation in order to obtain the initial thermal-hydraulics conditions. Since the power is negligible there is no need of coupling with APOLLO3 ®.

4. Initiation of xenon oscillation transient with APOLLO3 ®. The ejected control rod is identified as the one with the highest control rod worth (figure 4.1). At the xenon oscillation instant leading to the highest control rod worth and thus the more violent prompt neutron driven REA.

The obtained radial burn-up distribution at the end of cycle is illustrated in figure 4.3. The burn-up averaged at the level of the assembly ranges from $10\,GWd/t$ to $52\,GWd/t$. The resulting

xenon spatial distribution for the initial state is illustrated in figure 4.4. We can see the radial distribution at the axial slice with the maximum xenon concentration and the axial profile at the assembly where the control rod is ejected.

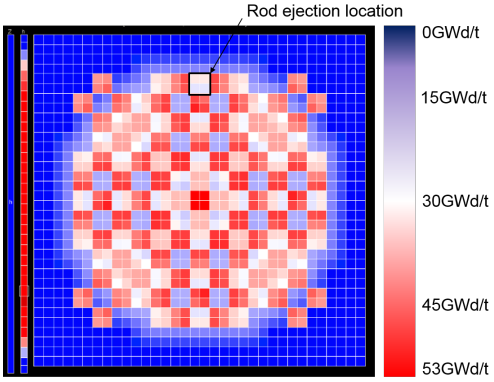

Figure 4.3: PWR core burn-up radial distribution in the core.

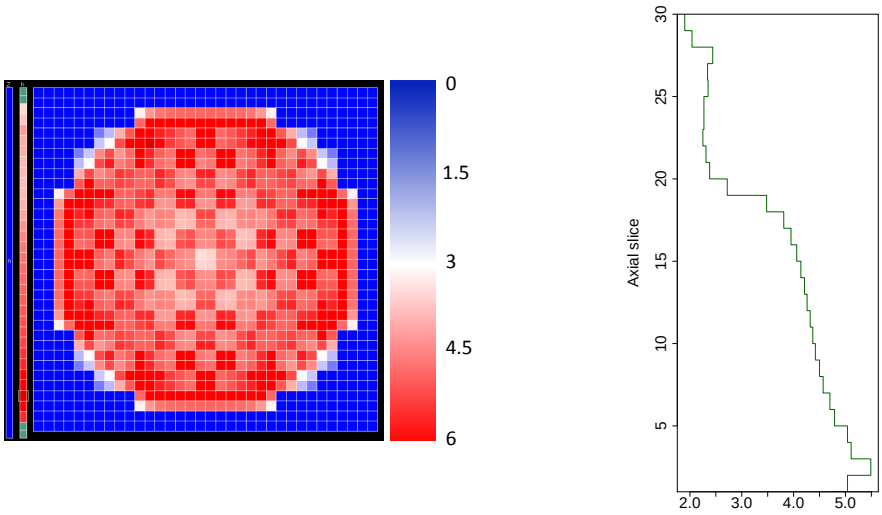

Figure 4.4: Xenon concentration in $10^{15}\,atoms/cm^3$ for the PWR core. The radial distribution (left) is at the axial slice with the maximum xenon concentration and the axial profile (right) is at the assembly where the control rod is ejected.

The core is critical at the initial state with negligible power distribution as can be seen in figure 4.5. In table 4.1 some of the core conditions are also described with same notation as in Section 3.2.3. The initial integral power is $3.8\,W$ and the fuel and moderator temperatures are $290°C$. Since the core is at the end of the cycle the boron concentration is quite low at $95.5\,ppm$. As used for the uncertainty studies in the MiniCore the boron concentration adjustment will be used to render the core critical since each input perturbation alters its initial critical state. This method was selected because it is the one that is the closest to the real operation of the core. However, in this PWR core the low initial boron concentration might not be enough for some cases. Fission production adjustment will be used in combination with boron adjustment in these cases.

Table 4.1: Characteristic conditions of the PWR core initial state.

Initial core power	$\mathbf{P_{core}^{init}}$ **(W)**	3.8
Moderator density	$\mathbf{D_{mod}}$ **(g/cm³)**	0.745
Pressure	**P (bar)**	155
Volumetric flow rate	**Q** (m^3/h)	90954
Fuel temperature	$\mathbf{T_f}$ **(°C)**	290
Moderator temperature	$\mathbf{T_m}$ **(°C)**	290
Boron concentration	$\mathbf{C_{bor}}$ **(ppm)**	95.5

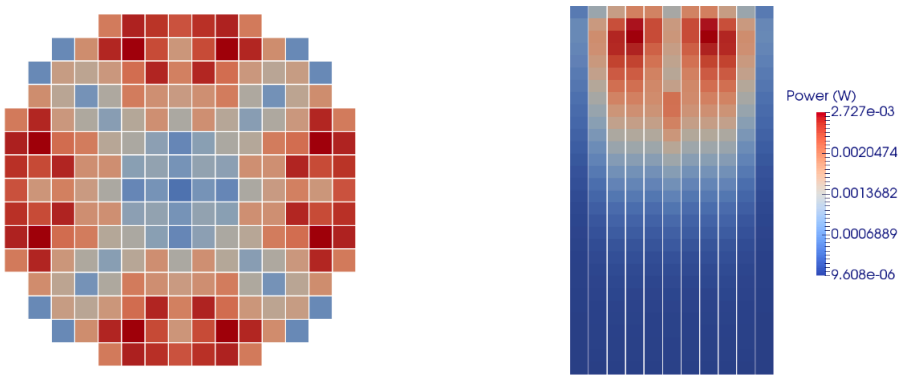

(a) (b)

Figure 4.5: Initial power distribution in the PWR core for the radial (a) and axial (b) cross-sections at the assembly where the control rod is ejected.

The reference (without uncertainties) REA characteristics obtained with an APOLLO3 ® - FLICA4 modeling are presented in table 4.2 and figure 4.6. The control rod worth is $\rho_{\text{worth}} = 1.2\,\$$ indicating a prompt driven transient. We observe a reduced margin to a $\rho_{\text{worth}} - \beta_{eff} < 0$ transition where the transient behavior changes sharply since it is mainly driven by the delayed neutrons. By applying the input uncertainties there is a non negligible probability to reach it. This effect will be studied in the preliminary static analysis of the section 4.4. In the figure on the right we can observe the created power pulse of width $\Gamma = 38\,ms$ with a maximum power of $P_{\text{core}}^{\text{max}} = 2.54P_{\text{nom}}$ at instant $t^{\text{max}} = 292\,ms$. Additionally, the F_{xyz} deformation factor evolution in time is plotted. It starts from a value of 5 and reaches up to 25 when the control rod is fully ejected $(0.1\,s)$.

Table 4.2: Characteristic quantities for the reference REA in the PWR core.

Effective delayed neutron fraction	β_{eff} **(pcm)**	569
Control rod worth	ρ_{worth} **(\$)**	1.2
Maximum core power	$\mathbf{P_{core}^{max}}$	$2.54P_{\text{nom}}$
Final core power	$\mathbf{P_{core}^{end}}$	$0.09P_{\text{nom}}$
Power pulse width	$\mathbf{\Gamma}$ **(ms)**	38
Time of maximum core power	$\mathbf{t^{max}}$ **(ms)**	292
Maximum $3D$ **deformation factor**	$\mathbf{F_{xyz}^{max}}$	25

If we compare with the MiniCore characteristics of table 3.2 we see that it is a less violent transient. This is attributed to the reduced leakage and to the more realistic xenon distribution. More realistic in the sense that its radial and axial distribution is issued from a xenon oscillations calculation with APOLLO3 ® in the PWR core. In the MiniCore we applied the same axial xenon distribution in all the fuel assemblies in order to obtain the most penalizing scenario in terms of ρ_{worth}.

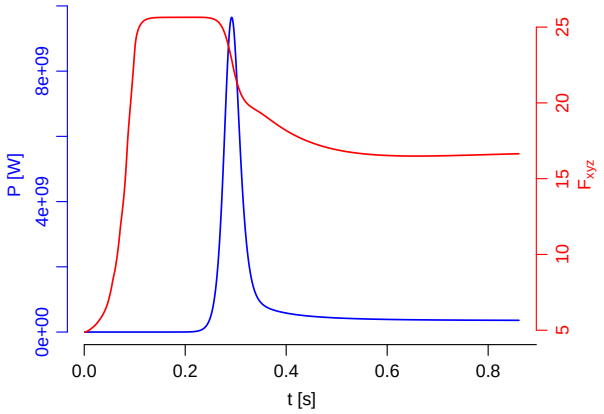

Figure 4.6: Integral power and F_{xyz} deformation factor evolution for the reference REA in the PWR core.

4.3 Input - Outputs uncertainties modeling

Different uncertainty quantification studies are performed on the PWR core. The identified uncertain inputs and outputs are based on the ones presented in Section 3.3.1. More precisely, all the inputs are considered except the power radial deformation due to difficulties in its implementation in the PWR core. The deformation is still modeled but it is not treated as uncertain. This is not expected to have any impact on the studies since from the MiniCore test its sensitivity was negligible. All the identified outputs in Section 3.3.1 are considered. This creates an initial input size of 21 and an output size of 3 scalars and 1 functional:

- **Inputs**: TD_1, TD_2, NF_1, NF_2, D_1, D_2, $S_{1\to2}$, IV_1, IV_2, β_{eff}, λ_{eff}, λ_f, λ_c, Cp_f, Cp_c, H_{gap}, T_R, H_c, R_{crit}, R_{v0}, H_{dnb}
- **Outputs**: P_{lin}^{max}, P_{lin}^{2D} (functional), H_f^{max}, DNB^{min}

These are the main outputs of interest for the application of the UQM in the PWR core. However, some case dependent outputs are also studied depending on the goal of each analysis. The inputs uncertainty quantification of Section 3.3.2 is used as well in all the studies of this Chapter.

4.4 Preliminary neutronics stand-alone static study

Before applying the UQM on the BE coupling for the REA it is important to study first the uncertain behavior of the initial static state. This will give us basic insight about the expected uncertain behavior of the REA. We saw that the reference ρ_{worth} is close to the β_{eff}. This study will allow to investigate if the limit of $\rho_{worth} - \beta_{eff} < 0$ is reached and with what probability. The only input parameters affecting the initial state are the two group macroscopic cross-sections. Static APOLLO3 ® stand-alone modeling is used since there is no impact of the other physics. The PWR core, as mentioned, is critical at HZP conditions. This means that for each cross-section perturbation the core has to be rendered critical. Similar to the MiniCore the boron concentration adjustment is used. The core is at the end of the cycle with low initial boron concentration thus there can be cases where it will not be enough. For these cases fission production adjustment is used by essentially dividing the fission production by the k_{eff}. For each cross-section perturbation a first static calculation computes the multiplication factor k_{eff}. The boron concentration C_{bor} is then adjusted in order to render the core critical and the k_{eff} is calculated. If it is not enough the fission production is divided by the current k_{eff}. Afterwards, a second static calculation is performed with the control rod extracted. The control rod worth ρ_{worth} is calculated together with the deformation factor when the control rod is ejected F_{xyz}^{ej}. The static neutronics equations as described in Section 1.3.3.4 are linear and thus linear models are used as surrogates for the different statistical analyses. The computational time needed for one code evaluation is 1 minute. The inputs, outputs and statistical tools used are the following:

- **Inputs:** TD_1, TD_2, NF_1, NF_2, D_1, D_2, $S_{1\to2}$.
- **Outputs:** k_{eff}, ρ_{worth}, C_{bor} and F_{xyz}^{ej}.
- **Statistical tools:**
  - **Surrogate models:** Linear.
  - **Uncertainty propagation:** Brute Monte Carlo using linear models for histogram empirical estimation.
  - **Global sensitivity analysis:** Shapley indices using linear models.

A LHS of size 100 is created in order to train the linear surrogate models for each output. The prediction error of each surrogate is estimated based on a second LHS of size 50. The result for the interpolation and prediction error are presented in table 4.3. Since the underlying equations are essentially linear, both interpolation and prediction errors are small. The largest prediction error is 2.42 % for C_{bor} and is attributed to the use of fission production adjustment in some few cases in conjunction with C_{bor}.

Table 4.3: Linear model interpolation and prediction errors for neutronics stand-alone static study in PWR core.

	Linear	
	$\boldsymbol{\varepsilon_{int}}$ (%)	$\boldsymbol{\varepsilon_{pred}}$ (%)
k_{eff}	$9.37e^{-3}$	$8.69e^{-3}$
ρ_{worth}	$2.82e^{-2}$	$6.21e^{-2}$
C_{bor}	1.04	2.42
F_{xyz}^{ej}	$5.60e^{-2}$	$4.68e^{-2}$

The linear models are used to propagate the uncertainties to the outputs and estimate empirically their histograms. Brute Monte Carlo with $1e^5$ samples is used and the results are presented in figure 4.7.

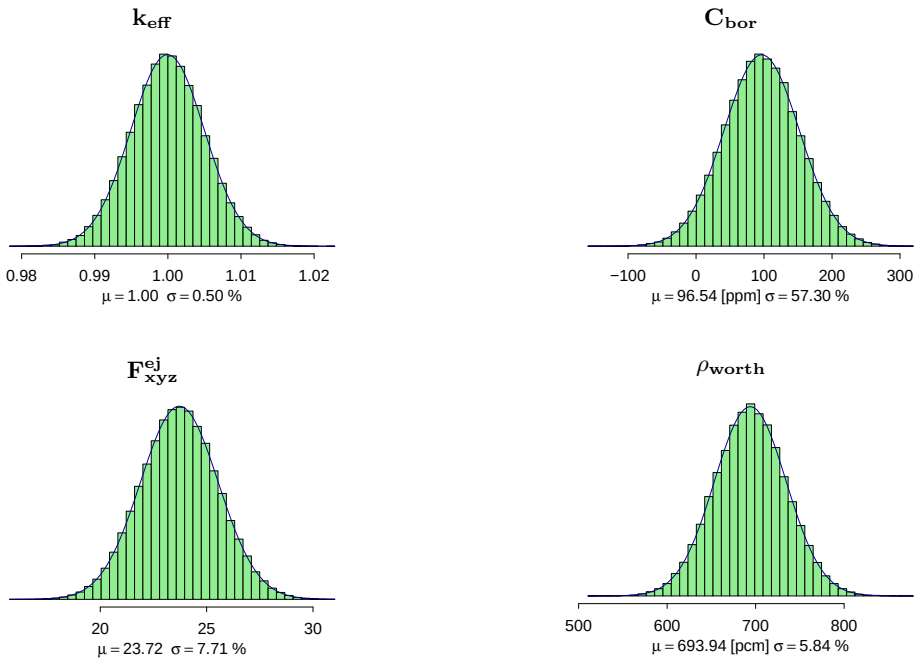

Figure 4.7: k_{eff}, C_{bor}, F_{xyz}^{ej} and ρ_{worth} estimated histograms for neutronics stand-alone static study in PWR core.

We can see the obtained histograms together with the estimated first two moments. We observe that since the inputs are multivariate normal and the underlying function is linear then all the outputs have also a normal pdf. The k_{eff} shows a relative standard deviation of 0.5 % or 500 pcm while for the C_{bor} is much larger at 57.30 %. The predicted negative values correspond to the fission production adjustment cases and occur with a probability of 4 %. From the standard deviation of k_{eff} and C_{bor} the differential efficiency of the boron concentration adjustment is found to be 9 pcm/ppm. For F_{xyz} the relative standard deviation is around 8 % and for ρ_{worth} is 6% which represents a significant increase compared to the MiniCore. The results for the ρ_{worth} in combination with the β_{eff} relative deviation of 8% around its mean value of 570 pcm show that there is a non negligible probability of reaching the delayed neutron driven REA limit.

For the quantification of the outputs sensitivity to each input Shapley indices are estimated using the linear models. The results are presented in figure 4.8. We see two different types of sensitivities. For k_{eff} and C_{bor} the most important input is NF_2 accounting for almost 50% of their variations. This can be understood by the fact that both of these quantities are strongly related to each other and depend on the fission production. For F^{ej}_{xyz} and ρ_{worth} almost 90% of their variations are explained by TD_1, D_1 and $S_{1\to2}$. This means that the neutrons absorption and diffusion are the dominant phenomena.

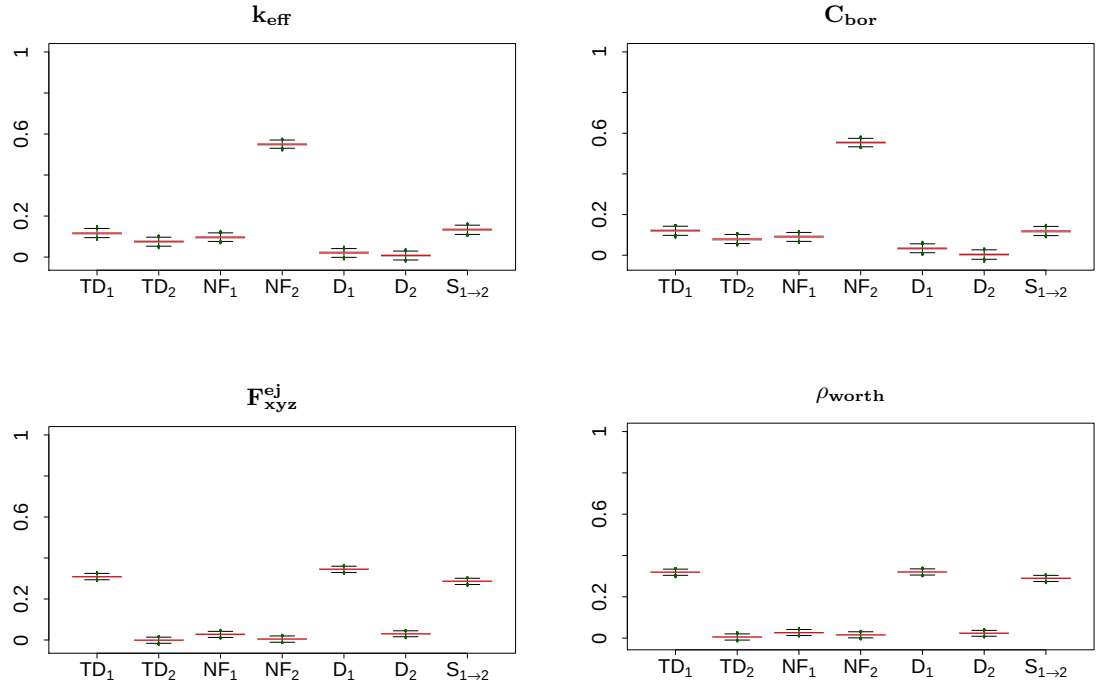

Figure 4.8: k_{eff}, C_{bor}, F^{ej}_{xyz} and ρ_{worth} Shapley indices for neutronics stand-alone static study in PWR core.

The most important results for this study is the fact that delayed neutron driven REA can occur with non negligible probability. The design points that lead to these transients are not important since they are less violent transients and thus out of interest. This motivates us to construct a predictive linear model that will estimate which input design points lead to $\rho_{worth} - \beta_{eff} < 0$. The identified input evaluations are rejected resulting in gain in computational cost. This will create holes in the Design of Experiments (DOE) reducing the surrogate models predictive capabilities in these regions. Since these regions are of low interest this is not a problem for the application of the UQM.

The predictive linear model is constructed between (TD_1, TD_2, NF_1, NF_2, D_1, D_2, $S_{1\to2}$, β_{eff}) and ($\rho_{worth} - \beta_{eff}$). The result is visualized in figure 4.9 for the two main independent dimensions of the inputs. The first is a linear combination of mainly TD_1, D_1 and $S_{1\to2}$ something expected by the corresponding Shapley indices in figure 4.8. The second one is the β_{eff} due to its explicit presence in the output definition and its independence with respect to the macroscopic cross-

sections. We can see the linear hyperplane and the different design points to be evaluated by the code. The points crossing the horizontal hyperplane at 0 are the ones in red and are rejected. The linear model results in very small prediction error, less than 0.1% and thus can be used with strong confidence. Using this linear model the probability of rejecting a design point can be calculated analytically and amounts to 2.25%. In the studied learning sample we see in figure 4.9 that 2 out of 100 design points are rejected. Since the $\rho_{worth} - \beta_{eff} < 0$ does not depend on inputs of the other physics this model can be used in all the following multi-physics coupled studies. For each DOE prior to code evaluations the predicted design points by the linear model will be rejected. The different statistical methods will be applied on this modified DOE.

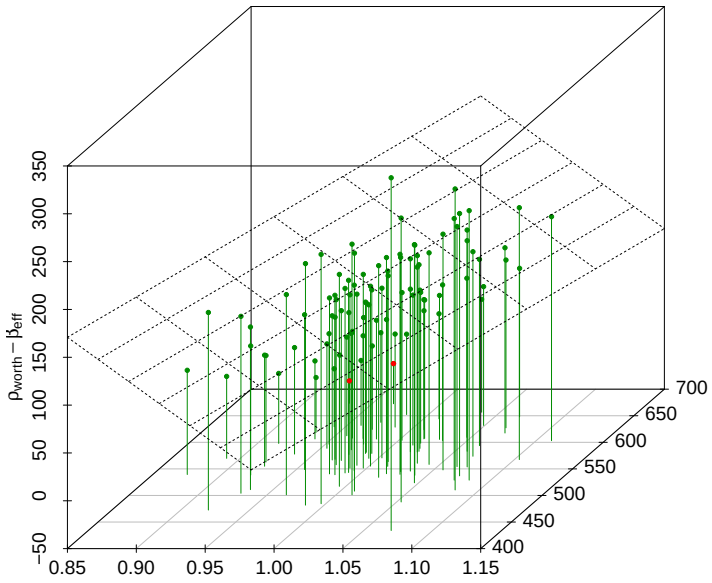

Figure 4.9: Linear model for $\rho_{worth} - \beta_{eff} < 0$ prediction in the PWR core. The red points are rejected from the DOE.

4.5 UQM application for BE coupling

In Section 3.5 we developed a four step UQM and tested it on the MiniCore. In this section we apply it on the PWR core for the identified inputs and outputs of section 4.3. The H_{gap} in this study is considered uniform as described in Section 3.5. The BE modeling is used with coupling of APOLLO3 ® - FLICA4. The computational cost of this modeling is 3 hours in average since the end time is adapted for each sampling.

The first step of the UQM consist in identifying important input subspaces using statistical significance tests based on HSIC indices. It is the IDRM process described in Section 3.5.2. A random sampling of size 125 is used as DOE for this step. The result for the identified subspaces are gathered in table 4.4 and can be grouped in two: $I_1 = (TD_1,\ NF_2,\ D_1, S_{1\to2}, IV_1, IV_2,\ \beta_{eff}, Cp_f\ H_{gap},\ T_R)$ and $I_2 = (TD_1,\ NF_2,\ D_1, S_{1\to2}, IV_1,\ \beta_{eff},\ H_{gap},\ H_c)$.

Table 4.4: UQM step 1 results for BE coupling study in the PWR core.

	Selected inputs
$\mathbf{P_{lin}^{max}}$	TD_1, NF_2, D_1,$S_{1\to2}$, β_{eff}, H_{gap}
$\mathbf{P_{lin,pc1}^{2D}}$	TD_1, NF_2, D_1,$S_{1\to2}$, β_{eff}, H_{gap}
$\mathbf{P_{lin,pc2}^{2D}}$	TD_1, NF_2, D_1,$S_{1\to2}$, β_{eff}, H_{gap}
$\mathbf{H_f^{max}}$	TD_1, NF_2, D_1, β_{eff}, Cp_f, H_{gap},T_R
$\mathbf{DNB^{min}}$	TD_1, NF_2, D_1,$S_{1\to2}$,IV_1, β_{eff}, H_{gap}, H_c

The second step of the UQM is the training of the kriging models for each output on LHS optimized in both the complete input space and the important subspaces as described in Section 3.5.3. A learning LHS of size 250 with optimized subspaces I_1 and I_2 is constructed for the training of the kriging models. The kriging models are trained on the identified input subspaces. The resulting prediction errors include the dimension reduction error. The interpolation, leave-one-out and prediction error are presented in table 4.5. The prediction error is estimated on an independent LHS of size 125. For all the outputs the prediction errors are small with larger errors for DNB^{min} (2%) and the second principal component of P_{lin}^{2D} (5.5%).

Table 4.5: UQM step 2 results for BE coupling study in the PWR core.

	ϵ_{int} (%)	ϵ_{loo} (%)	ϵ_{pred} (%)
$\mathbf{P_{lin}^{max}}$	0.00	$1.15e^{-1}$	$1.35e^{-1}$
$\mathbf{P_{lin,pc1}^{2D}}$	0.00	1.16^{-1}	$1.01e^{-1}$
$\mathbf{P_{lin,pc2}^{2D}}$	0.00	$6.16e^{-1}$	5.53
$\mathbf{H_f^{max}}$	0.00	$1.62e^{-1}$	$4.58e^{-1}$
$\mathbf{DNB^{min}}$	0.00	2.10	1.89

In the third step of the UQM the kriging models are used to propagate the uncertainties to the outputs and estimate empirically their histograms. Brute force Monte Carlo is used with $1e^5$ samples and the results are presented in figure 4.10. We observe quite larger relative standard deviation for P_{lin}^{max} of around 57 % compared to the MiniCore case. The result for P_{lin}^{2D} shows that the relative standard deviation distribution does not vary radially. For H_f^{max} a 20 % relative standard deviation is obtained with a normal distribution. For DNB^{min} a large mean value is obtained with large relative standard deviation of 57 % resulting in a very small probability of reaching boiling crisis.

The fourth and final step of the UQM is the global sensitivity analysis. Shapley indices are estimated for the scalar outputs and aggregate Shapley indices for the functional ones as defined in Chapter 2. The results are presented in figure 4.11. For P_{lin}^{max}, P_{lin}^{2D} and H_f^{max} the β_{eff} is responsible for 50% of the outputs variance with the other 50% attributed to the cross-sections TD_1, D_1, $S_{1\to2}$ and IV_1. All these cross-sections are highly correlated to each other and thus it is difficult to distinguish their separate contributions. This increased sensitivity of the cross-section compared to the MiniCore explains also the increased variance of P_{lin}^{max}. For the DNB^{min} the H_{gap} is the dominant input responsible for 50% of the outputs variation while the remaining 50% is attributed to the cross-sections and the β_{eff}. This is due to its large uncertainty ranges and thus gives an incentive to improve its modeling. The application of the methodology for the calibration of a simplified H_{gap} model and its introduction in the current BE modeling is the topic of the Section 4.6.

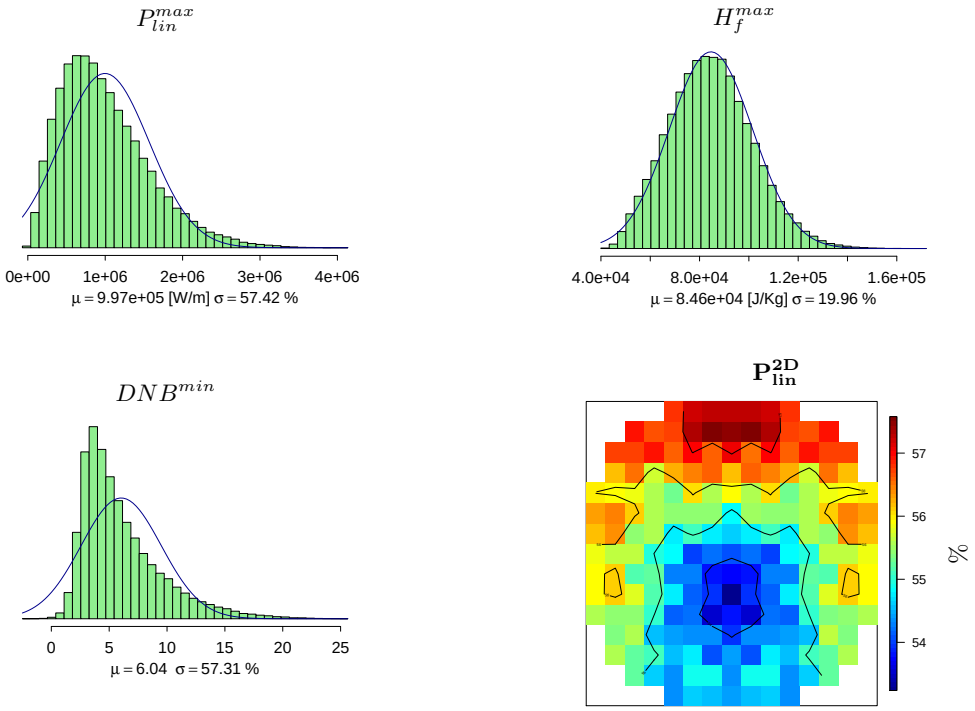

Figure 4.10: P_{lin}^{max}, H_f^{max} and DNB^{min} histograms and P_{lin}^{2D} relative standard deviation distribution for BE coupling study in the PWR core.

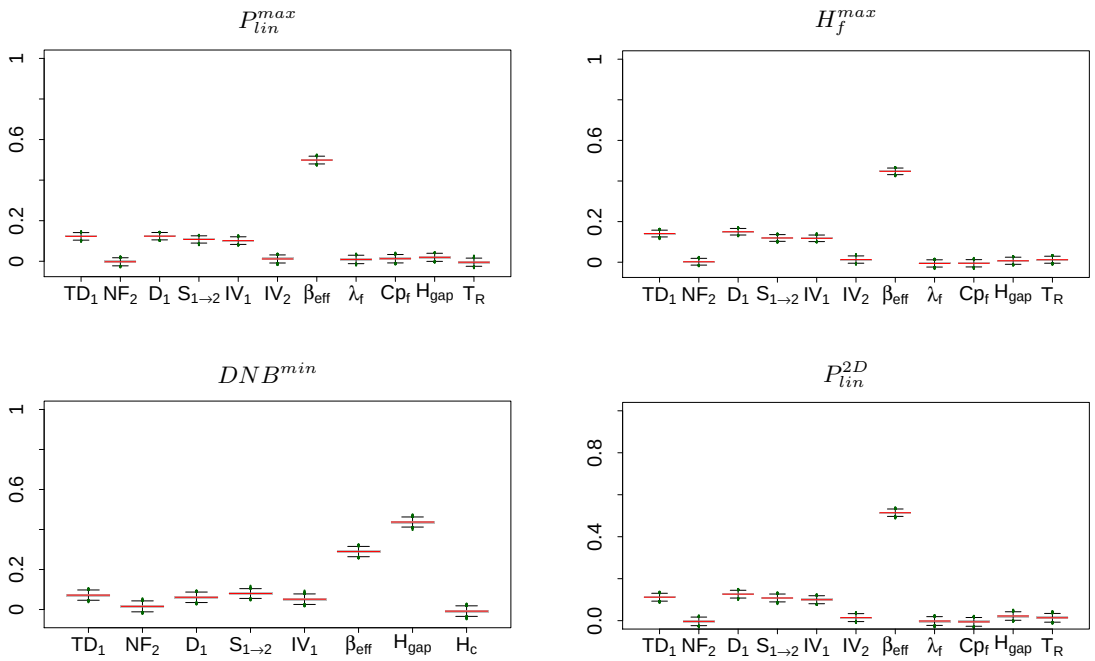

Figure 4.11: P_{lin}^{max}, H_f^{max} and DNB^{min} Shapley indices and P_{lin}^{2D} aggregate Shapley indices for BE coupling study in the PWR core.

4.6 IBE coupling taking into account simplified fuel-thermomechanics

4.6.1 Application of gap heat transfer calibration methodology

The Best Effort APOLLO3 ® - FLICA4 - ALCYONE V1.4 is not available for the PWR core and even if it was available the computational cost for the application of UQM would be prohibitive. As we observed in the study of Section 4.5 the BE APOLLO3 ® - FLICA4 coupling models quite

poorly the H_{gap} using a constant value with large ranges of variations. We saw that this has a significant impact on the DNB^{min}.

In Section 3.6 we developed and tested a methodology for the calibration of a simplified H_{gap} model on the MiniCore. We remind that the model is based on thermal expansions and includes two calibration parameters θ_1 and θ_2. The first one is related to the fuel temperature variations governing the thermal expansions. The second one is related to the energy deposed in the fuel and thus accounts for a historical effect. The methodology for the calibration of this model is based on decoupled ALCYONE V1.4 calculations and includes different steps. In this study we apply the complete methodology illustrated in figure 3.30 on the PWR core.

The initial preliminary step 0 consists in performing a multi-physics BE REA uncertainty analysis. To this purpose we consider the study of Section 4.5 where the UQM was applied on the PWR core using the BE APOLLO3 ® - FLICA4 coupling. Steps 1.1 and 1.2 consist in identifying the imposed boundary conditions in ALCYON3 V1.4. These boundary conditions are the axial and temporal evolution of the linear power and the cladding wall temperature and should cover most of the possible evolutions of the H_{gap}. There are both spatial variations due to the burn-up distribution in the core and random variations due to the inputs uncertainties.

The first step 1.1 consist in clustering assemblies with similar burn-ups in groups for which one H_{gap} model will be considered. In the MiniCore case this was straightforward since there where only three discrete values of burn-up. In the PWR core this is more complex since there is a $3D$ burn-up distribution. This leads to a total of $193 \times 4 \times 30/2 = 11580$ meshes (due to symmetry) with different H_{gap} evolutions due to different burn-ups and power histories. In order to avoid constructing one H_{gap} model for each mesh the grouping of the assemblies of different burn-ups is carried out. At first we consider only radial burn-ups, by averaging the axial variations. Thus decreases the different burn-ups to 772. Secondly, we observe that the burn-ups have radially small variations around three main values $15GWd/t$, $30GWd/t$ and $45GWd/t$ due to the PWR fuel loading pattern. We select thus to group the assemblies based on these three values and we add one group for the minimum $10GWd/t$ and maximum burn-up $52GWd/t$. This is done in order to have models covering all the burn-up variations. Additionally, it could be potentially used in the future for an application of the full $3D$ burn-up distribution by constructing models that interpolate the calibration parameters.

To recapitulate we consider a total of 5 fuel assembly groups and for each group a H_{gap} model will be constructed. We have to select for each group representative boundary conditions that vary both randomly and spatially since each group includes different assemblies. This is performed in step 1.2. The selected boundary conditions are presented in figure 4.12. We know that the REA is a local phenomenon located in the upper part of the core around the ejected control rod position as seen in the radial cross-section of the figure. We thus expect large variations of H_{gap} on the upper part and low to negligible variations in the lower part. For the random aspects we use from the results of step 0. More specifically, we consider that P_{lin}^{max} gives a good indicator of H_{gap} variations in REA. Based on this we select samples corresponding to the mean, the upper and lower 95% quantile of P_{lin}^{max}. From these samples we extract the linear power and cladding wall temperature axial and temporal evolutions. We combine both random and spatial aspects by selecting representative assemblies at the upper part for the mean and upper quantile while we select their mirror assemblies from the lower part. The selected assemblies are presented in 4.12 where each assembly has the burn-up value of its group. The green circles correspond to the selection for the mean and upper quantile while the yellow circles for the lower quantile. For the $10GWd/t$ and $52GWd/t$ groups there is only one possible assembly for each group. For the other groups from the many available options we prefer the assemblies close to the ejected control rod location. For $15GWd/t$ and $30GWd/t$ group we select two different assemblies while for the $45GWd/t$ we select three, since we consider that this group will have the largest H_{gap} variations due to its high burn-up.

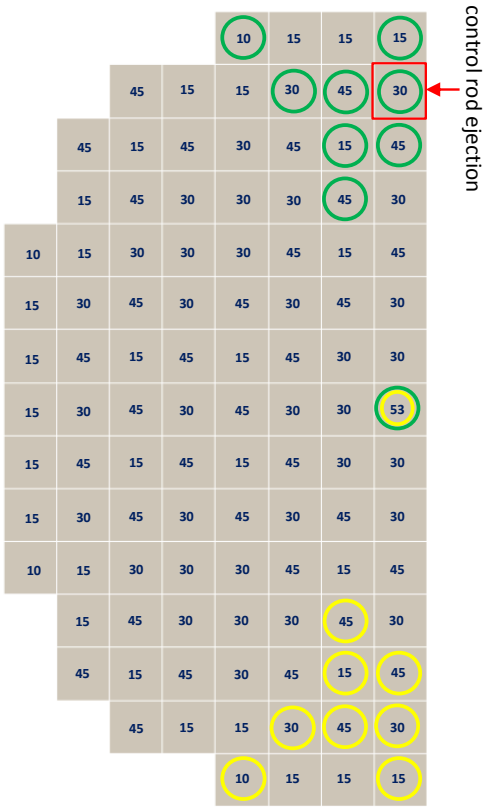

Figure 4.12: Selected assemblies on the symmetric 1/2 PWR geometry for each H_{gap} model group. The green circles indicate the selection of the mean and upper quantile and the yellow indicates the selection for the lower quantile

In step 2 the extracted boundary conditions are imposed in ALCYONE V1.4 and the REA stand-alone calculations are performed for each group. A representative fuel pin for each selected assembly in each sampling is modeled with the same axial discretization as the BE modeling. The H_{gap} and radial temperatures axial and temporal evolution during the REA are computed. These results together with the stored fuel energy are extracted and used for the H_{gap} model calibration of each group. Only the values corresponding to the time of the maximum and last value of H_{gap} during the REA for all the axial slices are kept for the calibration as in the MiniCore. The created dataset size varies for the different groups depending on the number of representative assemblies. For $10GWd/t$ and $52GWd/t$ groups the size is: 30(axial slices) $\times$ 3(samples) $\times$ 1 (assemblies) $\times$ 2 ($Hgap$ values) = 180. For $15GWd/t$ and $30GWd/t$ groups the size is: $30 \times 3 \times 2 \times 2 = 360$. For $45GWd/t$ group the size is: $30 \times 3 \times 3 \times 2 = 540$. The calibration parameters are optimized by minimizing the mean square error on these datasets. The resulting calibration errors for the three different models are presented in figure 4.13 and the estimated calibration parameters in table 4.6. As in the MiniCore, we observe that the calibration errors increase in general with burn-up. For the $52GWd/t$ this is not the case because its far from the REA location and thus the corresponding variations are very small.

Table 4.6: H_{gap} model calibration parameters for the PWR core

	10	**15**	**30**	**45**	**52**
$\boldsymbol{\theta_1}$	$2.9e^{-1}$	$1.7e^{-1}$	$-1.7e^{-2}$	$-7.3e^{-1}$	$-2.4e^{-1}$
$\boldsymbol{\theta_2}$ $[J^{-1}]$	$6.0e^{-6}$	$1.1e^{-5}$	$1.6e^{-5}$	$2.0e^{-5}$	$4.4e^{-6}$

For the uncertainty quantification of the calibration parameters θ_1, θ_2 we adopt the same process as for the MiniCore in Section 3.6.4. We make the assumption that they are positively fully correlated, which makes it possible to simplify significantly their uncertainty quantification. Additionally, as for all the other inputs they are also fully correlated spatially. This means that the calibration

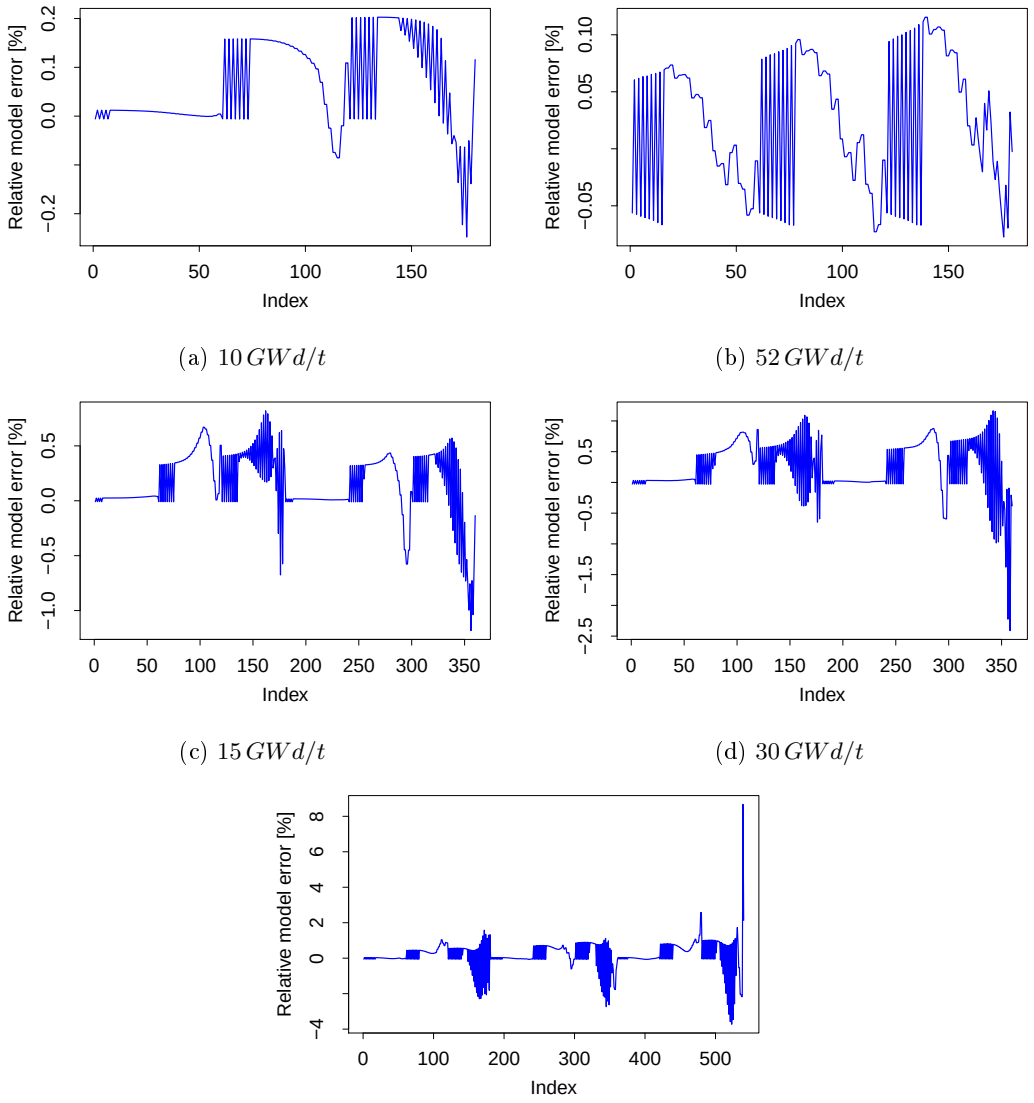

(a) $10\,GWd/t$

(b) $52\,GWd/t$

(c) $15\,GWd/t$

(d) $30\,GWd/t$

(e) $45\,GWd/t$

Figure 4.13: H_{gap} model calibration errors for the different assembly groups of the PWR core.

parameters of each group vary homogeneously. We attribute uniform pdf to each calibration parameter with ranges that cover the calibration errors. The results for the estimated ranges for each parameter are shown in table 4.7. The maximum error is of the order of 8 % for the $45GWd/t$ group. For the $45GWd/t$ group is 2.5, % and for the other groups is less than 1 %.

Table 4.7: H_{gap} model calibration parameters pdf estimation for the PWR core

	10	**15**	**30**	**45**	**52**
$\boldsymbol{\theta_1}$	$\mathcal{U}(2.4e^{-1}, 3.4e^{-1})$	$\mathcal{U}(1.4e^{-1}, 2.0e^{-1})$	$\mathcal{U}(-1.7e^{-1}, 1.3e^{-1})$	$\mathcal{U}(-1.3, -1.8e^{-1})$	$\mathcal{U}(-4.4e^{-1}, -4.0e^{-2})$
$\boldsymbol{\theta_2}$ $[J^{-1}]$	$\mathcal{U}(5.8e^{-6}, 6.3e^{-6})$	$\mathcal{U}(8e^{-6}, 1.4e^{-5})$	$\mathcal{U}(1.3e^{-5}, 1.8e^{-5})$	$\mathcal{U}(1.6e^{-5}, 2.4e^{-5})$	$\mathcal{U}(2.4e^{-6}, 6.4e^{-6})$

The pdf bounds are used for the prediction of the H_{gap} temporal evolution by the calibrated models. The results are compare to the ALCYONE V1.4 calculation and are illustrated in figures 4.14-4.16. For the comparison the axial slice with the maximum H_{gap} value for the three main groups is presented. The main groups are the $15GWd/t$, $30GWd/t$ and $45GWd/t$ since they are the groups closer to the REA location. The plotted H_{gap} predictions are also the ones with the largest errors and we can see that, as in the MiniCore, for all the predictions the ALCYONE V1.4

calculation is inside the uncertainty bounds created by the uncertain calibration parameters.

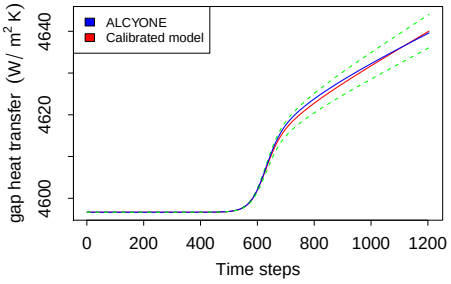

(a) Lower 95% Quantile

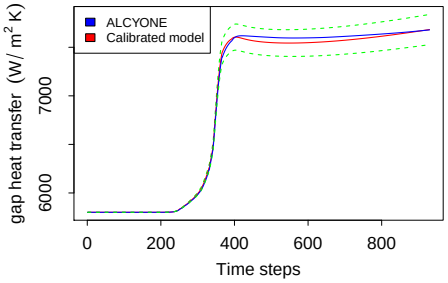

(b) Mean

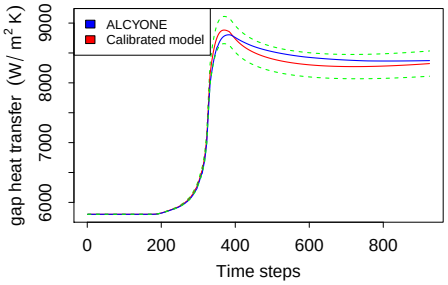

(c) Upper 95% Quantile

Figure 4.14: PWR core $15GWd/t$ group calibration results including the uncertainty bounds (green).

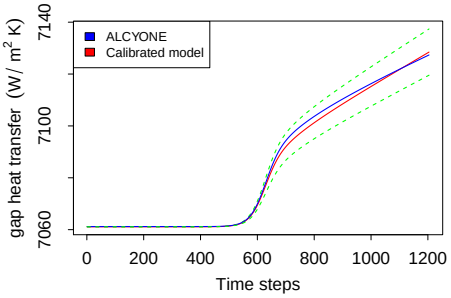

(a) Lower 95% Quantile

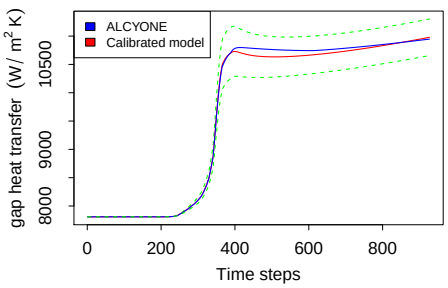

(b) Mean

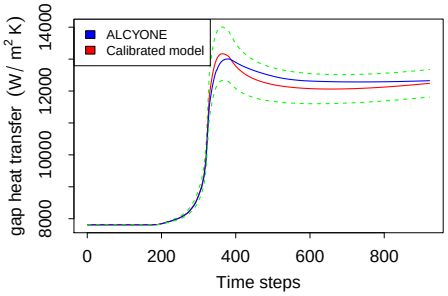

(c) Upper 95% Quantile

Figure 4.15: PWR core $30GWd/t$ group calibration results including the uncertainty bounds (green).

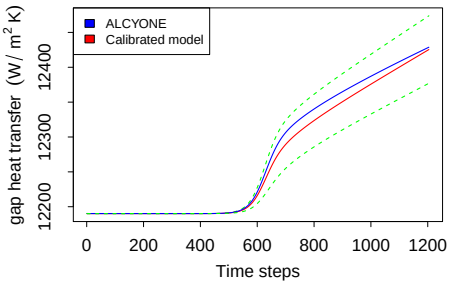

(a) Lower 95% Quantile

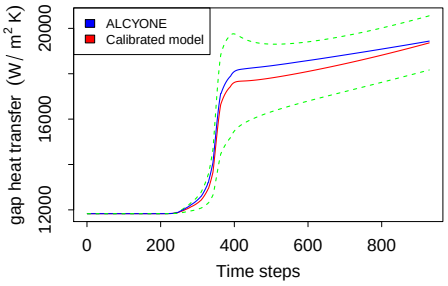

(b) Mean

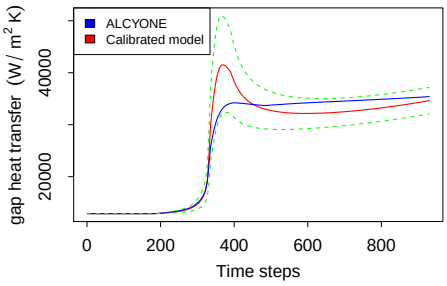

(c) Upper 95% Quantile

Figure 4.16: PWR core $45GWd/t$ group calibration results including the uncertainty bounds (green).

There are two different sources of uncertainties for the models. The first one is due to the calibration error and is quantified by the calibration parameters pdf. The parameters are assumed fully positively correlated. The second one is due to the initial conditions. Similar to the MiniCore case, a multiplication coefficient is used on the initial H_{gap} and pellet-cladding gap width with normal pdf and 10 % relative standard deviation $\mathcal{N}(1.0, 0.1)$. The results of an uncertainty propagation on fuel-thermomechanics evolution calculations with ALCYONE V1.4 showed that the two initial conditions are strongly (> 0.9) negatively correlated. We make thus the simplification assumption by considering them fully negatively correlated.

At the end, two new uncertain parameters replace the constant H_{gap} of the BE modeling. The one is related to the calibration error of the models $H_{g,m}$ and the other is related to the initial conditions $H_{g,i}$. In the following study of Section 4.6.2 the calibrated models together with their uncertainty quantification are introduced in the APOLLO3 ® - FLICA4 coupling without increasing the computational cost. This creates an Improved Best Estimate (IBE) modeling. The UQM is then applied again on this new modeling.

4.6.2 UQM application on IBE coupling

The calibrated H_{gap} models from Section 4.6.1 are introduced in the BE coupling to create an intermediate IBE multi-physics coupling. The complete UQM is applied on this improved modeling. It is important to mention that the computational cost does not increase. The uncertain inputs and outputs of Section 4.3 are used with the replacement of the constant H_{gap} uncertain input by the H_{gap} models uncertainties. The two new uncertain inputs are $H_{g,m}$ and $H_{g,i}$ related to the H_{gap} models calibration error and initial conditions. We remind that it is an explicit coupling with $0.001s$ incremental time step for adaptive total REA duration. The computational cost of this modeling is 3 hours.

For the step 1 of the UQM a random sampling of size 125 is used as DOE for the input dimension reduction. The result for the identified subspaces are gathered in table 4.8 and can be grouped in two: $I_1 = (TD_1,\ NF_2,\ D_1,\ \beta_{eff},\ Cp_f, H_{g,i},\ T_R)$ and $I_2 = (TD_1,\ NF_2,\ D_1,\ \beta_{eff},\ H_{g,i},\ H_c,\ R_{crit},\ T_R)$.

Table 4.8: UQM step 1 results for IBE on PWR core

	Selected inputs
$\mathbf{P_{lin}^{max}}$	TD_1, NF_2, D_1, β_{eff}, T_R
$\mathbf{P_{lin,pc1}^{2D}}$	TD_1, NF_2, D_1, β_{eff}, T_R
$\mathbf{P_{lin,pc2}^{2D}}$	TD_1, D_1, β_{eff}
$\mathbf{H_f^{max}}$	TD_1, NF_2, D_1, β_{eff}, Cp_f,$H_{g,i}$, T_R
$\mathbf{DNB^{min}}$	TD_1, NF_2, D_1, β_{eff}, $H_{g,i}$, H_c, R_{crit}, T_R

Compared to Section 4.5 we observe the inclusion of the $H_{g,i}$ in both subspaces while the $H_{g,m}$ is rejected. This means that for the outputs of interest the initial conditions are more important than the calibration parameters uncertainties. In step 2 of the UQM a learning LHS of size 250 with optimized subspaces I_1 and I_2 is constructed for the training of the kriging models. The result for the interpolation, leave-one-out and prediction error are presented in table 4.9. The prediction error is estimated on a second LHS of size 125. For all the outputs the prediction errors are small with larger errors for DNB^{min} (1.3%) and the second principal component of P_{lin}^{2D} (5.5%).

Table 4.9: UQM step2 results for IBE on PWR core

	ϵ_{int} (%)	ϵ_{loo} (%)	ϵ_{pred} (%)
$\mathbf{P_{lin}^{max}}$	0.00	$4.921.15e^{-1}$	$4.82e^{-1}$
$\mathbf{P_{lin,pc1}^{2D}}$	0.00	16.1^{-1}	$1.01e^{-1}$
$\mathbf{P_{lin,pc2}^{2D}}$	0.00	$6.16e^{-1}$	5.53
$\mathbf{H_f^{max}}$	0.00	$8.45e^{-1}$	$8.36e^{-1}$
$\mathbf{DNB^{min}}$	0.00	1.38	1.28

In step 3 of the UQM brute force Monte Carlo is used for uncertainty propagation with $1e^5$ samples for each output. The results are presented in figure 4.17. The obtained histogram for H_f^{max} is normal as for the UQM application with APOLLO3 ® - FLICA4. We observe small increase of 2 % in the mean value and a reduced relative standard deviation from 20 % to 16 %. For P_{lin}^{max} the mean value decreased significantly by 10 % with similar relative standard deviation. Concerning the relative standard deviation of P_{lin}^{2D} it is not affected by the improved H_{gap}. The quantity most impacted is the DNB^{min} with a an increase of 14 % for the mean value and a decrease of the relative standard deviation from 57 % to 42 %. This means that there is smaller probability to reach boiling crisis.

The impact on the different mean values is attributed to the more realistic modeling of the H_{gap} evolution during the REA. In the BE modeling the mean constant value of H_{gap} is $2.4e^4 W/m^2K$ much higher than the one predicted by the calibrated models and it is applied during the whole duration of the transient. This leads to a higher heat extracted from the fuel by the coolant. The fuel temperatures are lower with a corresponding weaker Doppler feedback and thus a higher maximum linear power. The increased heat extracted from the coolant in the BE modeling explains also the smaller minimum distance to boiling crisis compared to the IBE modeling. The lower fuel temperatures induce also the observed lower stored enthalpy.

The final step 4 of the UQM is performed and the Shapley indices are estimated for all the outputs. The results are presented in figure 4.18. For P_{lin}^{max}, P_{lin}^{2D} and H_f^{max} as in the BE modeling the β_{eff} is responsible for around 50% of the outputs variance and the TD_1 and D_1 are responsible for the remaining 50%. A significant difference in observed for the DNB^{min} sensitivities. The gap heat transfer is not any more the dominant input, instead as for the other outputs the β_{eff} and the TD_1 and D_1 account for most of the DNB^{min} variations. This explains also the significant reduction of the DNB^{min} relative standard deviation.

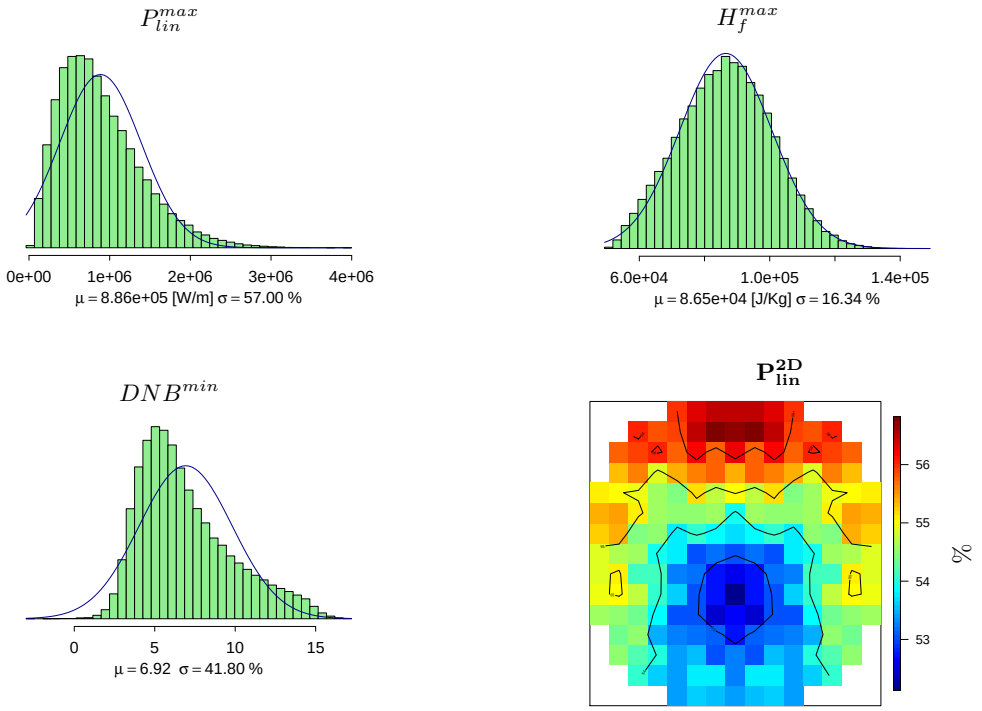

Figure 4.17: P_{lin}^{max}, H_f^{max} and DNB^{min} histograms and P_{lin}^{2D} relative standard deviation distribution for multi-physics IBE coupling study in PWR core.

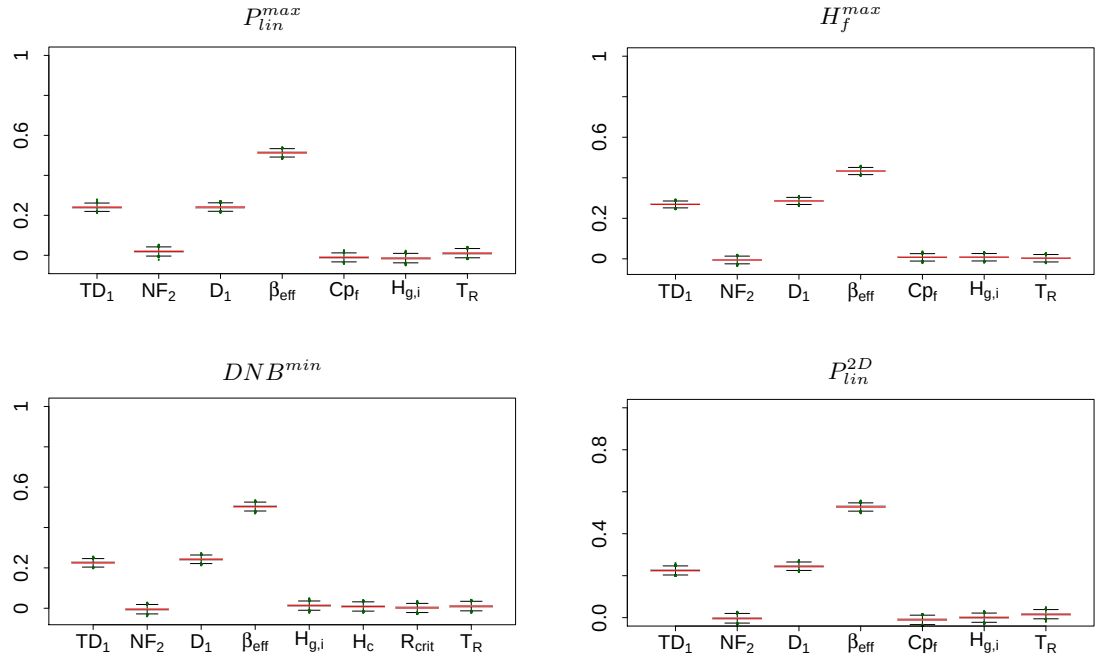

Figure 4.18: P_{lin}^{max}, H_f^{max} and DNB^{min} Shapley indices and P_{lin}^{2D} aggregate Shapley indices for multi-physics IBE coupling study in PWR core.

4.7 Complementary physical studies on the IBE modeling

4.7.1 Introduction

In this final Section we shift our focus from the uncertainty quantification to the physical modeling aspects. We study a large variety of outputs up to 3D fields in order to extract the maximum information. The effect of different modeling choices is compared. Three physical modelings are

compared with increasing computational cost:

1. The previously studied IBE modeling.
2. An IBE modeling with 3D thermal-hydraulics in order to investigate the impact of the transverse flows .
3. An IBE modeling using 3D thermal-hydraulic channels at the level of quarter of assembly in order to study the impact of the finer termal-hydraulic discretization.

The identified outputs for this study are the ones used in the UQM together with some quantities that are relevant to the transient modeling (e.g. exchanged quantities). The latter one are studied as 3D fields on a particular instant, usually where the maximum during REA is located. For all these outputs we perform uncertainty propagation and sensitivity analysis. The $3D$ functional quantities are treated using PCA representing 95% of the variance. Kriging models are constructed to approximate the underlying function between the inputs and the first principal components. For complex $3D$ fields the kriging models prediction error for the higher order principal components can become very large. In these cases the PCA representation variance will be decreased to 85% reducing the number of required principal components. It can be seen as a trade of between bias (number of principal components) and variance (prediction errors of higher order principal components). The selected 3D fields are:

- Linear power P_{lin}^{3D} at the instance of its local maximum.
- Stored enthalpy in the fuel H_f^{3D} at the instance of its local maximum.
- Cladding wall heat flux W_f^{3D} at the instance of its local maximum.
- Gap heat transfer H_{gap}^{3D} at the instance of its local maximum.
- Coolant density D_w^{3D} at the instance of its local minimum.

The 3D fields are difficult to visualize and to this purpose two cross-sections will be presented for each output: the radial and axial cross-sections at the position of the local maximum (or minimum). The mean and relative standard deviation distributions are calculated for these cross-sections. The sensitivity results are estimated for the whole $3D$ output fields. Since we do not focus on the UQM, the learning LHS of 250 that was used in the Section 4.5 is used for all the modelings. This allows also to obtain a point by point comparison. The inputs, outputs and statistical tools studied in the different physical modelings are:

- **Inputs:** TD_1, TD_2, NF_1, NF_2, D_1, D_2, $S_{1\to2}$, IV_1, IV_2, β_{eff}, λ_{eff}, λ_f, λ_c, Cp_f, Cp_c, $H_{g,m}$, $H_{g,i}$, T_R, H_c, R_{crit}, R_{v0}, H_{dnb}.
- **Outputs:** P_{lin}^{max}, H_f^{max}, DNB^{min}, P_{lin}^{3D} (95%), H_f^{3D} (95%), W_f^{3D} (85%), H_{gap}^{3D} (95%), D_w^{3D} (95%).
- **Statistical tools:**
  - **Surrogate models:** Kriging.
  - **Uncertainty propagation:** Brute Monte Carlo method using kriging surrogate models for histogram empirical estimation.
  - **Global sensitivity analysis:** Shapley indices estimated using kriging models.
  - **Functional outputs:** PCA is used to reduce the functional output dimensions. The principal components that represent 95 % for most quantities is used. In some cases where the kriging models show large prediction error the represented variance is reduced.

Since we do not apply the UQM, the surrogate models between the inputs and the principal components of the 3D fields are trained on one of the two subspaces identified by the UQM in Section 4.6. The one with smaller prediction error is used. For the estimation of the prediction error the leave-one-out error is used because there is no evaluation LHS. The uncertainty propagation is performed with brute Monte Carlo using $1e^4$ samples.

4.7.2 IBE modeling

In this study the IBE APOLLO3 ® - FLICA4 - HGAP coupling is used with multi-1D thermal-hydraulics modeling and one thermal-hydraulic channel per assembly. It is the same modeling used for the application of UQM in Section 4.5. Since the UQM outputs were presented there in this study we present only the identified 3D output fields. We remind the selected modeling options of this study:

- APOLLO3 ®: Two group diffusion with void boundary conditions. The discretization radially is 4 meshes per assembly and axially 34 meshes of which 30 for the fuel active height.
- FLICA4: 4 equation porous modeling with multi-1D axial flow. There are no transverse flows and only the fuel active part is considered. The discretization radially is one thermal-hydraulic channel per assembly and axially is 30 meshes corresponding to the fuel active height.
- H_{gap}: 5 simplified models calibrated on decoupled ALCYONE V1.4 calculations. Different initial conditions are used for the different types of assemblies creating a similar spatial mesh with FLICA4.

For P_{lin}^{3D} two principal components are needed to represent 95 % of its variance. For each principal component a kriging model is trained on subspace I_1 with prediction errors 0.5 % and 0.9 % for the first and second one respectively. The estimated mean and standard deviation for the radial and axial cross-sections at the location and instant of the local maximum are presented in figures 4.19 - 4.20.

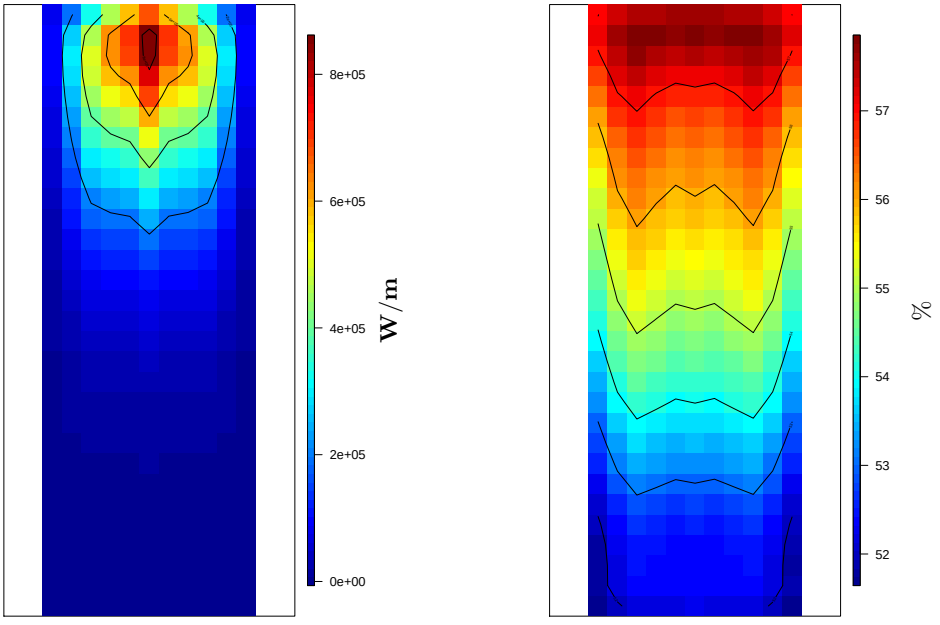

(a) Mean (b) Relative standard deviation

Figure 4.19: P_{lin}^{3D} estimated mean and relative standard deviation in the axial cross-section for IBE coupling study in PWR core.

We can see that we manage to obtain similar radial distribution as in Section 4.6 where we treated only the radial cross-section as functional output. The REA is very local both axially and radially explaining the large F_{xyz} deformation factor. The local maximum is located in the assembly where the control rod is ejected at one axial slice from the top. Usually for REA occurring in the periphery of the core the local maximum linear power is expected in the assembly between the reflector and the assembly with the control rod. This is not the case here due to the large thermal-hydraulic channels and the important gradient close to the REA position. In the last study we will investigate the impact of using smaller thermal-hydraulic channels. The relative standard deviation does not vary significantly and is in the order of 58 %. A small impact of the reflector can be observed in increasing slightly the uncertainty on the peripheral assemblies.

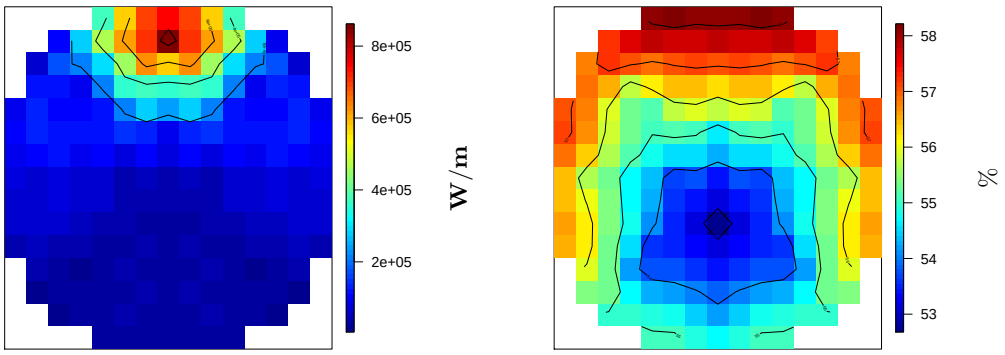

(a) Mean (b) Relative standard deviation

Figure 4.20: P_{lin}^{3D} estimated mean and relative standard deviation in the radial cross-section for IBE coupling study in PWR core.

The aggregate Shapley indices for P_{lin}^{3D} are estimated and presented in figure 4.21. As in Section 4.6 the β_{eff} explains 50 % of the variance while the remaining 50 % is explained by TD_1 and D_1. The latter macroscopic cross-sections represent the uncertainty of the control rod worth. We could say that the control rod worth and the effective delayed neutron fraction are responsible for the linear power variations. This is something expected by the underlying REA physics since the quantity $\rho_{worth} - \beta_{eff}$ determines the violence of the transient.

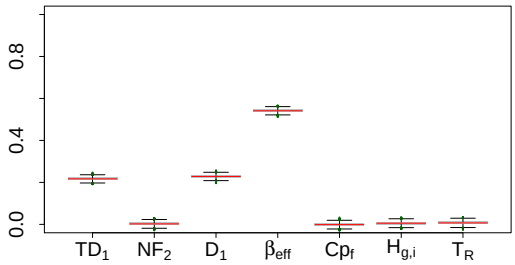

Figure 4.21: P_{lin}^{3D} Shapley indices for IBE coupling study in PWR core.

For H_f^{3D} two principal components are needed to represent 95 % of its variance. For each principal component a kriging model is trained on subprojection I_1 with prediction errors 0.95 % and 0.96 % for the first and second one respectively. The estimated mean and standard deviation for the radial and axial cross-sections at the location and instant of the local maximum are presented in figures 4.22 - 4.23. The local maximum is located at the same axial and radial position as the maximum local linear power. This is expected since the stored enthalpy depends strongly on the power generated in the fuel. The relative standard deviation distribution varies from 15 % to 22 %. The part of the core further from the REA location is the one exhibiting largest variations.

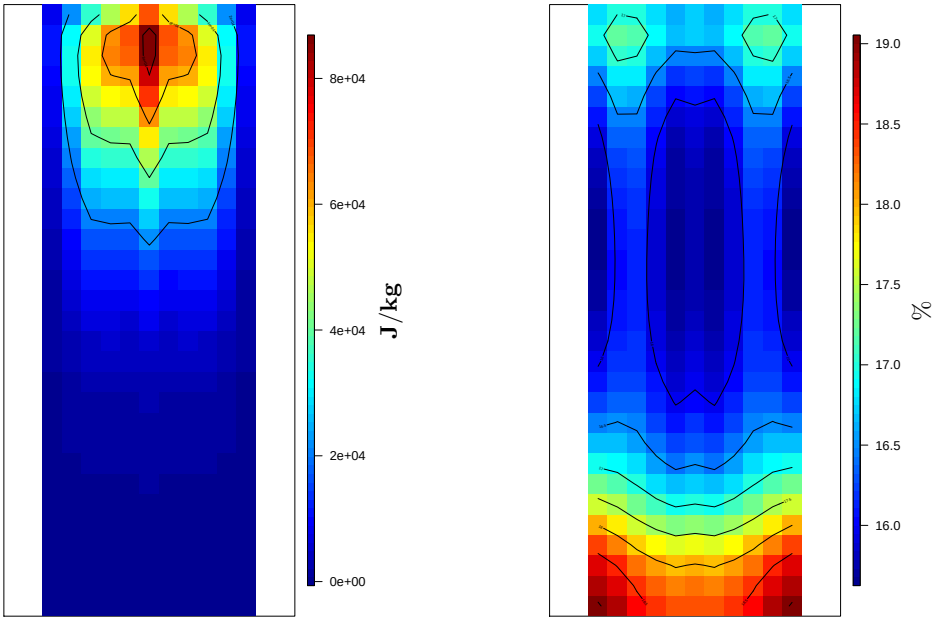

(a) Mean (b) Relative standard deviation

Figure 4.22: H_f^{3D} estimated mean and relative standard deviation in the axial cross-section for IBE coupling study in PWR core.

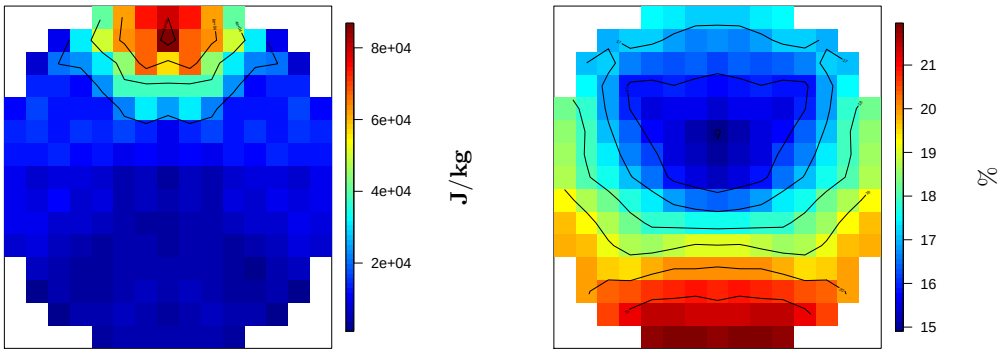

(a) Mean (b) Relative standard deviation

Figure 4.23: H_f^{3D} estimated mean and relative standard deviation in the radial cross-section for IBE coupling study in PWR core.

The aggregate Shapley indices for H_f^{3D} are estimated and presented in figure 4.24. Similar indices with P_{lin}^{3D} are obtained. It is interesting that while the Cp_f is directly involved in the enthalpy calculation its sensitivity is very small. This can be attributed to the small standard deviation in combination with the dominance of the generated power that is represented by the macroscopic cross-sections and the β_{eff}.

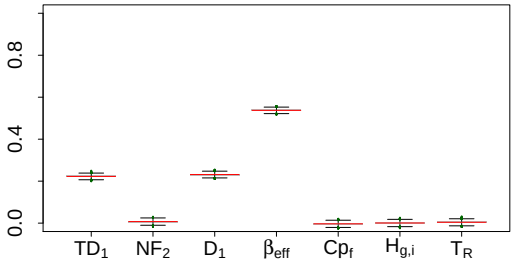

Figure 4.24: H_f^{3D} Shapley indices for IBE coupling study in PWR core.

For W_f^{3D} two principal components are needed to represent 85 % of its variance. We cannot represent more because the prediction errors of the higher principal components are very large. Kriging models are trained on subprojection I_2 for the first and second principal components with prediction errors 1.0 % and 5.5 % respectively.

The estimated mean and standard deviation for the radial and axial cross-sections at the location and instant of the local maximum are presented in figures 4.25 - 4.26. The local maximum is located at the assembly on the right and left of the assembly with the ejected control rod. This is because the fuel wall heat flux depends strongly on the gap heat transfer and the pellet-cladding gap width. These assemblies belong to the $45GWd/t$ group and are close to the REA location. This means that the initial gap heat transfer is high with a corresponding small gap. The power evolution seen by the assemblies create a temperature increase that drives the thermal expansion and closes even further the gap increasing the fuel wall heat flux. The relative standard deviation distribution exhibits large variations between 20 % to 34 % with larger uncertainties at the locations with high fuel wall heat flux.

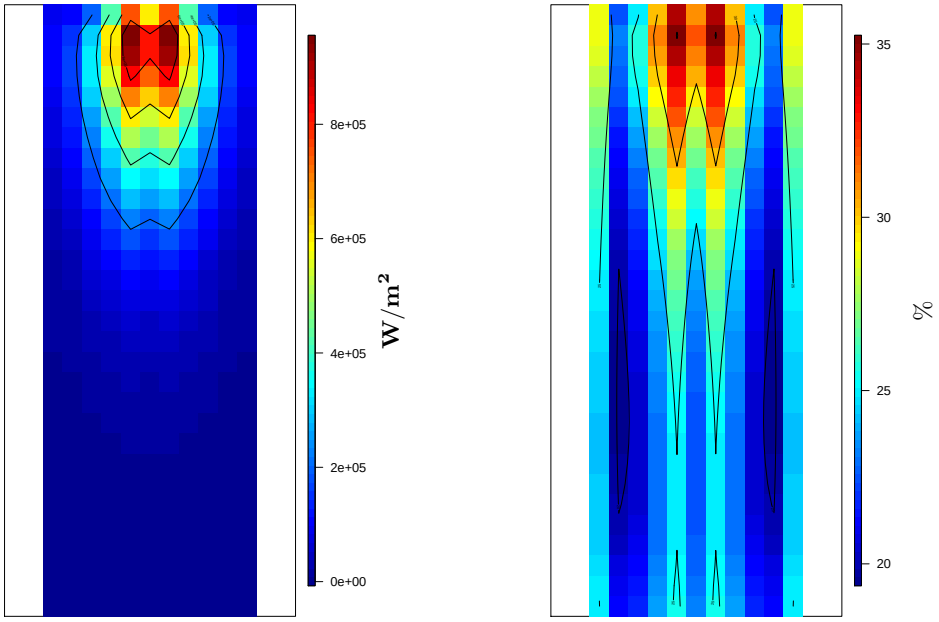

(a) Mean (b) Relative standard deviation

Figure 4.25: W_f^{3D} estimated mean and relative standard deviation in the axial cross-section for IBE coupling study in PWR core.

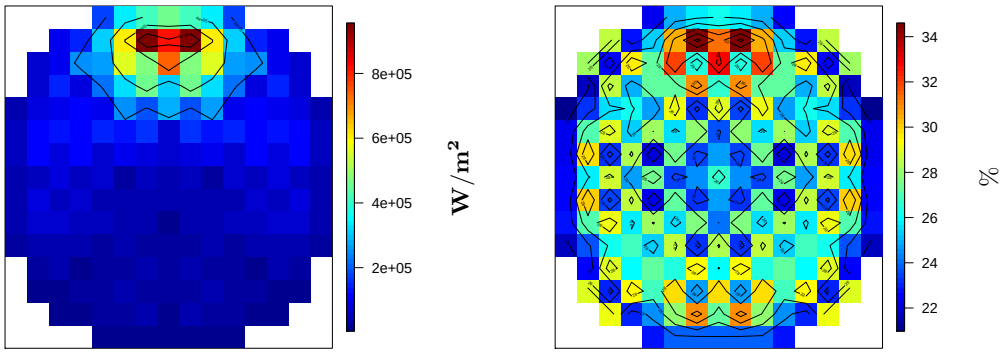

(a) Mean (b) Relative standard deviation

Figure 4.26: W_f^{3D} estimated mean and relative standard deviation in the radial cross-section for IBE coupling study in PWR core.

The aggregate Shapley indices for W_f^{3D} are estimated and presented in figure 4.27. Similar indices with P_{lin}^{3D} and H_f^{3D} are obtained. The $H_{g,i}$ has very small sensitivity meaning that while it is important for the mean value it does not have any impact on the variance.

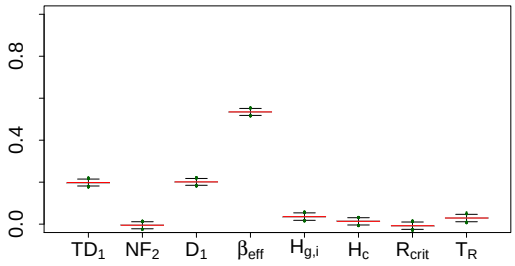

Figure 4.27: W_f^{3D} Shapley indices for IBE coupling study in PWR core.

For H_{gap}^{3D} two principal components are needed to represent 95 % of its variance. For each principal component a kriging model is trained on subprojection I_1 with prediction errors 0.08 % and 2.0 % for the first and second one respectively. The estimated mean and standard deviation for the radial and axial cross-sections at the location and instant of the local maximum are presented in figures 4.28 - 4.29.

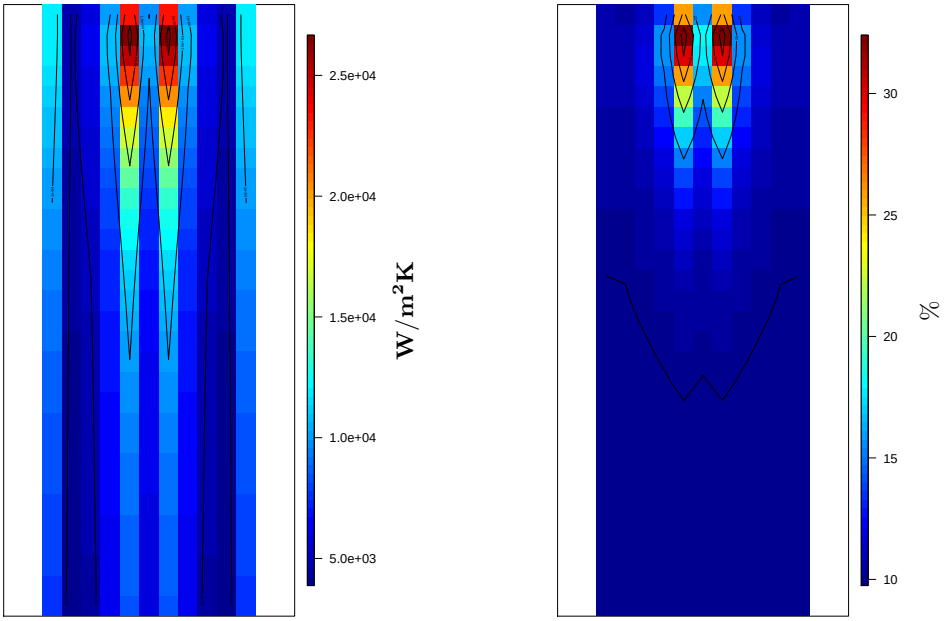

(a) Mean

(b) Relative standard deviation

Figure 4.28: H_{gap}^{3D} estimated mean and relative standard deviation in the axial cross-section for IBE coupling study in PWR core.

As expected by the calibrated H_{gap} models the assemblies with higher burn-up have also higher H_{gap}. The maximum value is obtained at the assemblies on the right and left of the assembly with the ejected control rod. This is for the same reason as for the W_f^{3D} due to the important power seen by these assemblies in combination with their high burn-up. The relative standard deviation distribution exhibits strong variations from 10 % up to 32 %. The assemblies with the maximum H_{gap} are the ones with the largest uncertainties.

The aggregate Shapley indices for H_{gap}^{3D} are estimated and presented in figure 4.30. In this case the $H_{g,i}$ is the dominant input responsible for 80 % of the outputs variance. The remaining 20 % is mainly explained by β_{eff}. This result is not surprising since the initial conditions determine the H_{gap} evolution as described in the calibration methodology of Chapter 3.

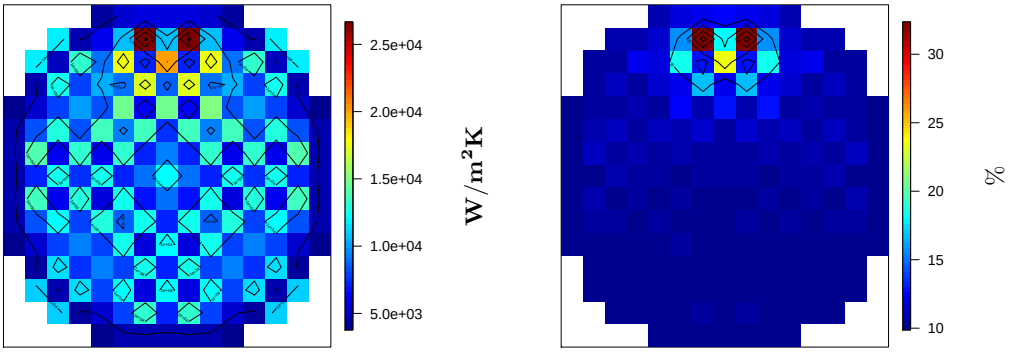

(a) Mean (b) Relative standard deviation

Figure 4.29: H_{gap}^{3D} estimated mean and relative standard deviation in the radial cross-section for IBE coupling study in PWR core.

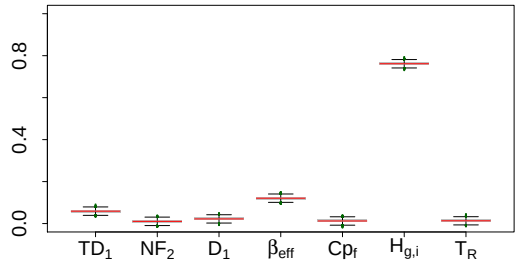

Figure 4.30: H_{gap}^{3D} Shapley indices for IBE coupling study in PWR core.

Finally, for D_w^{3D} three principal components are needed to represent 95 % of its variance. For each principal component a kriging model is trained on subprojection I_2 with prediction errors 0.7 %, 0.6 % and 5.5 % for the first, second and third one respectively. The estimated mean and standard deviation for the radial and axial cross-sections at the location and instant of the local maximum are presented in figures 4.31 - 4.32. The coolant density decreases as it flows through the thermal-hydraulic channel due to the heat extracted from the fuel and thus it is expected to obtain the minimum value at the top of the core. The extracted heat is much higher at the location of the control rod ejection and thus in this assembly is obtained the minimum coolant density. The relative standard deviation has very small values ranging from 0.1 % to 0.7 %. This means that for the REA and specifically when the boiling crisis is not reached and thus the coolant is mainly liquid water the coolant density remains essentially constant.

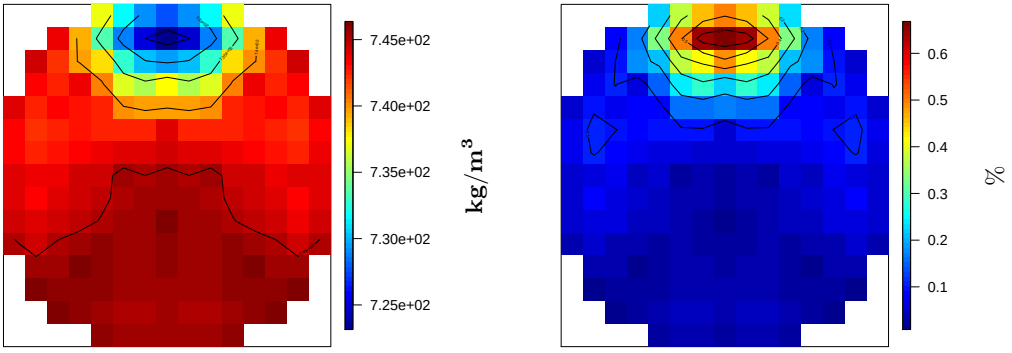

(a) Mean (b) Relative standard deviation

Figure 4.31: D_w^{3D} estimated mean and relative standard deviation in the radial cross-section for IBE coupling study in PWR core.

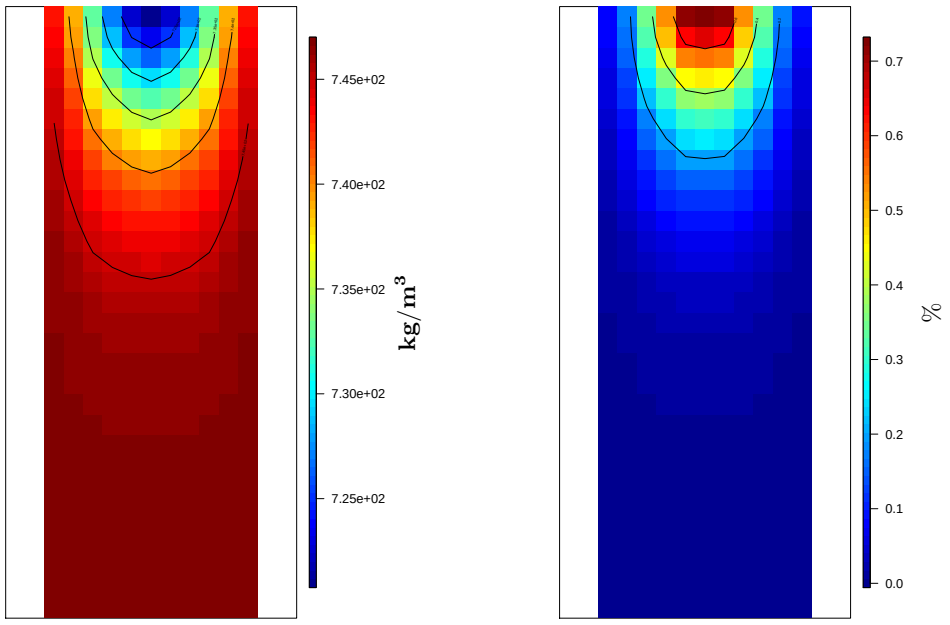

(a) Mean (b) Relative standard deviation

Figure 4.32: D_w^{3D} estimated mean and relative standard deviation in the axial cross-section for IBE coupling study in PWR core.

The aggregate Shapley indices for D_w^{3D} are estimated and presented in figure 4.33. As for most of the quantities the β_{eff} and the macroscopic cross-sections TD_1 and D_1 are the most important inputs.

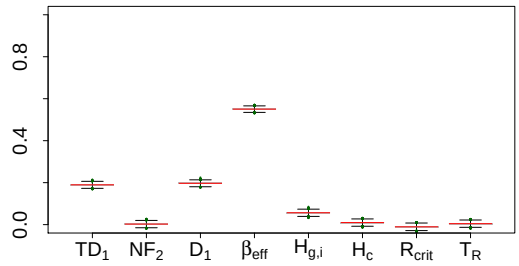

Figure 4.33: D_w^{3D} Shapley indices for IBE coupling study in PWR core.

4.7.3 IBE modeling with 3D thermal-hydraulics

The IBE APOLLO3 ® - FLICA4 coupling is used in this study with a 3D thermal-hydraulics modeling in FLICA4. The computational cost of this modeling is 3.5 hours. The impact of the transverse flows in X and Y direction is estimated. We remind the selected modeling options for this study:

- APOLLO3 ®: Two group diffusion with void boundary conditions. The discretization radially is 4 meshes per assembly and axially 34 meshes of which 30 for the fuel active height.
- FLICA4: 4 equation porous modeling with 3D flow in direction X, Y and Z (axial). The fuel active part is considered and the discretization radially is one thermal-hydraulic channel per assembly and axially is 30 meshes.
- H_{gap}: 5 simplified models calibrated on decoupled ALCYONE V1.4 calculations. Different initial conditions are used for the different types of assemblies creating a similar spatial mesh with FLICA4.

In figures 4.34 - 4.35 we present the mean distribution of the two velocities V_X^{3D} and V_Y^{3D}. Two representative radial and axial cross-sections are illustrated a few time steps after the power peak. The impact of the REA on the two velocities is obvious but still we see that their values are quite low compared to the axial flow velocity of around $4\,m/s$.

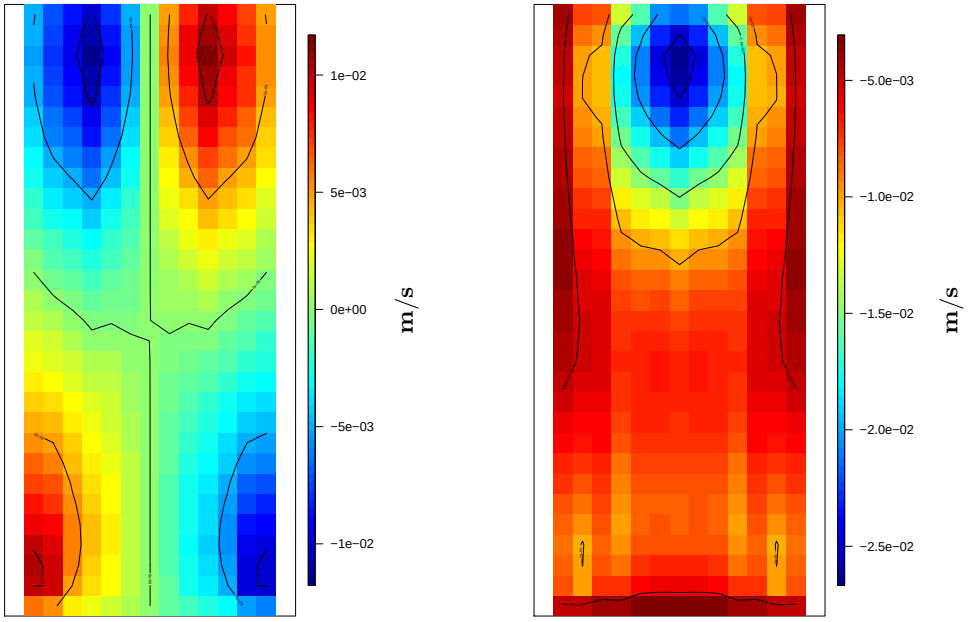

(a) V_X^{3D} (b) V_Y^{3D}

Figure 4.34: V_X^{3D} and V_Y^{3D} estimated mean distribution in the axial cross-section for $3D$ IBE coupling study.

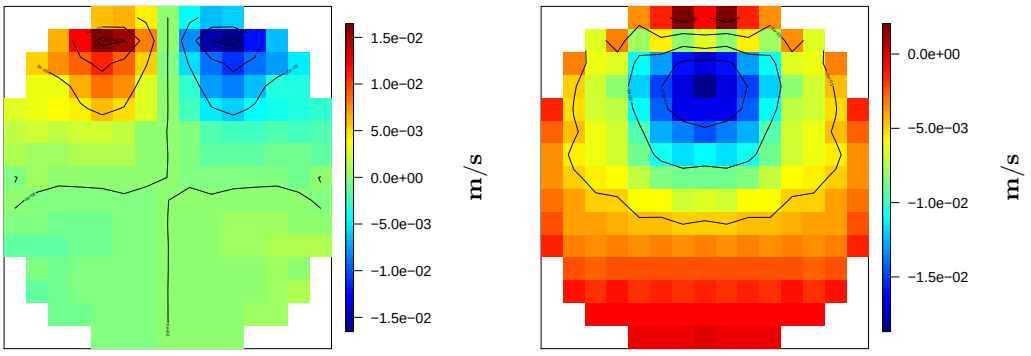

(a) V_X^{3D} (b) V_Y^{3D}

Figure 4.35: V_X^{3D} and V_Y^{3D} estimated mean distribution in the radial cross-section for $3D$ IBE coupling study.

The only quantity impacted by the transverse flows is the DNB^{min}. The constructed kriging models has a prediction error of 1.4 %. We can see the obtained histogram and Shapley indices in figure 4.36. We can conclude that the mean value of the DNB^{min} has decreased by 7 % increasing the probability of boiling crisis. This is due to the fact that the axial flow is reduced by the presence of transverse flows. The axial flow is slower and thus extracts more fuel heat flux leading to lower DNB^{min}. A secondary reason for the DNB^{min} decrease is due to the critical heat flux decrease. The critical heat flux correlation is a function of the axial flow. As the axial flow decreases the critical heat flux decreases as well. This leads to lower $DNBR$ and thus lower DNB^{min} The relative standard deviation and the sensitivities are not impacted by the transverse flows.

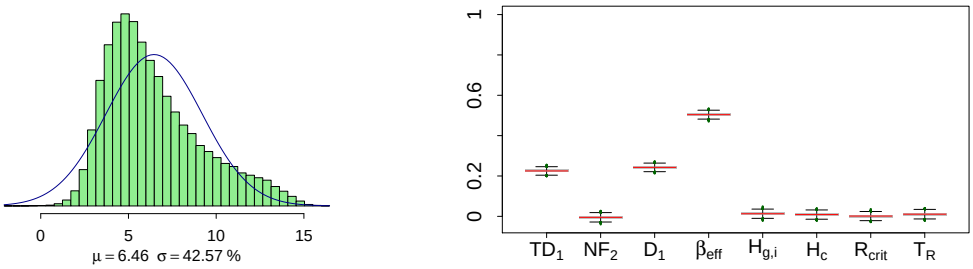

Figure 4.36: DNB^{min} estimated histogram and Shapley indices for $3D$ IBE coupling study.

4.7.4 IBE modeling with 3D thermal-hydraulics and finer spatial discretization

The final modeling option that we investigate is the thermal-hydraulic channel discretization size. More specifically based on the IBE 3D thermal-hydraulics modeling of Section 4.7.3 we use now one thermal-hydraulic channel per quarter of assembly. This leads to 4 times more spatial meshes and an increase in the computational cost at 12 hours. We remind the selected modeling options of this study:

- APOLLO3 ®: Two group diffusion with void boundary conditions. The discretization radially is 4 meshes per assembly and axially 34 meshes of which 30 for the fuel active height.
- FLICA4: 4 equation porous modeling 3D flow in direction X, Y and Z (axial). The fuel active part is considered and the discretization radially is four thermal-hydraulic channels per assembly and axially is 30 meshes corresponding to the fuel active height.
- H_{gap}: 5 simplified models calibrated on decoupled ALCYONE V1.4 calculations. Different initial conditions are used for the different types of assemblies creating a similar spatial mesh with FLICA4.

We can see the obtained V_X^{3D} and V_Y^{3D} 3D fields of transverse velocities in figures 4.37 - 4.38. We do not observe any significant impact of the discretization. This could mean that the transverse flows effects are the same with the modeling of Section 4.7.3 and thus any quantity with different behavior will be solely due to the spatial discretization effect.

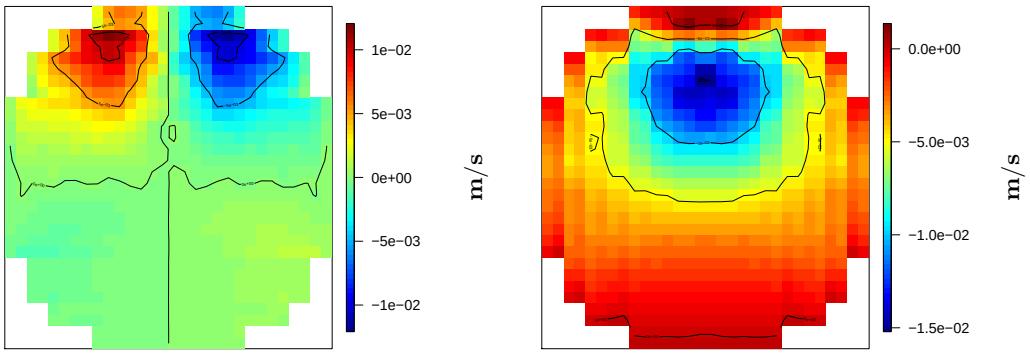

(a) V_X^{3D} (b) V_Y^{3D}

Figure 4.37: V_X^{3D} and V_Y^{3D} estimated mean distribution in the radial cross-section for $3D$ IBE with finer thermal-hydraulic channels coupling study.

All the identified outputs will be presented starting from the scalar outputs of the UQM. The kriging models were trained for P_{lin}^{max}, H_f^{max} and DNB^{min} on the identified subspaces of Section 4.6 and based on the same LHS as the previous studies of this Section. The prediction error estimated by the leave-one-out error for the three scalar outputs are: 0.5 % for P_{lin}^{max}, 0.7 % for H_f^{max} and 1.6 % for DNB^{min}.

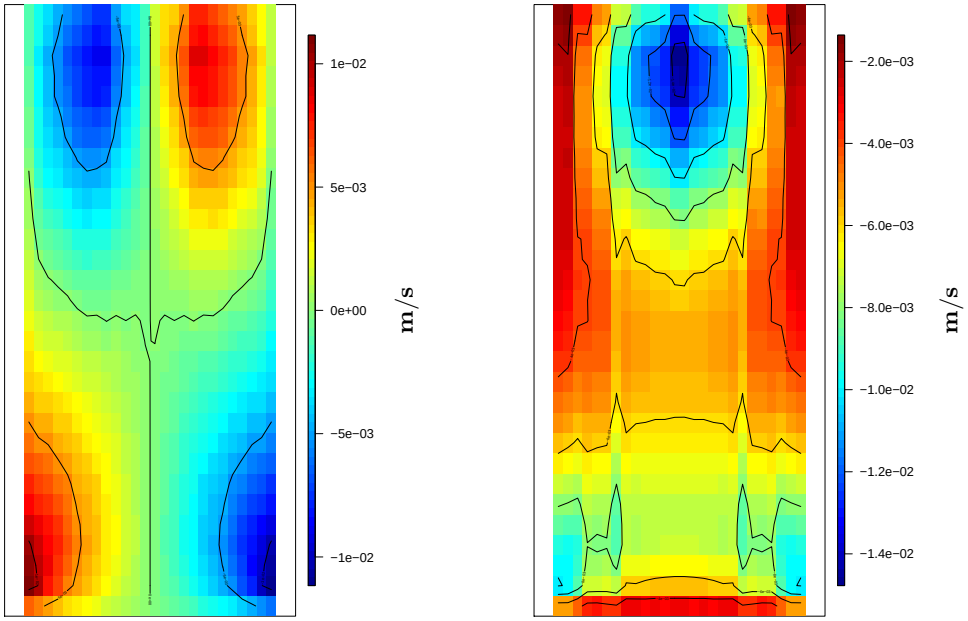

(a) V_X^{3D} (b) V_Y^{3D}

Figure 4.38: V_X^{3D} and V_Y^{3D} estimated mean distribution in the axial cross-section for $3D$ IBE with finer thermal-hydraulic channels coupling study.

Using the trained kriging models the uncertainties are propagated using $1e^5$ samples to estimate their histograms and first two moments. The results are presented in figure 4.39. The P_{lin}^{max} is not impacted. This can be justified by the fact that the neutronics modeling, which is more important for this quantity, is the same. We observe a 10 % increase in the mean H_f^{max} attributed to the thermal-hydraulics spatial discretization. H_f^{max} is a quantity calculated on the FLICA4 mesh and thus in the previous studies the neutronics power is averaged in the whole assembly. Specifically in the location of the maximum, that is close to the periphery, the gradient is quite strong leading to lower linear power values and thus lower H_f^{max}. For DNB^{min} a decrease of 4 % is seen in the mean value. This is for the same reason as H_f^{max}. In the study of Section 4.7.3 the averaged linear power at the level of assembly seen by FLICA4 is lower than this study leading to less fuel heat flux reaching the coolant and thus larger distance to the boiling crisis. The relative standard deviations of all the scalar outputs is not impacted.

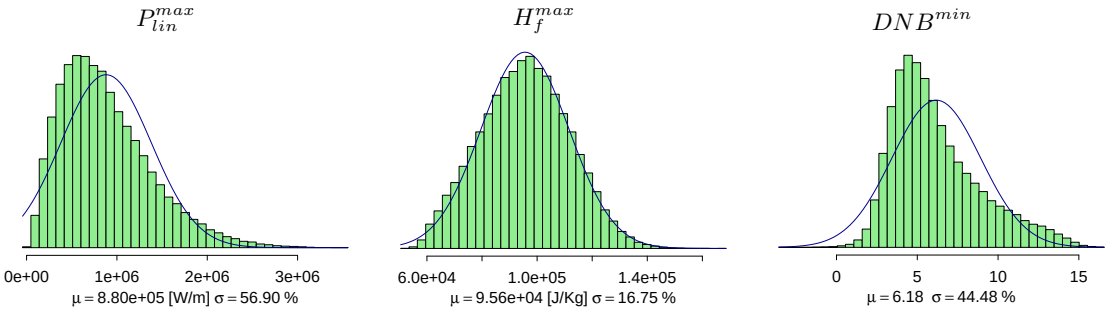

Figure 4.39: P_{lin}^{max}, H_f^{max} and DNB^{min} histograms for $3D$ IBE with finer thermal-hydraulic channels coupling study.

The global sensitivity analysis for the scalar outputs is carried out by using the kriging models to estimate the Shapley indices. The results are presented in figures 4.40 - 4.41. We conclude that the sensitivities are not impacted by the thermal-hydraulics spatial discretization.

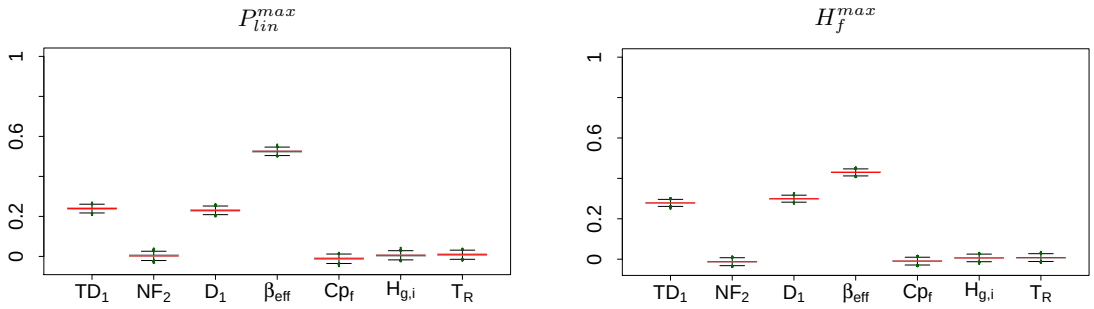

Figure 4.40: P_{lin}^{max} and H_f^{max} Shapley indices for $3D$ IBE with finer thermal-hydraulic channels coupling study.

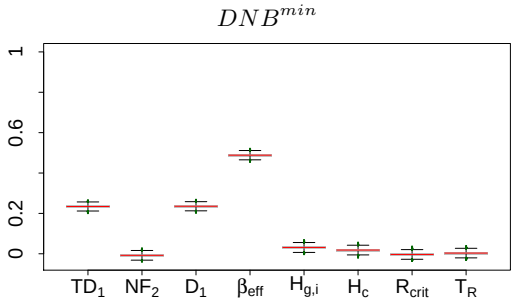

Figure 4.41: DNB^{min} Shapley indices for $3D$ IBE with finer thermal-hydraulic channels coupling study.

The functional UQM output P_{lin}^{2D} is not presented explicitly because it is identical to the radial cross-section of P_{lin}^{3D}. For the latter two principal components are needed to represent 95 % of its variance. For each principal component a kriging model is trained on subprojection I_1 with prediction errors 0.5 % and 0.8 % for the first and second one respectively. The estimated mean and standard deviation for the radial and axial cross-sections at the location and instant of the local maximum are presented in figures 4.42 - 4.43.

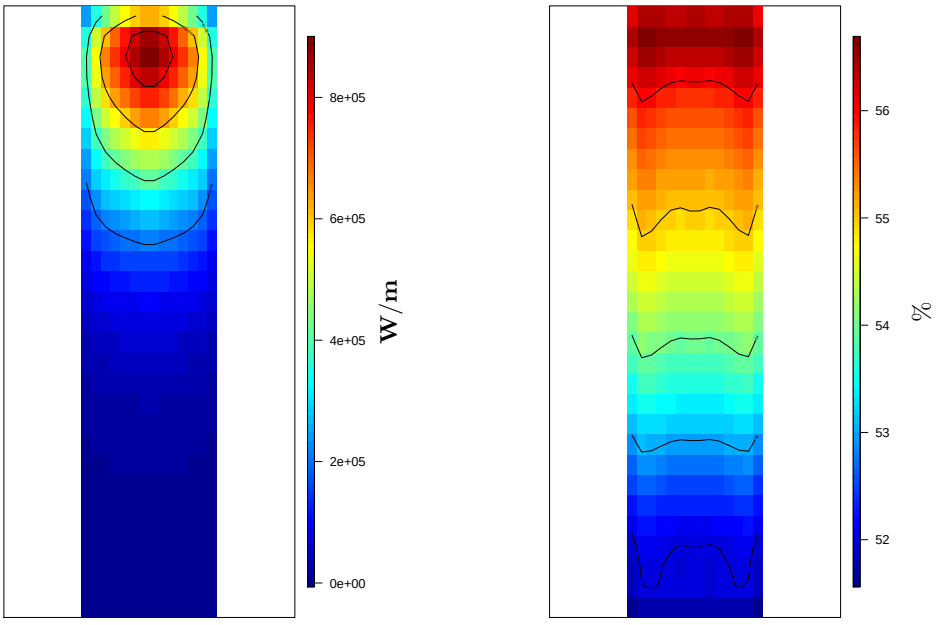

(a) Mean

(b) Relative standard deviation

Figure 4.42: P_{lin}^{3D} estimated mean and relative standard deviation in the axial cross-section for $3D$ IBE with finer thermal-hydraulic channels coupling study.

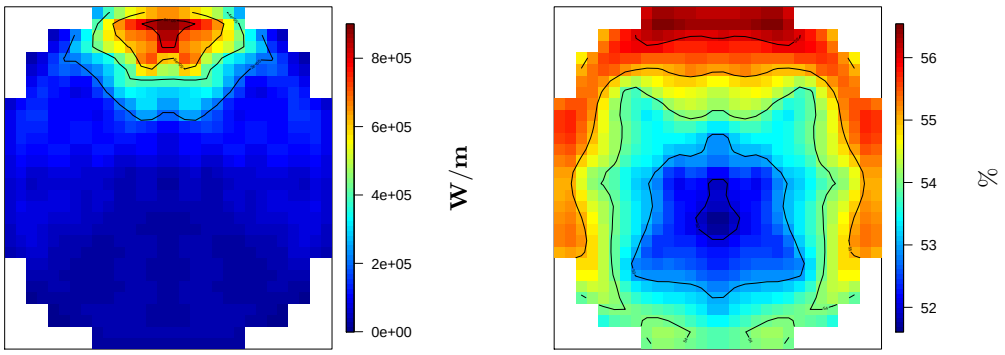

(a) Mean (b) Relative standard deviation

Figure 4.43: P_{lin}^{3D} estimated mean and relative standard deviation in the radial cross-section for $3D$ IBE with finer thermal-hydraulic channels coupling study.

The results show a shift of the local maximum value radially towards the assembly between the reflector and the assembly with the ejected control rod as expected by the REA physics. There is also an axial shift of one axial slice lower than the previous studies. We observe the large gradient in the proximity of the REA location leading to a higher maximum linear power in FLICA4. The relative standard deviations are not impacted by the thermal-hydraulics discretization. The aggregate Shapley indices for P_{lin}^{3D} are not impacted by the thermal-hydraulics discretization with β_{eff} explaining 50 % of the variance while the remaining 50 % is explained by TD_1 and D_1.

For H_f^{3D} two principal components are needed to represent 95 % of its variance. For each principal component a kriging model is trained on subprojection I_1 with prediction errors 0.8 % and 0.7 % for the first and second one respectively. The estimated mean and standard deviation for the radial and axial cross-sections at the location and instant of the local maximum are presented in figures 4.44 - 4.45. The local maximum follows the P_{lin}^{3D} and is shifted both axially and radially for the same reason. Neither the relative standard deviations or the estimated aggregated Shapley indices are impacted by the thermal-hydraulics discretization.

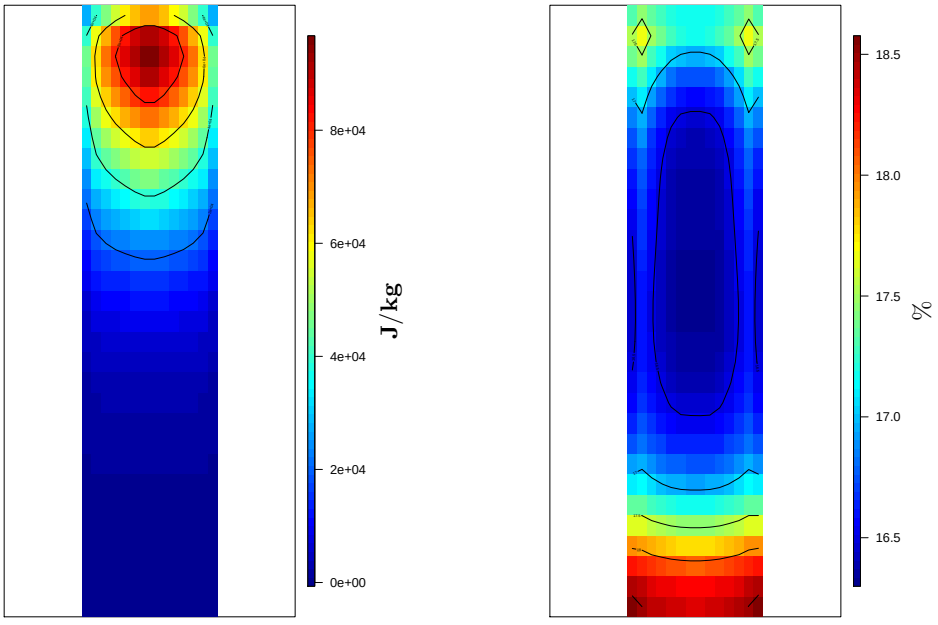

(a) Mean (b) Relative standard deviation

Figure 4.44: H_f^{3D} estimated mean and relative standard deviation in the axial cross-section for $3D$ IBE with finer thermal-hydraulic channels coupling study.

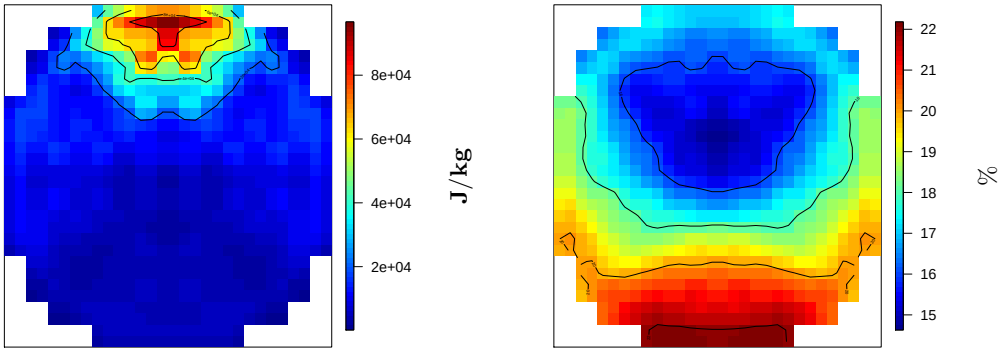

(a) Mean (b) Relative standard deviation

Figure 4.45: H_f^{3D} estimated mean and relative standard deviation in the radial cross-section for $3D$ IBE with finer thermal-hydraulic channels coupling study.

For W_f^{3D} two principal components are needed to represent 85 % of its variance. We cannot represent more because the prediction errors of the higher principal components are very large. Kriging models are trained on subprojection I_2 for the first and second principal components with prediction errors 1.1 % and 7 % respectively.

The estimated mean and standard deviation for the radial and axial cross-sections at the location and instant of the local maximum are presented in figures 4.46 - 4.47. The W_f^{3D} distribution and its local maximum position does not change. This is because it is governed mainly by the burn-up and since the burn-up distributions in all the studies is the same the position is not affected. Neither the relative standard deviations or the estimated aggregated Shapley indices are significantly impacted by the thermal-hydraulics discretization.

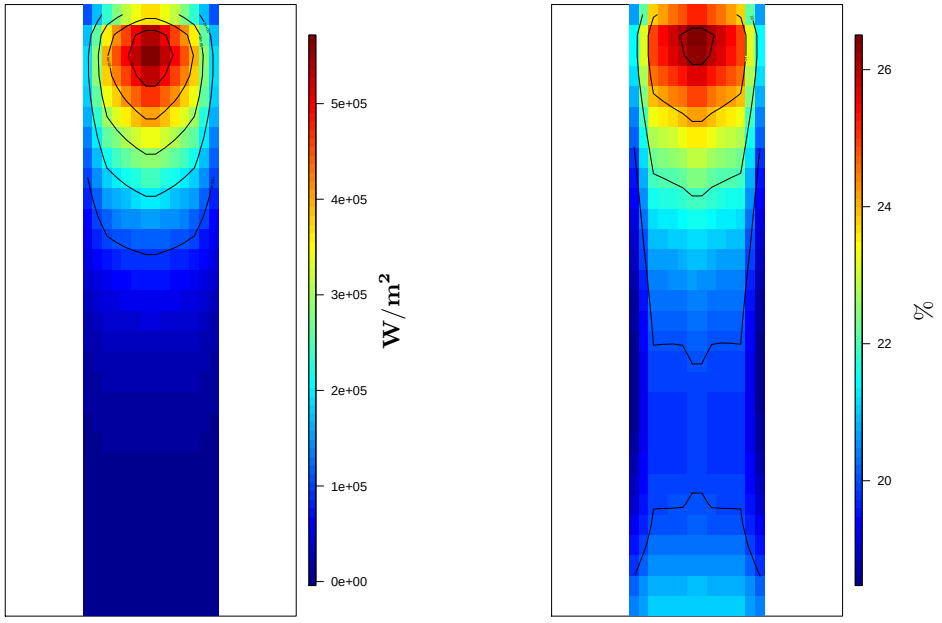

(a) Mean (b) Relative standard deviation

Figure 4.46: W_f^{3D} estimated mean and relative standard deviation in the axial cross-section for $3D$ IBE with finer thermal-hydraulic channels coupling study.

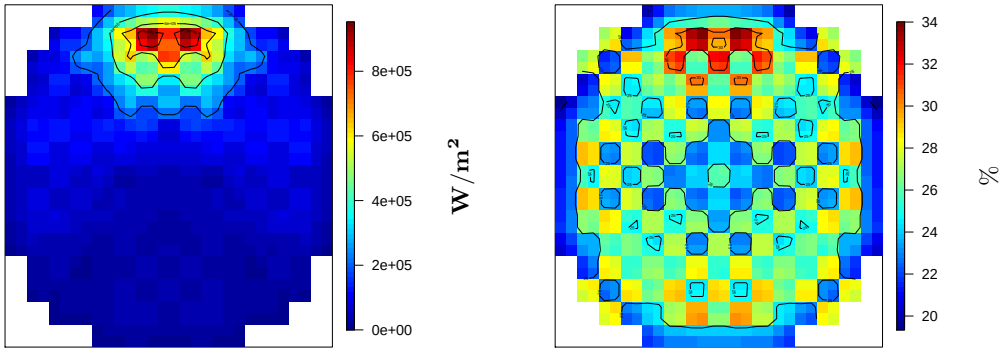

(a) Mean (b) Relative standard deviation

Figure 4.47: W_f^{3D} estimated mean and relative standard deviation in the radial cross-section for $3D$ IBE with finer thermal-hydraulic channels coupling study.

For H_{gap}^{3D} two principal components are needed to represent 95 % of its variance. For each principal component a kriging model is trained on subprojection I_1 with prediction errors 0.07 % and 2.0 % for the first and second one respectively.

The estimated mean and standard deviation for the radial and axial cross-sections at the location and instant of the local maximum are presented in figures 4.48 - 4.49. For the same reason as W_f^{3D} the H_{gap} distribution and its local maximum does not change in comparison with the previous studies. Neither the relative standard deviations or the estimated aggregated Shapley indices are significantly impacted by the thermal-hydraulics discretization.

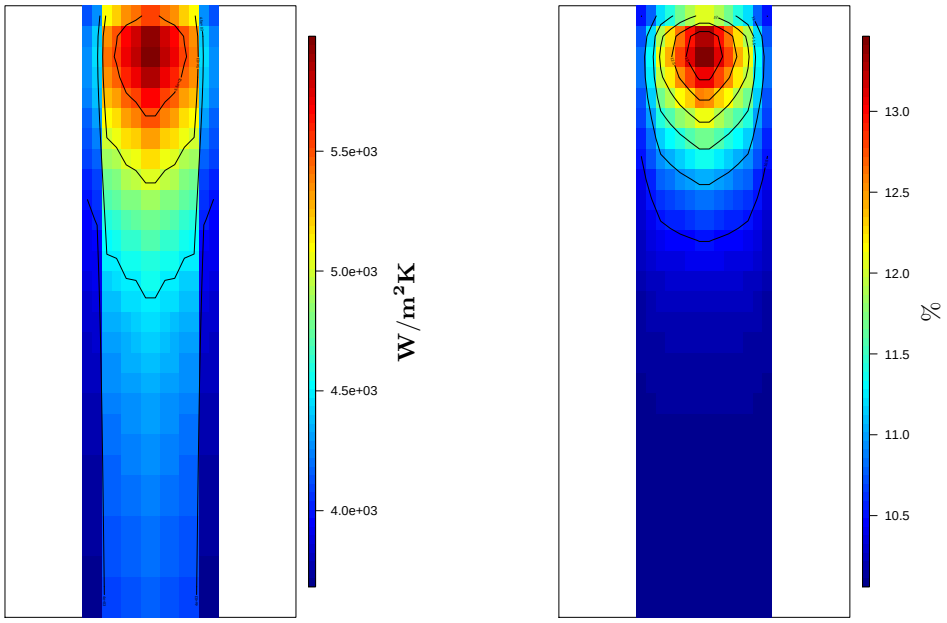

(a) Mean (b) Relative standard deviation

Figure 4.48: H_{gap}^{3D} estimated mean and relative standard deviation in the axial cross-section for $3D$ IBE with finer thermal-hydraulic channels coupling study.

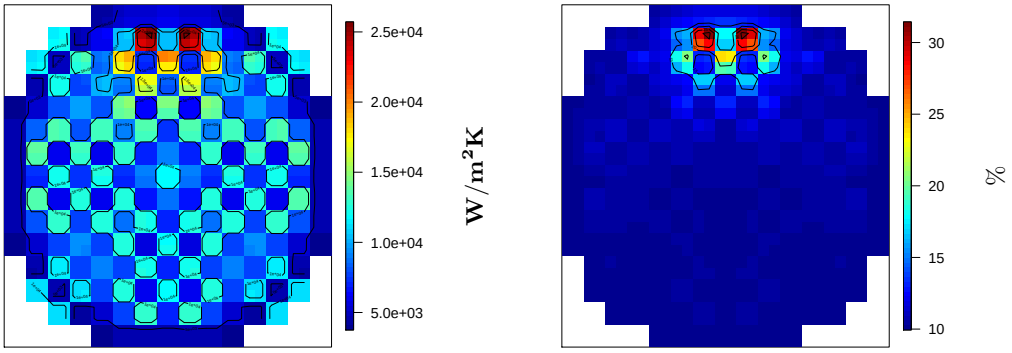

(a) Mean (b) Relative standard deviation

Figure 4.49: H_{gap}^{3D} estimated mean and relative standard deviation in the radial cross-section for $3D$ IBE with finer thermal-hydraulic channels coupling study.

Finally, for D_w^{3D} two principal components are needed to represent 90 % of its variance. We cannot represent more because the prediction errors of the higher principal components are very large. For each principal component a kriging model is trained on subprojection I_2 with prediction errors 0.7 % and 0.9 % for the first and second one respectively. The estimated mean and standard deviation for the radial and axial cross-sections at the location and instant of the local maximum are presented in figures 4.50 - 4.51.

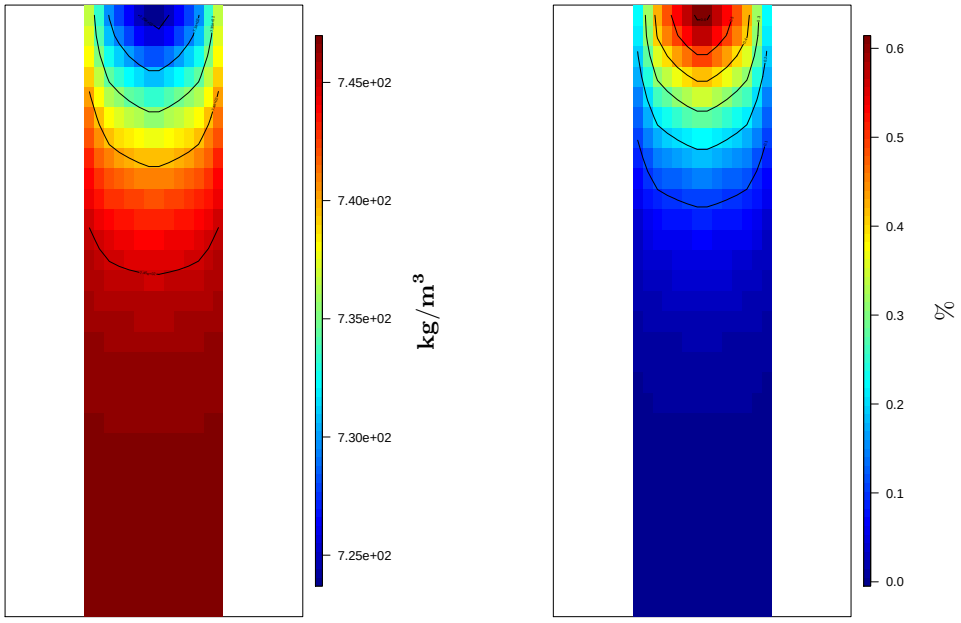

(a) Mean (b) Relative standard deviation

Figure 4.50: D_w^{3D} estimated mean and relative standard deviation in the axial cross-section for $3D$ IBE with finer thermal-hydraulic channels coupling study.

The coolant density depends on the heat extracted by the coolant as it flows through the thermal-hydraulic channels. Since we saw that the cladding wall heat flux distribution is not impacted by the thermal-hydraulic discretization, the coolant density is not impacted either. Neither the relative standard deviations or the estimated aggregated Shapley indices are significantly impacted by the thermal-hydraulic discretization.

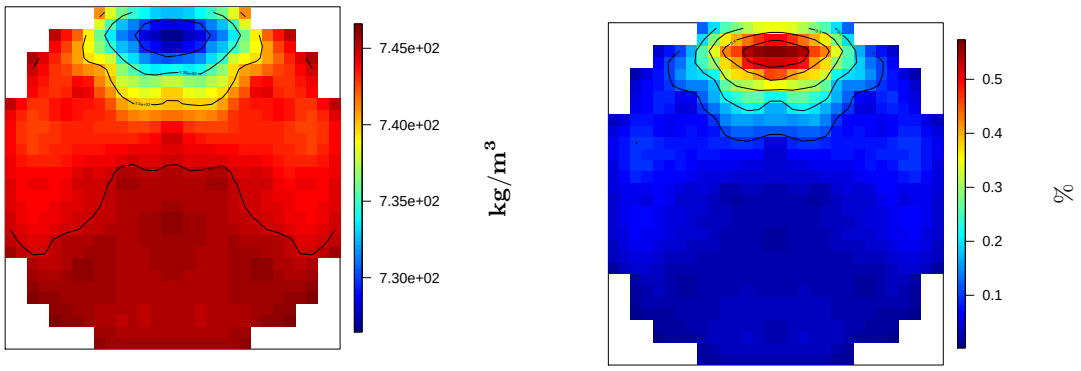

(a) Mean

(b) Relative standard deviation

Figure 4.51: D_w^{3D} estimated mean and relative standard deviation in the radial cross-section for $3D$ IBE with finer thermal-hydraulic channels coupling study.

4.7.5 Conclusions

In this Section we compared three different thermal-hydraulics modeling options for the IBE modeling established in Section 4.6. The three options are an increasing order of computational cost:

- **M1**: Multi-1D axial flow with one thermal-hydraulic channel per assembly. This was the option used in Section 4.6.
- **M2**: 3D flow with one thermal-hydraulic channel per assembly.
- **M3**: 3D flow with four thermal-hydraulic channels per assembly.

Different 3D functional outputs of interest for the coupling were studied together with the identified scalar outputs for the UQM. The same training LHS is used for all the models in order to study the effect on the uncertainty propagation and sensitivity analysis. The main observation from the comparison are summarized:

- The M2 compared to M1 has an impact only on the minimum distance to boiling crisis DNB^{min}. Its mean value decreases by 7 % due to the reduce of the axial flow caused by the presence of transverse flows. The impact is relatively small because the transverse flows are small. Reduced axial flow means that the coolant stays more time in the core and thus extracts more fuel heat flux leading to lower DNB^{min}. This increases the probability of boiling crisis.
- The M3 compared to both M2 and M1 shifts the position of the local maximum linear power P_{lin}^{max} from the assembly with the ejected control rod to the next assembly at the border of the reflector. Axially it is located at the third axial slice from the top, one axial slice lower than in M1 and M2. Additionally, the P_{lin}^{max} seen by FLICA4 is slightly higher because in M1 and M2 the value is a result of an averaging process since APOLLO3 ® has a discretization of four meshes for one assembly. This affects also the position of the local maximum stored enthalpy H_f^{max}, since it follows the position of P_{lin}^{max}. The H_f^{max} mean value is also increased.
- The M3 compared to M2 reduces even further the mean value of DNB^{min} due to the increased P_{lin}^{max} seen by FLICA4. This leads to higher heat flux to be extracted by the coolant that reduces DNB^{min}.
- The relative standard deviations of all the quantities and their sensitivities are in general not impacted by the modeling option.

We can conclude that M3 is more penalizing concerning P_{lin}^{max} and DNB^{min} and thus should definitely be used for safety analysis in comparison to M1 and M2. However, the computational cost is multiplied by four, something that renders difficult the uncertainty quantification. If we are mainly interested in sensitivities studies the model M2 is preferred since it is a good compromise in computational cost between M1 and M3.

4.8 Conclusions

In this Chapter we applied the UQM that was developed in Chapter 3 on a large scale PWR core for the study of a REA with a BE modeling. Additionally, we applied the calibration methodology of a simplified gap heat transfer H_{gap} model based on thermal expansions that was also developed in Chapter 3. The integration of the H_{gap} model in the BE coupling improves the REA modeling. Some complementary physical analyses were also carried out in order to investigate the impact of different thermal-hydraulics modeling options on a large set of outputs up to 3D fields.

Before applying the UQM a first preliminary static analysis showed that the uncertainty on the ρ_{worth} is larger than in the MiniCore. This can be attributed to the increased effect of the two group macroscopic cross-sections and mainly TD_1, D_1 and $S_{1\to 2}$. Besides that, for this core it was found out that there is a 2.25 % probability of reaching $\rho_{worth} - \beta_{eff} < 0$ conditions. These conditions are not interesting since they lead to less violent REA. A linear model was constructed in order to predict for each following DOE the points that lead to these non interesting conditions. The identified points are thus excluded from the DOE resulting in both a computational gain and allowing us to focus on the more interesting transients.

The application of the UQM on the PWR core resulted in the following conclusions for the outputs of interest:

- The local maximum linear power P_{lin}^{max} shows a relative standard deviation of 57% which is twice the value in the MiniCore. This is due to the increased sensitivity on the macroscopic cross-sections something reflected by the Shapley indices. The β_{eff} is responsible for 50 % of the variance and TD_1, D_1 and $S_{1\to 2}$ are responsible for the remaining 50 %.
- The linear power radial distribution P_{lin}^{2D} at the axial position and time instant of P_{lin}^{max} shows relative standard deviations with small spatial distribution ranging between 53 % and 57 %. The location of P_{lin}^{max} is the one that exhibits the highest relative standard deviation. The aggregate Shapley indices showed similar sensitivities to the P_{lin}^{max}.
- The maximum stored enthalpy H_f^{max} has 20 % relative standard deviation with a normal histogram. This reflects the linear behavior of this output. The same inputs as for P_{lin}^{max} are the dominant ones.
- The minimum distance to boiling crisis DNB^{min} is quite further than in the MiniCore case with a mean value of 6 and a relative standard deviation of 57 %. The H_{gap} is responsible for 50 % of the variance and β_{eff}, TD_1, D_1 and $S_{1\to 2}$ are responsible for the remaining 50 %.

For the calibration of the H_{gap} models 5 assembly groups were identified with one model per group. The resulting calibration errors for all the calibrated data are less than 8 %. The uncertainty of the calibration parameters was quantified using uniform pdf with bounds that cover the calibration errors. The uncertainty of the models initial conditions was quantified with $\mathcal{N}(1, 0.1)$ as in the MiniCore tests. The calibrated H_{gap} models were introduced in the Best Estimate coupling without increasing the computational cost. The UQM was applied again on this improved modeling. The most significant impact was on the DNB^{min} with an increase 14 % of its mean value reducing the probability of boiling crisis. The standard deviation of DNB^{min} was reduced to 42 %. The reason is the decreased sensitivity on the H_{gap} uncertainty due to its better uncertainty quantification and modeling. This is observed in the Shapley indices where now β_{eff} is responsible for 50 % of the variance and TD_1, D_1 and $S_{1\to 2}$ are responsible for the remaining 50 %.

In Section 4.7 we compared three different thermal-hydraulics modeling options for the IBE modeling of Section 4.6. The first option M1 is the Multi-1D axial flow thermal-hydraulic channel per assembly. The second option M2 is 3D flow with one thermal-hydraulic channel per assembly. The third one M3 is 3D flow with four thermal-hydraulic channels per assembly. Different 3D functional outputs of interest for the coupling were studied together with the identified scalar outputs for the UQM. The main observation that can be made are the following:

- The M2 compared to M1 has an impact only on the minimum distance to boiling crisis DNB^{min}. Its mean value decreases by 7 % due to the reduce of the axial flow caused by the presence of transverse flows.

- The M3 compared to both M2 and M1 shifts the position of P_{lin}^{max}. from the assembly with the ejected control rod to the next assembly at the border of the reflector. Axially it is also shifted to one axial slice lower.

- The M3 compared to M2 reduces even further the mean value of DNB^{min} due to the increased P_{lin}^{max} seen by FLICA4. This leads to higher heat flux to be extracted by the coolant that reduces DNB^{min}.

We can conclude that M3 is more penalizing concerning P_{lin}^{max} and DNB^{min} and thus should definitely be used for safety analysis in comparison to M1 and M2. However, this comes at a four times more computational cost that renders difficult the uncertainty analysis. If we are mainly interested in sensitivities studies the model M2 is preferred since it is a good compromise in computational cost between M1 and M3.

Conclusions and Perspectives

Conclusions

The main objective of this thesis was to develop an Uncertainty Quantification Methodology (UQM) for the multi-physics Best Estimate (BE) modeling of Rod Ejection Accident (REA). To this purpose the CORPUS coupling framework developed at CEA was used and more specifically the BE coupling between APOLLO3 ® and FLICA4 (thermal-hydraulics). This created many challenges:

- Computationally expensive modeling not allowing many code evaluations.
- Large input and output dimensions that can create difficulties for the application of the different statistical tools.
- Input dependencies that can lead to redundant inputs. This is the case when two inputs are strongly dependent and one is very important for an output while the other one is not. Most of the sensitivity methods will detect both of the inputs as very important.
- Interaction between inputs on the outputs variance. This can occur when one input is not directly significant to an output but only in conjunction with another input.
- Non-linear output behavior. It is not always easy for the surrogate model to correctly approximate a non-linear function, especially where there are discontinuities.

Fortunately as we saw in Chapter 2 there is a large variety of statistical tools that can be used in order to address some of these challenges. In Sections 3.4 - 3.5 these different statistical tools were tested on a small scale core (MiniCore) representative of a PWR in order to derive the UQM. Different tests were identified in order to select the statistical tools that will consist the UQM. Tests were carried out for neutronics, thermal-hydraulics, fuel-thermomechanics stand-alone studies using the CEA codes APOLLO3 ®, FLICA4 and ALCYONE V1.4 respectively. Afterwards, a multi-physics BE APOLLO3 ® - FLICA4 test was performed. The conclusions drawn from all these studies were used to develop the UQM presented in 4.52.

The UQM consists of four main steps. The initial step 0 is the definition of the case study with the desired uncertain inputs and outputs and the input uncertainty quantification. Since we assume that in the general case the input dimension can be large the step 1 consists in identifying the important input subspaces using Input Dimension Reduction Method (IDRM) for both scalar and functional outputs. This step is based on an initial random sampling. IDRM was developed based on HSIC statistical significance tests. This method aims at identifying an important input subspace by addressing the dependence of inputs, potential interactions and redundancies. The method was tested on the Morris function and on multi-physics BE REA coupling with very satisfactory results. The step 2 is the training of the kriging models for each output on the identified subspaces. The training LHS is constructed with good space-filling properties in both the original input space and the important subspaces. To achieve this the maximin criterion is maximized by minimizing the ϕ_p criterion. A modified version of the Simulated Annealing optimization algorithm was implemented in order to optimize the criterion in both the original space and the important subspaces. The test on the multi-physics BE modeling showed a significant gain for the space-filling criterion optimization in the identified subspaces. Using the improved LHS kriging models are trained directly for the scalar outputs while for the functional ones the kriging models are constructed for the first principal components that represent 95% of the outputs variance. The prediction errors

of the kriging models are estimated using a second LHS. The step 3 is the brute force Monte Carlo uncertainty propagation with the empirical estimations of the first two statistical moments and the histogram. Finally, in step 4 the global sensitivity analysis is performed using Shapley indices for scalar outputs and aggregated Shapley indices for functional ones.

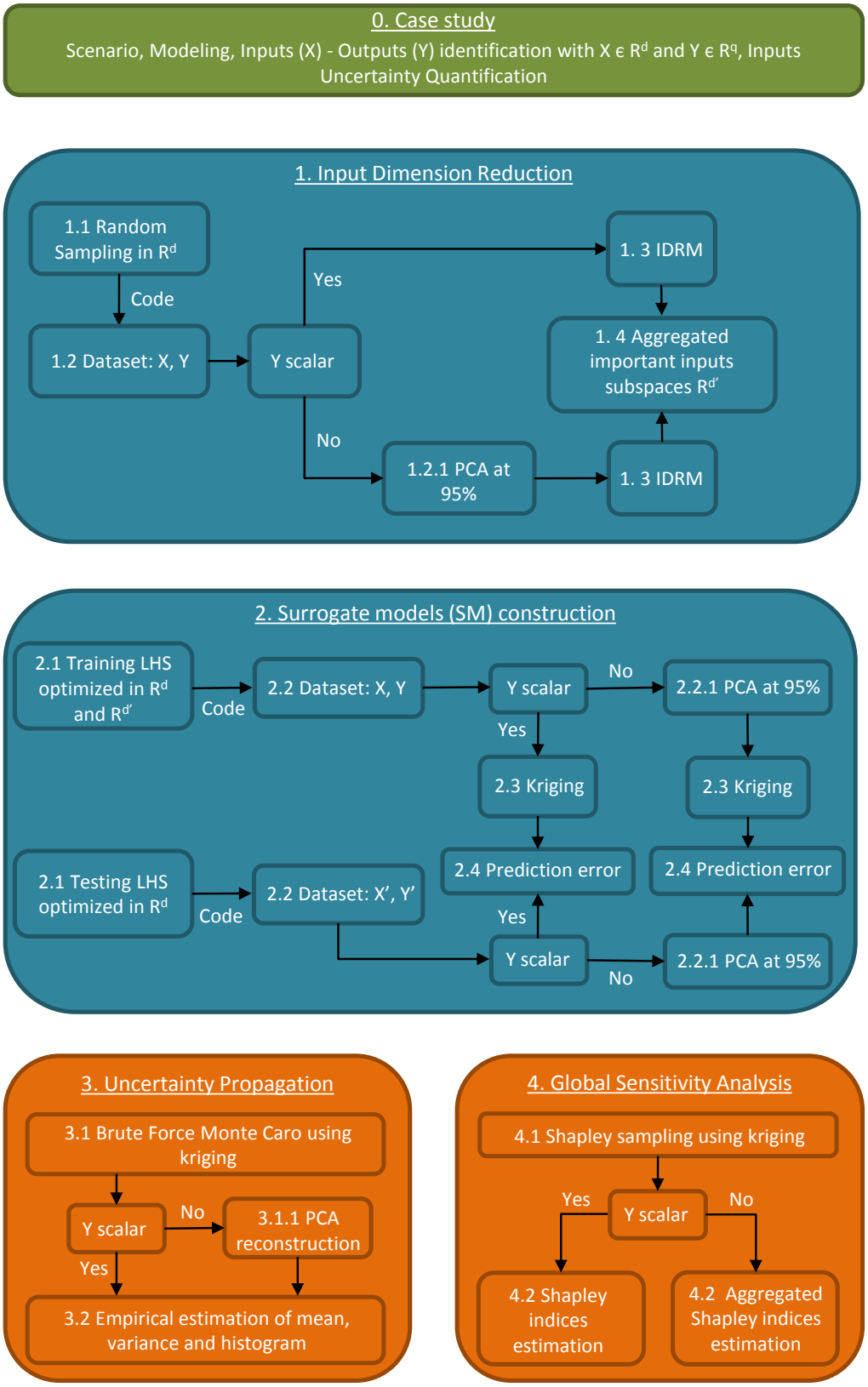

Figure 4.52: Uncertainty Quantification Methodology scheme

The developed UQM was applied to REA BE modeling in a large scale PWR core in Section 4.5. The studied outputs of interest where: the local maximum linear power P_{lin}^{max}, the linear power radial distribution P_{lin}^{2D} at the axial position and time instant of P_{lin}^{max}, the maximum stored enthalpy H_f^{max}, the minimum distance to boiling crisis DNB^{min}. The main conclusions drawn are:

- P_{lin}^{max} shows a relative standard deviation of 57% which is twice the value in the MiniCore tests. This is due to the increased sensitivity on the macroscopic cross-sections something reflected by the Shapley indices. The β_{eff} is responsible for 50 % of the variance and TD_1, D_1 and $S_{1\to 2}$ are responsible for the remaining 50 %.

- P_{lin}^{2D} shows relative standard deviations with small spatial distribution ranging between 53 % and 57 %. The location of P_{lin}^{max} is the one that exhibits the highest relative standard deviation. The aggregate Shapley indices showed similar sensitivities to the P_{lin}^{max}.

- H_f^{max} has 20 % relative standard deviation with a normal histogram. This reflects the linear behavior of this output. The same inputs as for P_{lin}^{max} are the dominant ones.

- DNB^{min} is quite further than in the MiniCore case with a mean value of 6 and a relative standard deviation of 57 %. The H_{gap} is responsible for 50 % of the variance and β_{eff}, TD_1, D_1 and $S_{1\to 2}$ are responsible for the remaining 50 %.

A second objective of the thesis was the development of a methodology for improving the BE modeling in terms of its uncertainty representation. Apart from the BE coupling in the CORPUS framework there exists a Best Effort coupling including ALCYONE V1.4 code for a detailed modeling of fuel-thermomechanics behavior. However, this modeling has a very high computational cost and its use for uncertainty quantification of REA is prohibited. One of the main REA modeling differences between BE and Best Effort coupling is the treatment of the gap heat transfer H_{gap}. In FLICA4 a constant value is used as an input of the code while in ALCYONE V1.4 the gap heat transfer is calculated taking into account the pellet-cladding gap behavior during the REA. Additionally, in the UQM application for the PWR core we observed that the H_{gap} is the most important input concerning DNB^{min}. There is thus a strong interest in extracting knowledge from ALCYONE V1.4 about the H_{gap} evolution during REA and apply it into the BE modeling.

We used a simplified H_{gap} model based on thermal expansions and including two calibration parameters: one related to the fuel temperature and one related to the stored energy. The latter captures a historical impact during the REA. In Section 3.6 we developed a methodology for calibrating this H_{gap} model that is presented in in figure 4.53. As for the UQM, this methodology was tested on the MiniCore and then applied to a PWR core in Section 4.6.

The H_{gap} calibration methodology includes three main steps. In step 1.1 the assemblies are grouped by burn-up with one model for each group. In step 1.2 the REA linear power and cladding wall temperature profiles are selected in such a way to cover the possible H_{gap} variations due to both spatial and statistical aspects. In step 2 these profiles are used as boundary conditions imposed in ALCYONE V1.4 REA decoupled calculations. In step 3.1, on the obtained results, the H_{gap} models are calibrated by mean square error minimization. Additionally, in step 3.2 the uncertainty of the models is quantified through two effective parameters, one representing the calibration error $H_{g,m}$ and one representing the model initial conditions $H_{g,i}$. The quantification of the H_{gap} models uncertainty is very interesting since it allows to propagate this uncertainty through the BE coupling. Finally, the calibrated H_{gap} models are introduced in the BE coupling improving its REA modeling.

In Section 3.6 the methodology was tested on the MiniCore geometry with very promising results. Small calibration errors were observed and the defined uncertainty ranges of the calibration parameters covered in all the cases the H_{gap} evolution during the REA predicted by ALCYONE V1.4. The calibrated H_{gap} models were then included in the BE coupling. This created the Improved Best Estimate (IBE) modeling. The UQM was tested on this improved modeling affecting mainly the margin to boiling crisis uncertainty quantification. The sensitivity of the H_{gap} decreased significantly due to its better modeling. Finally, the IBE modeling was compared to the Best Effort

modeling on three different design points in terms of the H_{gap} prediction. The resulting comparison showed an underestimation of the H_{gap} between $13\% - 17\%$. This is attributed to the many assumptions of the calibrated model and to the differences of the fuel-thermomechanics modeling in FLICA4 and ALCYONE V1.4. This indicates that IBE cannot replace the Best Effort modeling since there are many limiting assumptions but it can be used for a more realistic UQM on the large scale PWR core, where the Best Effort coupling is unfeasible.

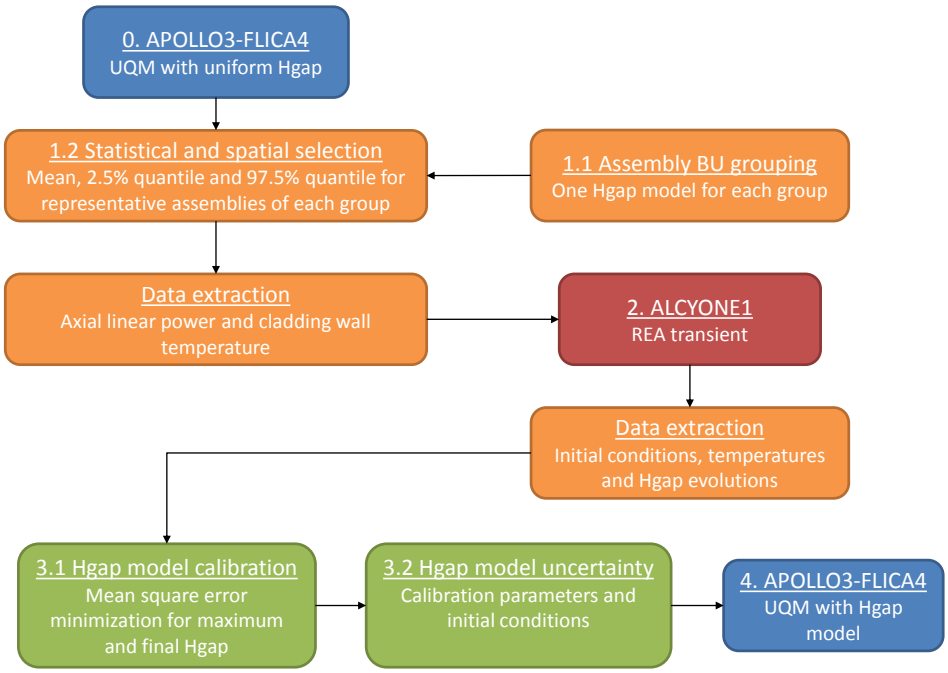

Figure 4.53: H_{gap} model calibration methodology

The H_{gap} model calibration methodology was applied to the PWR core in Section 4.6. For the calibration of the H_{gap} models 5 assembly groups were identified with one model per group. The resulting calibration errors for all the calibrated data are less than $8\,\%$. The calibrated H_{gap} models were introduced in the BE coupling and the UQM was applied again on the established IBE. The most significant impact was on the DNB^{min} with an increase $14\,\%$ of its mean value reducing the probability of boiling crisis. This is attributed to the more realistic modeling of the H_{gap} evolution during the REA. In the BE modeling the mean constant value of H_{gap} is $2.4e^4 W/m^2K$ much higher than the one predicted by the calibrated models and it is applied during the whole duration of the transient. This leads to a higher heat extracted from the fuel by the coolant in the BE modeling, something that explains the smaller DNB^{min} compared to the IBE modeling. The standard deviation of DNB^{min} was reduced to $42\,\%$. The reason is the decreased sensitivity on the H_{gap} uncertainty due to its better uncertainty quantification and modeling. This is observed in the Shapley indices for DNB^{min} where now β_{eff} is responsible for $50\,\%$ of the variance and TD_1, D_1 and $S_{1\to 2}$ for the remaining $50\,\%$.

In the last part of Chapter 4 (Section 4.7) three different thermal-hydraulics modeling options were compared for the IBE modeling. The first option M1 is the Multi-1D axial flow thermal-hydraulic channel per assembly. The second option M2 is 3D flow with one thermal-hydraulic channel per assembly. The third one M3 is 3D flow with four thermal-hydraulic channels per assembly. Different 3D functional outputs of interest for the coupling were studied together with the identified scalar outputs for the UQM. The main observation that can be made are the following:

- The M2 compared to M1 has an impact only on the minimum distance to boiling crisis DNB^{min}. Its mean value decreases by $7\,\%$ due to the reduction of the axial flow caused by the presence of transverse flows.
- The M3 compared to both M2 and M1 shifts the position of P_{lin}^{max} from the assembly with the ejected control rod to the next assembly at the border of the reflector. Axially it is also

shifted to one axial slice lower.

- The M3 compared to M2 reduces even further the mean value of DNB^{min} due to the increased P_{lin}^{max} seen by FLICA4. This leads to higher heat flux to be extracted by the coolant that reduces DNB^{min}.

We can conclude that M3 is more penalizing concerning P_{lin}^{max} and DNB^{min} and thus should definitely be used for safety analysis in comparison to M1 and M2. However, this comes at a four times more computational cost that renders difficult the uncertainty analysis. If we are mainly interested in sensitivities studies the model M2 is preferred since it is a good compromise in computational cost between M1 and M3.

Perspectives

The work done in this thesis can be seen as a first approach on a very complex problem. We remind its position in the identified transient and uncertainty quantification modeling evolution of figure 4.54. In this figure the example of the neutronic modeling is used. The developed methodologies for both uncertainty quantification and H_{gap} model calibration leave room for many improvements. The improvements can be inside the current modeling level or towards higher ones.

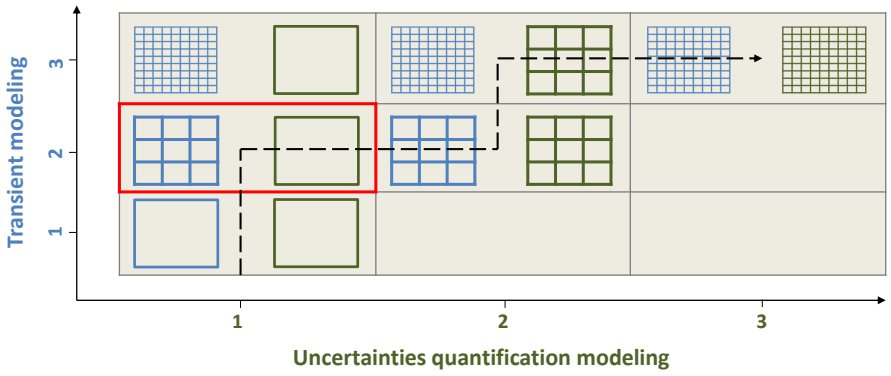

(1, 1)	Point kinetics with uncertainties on the core effective quantities (control rod worth, Doppler coefficient, etc.).
(1, 2)	Assembly level of homogenization with uncertainties on macroscopic cross-section applied homogeneously in the whole core.
(1, 3)	Pin by Pin level of homogenization with uncertainties on macroscopic cross-section applied homogeneously in the whole core.
(2, 2)	Assembly level of homogenization with uncertainties on macroscopic cross-section taking into account spatial correlations.
(2, 3)	Pin by Pin level of homogenization with uncertainties on macroscopic cross-section taking into account spatial correlations.
(3, 3)	Pin by Pin level of homogenization with uncertainties on microscopic cross-sections.

Figure 4.54: Different levels of possible transient (blue) and uncertainty quantification (green) modeling with examples for neutronics. With red borders we highlight the levels used in this thesis.

At the current (1,2) level, where we have an assembly level of homogenization for the REA and we apply the uncertainties homogeneously on the whole core, some interesting perspectives are identified :

- Extension of the UQM to include treatment of discontinuities. An example can be the post-DNB conditions.

- Improvement of the functional outputs treatment in the UQM by including advanced reduce order modeling techniques. This can even lead to a complete replacement of parts of the codes.
- Use of advanced feature extraction methods to improve the identification of important subspaces in the UQM.
- Application of the UQM in other types of transients such as LOCA.
- Investigate other sources of uncertainties such as: modeling and discretization options.
- Increase the complexity of the H_{gap} model. The simplified model used in this thesis is based on thermal expansions. This does not consider important phenomena such as: the "rim" region, fission gas releases and physico-chemical reactions. Simplified models for these phenomena could be included in the calibrated H_{gap} model.
- Adapt the H_{gap} model for allowing interpolation of the calibration parameters for each spatial mesh based on local quantities such as: burn-up and power. With this approach we could avoid the grouping of different fuel assemblies. The H_{gap} models will have the same discretization as the neutronics and thermal-hydraulics.
- More extensive comparison with Best Effort modeling and better quantification of the approximation error.

The possibility to increase the level of either the transient modeling or the uncertainty quantification modeling leads to the following perspectives:

- Extension of the UQM to functional inputs. This will allow for example to take into account spatial correlations of the macroscopic cross-sections. It can be seen as the level 2 uncertainty quantification modeling of figure 4.54. The correlations can be estimated by neutronic lattice calculations or as a first approach an artificial correlation distribution in the core can be used (e.x. based on the distance).
- Use a pin by pin level of homogenization. It can be seen as the level 3 the transient modeling of figure 4.54 and is very challenging due to increase of the computational cost. However, as a first approach the MiniCore geometry could be used. The uncertainty quantification modeling could be either at level 1 or 2.

Bibliography

[1] A. Targa. *Development of multi-physics and multi-scale Best Effort Modelling of pressurized water reactor under accidental situations.* Theses, Université Paris-Saclay, 2017.

[2] https://www.energy.gov/photos/yucca mountain.

[3] V. Jouaultn, J.-M. Palau, and G. Rimpault. New calculation method for PWR control rod assemblies with APOLLO3®. *Annals of Nuclear Energy*, 110:282 – 289, 2017.

[4] P. Reuss. *Précis de neutronique.* Collection Génie Atomique, EDP science.

[5] CEA. *Nuclear fuels.* Commissariat à l'Energie Atomique et aux Energies Alternatives (CEA), eDEN/DM2S/CEA, 2009.

[6] NEA. *Nuclear Fuel Behaviour Under Reactivity-initiated Accident (RIA) Conditions.* Number 6847. NEA/CSNI,R(2010)1, OCDE, 2010.

[7] F. D'Auria, N. Debrecin, and H. Glaeser. Strengthening nuclear reactor safety and analysis. *Nuclear Engineering and Design*, 324:209 – 219, 2017.

[8] International Nuclear Safety Advisory Group. Defence in Depth in Nuclear Safety. Technical Report INSAG-10, IAEA, 1996.

[9] CEA. *La neutronique - Les méthodes de la neutronique.* Commissariat à l'Energie Atomique et aux Energies Alternatives (CEA), eDEN/DM2S/CEA, http://www.cea.fr/energie/la-neutronique, 2013.

[10] A. Hébert. *Neutronique.* Ecole Polythechnique de Montréal, 1983.

[11] M. DeHart and S. Bowman. Reactor physics methods and analysis capabilities in SCALE. *Nuclear Technology*, 174(2):196–213, 2011.

[12] M. Herman and A. Trkov. Endf-6 formats manual. Technical report, National Nuclear Data Center, BNL, Upton, New York, 2005.

[13] W. M. Stacey. *Nuclear Reactor Physics.* John Wiley & Sons, 2007.

[14] C. Poinot-Salanon, A. Nicolas, and M. Soldevila. Methode de calcul neutronique des coeurs. *Technique de l'ingenieur bn3070*, 2013.

[15] A. Hébert. *Applied Reactor Physics.* Presse internationales Polytechnique, 2009.

[16] A. J. Koning et al. Status of the JEFF Nuclear Data Library. *Proceeding of the international conference on Nuclear Data for science and technology, Nice, France*, 2007.

[17] P. Mosca. *Conception et développement d'un mailleur énergétique adaptif pour la génération des bibliothèques multigroupes des codes de transport.* Theses, Université Paris Sud - Paris XI, December 2009.

[18] R. Sanchez, I. Zmijarevic, M. Coste-Delclaux, E. Masiello, S. Santandrea, E. Martinolli, L. Villate, N. Schwartz, and N. Guler. Apollo2 year 2010. *Nuclear Engineering and Technology*, 42, 10 2010.

[19] D. Schneider et al. APOLLO3®: CEA/DEN deterministic multi-purpose code for reactor physics analysis. *PHYSOR 2016, Sun Valley, Idaho, USA, May 1-5*, 2016.

[20] J. J. Duderstadt and L. J. Hamilton. *Nuclear Reactor Analysis*. John Wiley & Sons, 1976.

[21] C. Chabert and A. Santamarina. Calcul du coefficient Doppler pour les réacteur à eau. Technical report, CEA/DEN/CAD/DER/SPRC.LEPH/99-205, 1999.

[22] J.-C. Le Pallec. *Modelisation réaliste d'un accident de réactivité dans les REP et analyse d'incertitudes*. PhD thesis, Institut Nationale Polytechnique de Grenoble, 2002.

[23] A.-M. Baudron, J.-J. Lautard, Y. Maday, M. K. Riahi, and J. Salomon. Parareal in time 3D numerical solver for the LWR Benchmark neutron diffusion transient model. *Journal of Computational Physics, Elsevier*, 279:pp. 67–79, 10 2014.

[24] NEA. State-of-the-Art Report on Multi-scale Modelling of Nuclear Fuels. Technical report, NEA/NSC/R/(2015)5, OCDE, 2015.

[25] L. S. Tong and J. Weisman. *Thermal analysis of pressurized water reactors*. American Nuclear Society, 1996.

[26] V. MARELLE, V. BOUINEAU, A. BOULORE, C. FILLAUX, P. GOLDBRONN, T. HELFER, G. JOMARD, J. JULIEN, R. MASSON, B. MICHEL, L. NOIROT, and I. RAMIERE. ALCYONE V1.4: Notice de Présentation. Technical report, CEA/DEN/DEC/SESC/LSC NT 13-034, december 2013.

[27] R. L. Williamson, J. D. Hales, S. R. Novascone, M. R. Tonks, D. R. Gaston, C. J. Permann, D. Andrs, and R. C. Martineau. Multidimensional multiphysics simulation of nuclear fuel behavior. *Journal of Nuclear Materials*, 423(1):149 – 163, 2012.

[28] Paul Van Uffelen. *Modelling of Nulcear Fuel Behavior*. Institute for Transuranium Elements, 2006.

[29] B. Michel, J. Sercombe, G. Thouvenin, and R. Chatelet. 3D fuel cracking modelling in pellet cladding mechanical interaction. *Engineering Fracture Mechanics*, 75:3581 – 3598, 2008.

[30] L. Noirot. MARGARET: A comprehensive code for the description of fission gas behavior. *Nuclear Engineering and Design*, 241:2099–2118, 2011.

[31] M. Le Saux. *Comportement et rupture de gaines en Zircaloy-4 détendu vierges hydrurées ou irradiées en situation accidentelle de type RIA*. Phd thesis, Ecole des Mines de Paris, 2008.

[32] MATPRO (NUREC). *MATPRO - VERSION 11, A HANDBOOK OF MATERIALS PROPERTIES FOR USE IN THE ANALYSIS OF LIGHT WATER REACTOR FUEL ROD BEHAVIOR*. NUREC/CR-0497, TREE-1280, US. Nuclear Regulatory Commission, 1979.

[33] K. Lassmann and F. Hohlefeld. The revised urgap model to describe the gap conductance between fuel and cladding. *Nuclear Engineering and Design*, 103(2):215 – 221, 1987.

[34] J. Brochard et al. Modelling of pellet cladding interaction in pwr fuel. *SMIRT 16*, 2001.

[35] V. E. A. Marelle. New developments in ALCYONE 2.0 fuel performance code. *TOP FUEL ANS*, 2016.

[36] D. Planco. PLEIADES: a unified environment for multi-dimensional fuel performance modelling. *International Meeting on LWR Fuel Performance*, 19-22 September 2004.

[37] CASTEM. http://www-cast3m.cea.fr/cast3m/index.jsp.

[38] N. E. Todreas and M. S. Kazimi. *Nuclear Systems I: Thermal Hydraulic Fundamentals*. Taylor and Francis, 1993.

[39] D. Bestion. From the direct numerical simulation to system codes-perspective for the multi-scale analysis of LWR thermal hydraulics. *Nuclear Engineering and Technology*, 42(6):608 – 619, 2010.

[40] D. Bestion. Applicability of two-phase CFD to nuclear reactor thermalhydraulics and elaboration of Best Practice Guidelines. *Nuclear Engineering and Design*, 253:311–321, 2012.

[41] Gregoire, O. Établissement formel d'un modèle diphasique macroscopique à 6 equations, lien avec le modèle macroscopique à 4 equations. Technical report, CEA, 2008.

[42] S. Aniel, A. Bergeron, P. Fillion, G. Danielle, F. Gaudier, O. Grégoire, M. Martin, E. Richebois, E. Royer, P. Salvatore, S. Zimmer, T. Chataing, P. Clement, and F. François. Flica4: status of numerical and physical models and overview of applications. 10 2005.

[43] P. Fillion, A. Bergeron, D. Gallo, O. Gregoire, E. Richebois, E Royer, and S. Zimmer. FLICA4: Version 1.11.2 PUB, User guide, Reference manual of modules and procedures. *CEA Report*, 2013.

[44] I. Toumi et al. FLICA4: a three dimensional two-phase flow computer code with advanced numerical methods for nuclear applications. *Nuclear Engineering and Design*, 200:139–155, 2000.

[45] P. Fillion, A. Chanoine, S. Dellacherie, and A. Kumbaro. Flica-ovap: A new platform for core thermal–hydraulic studies. *Nuclear Engineering and Design*, 241(11):4348 – 4358, 2011. 13th International Topical Meeting on Nuclear Reactor Thermal Hydraulics (NURETH-13).

[46] JC. Le Pallec, V. Bergeaud, and C Delavaud. Uncertainties propagation in the framework of a rod ejection accident modeling based on a multiphysics approach. *Proceedings of ICAPP 2012*, Chicago, USA, June 24-28 2012.

[47] NEA. Fuel safety criteria in NEA member countries. Technical report, NEA/CSNI/R/(2003) 10, 2003.

[48] P. Turinsky, D. Kothe, and D. E. Burns. Update on capabilities development at casl. 05 2015.

[49] CASL. https://www.casl.gov/.

[50] NEAMS. https://www.energy.gov/sites/prod/files/2013/07/f2/NEAMS%20Executive%20Program%20Plan.pdf.

[51] NURESAFE. http://www.nuresafe.eu/.

[52] J.-C. Le Pallec and K. Mer-Nkonga. Neutronics/Fuel Thermomechanics coupling in the framework of a REA (Rod Ejection Accident) Transient Scenario Calculation. *PHYSOR 2016, Sun Valley, Idaho, USA, May 1-5*, 2016.

[53] SALOME. http://www.salome-platform.org/.

[54] F. D'Auria. BEPU status and perspectives. *ANS Best Estimate Plus Uncertainty International Conference, BEPU*, May 2018.

[55] T. Wickett (Editor) et al. Report of the Uncertainty Method Study for advanced best estimate thermal-hydraulic code application. Technical report, Vols. I and II NEA/CSNI R (97) 35, Paris(F), 1998.

[56] F. Reventos, H. Glaeser, and A. de Crecy. Main Results of the OECD BEMUSE Programme. *Nuclear Energy Agency of the OECS (NEA)*, 2013.

[57] NEA. PREMIUM: A Benchmark on the Quantification of the Uncertainty of the Physical Models in System Thermal-hydraulic Codes. Technical report, NEA/CSNI/R(2016)9, OCDE, 2016.

[58] J. Baccou, D. Bestion, M. Couplet, G. Damblin, P. Fillion, F. Fouet, J. Freixa, B. Iooss, R. Mendizábal, D. Yeon Oh, A. Petruzzi, P. Probst, F. Reventos, T. Skorek, T. Takeda, and J. Zhang. SAPIUM: A Systematic Approach for Input Uncertainty Quantification. *ANS Best Estimate Plus Uncertainty International Conference, BEPU*, May 2018.

[59] K. Ivanov, M. Avramova, S. Kamerow, I. Kodeli, E. Sartori, E. Ivanov, and O. Cabellos. Benchmarks for uncertainty analysis in modelling (UAM) for the design, operation and safety analysis of LWRs. *OECD Nucl. Energy Agency Volume I Specif. Support Data Neutronics Cases (Phase I), NEA/NSC/DOC(2013)7*, 2013.

[60] U. S. Rohatgi. Historical perspectives of BEPU research in US. *ANS Best Estimate Plus Uncertainty International Conference, BEPU*, May 2018.

[61] F. D'Auria, D. Cacuci, and A. Petruzzi. Approaches for computing uncertainties in predictionsof complex-codes. *International Nuclear Atlantic Conference 2007, INAC 2007*, 1, 2008.

[62] H. Glaeser. Methodologies for uncertainty evaluation of Best Estimate results: advangates and disadvantages of different approaches. *ANS Best Estimate Plus Uncertainty International Conference, BEPU*, May 2018.

[63] F. D'Auria, H. Glaeser, S. Lee, J. Misák, M. Modro, and R. Schultz. Best Estimate Safety Analysis for Nuclear Power Plants: Uncertainty Evaluation. *IAEA Safety Report Series*, 52, 2008.

[64] A. Petruzzi and F. D'Auria. Uncertainties in predictions by system thermal-hydraulic codes: The CASUALIDAD Method. *International Conference on Nuclear Engineering, Proceedings, ICONE*, 2, July 2014.

[65] A. Petruzzi. The CASUALIDAD method for uncertainty evaluation of Best Estimate system Thermal-Hydraulics calculations. *ANS Best Estimate Plus Uncertainty International Conference, BEPU*, May 2018.

[66] L. Brigs et al. Uncertainty quantification approaches for advanced reactor analyses. Technical report, Argonne National Laboratory (ANL), 2009.

[67] W. L. Oberkampf, S. M. DeLand, B. Rutherford, K. V. Diegert, and K. F. Alvin. Error and uncertainty in modeling and simulation. *Reliability Engineering & System Safety*, 75:333 – 357, 2002.

[68] S. Lutsanych. *Improving Best Estimate approaches with uncertainty quantification in nuclear reactory Thermal-Hydraulics.* PhD thesis, Univerisità di Pisa, 2016.

[69] C. Mesado. *Uncertainty Quantification and Sensitivity Analysis for Cross Sections and Thermohydraulic Parameters in Lattice and Core Physics Codes. Methodology for Cross Section Library Generation and Application to PWR and BWR.* PhD thesis, Universitat Politècnica de València, June 2017.

[70] F. Sanchez-Saez, A.I. Sánchez, J.F. Villanueva, S. Carlos, and S. Martorell. Uncertainty analysis of a large break loss of coolant accident in a pressurized water reactor using nonparametric methods. *Reliability Engineering & System Safety*, 174:19 – 28, 2018.

[71] S. Martorell, S. Sánchez-Sáez, J.F. Villanueva, and S. Carlos. An extended bepu approach integrating probabilistic assumptions on the availability of safety systems in deterministic safety analyses. *Reliability Engineering & System Safety*, 167:474 – 483, 2017. Special Section: Applications of Probabilistic Graphical Models in Dependability, Diagnosis and Prognosis.

[72] C. Blakely, H. Zhang, R. Szilard, A. Epiney, R. Vaghetto, and H. Ban. Demonstration of lotus multiphysics bepu analysis framework for lb-loca simulations. *Annals of Nuclear Energy*, 122:8 – 22, 2018.

[73] B. Sudret. *Uncertainty propagation and sensitivity analysis in mechanical models Contributions to structural reliability and stochastic spectral methods.* Habilitation à Diriger des Recherches Université BLAISE PASCAL-Clermont II, 2007.

[74] E. Omey and S. Van Gulck. *Central limit theorems for variances and correlation coefficients.* HUB, Brussels, 2008.

[75] Wold H. Estimation of principal components and related models by iterative least squares. *Academic Press*, pages 391 – 420, 1966.

[76] A. Alexanderian. *A brief note on the Karhunen-Loève expansion.* North Carolina State University, 2015.

[77] J.O. Ramsey and B.W. Silverman. *Functional Data Analysis.* Springer, New York, 2005.

[78] S. Nanty. *Stochastic methods for uncertainty treatment of functional variables in computer codes : application to safety studies.* These, Université Grenoble Alpes, October 2015.

[79] C. V. Mai and B. Sudret. Surrogate models for oscillatory systems using sparse polynomial chaos expansions and stochastic time warping. 2016.

[80] T. Hastie, R. Tibshirani, and J. H. Friedman. *The Elements of Statistical Learning: Data Mining, Inference, and Prediction.* Springer series in statistics. Springer, 2001.

[81] R. G. Ghanem and P. D. Spanos. *Stochastic Finite Elements: A Spectral Approach.* Springer, Verlag New York Inc., 1991.

[82] G. Blatman. *Adaptive sparse polynomial chaos expansions for uncertainty propagation and sensitivity analysis.* PhD thesis, 2009.

[83] F. Bachoc. *Estimation paramétrique de la fonction de covariance dans le modèle de Krigeage par processus Gaussiens : application à la quantification des incertitues en simulation numérique.* PhD thesis, 2013. Thèse de doctorat dirigée par Garnier, Josselin Mathématiques appliquées Paris 7 2013.

[84] C. E. Rasmussen and C. K. I. Williams. *Gaussian Processes for Machine Learning.* the MIT Press, Cambridge, Massachusetts, 2006.

[85] M. De lozzo. *Modèles de substitution spatio-temporels et multifidélité : Application à l'ingénierie thermique.* PhD thesis, 2013. Thèse de doctorat dirigée par Laurent, Béatrice et Harran-Klotz, Patricia Mathématiques Appliquées Toulouse, INSA 2013.

[86] T. J. Santner, B. J. Williams, and W. I. Notz. *The Design and Analysis of Computer Experiments.* Springer Series in Statistics. Springer New York, 2013.

[87] M. Griebel. Sparse grids and related approximation schemes for higher dimensional problems. In L. Pardo, A. Pinkus, E. Suli, and M.J. Todd, editors, *Foundations of Computational Mathematics (FoCM05), Santander*, pages 106–161. Cambridge University Press, 2006.

[88] J. Franco. *Exploratory Designs for Computer Experiments of Complex Physical Systems Simulation.* Theses, Ecole Nationale Supérieure des Mines de Saint-Etienne, Sep 2008.

[89] L. Pronzato and W. G. Müller. Design of computer experiments: space filling and beyond. *Statistics and Computing*, 22(3):681–701, May 2012.

[90] M. D. Morris and T. J. Mitchell. Exploratory designs for computational experiments. *Journal of Statistical Planning and Inference*, 43(3):381 – 402, 1995.

[91] G. Damblin, M. Couplet, and B. Iooss. Numerical studies of space-filling designs: optimization of latin hypercube samples and subprojection properties. *J. Simulation*, 7:276–289, 2013.

[92] A. Marrel. *Mise en oeuvre et exploitation du métamodèle processus gaussien pour l'analyse de modèles numériques - Application à un code de transport hydrogéologique.* These, INSA Toulouse, France, 2008.

[93] R. Jin, W. Chen, and A. Sudjianto. An efficient algorithm for constructing optimal design of computer experiments. *Journal of Statistical Planning and Inference*, 134(1):268–287, 9 2005.

[94] B. Iooss and P. Lemaître. A review on global sensitivity analysis methods. In C. Meloni and G. Dellino, editors, *Uncertainty management in Simulation-Optimization of Complex Systems: Algorithms and Applications.* Springer, 2015.

[95] I. M. Sobol. Sensitivity estimates for nonlinear mathematical models. *Mat. Model. 2*, page 112–118, 1990.

[96] A. B. Owen and C. Prieur. On Shapley value for measuring importance of depedent inputs. Technical report, STANFORD UNIVERSITY, March 2017.

[97] A. Saltelli. Making best use of model evaluations to compute sensitivity indices. *Computer Physics Communications*, (145):280–297, 2002.

[98] E. Song, B. L. Nelson, and J. Staum. Shapley effects for global sensitivity analysis: Theory and computation. *SIAM/ASA J. UNCERTAINTY QUANTIFICATION*, 4:1060–1083, 2016.

[99] S. Da Veiga. Global sensitivity analysis with dependence measures. *Journal of Statistical Computation and Simulation*, 85(7):1283–1305, 2015.

[100] G. J. Székely, M. L. Rizzo, and N. K. Bakirov. Measuring and testing dependence by correlation of distances. *The Annals of Statistics*, 35:2769–2794, 2007.

[101] A. Gretton, O. Bousquet, A. Smola, and B. Schölkopf. Measuring statistical dependence with hilbert-schmidt norms. In Sanjay Jain, H.U. Simon, and E. Tomita, editors, *Algorithmic Learning Theory*, pages 63–77, Berlin, Heidelberg, 2005. Springer Berlin Heidelberg.

[102] A. Friedman. *Foundations of Modern Analysis*. 2nd ed., New York, NY, USA: Dover, 1982.

[103] A. Aronsjanin. Theory of reproducing kernels. *Transactions of the American Mathematical Society*, 68(3):337–404, 1950.

[104] A. Gretton, R. Herbrich, A. Smola, O. Bousquet, and B. Schölkopf. Kernel methods for measuring independence. *Journal of Machine Learning Research*, 6:2075–2129, 12 2005.

[105] M. De Lozzo and A. Marrel. New improvements in the use of dependence measures for sensitivity analysis and screening. *Journal of Statistical Computation and Simulation*, 86(15):3038–3058, 2016.

[106] F. Gamboa, A. Janon, T. Klein, and A. Lagnoux. Sensitivity analysis for multidimensional and functional outputs. *Electronic Journal of Statistics*, 8:575–603, 2014.

[107] F. Ferraty and P. Vieu. *Nonparametric functional data analysis : theory and practice*. Springer New York, 2006.

[108] M. De Lozzo and A. Marrel. Sensitivity analysis with dependence and variance-based measures for spatio-temporal numerical simulators. working paper or preprint, January 2016.

[109] M. Carmassi, P. Barbillon, M. Keller, E. Parent, and M. Chiodetti. Bayesian calibration of a numerical code for prediction. *Journal de la Société Française de Statistique*, 160(1):1–30, 03 2019.

[110] M. C. Kennedy and A. O'Hagan. Bayesian calibration of computer models. *Journal of the Royal Statistical Society: Series B (Statistical Methodology)*, 63:425–464, 2001.

[111] H. Jeffreys. *Theory of Probability*. Oxford University Press, London, 1961.

[112] Liu et al. Modularization in bayesian analysis with emphasis on analysis of computer models. *Bayesian Analysis*, 4:119–150, 2009.

[113] K. Balasubramanian, S. Sriperumbudur, B. K., and G. Lebanon. Ultrahigh dimensional feature screening via rkhs embeddings. *Journal of Machine Learning Research*, 31:126–134, 1 2013.

[114] M. Yamada, J. Tang, J. Lugo-Martinez, E. Hodzic, R. Shrestha, A. Saha, H. Ouyang, D. Yin, H. Mamitsuka, C. Sahinalp, P. Radivojac, F. Menczer, and Y. Chang. Ultra high-dimensional nonlinear feature selection for big biological data. *IEEE Transactions on Knowledge and Data Engineering*, 30(7):1352–1365, July 2018.

[115] J. Chen, M. Stern, M. J. Wainwright, and M. I. Jordan. Kernel feature selection via conditional covariance minimization. In *Proceedings of the 31st International Conference on Neural Information Processing Systems*, NIPS'17, pages 6949–6958, USA, 2017. Curran Associates Inc.

[116] Y. Wang, H. Yao, and S. Zhao. Auto-encoder based dimensionality reduction. *Neurocomputing*, 184:232 – 242, 2016. RoLoD: Robust Local Descriptors for Computer Vision 2014.

[117] B. Iooss and A. Marrel. Advanced methodology for uncertainty propagation in computer experiments with large number of inputs. *Nuclear Technology*, pages 1 – 19, March 2019.

[118] M. A. Bouhlel, N Bartoli, A. Otsmane, and J. Morlier. Improving kriging surrogates of high-dimensional design models by partial least squares dimension reduction. *Structural and Multidisciplinary Optimization*, 53(5):935–952, May 2016. Thanks to Springer editor. The definitive version is available at https://link.springer.com/article/10.1007%2Fs00158-015-1395-9.

[119] G. Aversano, A. Bellemans, Z. Li, A. Coussement, O. Gicquel, and A. Parente. Application of reduced-order models based on PCA & Kriging for the development of digital twins of reacting flow applications. *Computers & Chemical Engineering*, 121:422 – 441, 2019.

[120] C. Lataniotis, S. Marelli, and B. Sudret. Extending classical surrogate modelling to ultrahigh dimensional problems through supervised dimensionality reduction: a data-driven approach. *CoRR*, abs/1812.06309, 2018.

[121] S. Demeyer, N. Fischer, and D. Marquis. Surrogate model based sequential sampling estimation of conformance probability for computationally expensive systems: application to fire safety science. *Journal de la société française de statistique*, Volume 158:111–138, 01 2017.

[122] G. Damblin, P. Barbillon, M. Keller, A. Pasanisi, and E. Parent. Adaptive numerical designs for the calibration of computer codes. *SIAM/ASA Journal on Uncertainty Quantification*, 6(1):151–179, 2018. AMS subject classifications. 62K99, 62L05, 60G15.

[123] G. Chastaing, F. Gamboa, and C. Prieur. Generalized sobol sensitivity indices for dependent variables: numerical methods. *Journal of Statistical Computation and Simulation*, 85(7):1306–1333, 2015.

[124] D. Lopez-Paz, P. Hennig, and B. Schölkopf. The randomized dependence coefficient. In *Proceedings of the 26th International Conference on Neural Information Processing Systems - Volume 1*, NIPS'13, pages 1–9, USA, 2013. Curran Associates Inc.

[125] L. Clouvel, P. Mosca, J.M. Martinez, and G.-K. Delipei. Shapley and johnson values for sensitivity analysis of pwr power distribution in fast fluence calculation. *ANS M&C International Conference on Mathematics and Computational Methods Applied to Nuclear Science and Engineering*, August 2019.

[126] J.-C. Fort, T. Klein, and N. Rachdi. New sensitivity analysis subordinated to a contrast. *Communications in Statistics - Theory and Methods*, 45(15):4349–4364, 2016.

[127] T. Browne, J.-C. Fort, B. Iooss, and L. Le Gratiet. Estimate of quantile-oriented sensitivity indices. working paper or preprint, January 2017.

[128] P. Lemaître, E. Sergienko, A. Arnaud, N. Bousquet, F. Gamboa, and B. Iooss. Density modification-based reliability sensitivity analysis. *Journal of Statistical Computation and Simulation*, 85(6):1200–1223, 2015.

[129] A. Bouloré, C. Struzik, and F. Gaudier. Uncertainty and sensitivity analysis of the nuclear fuel thermal behavior. *Nuclear Engineering and Design*, 253:200 – 210, 2012.

[130] G. Pastore, L.P. Swiler, J. Hales, S. Novascone, D.M. Perez, B. Spencer, l. Luzzi, P. Van Uffelen, and R. Williamson. Uncertainty and sensitivity analysis of fission gas behavior in engineering-scale fuel modeling. *Journal of Nuclear Materials*, 456:398–408, 01 2015.

[131] T. Ikonen and V. Tulkki. The importance of input interactions in the uncertainty and sensitivity analysis of nuclear fuel behavior. *Nuclear Engineering and Design*, 275:229 – 241, 2014.

[132] Dan G. Cacuci, M. Ilic, M. C. Badea, and R. Fang. Second-order adjoint sensitivity and uncertainty analysis of a heat transport benchmark problem—ii: Computational results using g4m reactor thermal-hydraulic parameters. *Nuclear Science and Engineering*, 183(1):22–38, 2016.

[133] X. Wu, C. Wang, and T. Kozlowski. Kriging-based surrogate models for uncertainty quantification and sensitivity analysis. *M&C 2017 - International Conference on Mathematics and Computational Methods Applied to Nuclear Science and Engineering*, 04 2017.

[134] D. Huang, H. Abdel-Khalik, C. Rabiti, and F. Gleicher. Dimensionality reducibility for multi-physics reduced order modeling. *Annals of Nuclear Energy*, 110:526 – 540, 2017.

[135] D. Rochman et al. Nuclear data uncertainties for typical lwr fuel assemblies and a simple reactor core. *Nuclear Data Sheets*, 139:1 – 76, 2017. Special Issue on Nuclear Reaction Data.

[136] E. Castro, S. Sánchez-Cervera, N. García-Herranz, and D. Cuervo. Impact of the homogenization level, nodal or pin-by-pin, on the uncertainty quantification with core simulators. *Progress in Nuclear Energy*, 104:218 – 228, 2018.

[137] C. Maunier and A. Lottin. Simulation par le code APOLLO2 de l'evolution du combustible REP enrichi à 4.5des concentrations globales et radiales avec les résultats expérimentaux. Technical report, DMT/93/445, 1993.

[138] T. A. Mara and S. Tarantola. Variance-based sensitivity indices for models with dependent inputs. *Reliability Engineering and System Safety*, 107:115–121, 2012.

[139] G. K. Delipei, J. Garnier, J.-C. Le Pallec, and B. Normand. Multi-physics uncertainty propagation in a PWR rod ejection accident modeling- Analysis methodology and first results. *ANS Best Estimate Plus Uncertainty International Conference (BEPU), Lucca*, May 2018.

[140] M. D. Morris, L. M. Moore, and M. D. McKay. Sampling plans based on balanced incomplete block designs for evaluating the importance of computer model inputs. *Journal of statistical planning and inference*, 136:3203–3220, May 2006.

[141] E. Gul, V. R. Joseph, and S. Ba. Maximum projection designs for computer experiments. *Biometrika*, 102(2):371–380, 03 2015.

[142] JC. Le Pallec, K. Mer-Nkonga, V., and N. Crouzet. Modélisation de type best-effort d'un transitoire ria sur un coeur rep1300 en gestion gemmes – mise en oeuvre d'un couplage apollo3®/flica4/alcyone-v1 dans corpus v2. Technical report, DEN/DANS/DM2S/SERMA/LPEC, 2018.

[143] A. Avvakumov, V. Malofeev, and V. Sidorov. Spatial Effects and Uncertainty Analysis for Rod Ejection Accidents in a PWR. Technical report, U.S. Nuclear Regulatory Commission, 2007.

Appendix A

Multi-parametric two group cross-sections

For the different studies in this thesis the two group macroscopic cross-sections of [1] are used. They are calculated at different core conditions and stored in multi-parametric tabulations. These tabulations of the cross-sections were created with APOLLO2 lattice calculations. The parameters of the tabulation are the burn-up BU, boron concentration C_{bor}, the fuel temperature T_f, the moderator density D_{mod} and the control rod presence CR. There are two fuel assemblies types and one reflector: the UO_2, $UO_2 - GdO_3$ and $REFL$. Their multi-parametric tabulation is presented in table A.1.

Table A.1: Multi-parametric tabulation of the two group macroscopic cross-section.

	UO_2		$U0_2 - GdO_3$		$REFL$	
	Range	Points	Range	Points	Range	Points
$C_{bor}\,[ppm]$	$[0, 2000]$	4	$[0, 2000]$	4	$[0, 1800]$	6
$T_f\,[°C]$	$[286, 2000]$	5	$[286, 2000]$	5	-	-
$D_{mod}\,[g/cm^3]$	$[0.598, 0.754]$	4	$[286, 2000]$	5	-	-
CR	$[0, 3]$	4	$[0, 3]$	4	-	-
$BU\,[GWd/t]$	$[0, 72]$	31	$[0, 72]$	57	-	-

In transient calculations the core conditions change and the cross-sections are linearly interpolated from their multi-parametric tabulation. For the CR parameter there are four different values indicating: the absence of control rod or the presence one out of three different types of control rods. The different types are based on their neutrons absorption capabilities. In each assembly the cross-sections represent a macro-isotope resulting from the homogenization of the different isotopes in the fuel assembly at Step 2 of the neutronic deterministic method presented in figure 1.7. However, some isotopes are not lumped in the macro-isotope and are treated separately. This usually is done for some isotopes with particular functionality like the poison isotopes. In this thesis the main isotopes are: $Xe - 135$, $I - 135$, $Nd - 147$, $Pm - 147$, $Pm - 148$, $Pm - 149$, $Sm - 149$, $B - 10$ and $B - 11$. Each individual isotope is described by its concentration and its microscopic cross-section. This allows the reconstruction of the final two group macroscopic cross-section including these isotopes.

Appendix B

Input uncertainty quantification

For the Uncertainty Quantification Methodology (UQM) development and application we identified 22 uncertain inputs spanning neutronics, fuel-thermomechanics and thermal-hydraulics. The inputs uncertainty quantification is based on a mixture of expert judgment and previous uncertainty propagation results.

In neutronics we have 11 inputs: TD_1, TD_2, NF_1, NF_2, D_1, D_2, $S_{1\to2}$, IV_1, IV_2, β_{eff}, λ_{eff}. For their uncertainty quantification multivariate normal distribution is considered $\mathcal{N}(\mathbf{\Sigma_{CEA}}, \mathbf{C_{UAM}})$ with mean vector $\mathbf{\Sigma_{CEA}}$ the reference two group macroscopic cross-sections generated using *APOLLO*2 and covariance matrix $\mathbf{C_{UAM}}$ estimated using data from UAM benchmark. The data from UAM are in the form of 100 cross-section evaluations. In order to apply these uncertainties on our reference cross-sections we estimate the relative standard deviation and the correlation matrix from UAM data. The provided cross-sections are: A_1, A_2, NF_1, NF_2, D_1, D_2, $S_{1\to2}$, IV_1, IV_2, β_{eff}, λ_{eff}. We see that the absorption cross-section A_1 and A_2 are provided instead of the total cross-sections T_1 and T_2 used by APOLLO3 ®. We can write the total cross-sections as:

$$T_1 = A_1 + S_{1\to2} + S_{1\to1} + N_{exc1} \tag{B.1}$$

$$T_2 = A_2 + S_{2\to1} + S_{2\to2} + N_{exc2} \tag{B.2}$$

Where:

- N_{exc1} and N_{exc2} are the $n-2n, n-3n\ldots$ cross-sections producing more than one neutron for the two groups.
- $S_{1\to1}$ and $S_{2\to2}$ are the self-scattering cross-sections.

We define the disappearance cross-sections as $TD_1 = T_1 - S_{1\to1}$ and $TD_2 = T_2 - S_{2\to2}$ and re-write the previous equations as:

$$TD_1 = A_1 + S_{1\to2} + N_{exc1} \tag{B.3}$$

$$TD_2 = A_2 + S_{2\to1} + N_{exc2} \tag{B.4}$$

By neglecting the uncertainties on the up-scattering cross-section $S_{2\to1}$ and the $n-2n, n-3n\ldots$ cross-sections then the TD_1 and TD_2 from UAM can be calculated. Then the correlation matrix $\mathbf{R_{UAM}}$ and the relative standard deviation vector $\mathbf{Sr_{UAM}}$ are estimated empirically. By multiplying the $\mathbf{Sr_{UAM}}$ with the reference values $\mathbf{\Sigma_{CEA}}$ we obtain the standard deviation vector $\mathbf{S_{UAM}}$. Finally the covariance matrix for our reference cross-sections is calculated by:

$$\mathbf{C_{UAM}} = \mathbf{S_{UAM}}\,\mathbf{S_{UAM}}^T\mathbf{R_{UAM}} \tag{B.5}$$

For simplifying the neutronic input uncertainty quantification they are considered fully positively correlated in all the spatial meshes and for all the multi-parametric points.

In fuel-thermomechanics the following inputs are considered as independent: λ_f, λ_c, Cp_f, Cp_c, H_{gap}, P_r, T_R. For the fuel and cladding material laws (λ_f, λ_c, Cp_f, Cp_c) the UAM recommendations were followed by using normal pdf for multiplication coefficients on the different laws as presented in table 3.4. For H_{gap} in the initial Best Estimate coupling a uniform pdf bounded by its value for a complete open gap ($2e^3\,Wm^{-2}K^{-1}$) and for a pellet-cladding contact ($5e^4\,Wm^{-2}K^{-1}$) is used. However, in the IBE coupling simplified H_{gap} models were calibrated for different assembly groups. The models included two calibration parameters. For their uncertainty quantification as for the cross-section they were considered as fully positevely correlated with bounds that cover the calibration error as discussed in Section 3.6. This leads to one uncertain quantity representing the calibration error $H_{g,m}$. Additionally, uncertain initial conditions are considered for the models. More specifically the initial gap heat transfer H_{gap}^{init} and gap width e_{gap}^{init}. Based on previous uncertainty propagation results of ALCYONE V1.4 fuel evolution calculations these two quantities were found fully negatively correlated. The estimated relative standard deviation is 10%. The uncertainty is applied as a multiplication coefficient on both quantities with pdf $\mathcal{N}(1.0, 0.1)$. This leads to a second uncertain quantity representing the initial conditions $H_{g,i}$. The power radial profile is modeled by a burn-up function $P_r^{1D} = f(BU)$ defined in [137]. The problem is that the we have uncertainty of 1.75% relative standard deviation for the power at the external surface due to the radial discretization used for the fitting of the function. Besides, that we also know that there is an 8 % impact of the presence or not of a guide tube near the fuel pin as was found in [22]. We model these two uncertainties as a sum of two independent pdf $\mathcal{N}(0, 0.0175)$ and $\mathcal{U}(1, 1.08)$ applied as a multiplication coefficient on the power at the external surface. For the Rowlands temperature T_R a uniform distribution was considered on the weight fraction of the fuel centerline temperature. In the reference situation the Rowlands temperature has a 4/9 weight on the fuel centerline temperature and 5/9 on the fuel external surface temperature. By using an uncertain multiplication factor with $\mathcal{U}(0, 1)$ on the centerline temperature weight we consider that it can only decrease uniformly between 4/9 and zero with a corresponding increase in the external surface temperature weight.

In thermal-hydraulics the following uncertain inputs are considered: H_c, R_{crit}, K_{v0}, H_{dnb}. All of them are quantified based on expert judgments and presented in table 3.4.

Appendix C

Criticality method impact on sensitivity

The core prior to the REA is at critical state, meaning that for each perturbation of cross-sections the core has to be rendered critical. The method used to achieve this can affect the uncertainty analysis of the transient. In this study we investigate the criticality method impact on APOLLO3 ® static stand-alone calculations. Three different methods are tested in order to identify the most suitable:

1. Fission rate adjustment: the k_{eff} is computed and the fission rate is normalized by this value, establishing the balance between production and absorption.
2. Boron adjustment: The boron absorbs neutrons and by modifying its concentration in the whole core criticality can be achieved.
3. Leakage adjustment: The leakage of neutrons is adjusted by modifying the reflector's diffusion coefficient of fast neutrons.

Each method alters the neutron spectrum and the leakage at the reflector-fuel interface. The effect on those quantities is estimated by the average flux ratio of fast and thermal neutrons ($\frac{\phi_1}{\phi_2}$) for the first and by the average of the albedo on the reflector-fuel surface (a) for the second. Besides that, criticality method's effect on the neutron spectrum and the albedo should not vary significantly with the core's size in order to be applicable to larger scale cores. The original MiniCore geometry and two larger cores by adding 1 and 2 fuel rings respectively were studied. For each geometry the neutron spectrum and albedo were estimated at the reference and $\pm 2\sigma$ of their k_{eff} pdf. In Section 3.4.2.1 we saw that k_{eff} has a standard deviation of $550\,pcm$.

The criticality methods have effects that may vary with the core geometry. We show such variations in figures C.1 - C.3. The first observation is that the leakage adjustment is the only method that varies with geometry passing from 5% effect on albedo to 80% and thus is rejected. The other two methods are not impacted significantly but it should be noted that as expected the boron concentration adjustment alters the neutron spectrum due to the increase of epithermal neutrons absorption, impacting the $S_{1\to 2}$ cross-section.

Criticality methods have an impact on two quantities directly linked to REA: control rod worth ρ_{worth} and 3D deformation factor $Fxyz_{\text{ext}}$ with the control extracted. For the two remaining methods their impact on the sensitivity analysis is studied. The results for $Fxyz_{\text{ext}}$ do not show any effect of the methods. However, the results on ρ_{worth} vary significantly as shown in figure C.4. The Shapley indices of NF_1 and NF_2 are strongly reduced in fission adjustment. This indicates that the criticality method selection has an important effect on the static analysis sensitivity.

Boron concentration adjustment is selected for the transient analysis, because it is applicable on larger cores and it is a more realistic method from the reactor operation point of view.

In [139] a sensitivity analysis was carried out for REA transient APOLLO3 ® stand-alone modeling. As uncertain inputs the two group macroscopic cross-sections together with an additional

discrete input parameter indicating the criticality method used. The three different methods were considered with 1/3 probability. The resulting Shapley indices indicate that the criticality method amounts up to 20% of the maximum local linear power variance.

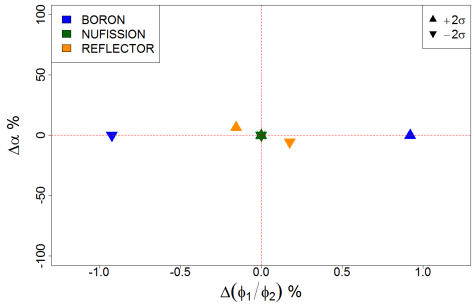

Figure C.1: Criticality methods effect for the MiniCore

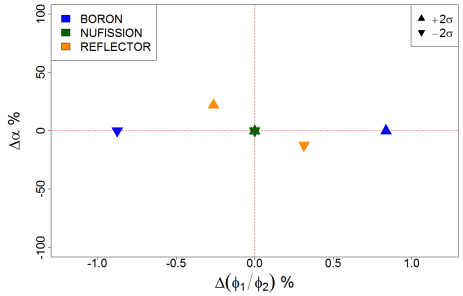

Figure C.2: Criticality methods effect for geometry with 1 added fuel ring (4x4 fuel cluster)

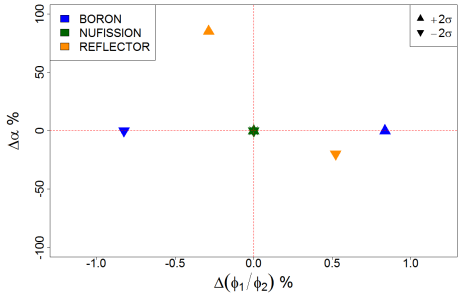

Figure C.3: Criticality methods effect for geometry with 2 added fuel ring (5x5 fuel cluster)

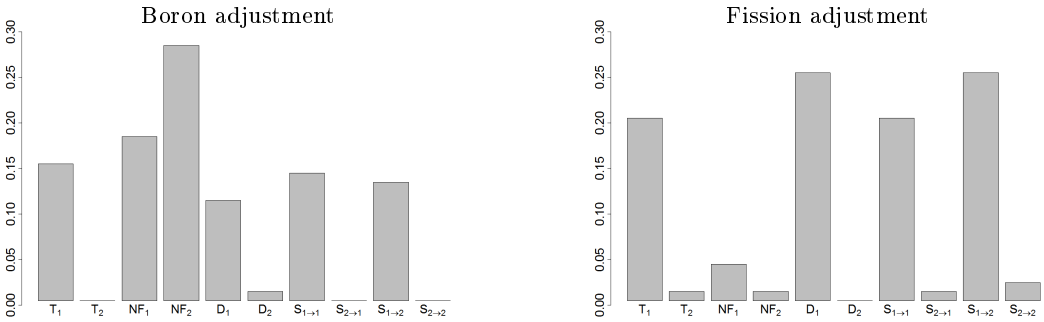

Figure C.4: ρ_{worth} Shapley indices with boron adjustment and fission adjustment.

Appendix D

Point kinetics REA uncertainty analysis

It is possible to obtain an analytic expression for the local maximum linear power during the REA if point kinetics is used for the neutronic modeling. It is called the Nordheim-Fuchs model and is valid for prompt neutron driven REA [143]. The reactivity evolution during the transient can be written as:

$$\rho(t) = \rho_{worth} + \theta_d E(t) \tag{D.1}$$

Where:

- ρ_{worth} is the control rod worth of the ejected rod.
- θ_d is the feedback parameter.
- E is the energy deposition in the fuel.

The maximum power during the transient can be expressed then as:

$$P^{max} = \frac{(\rho_{worth} - \beta_{eff})^2}{2\Lambda\theta_d} \tag{D.2}$$

Where:

- Λ is the prompt neutron lifetime.

By making the following assumptions the θ_d can be calculated as in [143] :

- Adiabatic fuel thermal treatment.
- Constant Doppler coefficient during REA .
- Constant specific fuel heat capacity during REA.

The values used in [143] are adopted for this study and are synthesized together with the values related to the MiniCore case in table D.1.

$\boldsymbol{\rho_{worth}}$ **(pcm)**	959
$\boldsymbol{\beta_{eff}}$ **(pcm)**	569
$\boldsymbol{\Lambda}$ **(s)**	$1.87e^{-5}$
$\boldsymbol{\theta_d}$ **(MJ^{-1})**	$2.56e^{-6}$

Table D.1: Point kinetic model parameters values.

For the maximum local linear power the multiplication coefficient of the MiniCore is used. For the uncertainty analysis we consider the following uncertain inputs: ρ_{worth}, β_{eff} and θ_d. This is done in order to be closer to the MiniCore study. For ρ_{worth} a normal distribution is used with mean and standard deviation from the results of Section 3.4.2.1. For β_{eff} a normal distribution is used with mean and standard deviation as in the inputs uncertainty quantification of table 3.4. For θ_d a normal law is used with the relative standard deviation of [143]. The uncertainty quantification is summarized in table D.2.

$\boldsymbol{\rho_{worth}}$ **(pcm)**	$\mathcal{N}(970, 13.58)$
$\boldsymbol{\beta_{eff}}$ **(pcm)**	$\mathcal{N}(970, 43.89)$
$\boldsymbol{\theta_d}$ **(MJ^{-1})**	$\mathcal{N}(2.56e^{-6}, 1.28e^{-7})$

Table D.2: Point kinetic model parameters uncertainty quantification.

The results of applying all the uncertain parameters is presented in figure D.1, where we can see the estimated histogram. It is quite close to the $3D$ APOLLO3 ® study indicating the persistence of the point kinetics concerning the P_{lin}^{max} calculation.

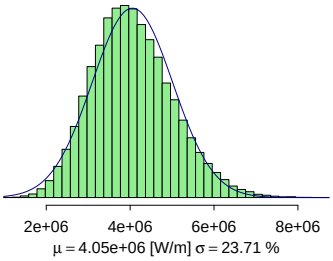

Figure D.1: Estimated histogram of P_{lin}^{max} for point kinetics study.

In this study the inputs are considered independent. It is thus interesting to investigated the effect of fixing some of the uncertain inputs in their reference values and see the remaining part of the variance. This would be equivalent to estimating the total Sobol indices of each input. The inputs considered as uncertain for the different analyses are:

- **A1**: $\boldsymbol{\rho_{worth}}$, $\boldsymbol{\beta_{eff}}$, $\boldsymbol{\theta_d}$.
- **A2**: $\boldsymbol{\rho_{worth}}$, $\boldsymbol{\beta_{eff}}$.
- **A3**: $\boldsymbol{\rho_{worth}}$, $\boldsymbol{\theta_d}$.
- **A4**: $\boldsymbol{\beta_{eff}}$, $\boldsymbol{\theta_d}$.
- **A5**: $\boldsymbol{\rho_{worth}}$.
- **A6**: $\boldsymbol{\beta_{eff}}$.
- **A7**: $\boldsymbol{\theta_d}$.

The results for the different analyses are gathered in table D.3. We can see that the dominant input as in the MiniCore is the β_{eff}. The control rod worth uncertainty amounts to a total of 6.5% of output's relative standard deviation. The feedback (Doppler) parameter leads to a total of 5% of output's relative standard deviation.

	Relative Standard Deviation (%)
A1	23.7
A2	23.2
A3	8.2
A4	22.9
A5	6.4
A6	22.3
A7	5.0

Table D.3: Point kinetic uncertainty analysis results.

Appendix E

Complementary results for PWR IBE coupling

In Section 4.7.2 we presented uncertainty quantification results for the Improved Best Estimate (IBE) modeling. We focused on the analysis of $3D$ fields for the following identified outputs of interest:

- Linear power P_{lin}^{3D} at the instance of its local maximum.
- Stored enthalpy in the fuel H_f^{3D} at the instance of its local maximum.
- Cladding wall heat flux W_f^{3D} at the instance of its local maximum.
- Gap heat transfer H_{gap}^{3D} at the instance of its local maximum.
- Coolant density D_w^{3D} at the instance of its local minimum.

The 3D fields are difficult to visualize and for this reason in Section 4.7.2 two cross-sections were presented for each output: the radial and axial cross-sections at the position of the local maximum (or minimum). For these cross-section the mean and relative standard deviation distributions were estimate. In this Section we present a larger variety of results. For each functional $3D$ output we illustrate the histograms for the highlighted part of figure E.1 at the axial slice of the P_{lin}^{max}. This part corresponds to the 1/8 of the PWR core and includes the assembly with the ejected control rod.

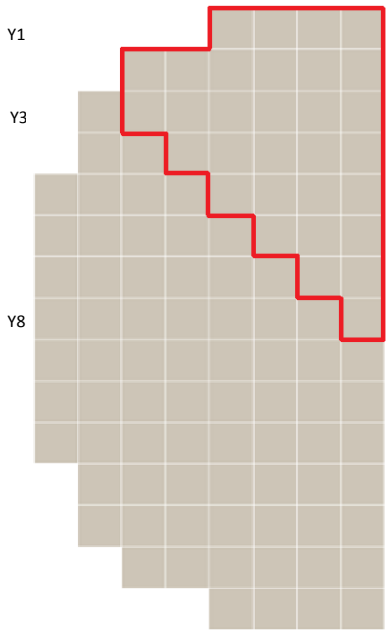

Figure E.1: 1/2 PWR geometry with highlighted (red borders) the locations for which we estimate the histograms of the different $3D$ outputs.

Additionally, for each functional output we provide the result for the mean and standard deviation distributions at 6 different cross-sections. Axially we focus on three cross-sections along the Y axis at the locations seen in figure E.1. Two cross-section around the location of the maximum linear power at $Y1$ and $Y3$ and one cross-section at the center of the core ($Y8$). Radially we focus on three cross-sections along the Z axis at the bottom ($Z1$), middle ($Z15$) and top ($Z30$) axial slices. We present first all the results and afterwards at the end we analyze them.

Results for P_{lin}^{3D}

- **Histograms**

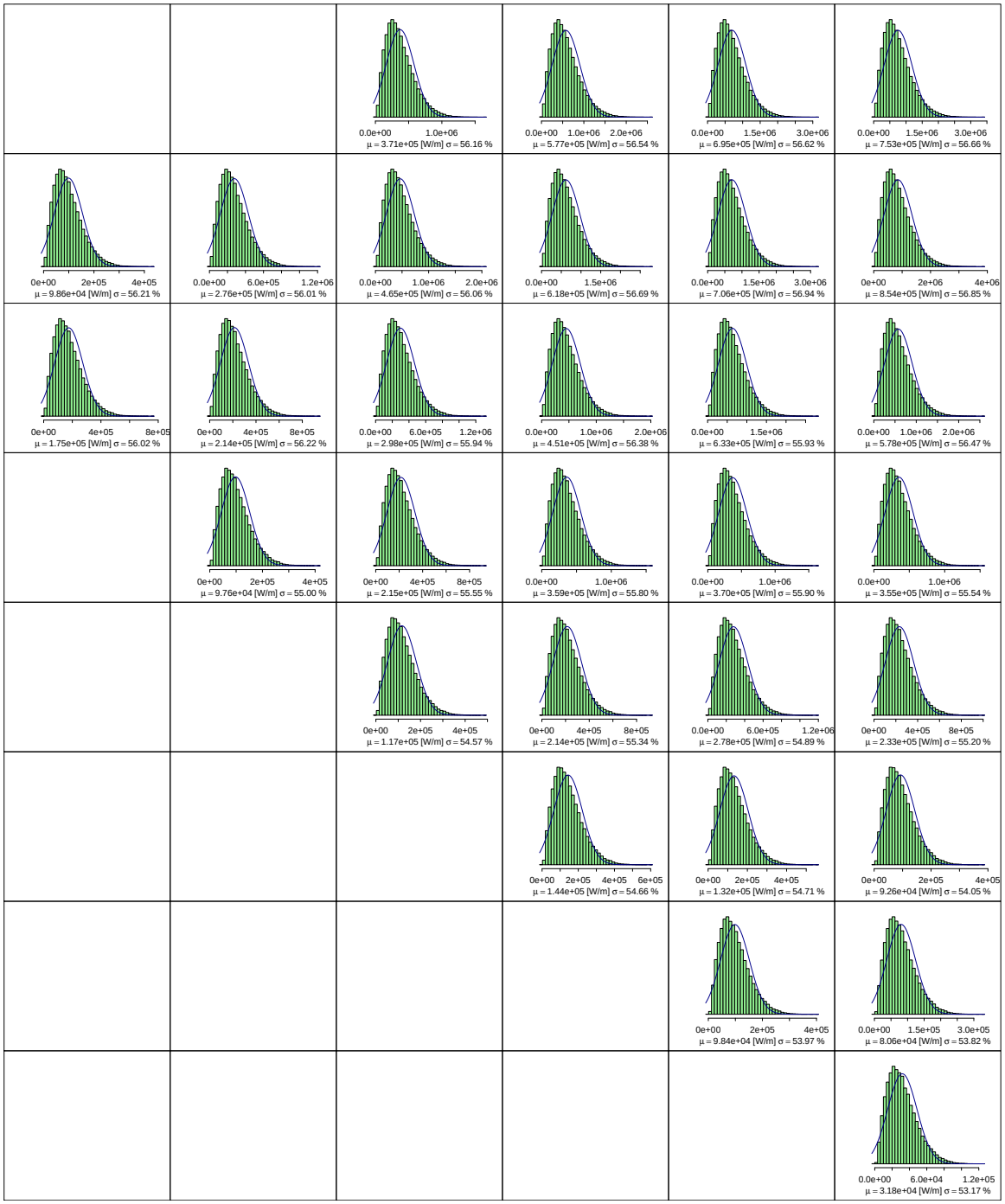

Figure E.2: P_{lin}^{3D} estimated histograms for IBE coupling study in PWR core.

- **Y1 cross-section**

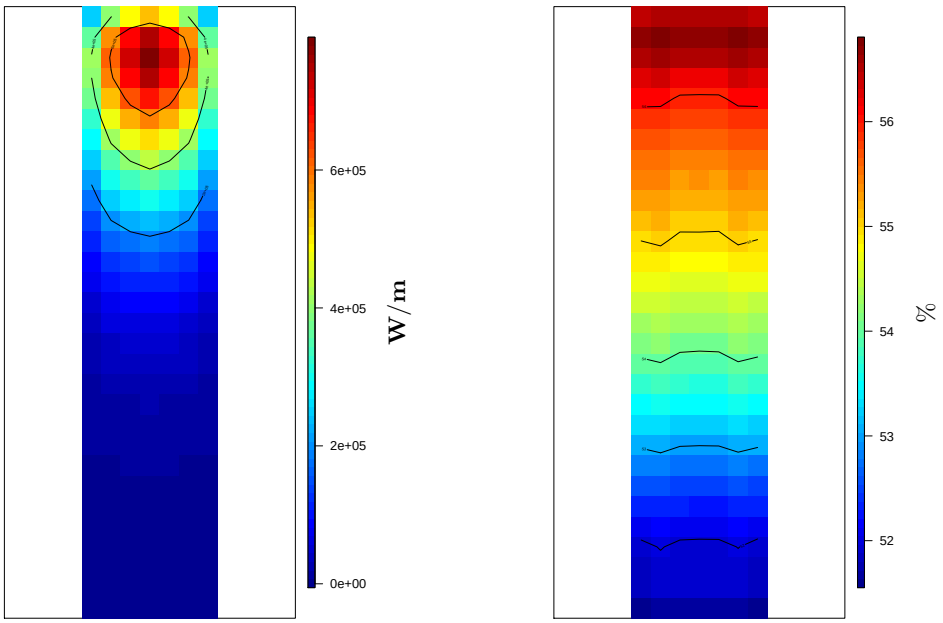

(a) Mean (b) Relative standard deviation

Figure E.3: P_{lin}^{3D} estimated mean and relative standard deviation in the axial cross-section at $Y1$ for IBE coupling study in PWR core.

- **Z1 cross-section**

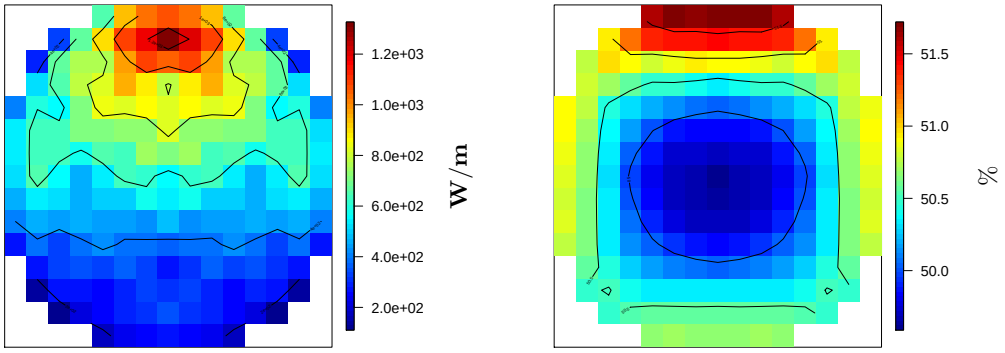

(a) Mean (b) Relative standard deviation

Figure E.4: P_{lin}^{3D} estimated mean and relative standard deviation in the radial cross-section at $Z1$ for IBE coupling study in PWR core.

- **Y3 cross-section**

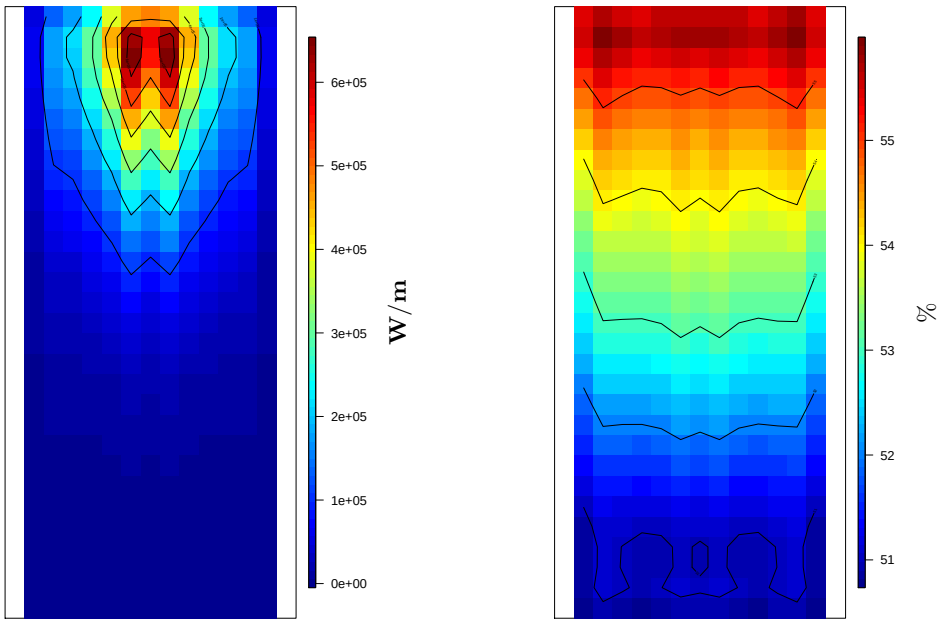

(a) Mean (b) Relative standard deviation

Figure E.5: P_{lin}^{3D} estimated mean and relative standard deviation in the axial cross-section at $Y3$ for IBE coupling study in PWR core.

- **Z15 cross-section**

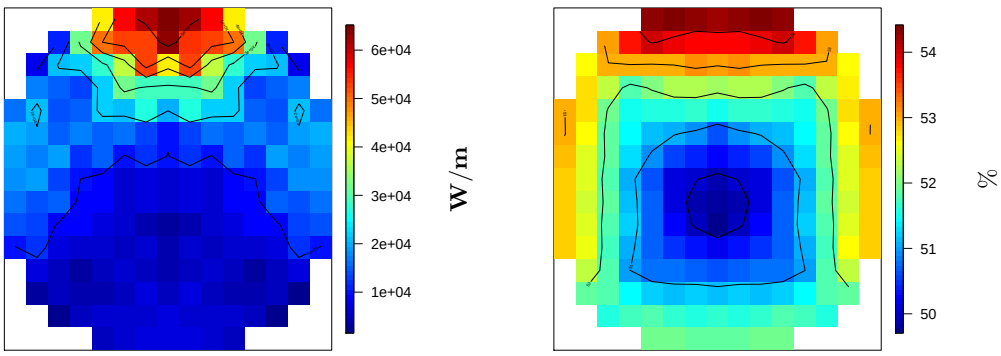

(a) Mean (b) Relative standard deviation

Figure E.6: P_{lin}^{3D} estimated mean and relative standard deviation in the radial cross-section at $Z15$ for IBE coupling study in PWR core.

- **Y8 cross-section**

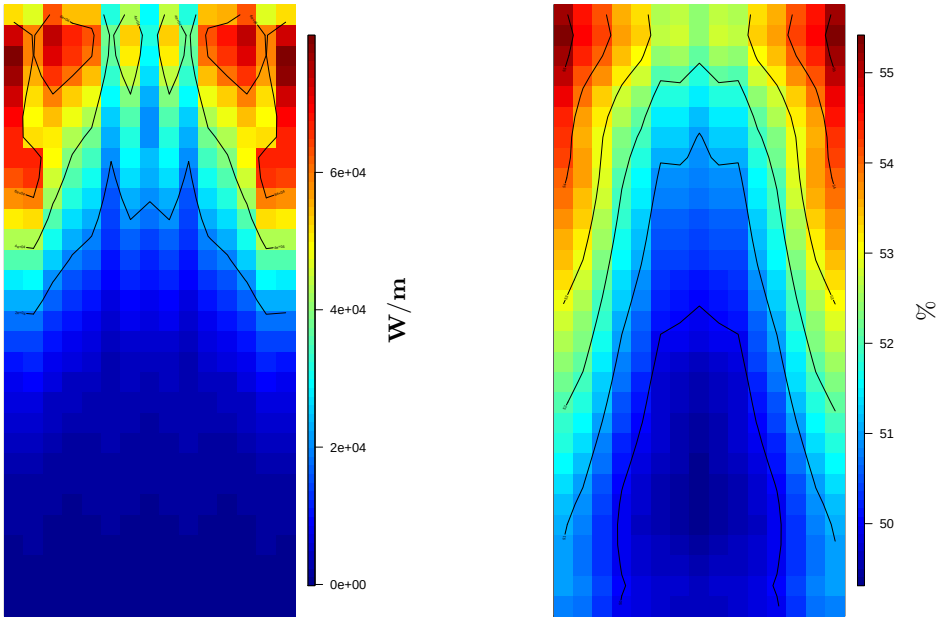

(a) Mean (b) Relative standard deviation

Figure E.7: P_{lin}^{3D} estimated mean and relative standard deviation in the axial cross-section at $Y8$ for IBE coupling study in PWR core.

- **Z30 cross-section**

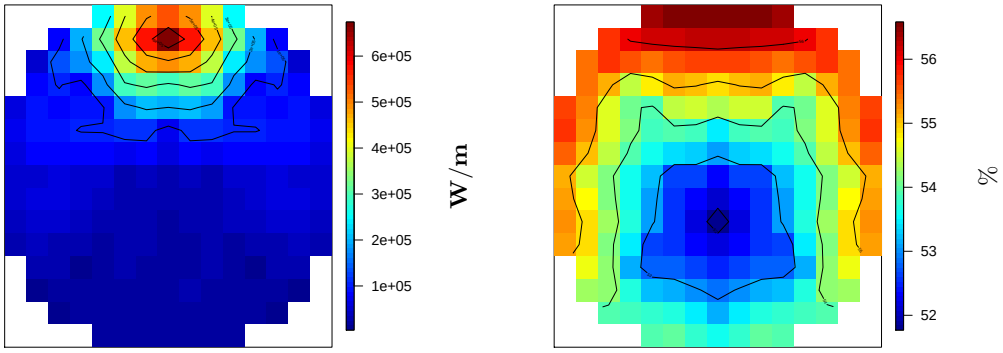

(a) Mean (b) Relative standard deviation

Figure E.8: P_{lin}^{3D} estimated mean and relative standard deviation in the radial cross-section at $Z30$ for IBE coupling study in PWR core.

Results for H_f^{3D}

- **Histograms**

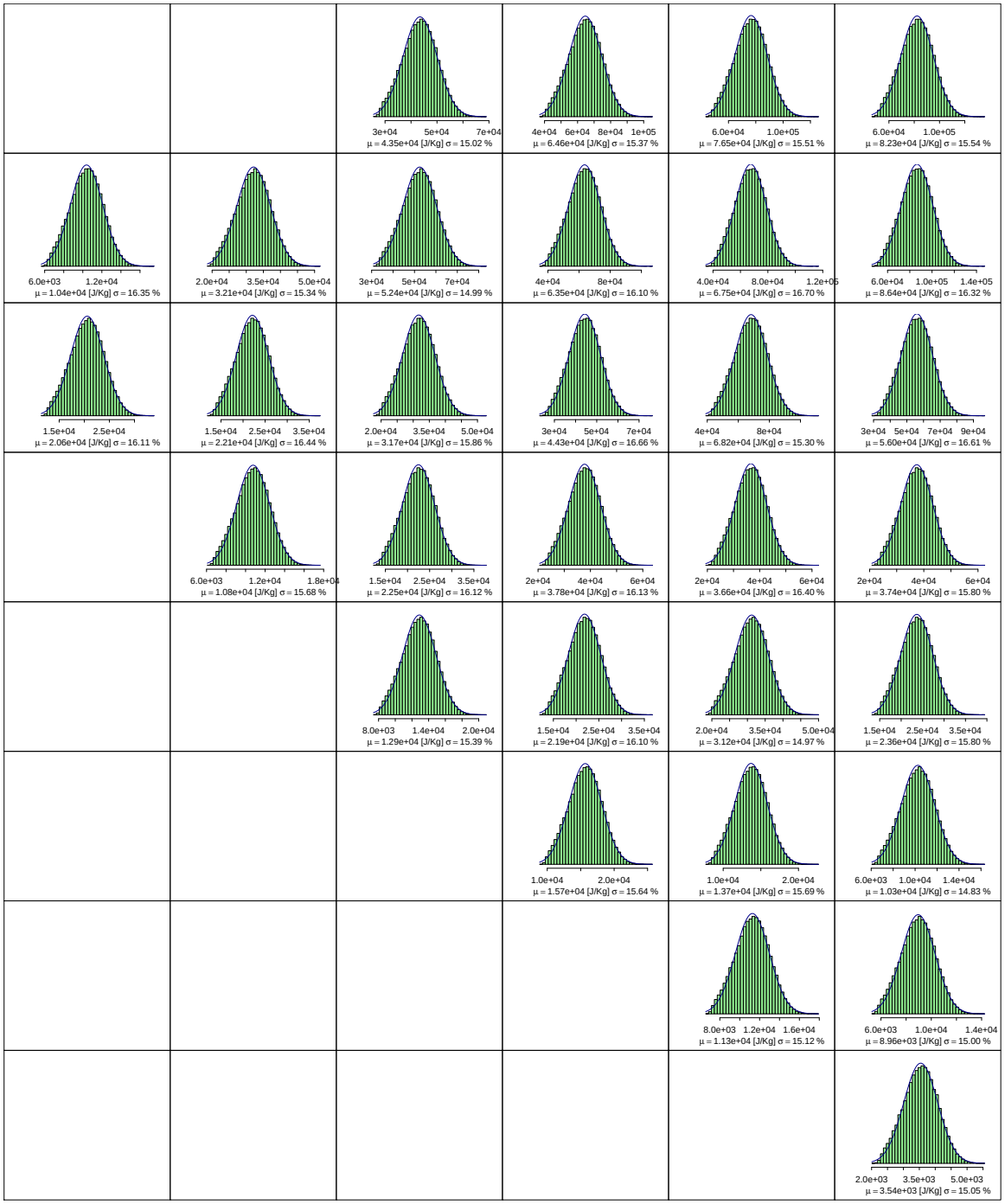

Figure E.9: H_f^{3D} estimated histograms for IBE coupling study in PWR core.

- **Y1 cross-section**

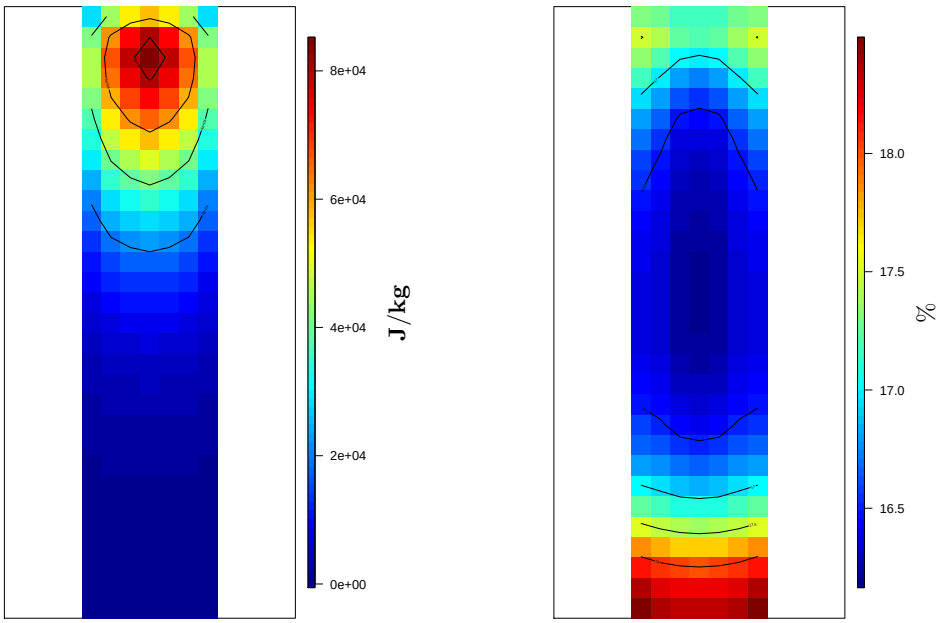

(a) Mean (b) Relative standard deviation

Figure E.10: H_f^{3D} estimated mean and relative standard deviation in the axial cross-section at $Y1$ for IBE coupling study in PWR core.

- **Z1 cross-section**

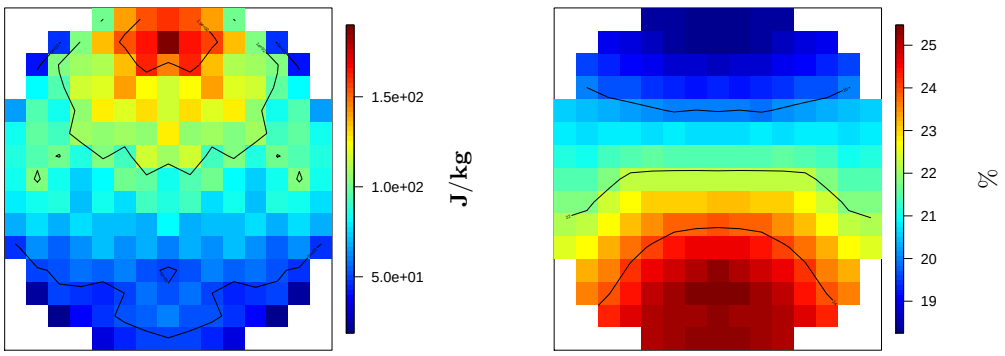

(a) Mean (b) Relative standard deviation

Figure E.11: H_f^{3D} estimated mean and relative standard deviation in the radial cross-section at $Z1$ for IBE coupling study in PWR core.

- **Y3 cross-section**

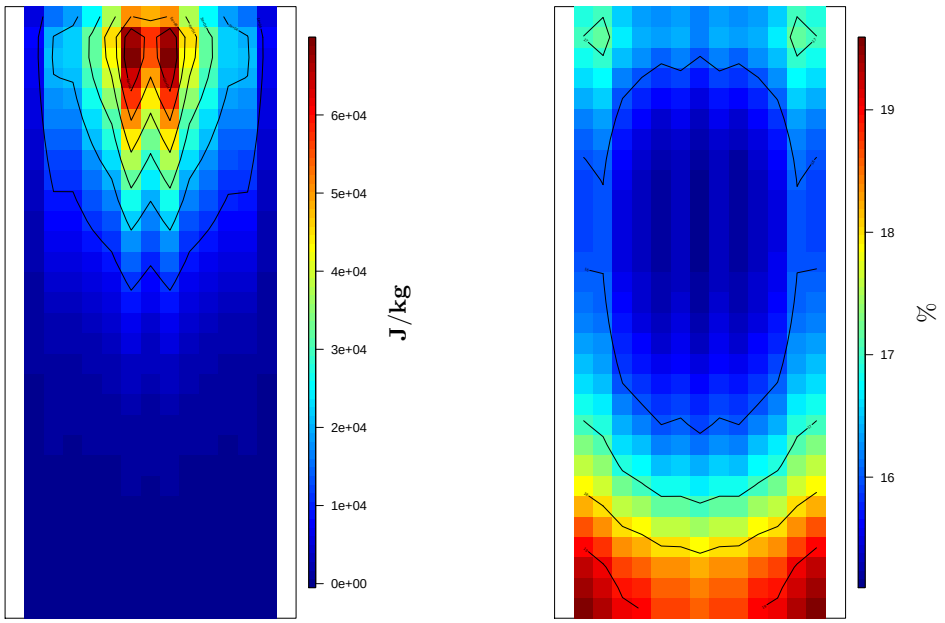

(a) Mean (b) Relative standard deviation

Figure E.12: H_f^{3D} estimated mean and relative standard deviation in the axial cross-section at $Y3$ for IBE coupling study in PWR core.

- **Z15 cross-section**

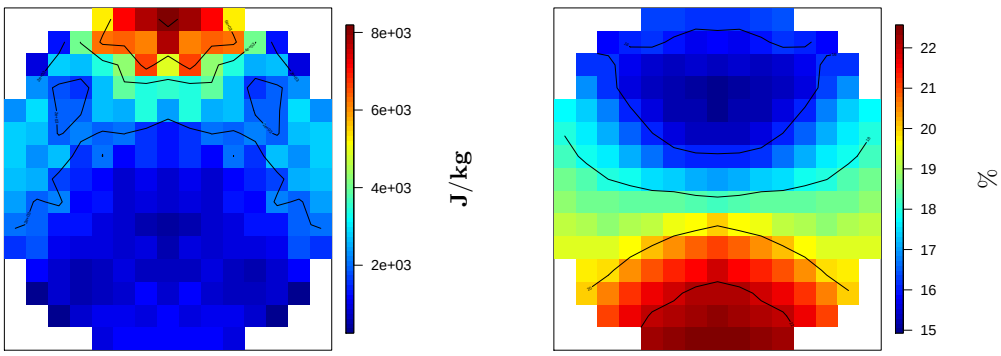

(a) Mean (b) Relative standard deviation

Figure E.13: H_f^{3D} estimated mean and relative standard deviation in the radial cross-section at $Z15$ for IBE coupling study in PWR core.

- **Y8 cross-section**

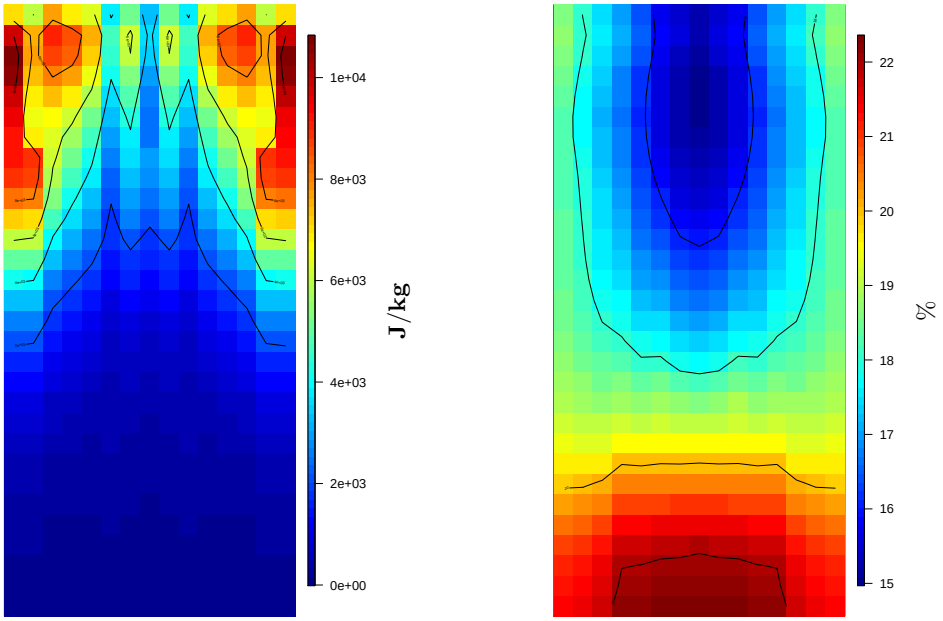

(a) Mean (b) Relative standard deviation

Figure E.14: H_f^{3D} estimated mean and relative standard deviation in the axial cross-section at $Y8$ for IBE coupling study in PWR core.

- **Z30 cross-section**

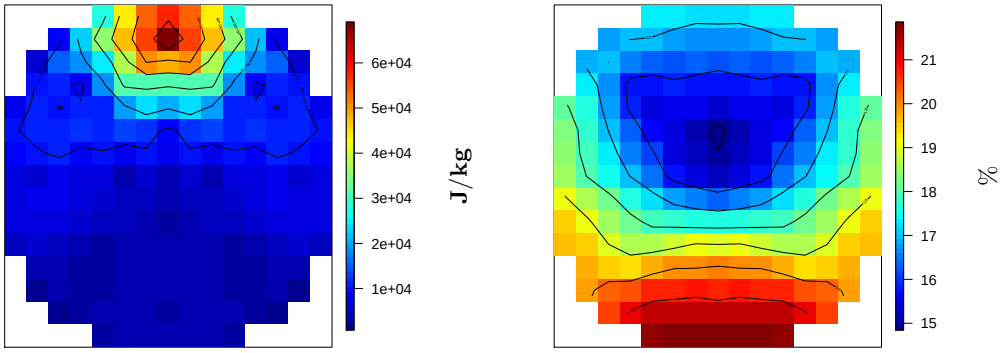

(a) Mean (b) Relative standard deviation

Figure E.15: H_f^{3D} estimated mean and relative standard deviation in the radial cross-section at $Z30$ for IBE coupling study in PWR core.

Results for W_f^{3D}

- **Histograms**

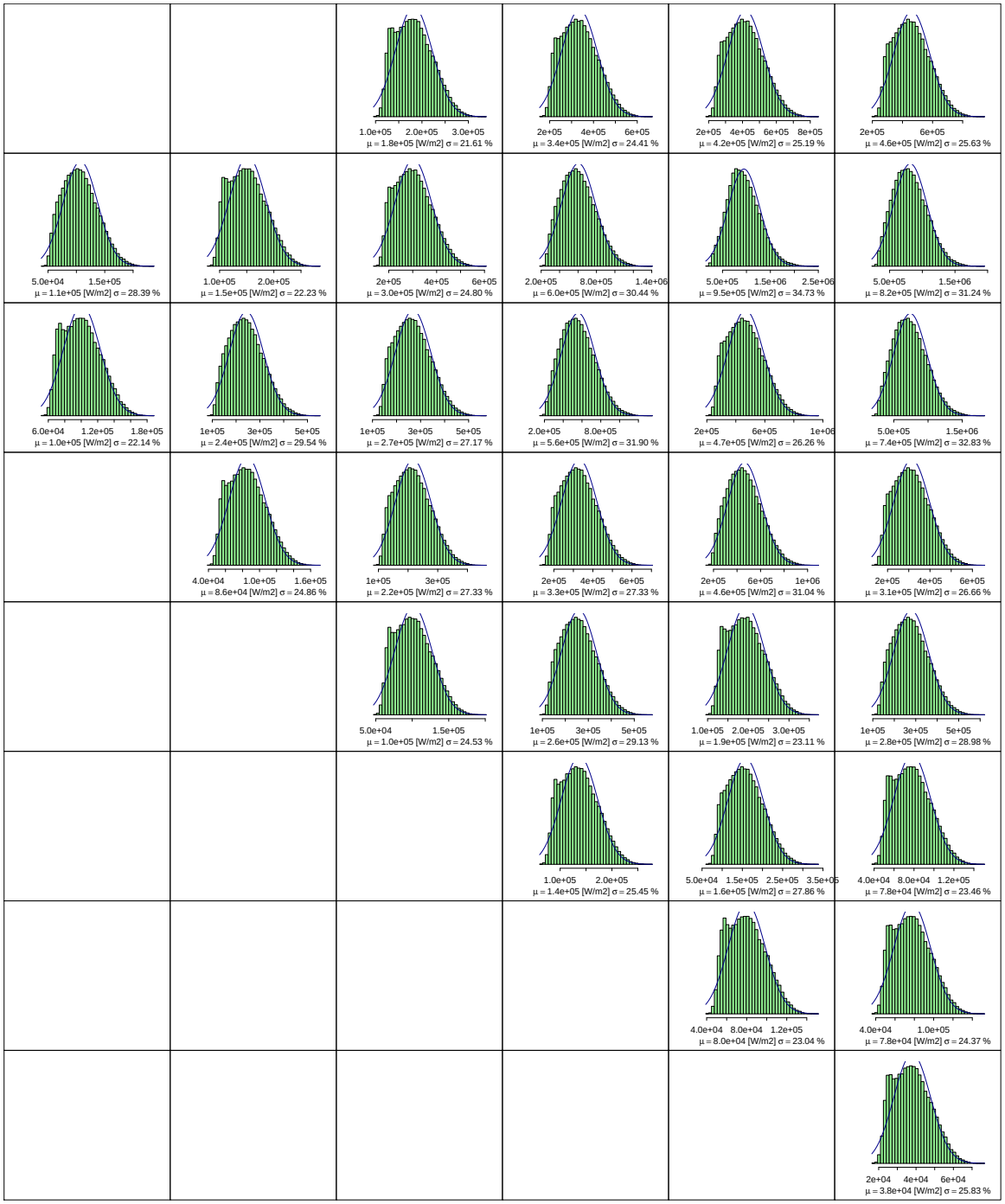

Figure E.16: W_f^{3D} estimated histograms for IBE coupling study in PWR core.

- **Y1 cross-section**

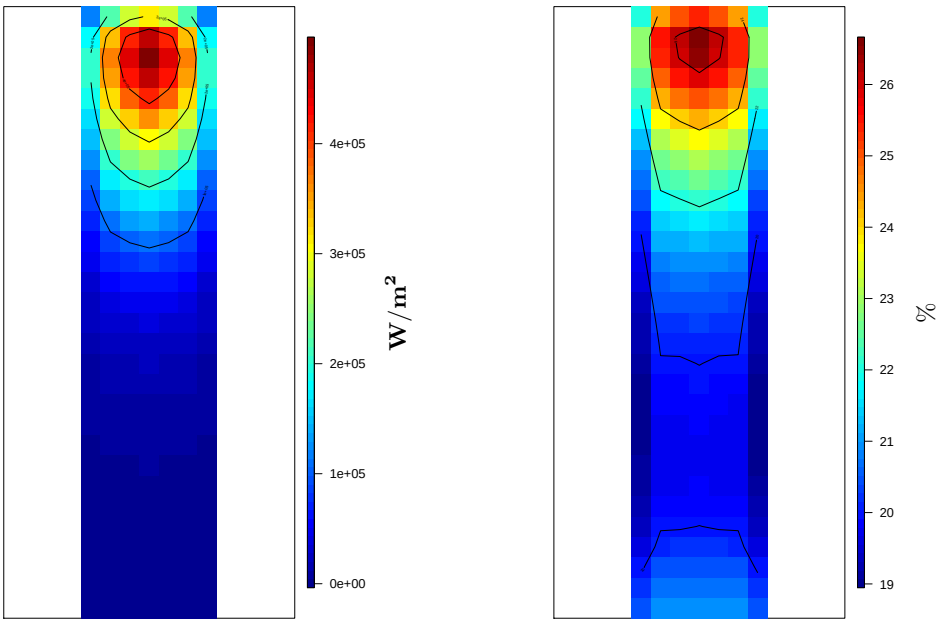

(a) Mean (b) Relative standard deviation

Figure E.17: W_f^{3D} estimated mean and relative standard deviation in the axial cross-section at $Y1$ for IBE coupling study in PWR core.

- **Z1 cross-section**

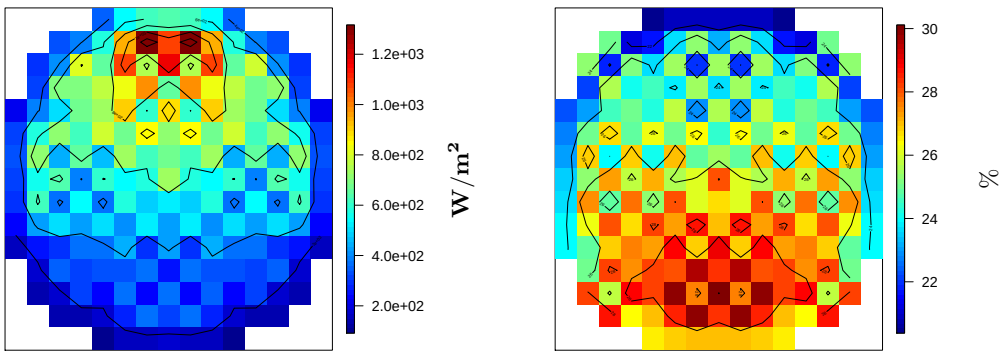

(a) Mean (b) Relative standard deviation

Figure E.18: W_f^{3D} estimated mean and relative standard deviation in the radial cross-section at $Z1$ for IBE coupling study in PWR core.

- **Y3 cross-section**

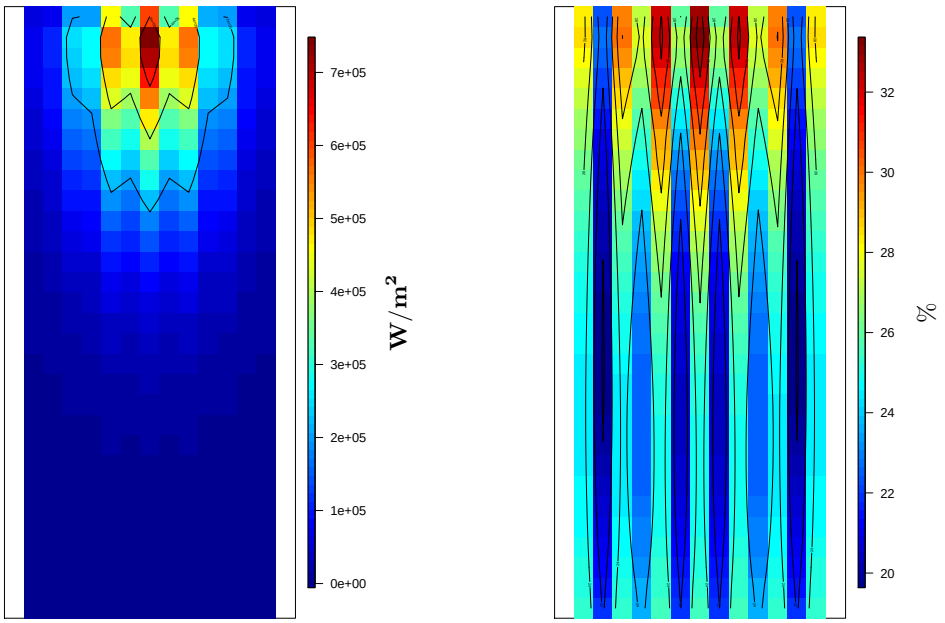

(a) Mean (b) Relative standard deviation

Figure E.19: W_f^{3D} estimated mean and relative standard deviation in the axial cross-section at $Y3$ for IBE coupling study in PWR core.

- **Z15 cross-section**

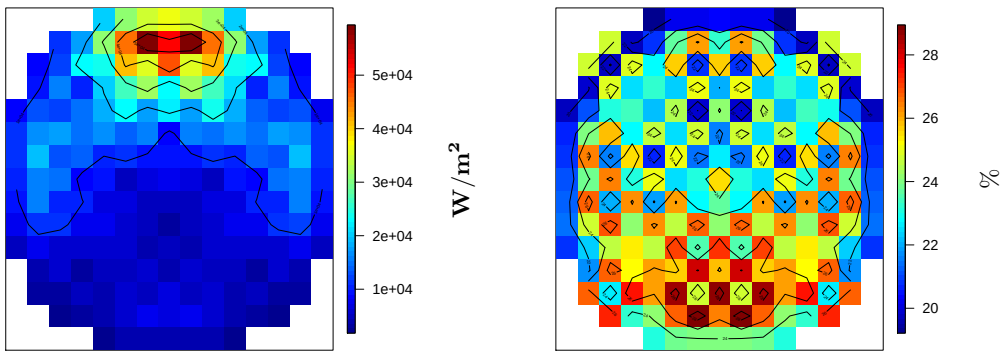

(a) Mean (b) Relative standard deviation

Figure E.20: W_f^{3D} estimated mean and relative standard deviation in the radial cross-section at $Z15$ for IBE coupling study in PWR core.

- **Y8 cross-section**

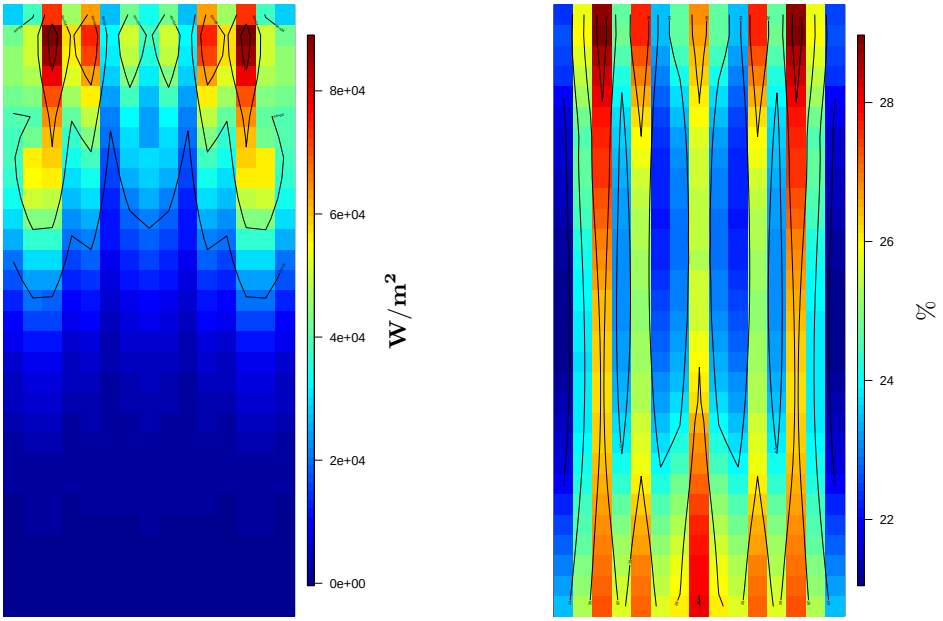

(a) Mean (b) Relative standard deviation

Figure E.21: W_f^{3D} estimated mean and relative standard deviation in the axial cross-section at $Y8$ for IBE coupling study in PWR core.

- **Z30 cross-section**

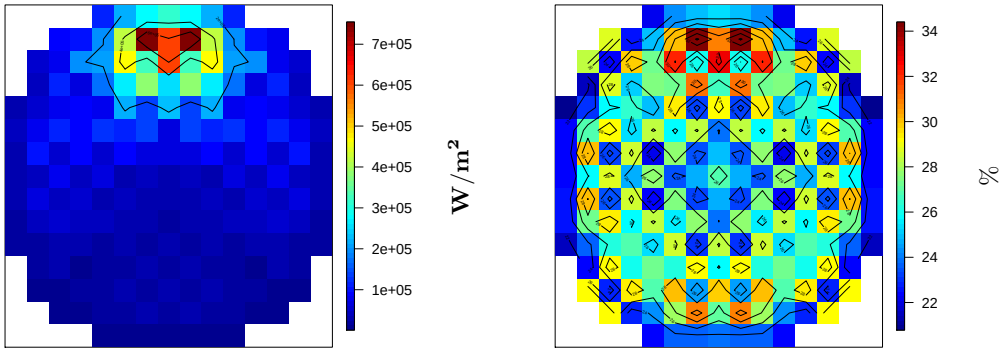

(a) Mean (b) Relative standard deviation

Figure E.22: W_f^{3D} estimated mean and relative standard deviation in the radial cross-section at $Z30$ for IBE coupling study in PWR core.

Results for H_{gap}^{3D}

- **Histograms**

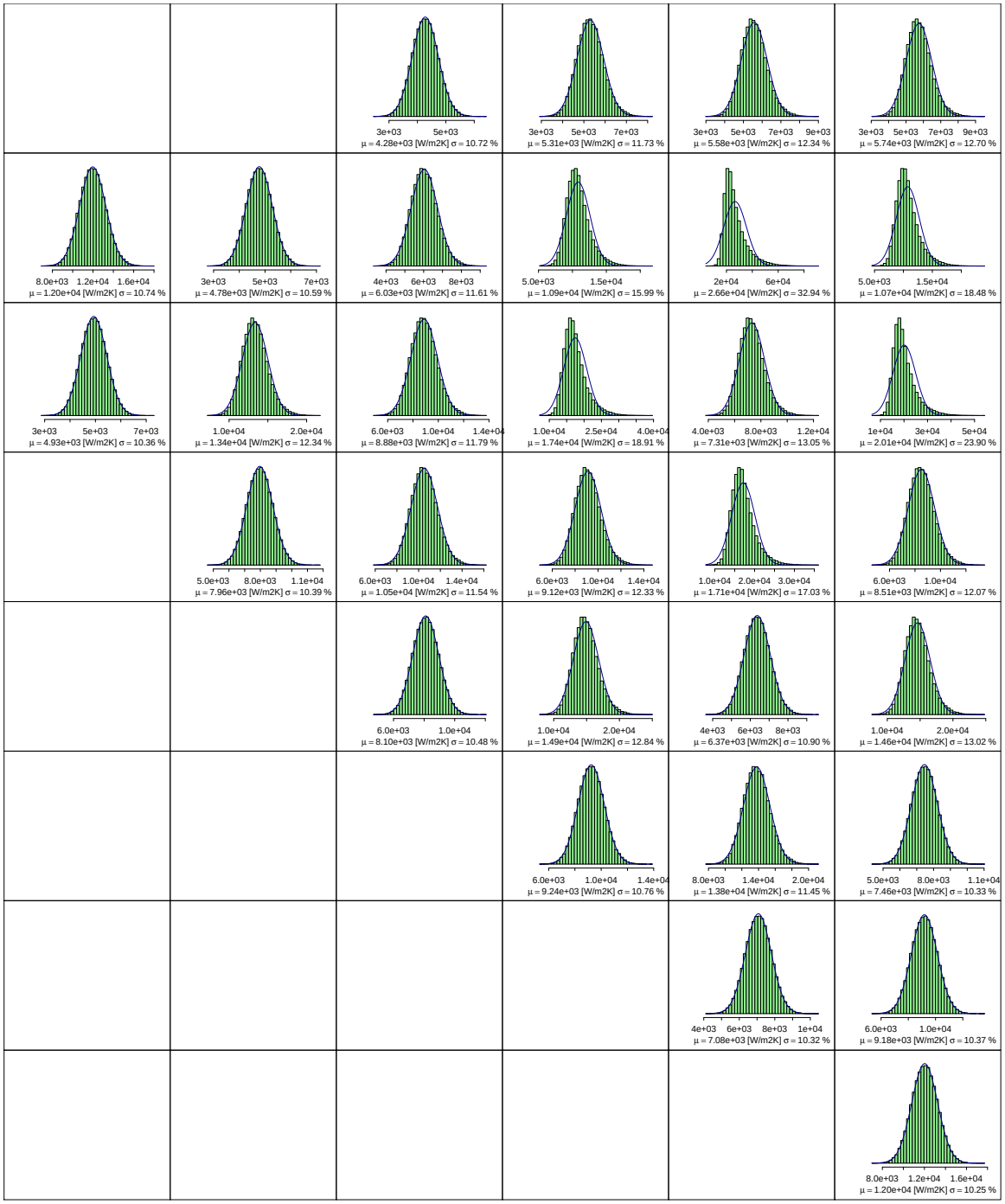

Figure E.23: H_{gap}^{3D} estimated histogram for IBE coupling study in PWR core.

- **Y1 cross-section**

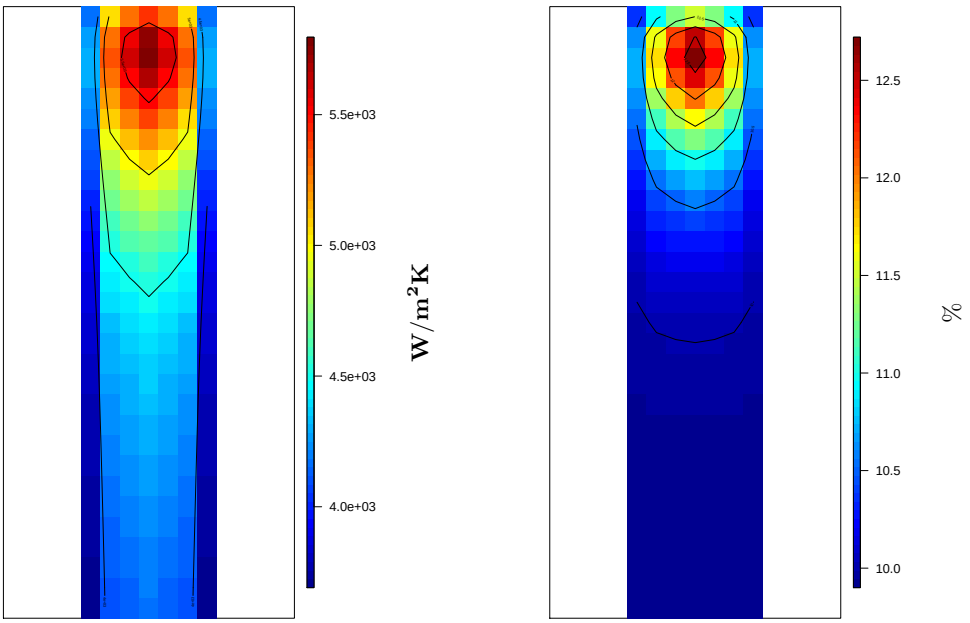

(a) Mean (b) Relative standard deviation

Figure E.24: H_{gap}^{3D} estimated mean and relative standard deviation in the axial cross-section at $Y1$ for IBE coupling study in PWR core.

- **Z1 cross-section**

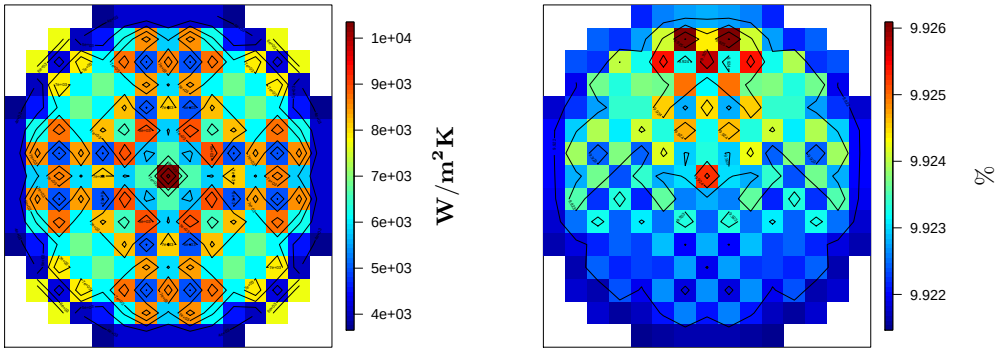

(a) Mean (b) Relative standard deviation

Figure E.25: H_{gap}^{3D} estimated mean and relative standard deviation in the radial cross-section at $Z1$ for IBE coupling study in PWR core.

- **Y3 cross-section**

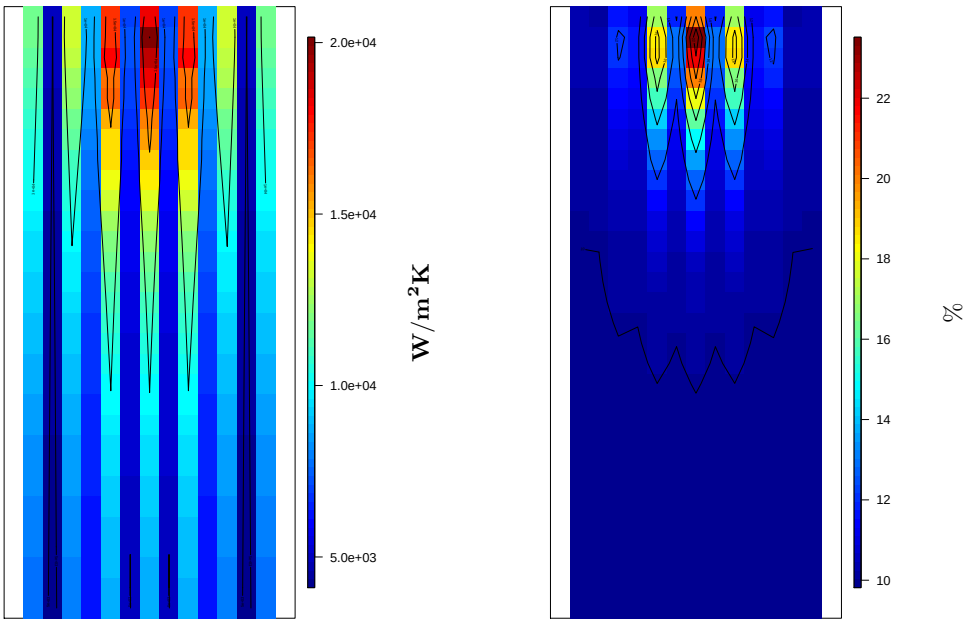

(a) Mean (b) Relative standard deviation

Figure E.26: H_{gap}^{3D} estimated mean and relative standard deviation in the axial cross-section at $Y3$ for IBE coupling study in PWR core.

- **Z15 cross-section**

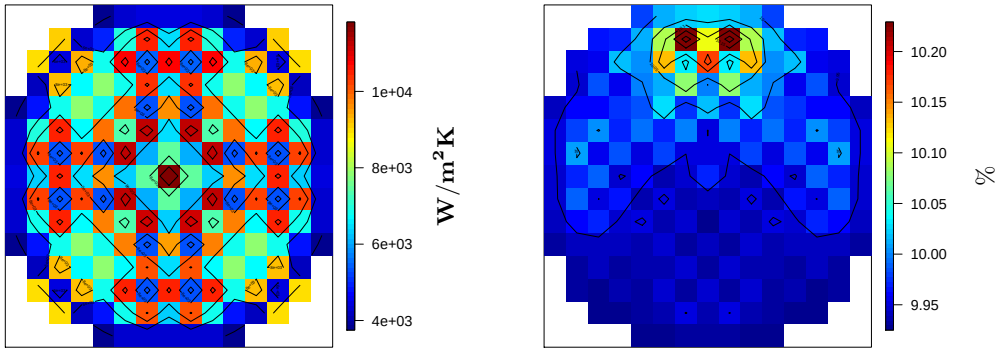

(a) Mean (b) Relative standard deviation

Figure E.27: H_{gap}^{3D} estimated mean and relative standard deviation in the radial cross-section at $Z15$ for IBE coupling study in PWR core.

- **Y8 cross-section**

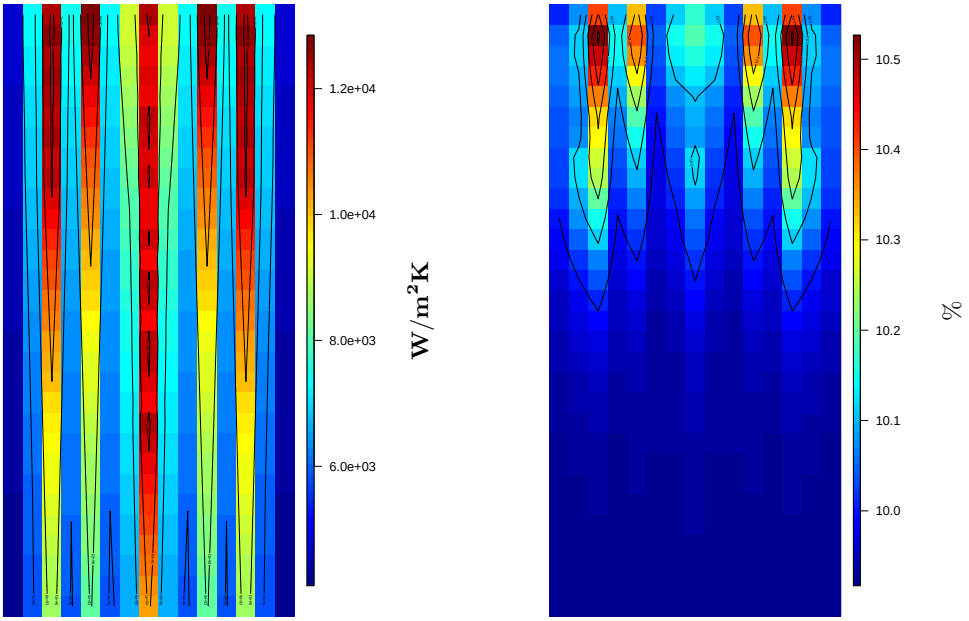

(a) Mean (b) Relative standard deviation

Figure E.28: H_{gap}^{3D} estimated mean and relative standard deviation in the axial cross-section at $Y8$ for IBE coupling study in PWR core.

- **Z30 cross-section**

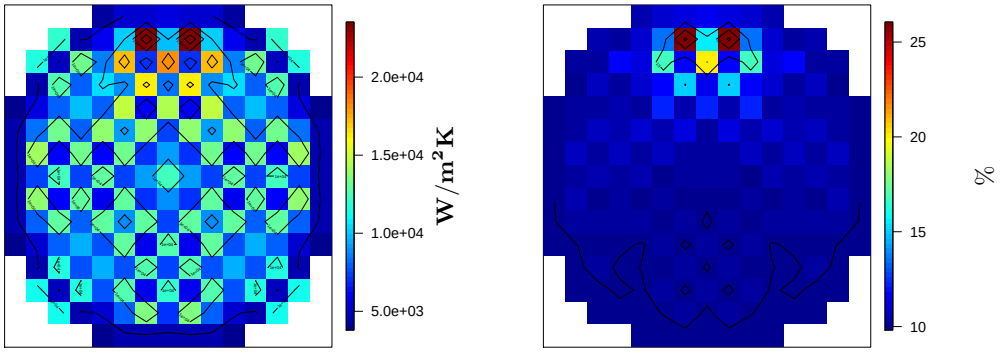

(a) Mean (b) Relative standard deviation

Figure E.29: H_{gap}^{3D} estimated mean and relative standard deviation in the radial cross-section at $Z30$ for IBE coupling study in PWR core.

Results for D_w^{3D}

- **Histograms**

Figure E.30: D_w^{3D} estimated histograms for IBE coupling study in PWR core.

- **Y1 cross-section**

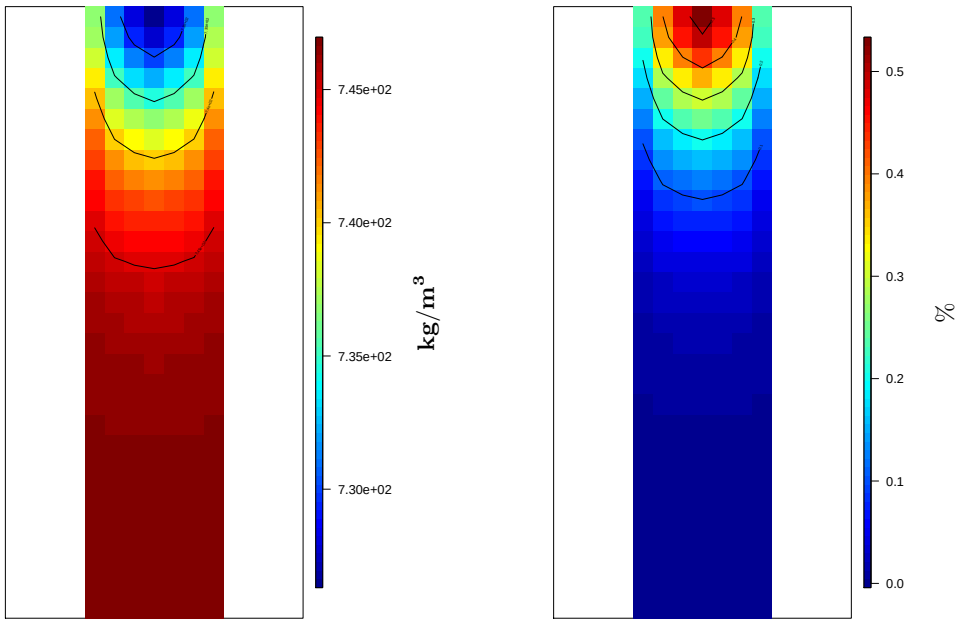

(a) Mean (b) Relative standard deviation

Figure E.31: D_w^{3D} estimated mean and relative standard deviation in the axial cross-section at $Y1$ for IBE coupling study in PWR core.

- **Z1 cross-section**

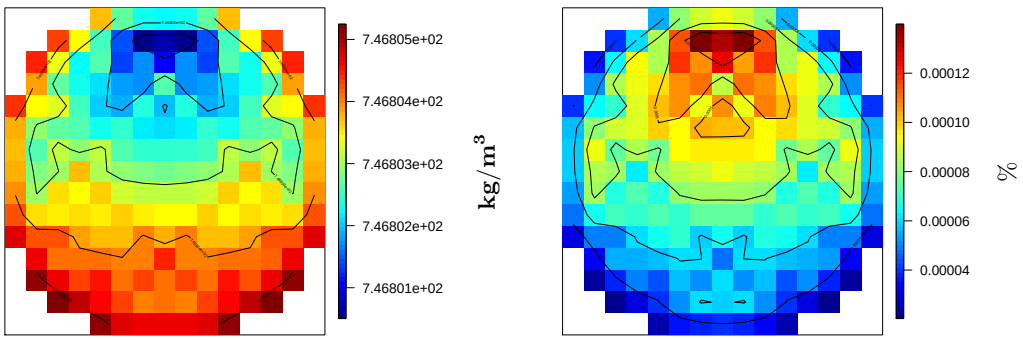

(a) Mean (b) Relative standard deviation

Figure E.32: D_w^{3D} estimated mean and relative standard deviation in the radial cross-section at $Z1$ for IBE coupling study in PWR core.

- **Y3 cross-section**

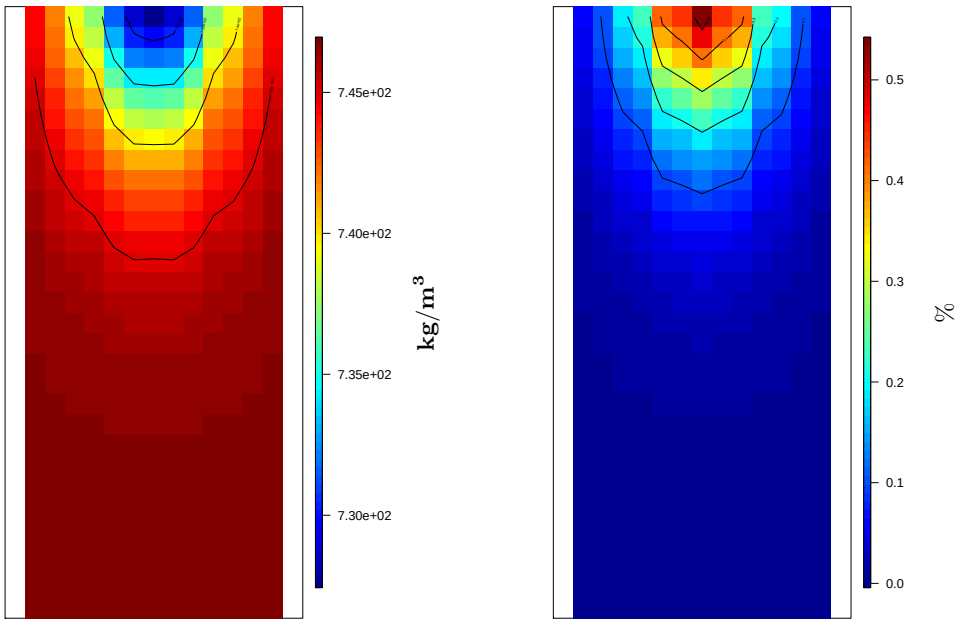

(a) Mean (b) Relative standard deviation

Figure E.33: D_w^{3D} estimated mean and relative standard deviation in the axial cross-section at $Y3$ for IBE coupling study in PWR core.

- **Z15 cross-section**

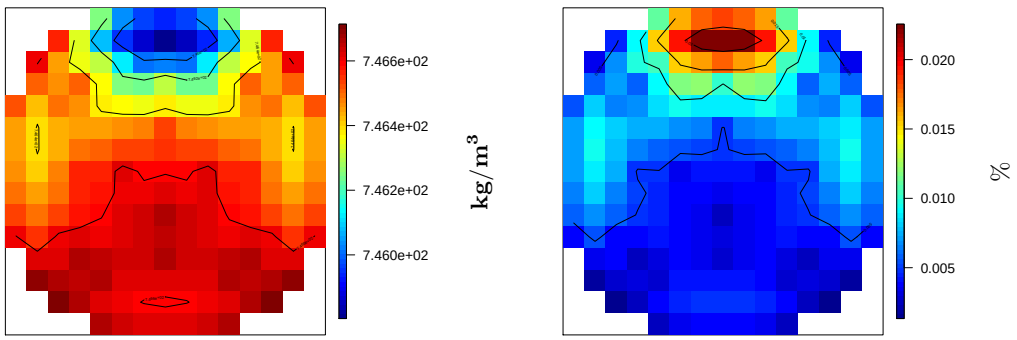

(a) Mean (b) Relative standard deviation

Figure E.34: D_w^{3D} estimated mean and relative standard deviation in the radial cross-section at $Z15$ for IBE coupling study in PWR core.

- **Y8 cross-section**

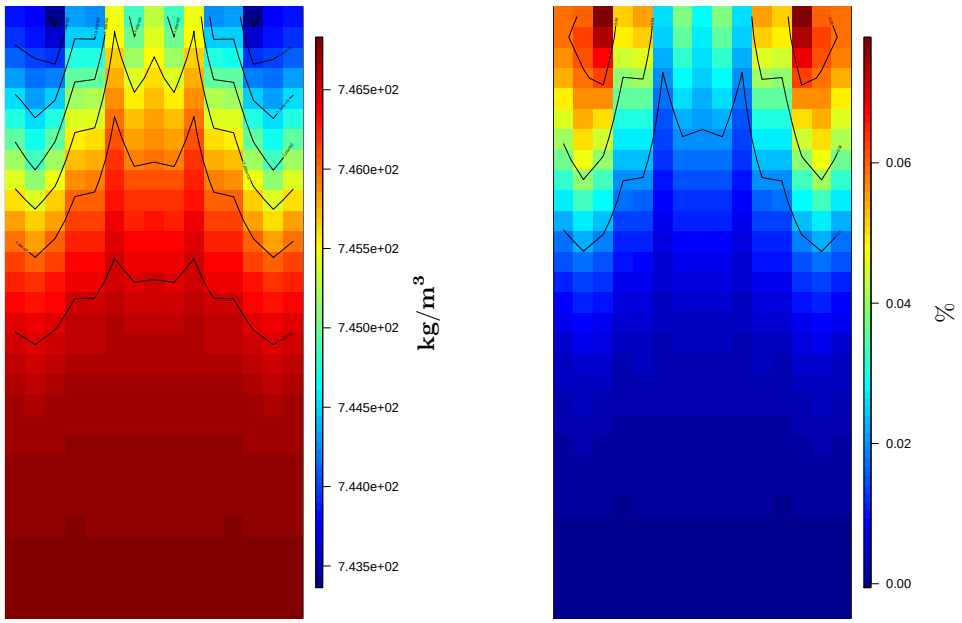

(a) Mean (b) Relative standard deviation

Figure E.35: D_w^{3D} estimated mean and relative standard deviation in the axial cross-section at $Y8$ for IBE coupling study in PWR core.

- **Z30 cross-section**

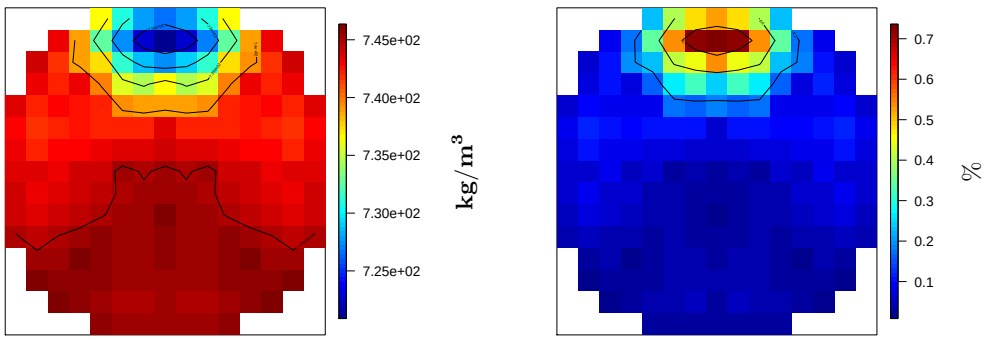

(a) Mean (b) Relative standard deviation

Figure E.36: D_w^{3D} estimated mean and relative standard deviation in the radial cross-section at $Z30$ for IBE coupling study in PWR core.

For P_{lin}^{3D} we observe similar non normal pdf for all the histograms of the considered radial cross-sections. The axial cross-sections $Y1$ and $Y3$ close to the location of the control rod ejection show similar mean distribution as in Section 4.7.2 with lower maximum value since they are farther from the local maximum. The value is higher for $Y1$ than $Y3$. This can be explained by the reflector effect. At $Y8$ cross-section the estimated mean has values of one order of magnitude lower with a distribution that is impacted strongly by the reflector and the burn-up. The relative standard deviation distribution of the axial cross-sections is similar to Section 4.7.2. Concerning the radial cross-sections the mean distribution remains the same. Compared to Section 4.7.2 the estimated values vary from two orders of magnitudes lower for $Z1$, one order of magnitude for $Z15$ and similar order of magnitudes for $Z30$. The relative standard deviation distribution varies from almost constant at the bottom of the core to the distribution of Section 4.7.2 at the top.

For H_f^{3D} we observe similar normal pdf for all the histograms of the examined radial cross-section. The conclusions drawn for H_f^{3D} follow the ones of P_{lin}^{3D}. The axial cross-sections $Y1$ and $Y3$ close to the location of the control rod ejection show similar mean distribution as in Section 4.7.2 with lower maximum value since they are farther from the local maximum. The value is higher for $Y1$ than $Y3$ attributed to the reflector presence. At $Y8$ cross-section the mean has values of one order of magnitude lower than Section 4.7.2 with a distribution that is impacted strongly by the reflector. The radial cross-sections compared to Section 4.7.2 show similar mean distribution with values that vary from two orders of magnitudes lower for $Z1$, one order of magnitude for $Z15$ and similar order of magnitudes for $Z30$. The relative standard deviation distributions for both axial cross-sections are similar to Section 4.7.2.

For W_f^{3D} we observe a different behavior in some histograms. This happens for meshes farther from the control rod ejection location, especially for their values at low quantiles. This can be attributed to the fact that W_f^{3D} is the only quantity for which we decreased the PCA variance representation to 85%. It is quite possible that to capture correctly the behavior at locations far from the ejection location we need higher variance representation and thus more principal components. The distributions of mean and relative standard deviation on the different cross-sections depend strongly on both the burn-up and the power. In cross-section $Y1$ where all the assemblies have similar burn-up we clearly see only the impact of the power. By inspecting the other cross-sections we observe that in the meshes close to the control rod ejection, where the power is high, there is an impact of the burn-up as well. As we move farther from the control rod ejection location we see that the power impact is mainly driven by the reflector presence. This means that for assemblies of similar burn-up the ones closer to the reflector have higher mean and relative standard deviation than the ones closer to the control rod ejection location. It is easier to see this behavior in $Y8$ and $Z30$ cross-sections where the assemblies with high burn-up ($45GWd/t$) and closer to the reflector have the highest mean and relative standard deviation. The assemblies towards the center of the core with similar or higher burn-up and closer to the control rod ejection location exhibit lower mean and relative standard deviation. In general we can conclude that for the mean value distribution the power is more important than the burn-up but for the relative standard deviation the burn-up is more significant.

For the H_{gap}^{3D} histograms an interesting behavior is observed. While in most of the meshes the pdf are close to normal for few meshes close to the control rod ejection location this is not the case. This behavior is observed in assemblies with high power and high burn-up (above $30GWd/t$). This could be attributed to the impact of the H_{gap} model initial conditions uncertainty $H_{g,i}$. Uniform pdf is used for $H_{g,i}$ and their impact increases with burn-up since the gap width is smaller. This creates the strongly non normal pdf. The distributions of mean and relative standard deviation on the different cross-sections similarly to W_f^{3D} depend strongly on both the burn-up and the power. In cross-section $Y1$ where all the assemblies have similar burn-up we clearly see only the impact of the power. From the rest cross-sections we conclude that in the meshes close to the control rod ejection, where the power is high, the impact of both burn-up and the power. In general we can conclude that the burn-up effect is stronger than the power due to the $H_{g,i}$ increasing impact.

For D_w^{3D} we observe similar close to normal pdf for all the histograms of the examined radial cross-section. The mean and relative standard deviation follow an expected behavior similar to Section 4.7.2 results. The density decreases axially as the coolant extracts heat from the core with

minimum value at the top axial slice. We see that the D_w^{3D} behavior follows the P_{lin}^{3D}. This is due to the fact that the coolant heating by gamma deposition is stronger than by the heat flux reaching the cladding external surface. In the location of higher P_{lin}^{3D} the density decreases faster. The relative standard deviation is very small for all the cross-sections.

Appendix F

Complementary results for PWR IBE coupling with 3D thermal-hydraulic finer discretized channels

In Section 4.7.4 we presented uncertainty quantification results for the Improved Best Estimate (IBE) modeling with 3D flows and finer thermal-hydraulics channels. We focused on the analysis of $3D$ fields for the following identified outputs of interest:

- Linear power P_{lin}^{3D} at the instance of its local maximum.
- Stored enthalpy in the fuel H_f^{3D} at the instance of its local maximum.
- Cladding wall heat flux W_f^{3D} at the instance of its local maximum.
- Gap heat transfer H_{gap}^{3D} at the instance of its local maximum.
- Coolant density D_w^{3D} at the instance of its local minimum.

The 3D fields are difficult to visualize and for this reason in Section 4.7.4 two cross-sections were presented for each output: the radial and axial cross-sections at the position of the local maximum (or minimum). For these cross-section the mean and relative standard deviation distributions were calculated for these cross-sections. In this Section we present a larger variety of results. For each functional $3D$ output we provide the result for the mean and standard deviation distributions at 6 different cross-sections. Axially we focus on three cross-sections along the Y axis similar to the locations presented in figure E.1. The only difference is that now we have four channels for each assembly. Two cross-section around the location of the maximum linear power ($Y2$) at $Y1$ and $Y3$ and one cross-section at the center of the core ($Y16$). Radially we focus on three cross-sections along the Z axis at the bottom ($Z1$), middle ($Z15$) and top ($Z30$) axial slices. First we present all the results and afterwards at the end we analyze them.

Results for P_{lin}^{3D}

- **Y1 cross-section**

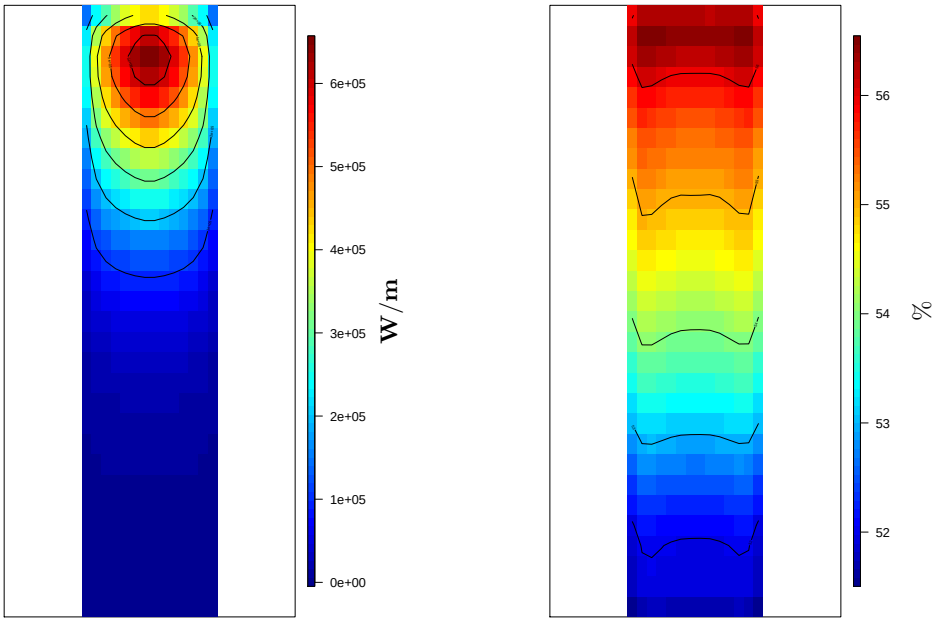

(a) Mean (b) Relative standard deviation

Figure F.1: P_{lin}^{3D} estimated mean and relative standard deviation in the axial cross-section at $Y1$ for IBE with 3D and finer discretized thermal-hydraulic channels coupling study in PWR core.

- **Z1 cross-section**

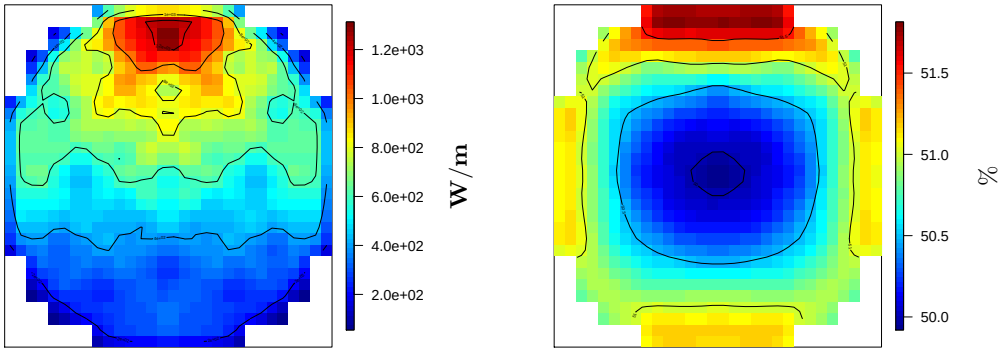

(a) Mean (b) Relative standard deviation

Figure F.2: P_{lin}^{3D} estimated mean and relative standard deviation in the radial cross-section at $Z1$ for IBE with 3D and finer discretized thermal-hydraulic channels coupling study in PWR core.

- **Y3 cross-section**

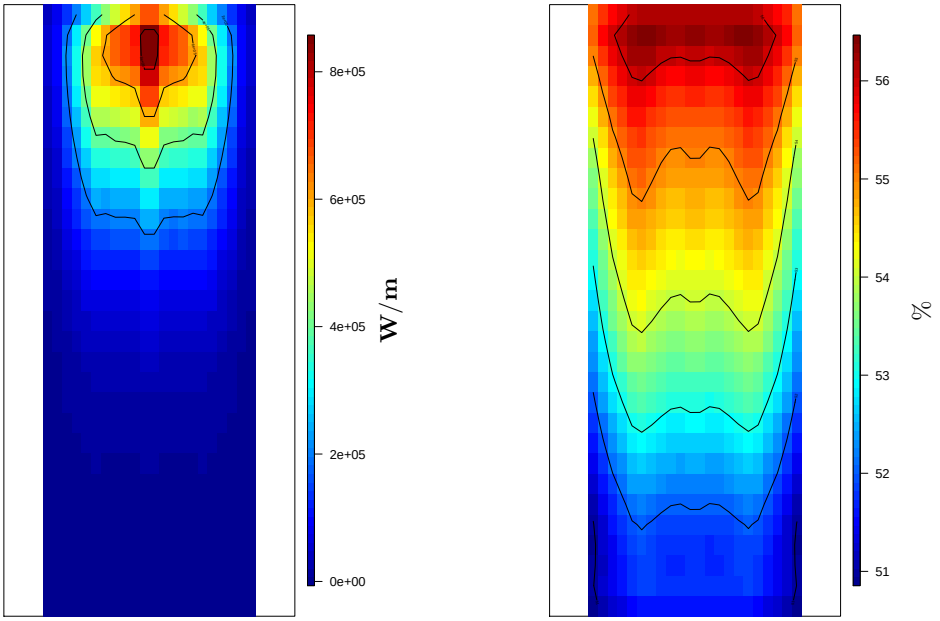

(a) Mean (b) Relative standard deviation

Figure F.3: P_{lin}^{3D} estimated mean and relative standard deviation in the axial cross-section at $Y3$ for IBE with 3D and finer discretized thermal-hydraulic channels coupling study in PWR core.

- **Z15 cross-section**

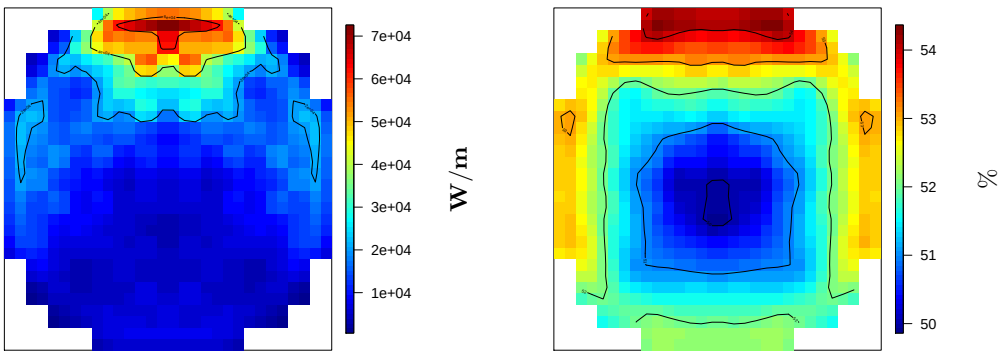

(a) Mean (b) Relative standard deviation

Figure F.4: P_{lin}^{3D} estimated mean and relative standard deviation in the radial cross-section at $Z15$ for IBE with 3D and finer discretized thermal-hydraulic channels coupling study in PWR core.

- **Y16 cross-section**

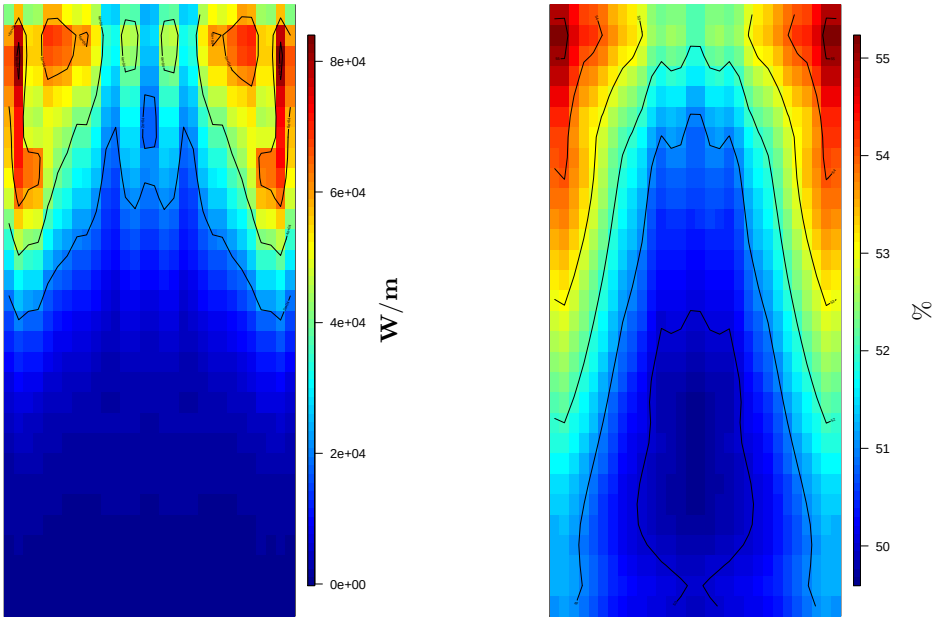

(a) Mean (b) Relative standard deviation

Figure F.5: P_{lin}^{3D} estimated mean and relative standard deviation in the axial cross-section at $Y16$ for IBE with 3D and finer discretized thermal-hydraulic channels coupling study in PWR core.

- **Z30 cross-section**

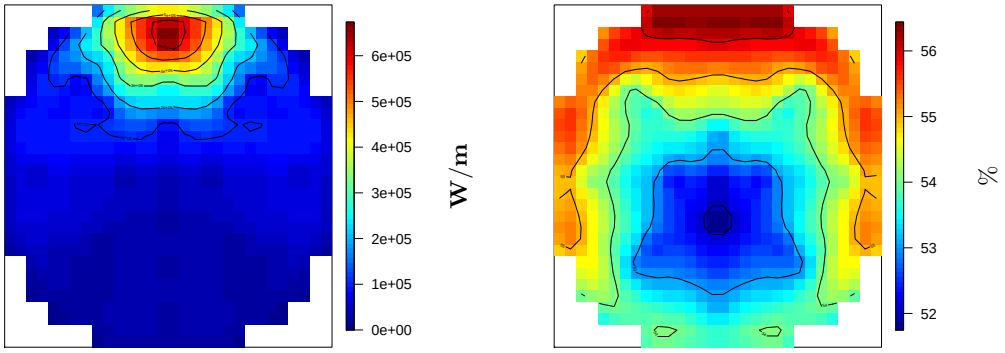

(a) Mean (b) Relative standard deviation

Figure F.6: P_{lin}^{3D} estimated mean and relative standard deviation in the radial cross-section at $Z30$ for IBE with 3D and finer discretized thermal-hydraulic channels coupling study in PWR core.

Results for H_f^{3D}

- **Y1 cross-section**

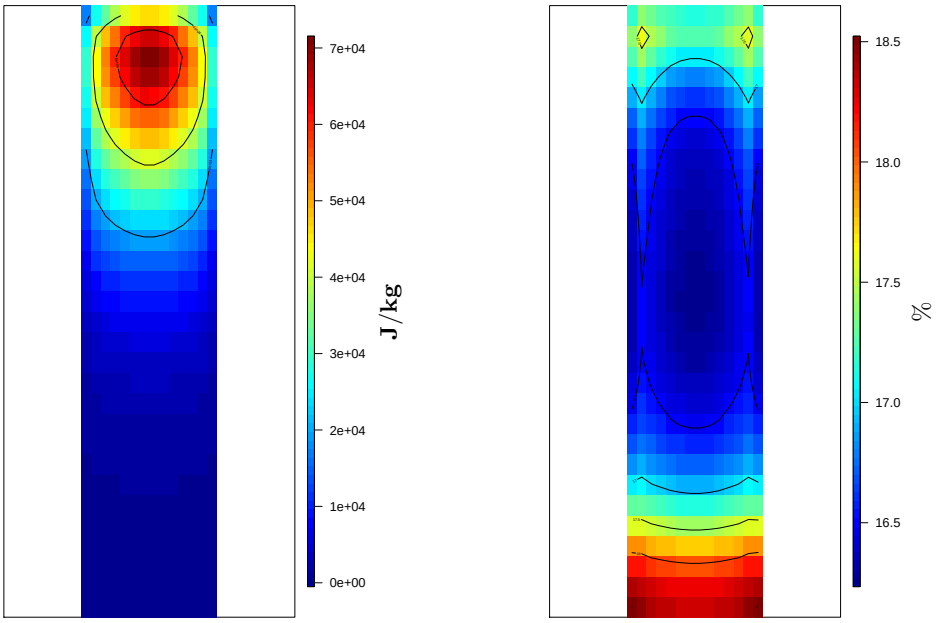

(a) Mean (b) Relative standard deviation

Figure F.7: H_f^{3D} estimated mean and relative standard deviation in the axial cross-section at $Y1$ for IBE with 3D and finer discretized thermal-hydraulic channels coupling study in PWR core.

- **Z1 cross-section**

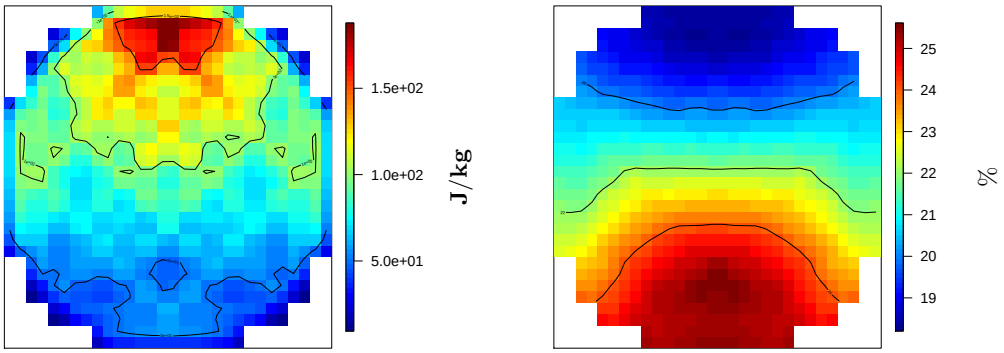

(a) Mean (b) Relative standard deviation

Figure F.8: H_f^{3D} estimated mean and relative standard deviation in the radial cross-section at $Z1$ for IBE with 3D and finer discretized thermal-hydraulic channels coupling study in PWR core.

- **Y3 cross-section**

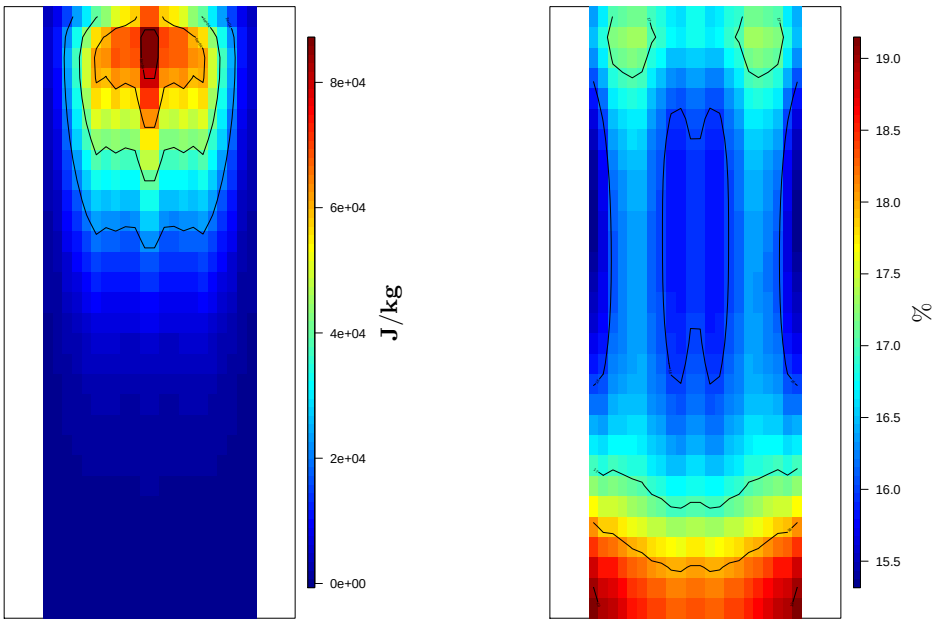

(a) Mean (b) Relative standard deviation

Figure F.9: H_f^{3D} estimated mean and relative standard deviation in the axial cross-section at $Y3$ for IBE with 3D and finer discretized thermal-hydraulic channels coupling study in PWR core.

- **Z15 cross-section**

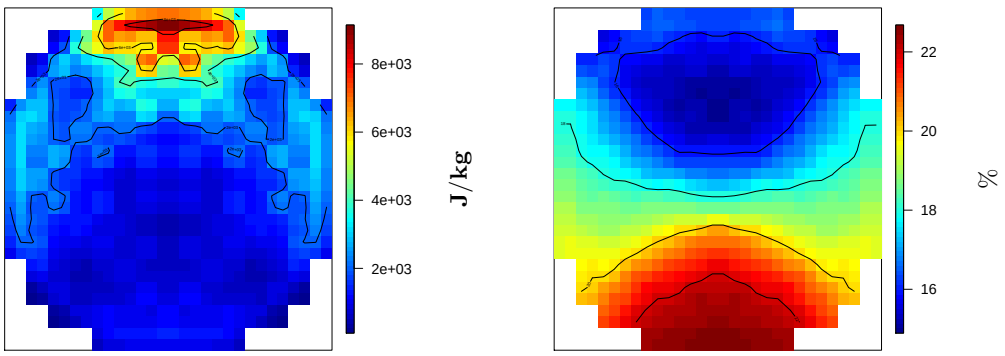

(a) Mean (b) Relative standard deviation

Figure F.10: H_f^{3D} estimated mean and relative standard deviation in the radial cross-section at $Z15$ for IBE with 3D and finer discretized thermal-hydraulic channels coupling study in PWR core.

- **Y16 cross-section**

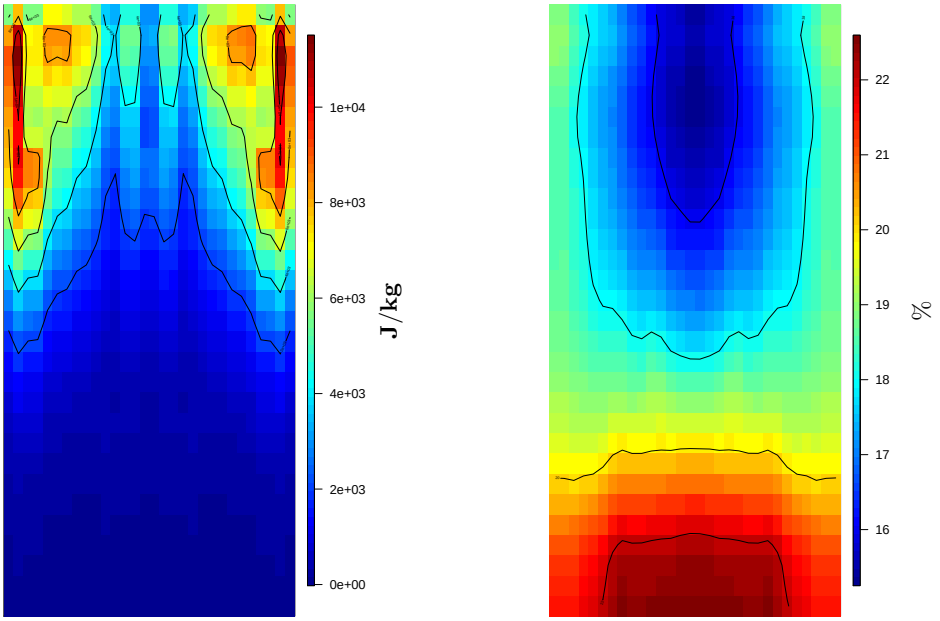

(a) Mean (b) Relative standard deviation

Figure F.11: H_f^{3D} estimated mean and relative standard deviation in the axial cross-section at $Y16$ for IBE with 3D and finer discretized thermal-hydraulic channels coupling study in PWR core.

- **Z30 cross-section**

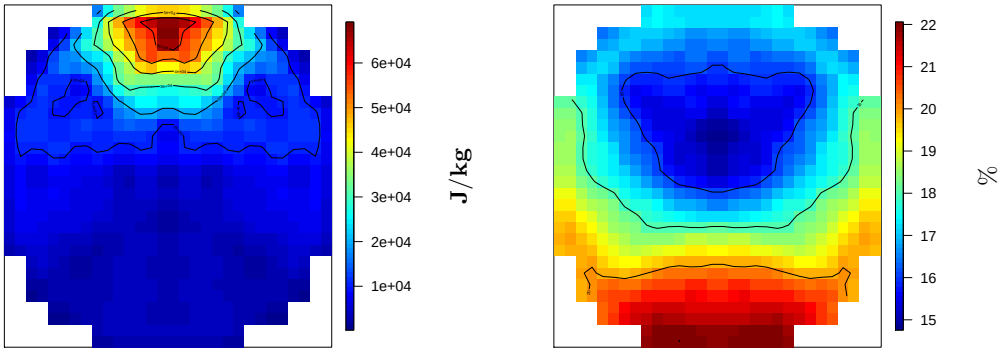

(a) Mean (b) Relative standard deviation

Figure F.12: H_f^{3D} estimated mean and relative standard deviation in the radial cross-section at $Z30$ for IBE with 3D and finer discretized thermal-hydraulic channels coupling study in PWR core.

Results for W_f^{3D}

- **Y1 cross-section**

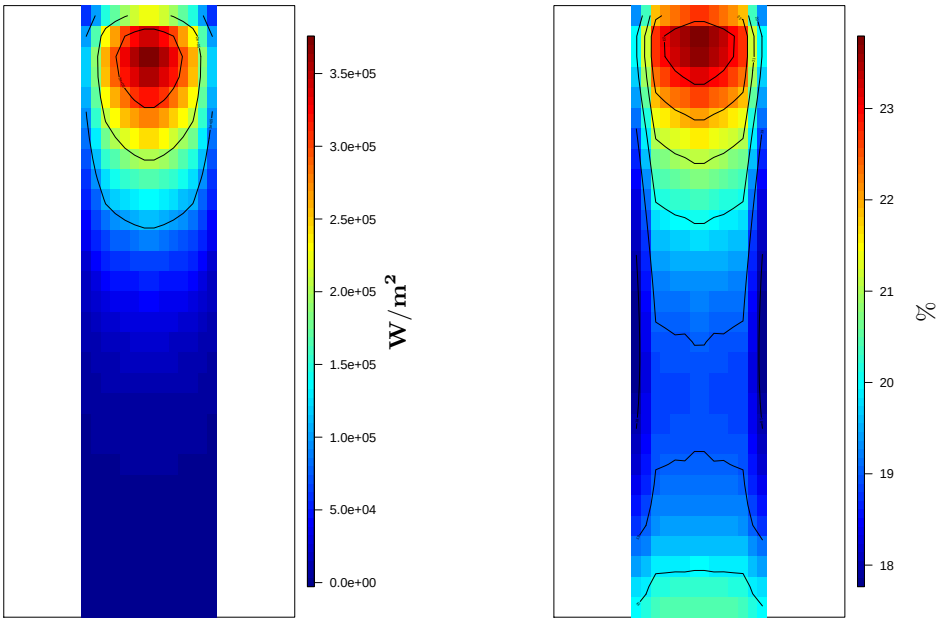

(a) Mean (b) Relative standard deviation

Figure F.13: W_f^{3D} estimated mean and relative standard deviation in the axial cross-section at $Y1$ for IBE with 3D and finer discretized thermal-hydraulic channels coupling study in PWR core.

- **Z1 cross-section**

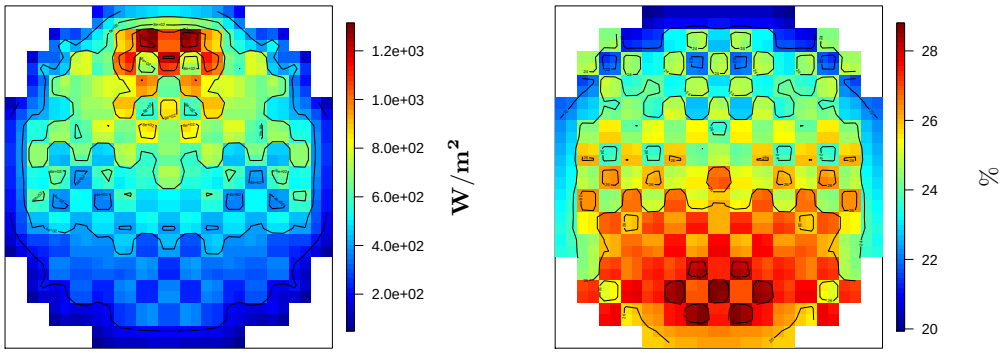

(a) Mean (b) Relative standard deviation

Figure F.14: W_f^{3D} estimated mean and relative standard deviation in the radial cross-section at $Z1$ for IBE with 3D and finer discretized thermal-hydraulic channels coupling study in PWR core.

- **Y3 cross-section**

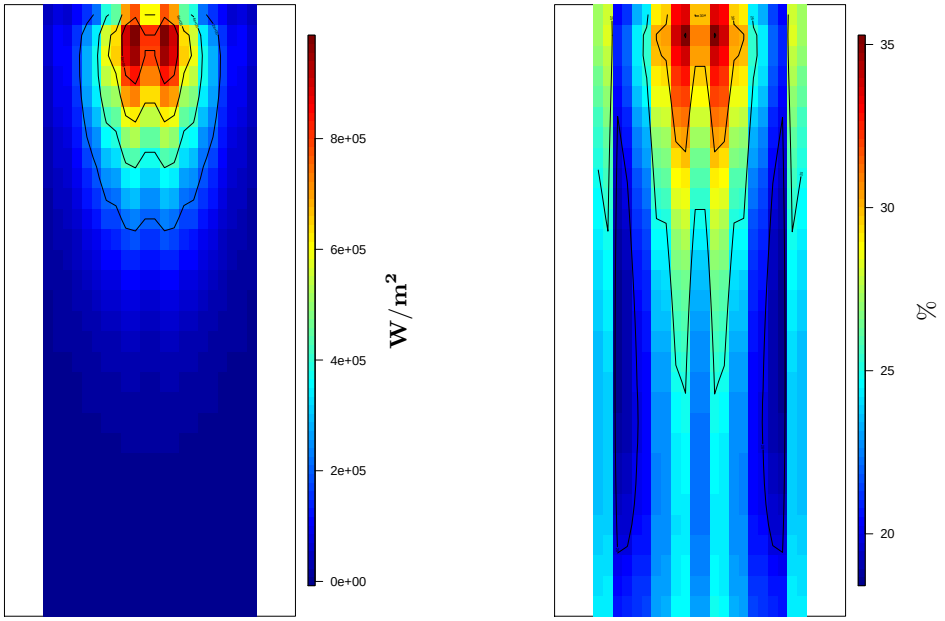

(a) Mean (b) Relative standard deviation

Figure F.15: W_f^{3D} estimated mean and relative standard deviation in the axial cross-section at $Y3$ for IBE with 3D and finer discretized thermal-hydraulic channels coupling study in PWR core.

- **Z15 cross-section**

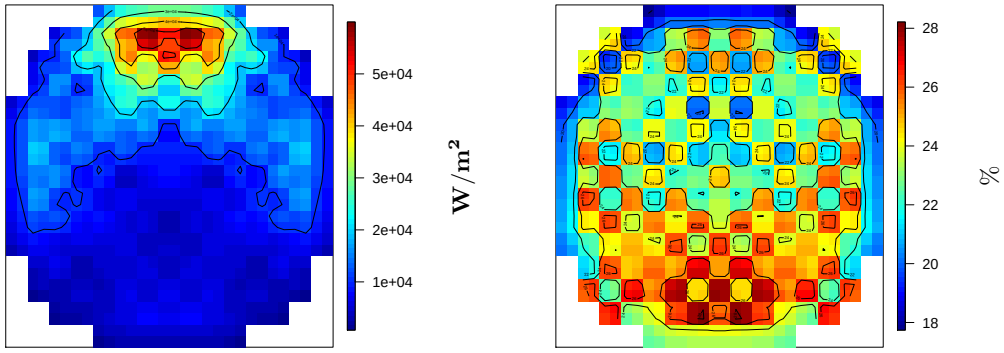

(a) Mean (b) Relative standard deviation

Figure F.16: W_f^{3D} estimated mean and relative standard deviation in the radial cross-section at $Z15$ for IBE with 3D and finer discretized thermal-hydraulic channels coupling study in PWR core.

- **Y16 cross-section**

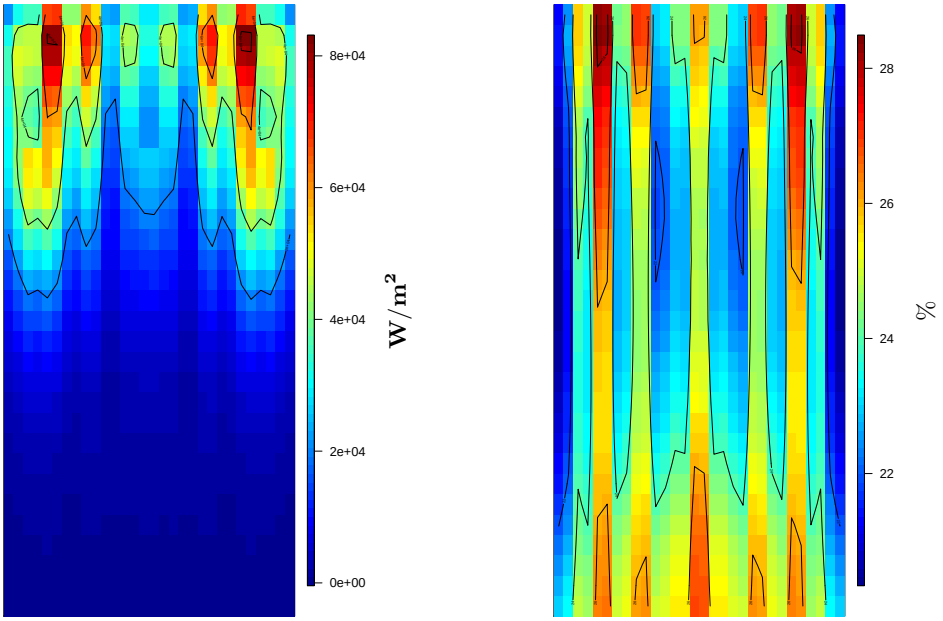

(a) Mean (b) Relative standard deviation

Figure F.17: W_f^{3D} estimated mean and relative standard deviation in the axial cross-section at $Y16$ for IBE with 3D and finer discretized thermal-hydraulic channels coupling study in PWR core.

- **Z30 cross-section**

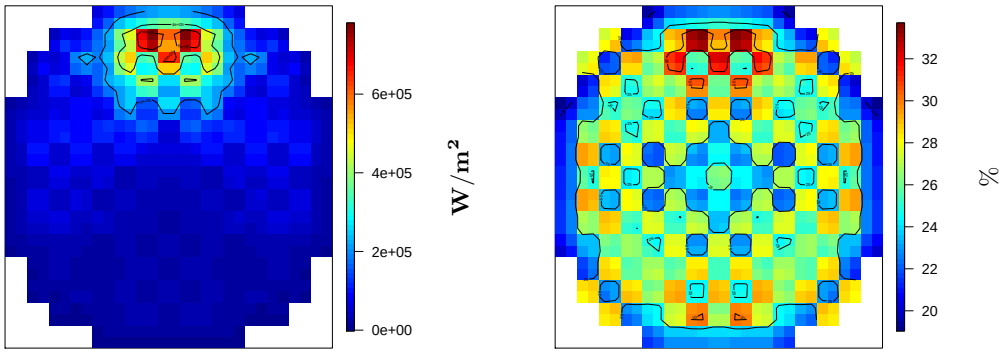

(a) Mean (b) Relative standard deviation

Figure F.18: W_f^{3D} estimated mean and relative standard deviation in the radial cross-section at $Z30$ for IBE with 3D and finer discretized thermal-hydraulic channels coupling study in PWR core.

Results for H_{gap}^{3D}

- **Y1 cross-section**

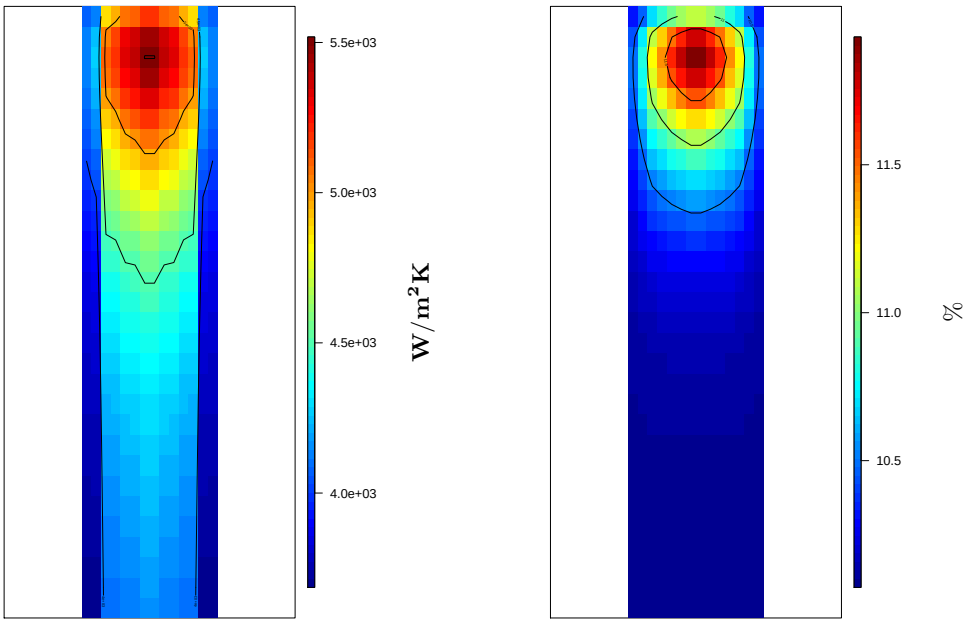

(a) Mean (b) Relative standard deviation

Figure F.19: H_{gap}^{3D} estimated mean and relative standard deviation in the axial cross-section at $Y1$ for IBE with 3D and finer discretized thermal-hydraulic channels coupling study in PWR core.

- **Z1 cross-section**

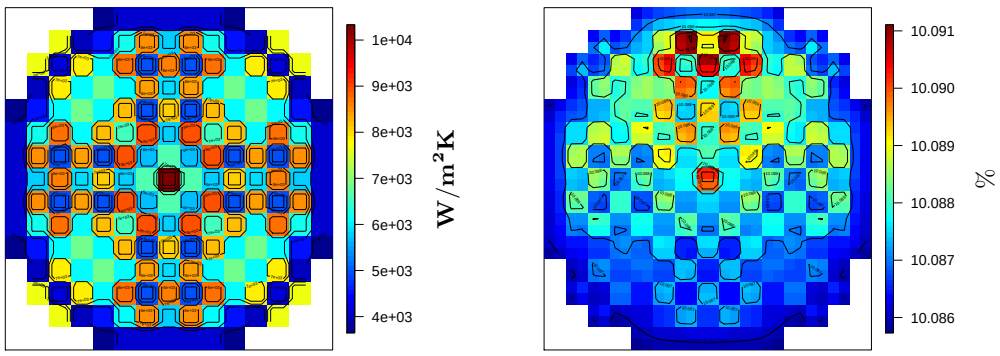

(a) Mean (b) Relative standard deviation

Figure F.20: H_{gap}^{3D} estimated mean and relative standard deviation in the radial cross-section at $Z1$ for IBE with 3D and finer discretized thermal-hydraulic channels coupling study in PWR core.

- **Y3 cross-section**

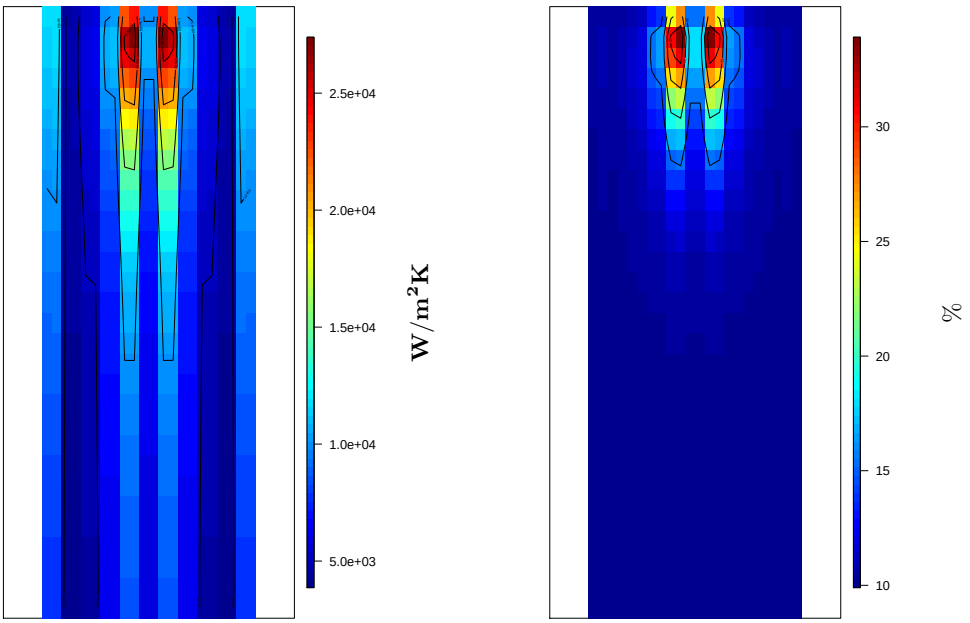

(a) Mean (b) Relative standard deviation

Figure F.21: H_{gap}^{3D} estimated mean and relative standard deviation in the axial cross-section at $Y3$ for IBE with 3D and finer discretized thermal-hydraulic channels coupling study in PWR core.

- **Z15 cross-section**

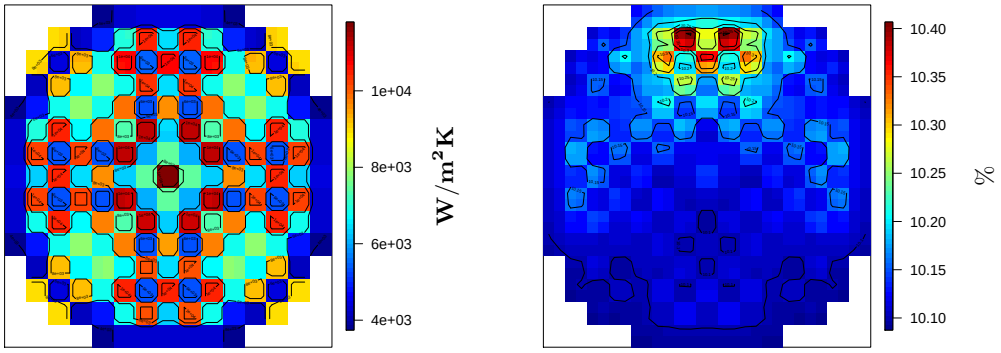

(a) Mean (b) Relative standard deviation

Figure F.22: H_{gap}^{3D} estimated mean and relative standard deviation in the radial cross-section at $Z15$ for IBE with 3D and finer discretized thermal-hydraulic channels coupling study in PWR core.

- **Y16 cross-section**

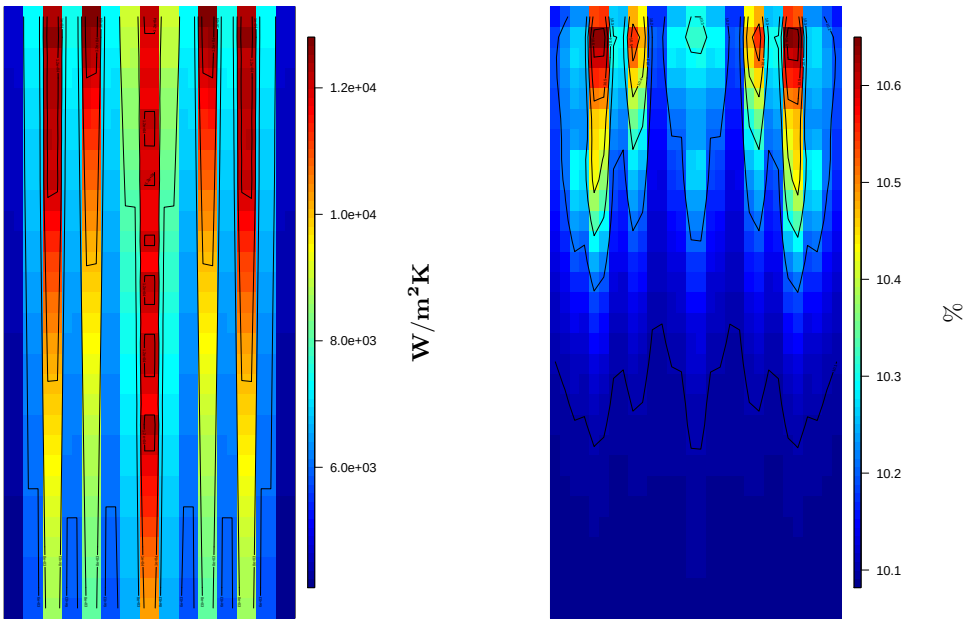

(a) Mean (b) Relative standard deviation

Figure F.23: H_{gap}^{3D} estimated mean and relative standard deviation in the axial cross-section at $Y16$ for IBE with 3D and finer discretized thermal-hydraulic channels coupling study in PWR core.

- **Z30 cross-section**

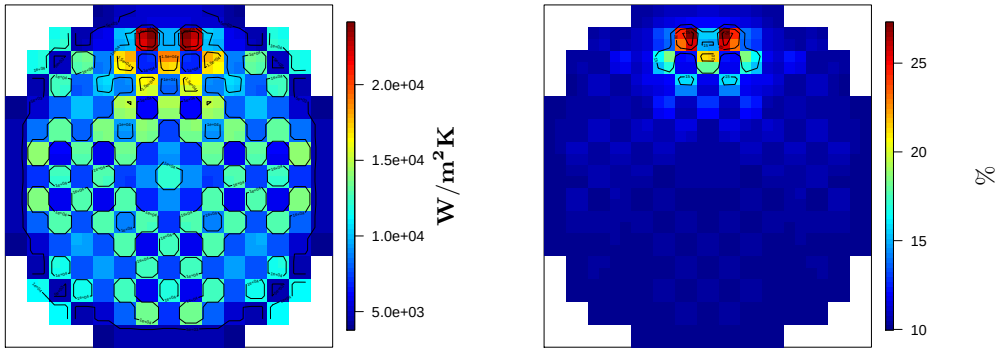

(a) Mean (b) Relative standard deviation

Figure F.24: H_{gap}^{3D} estimated mean and relative standard deviation in the radial cross-section at $Z30$ for IBE with 3D and finer discretized thermal-hydraulic channels coupling study in PWR core.

Results for D_w^{3D}

- **Y1 cross-section**

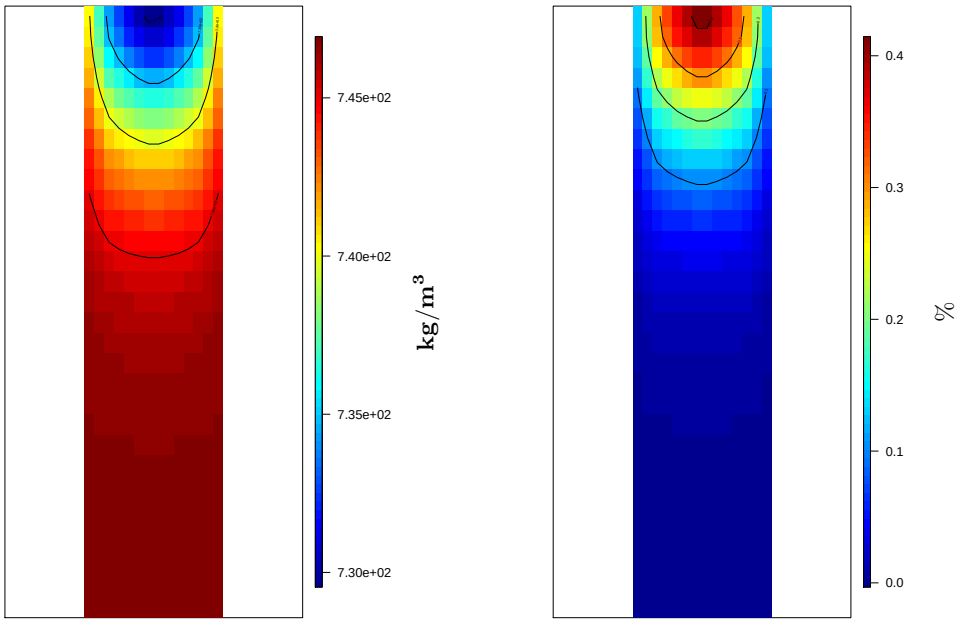

(a) Mean (b) Relative standard deviation

Figure F.25: D_w^{3D} estimated mean and relative standard deviation in the axial cross-section at $Y1$ for IBE with 3D and finer discretized thermal-hydraulic channels coupling study in PWR core.

- **Z1 cross-section**

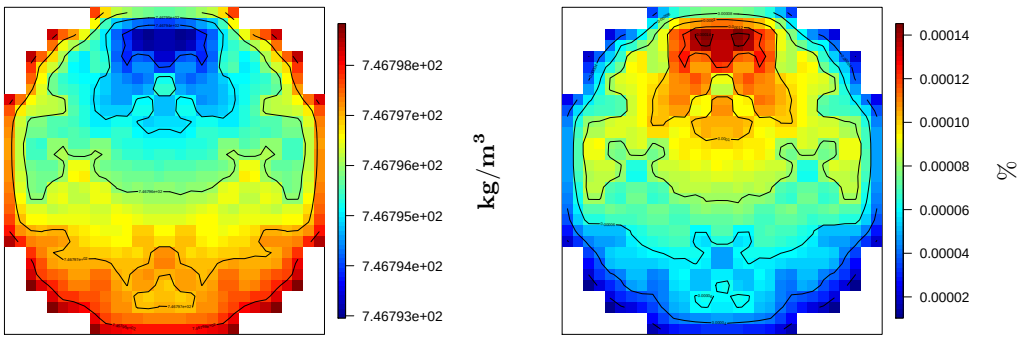

(a) Mean (b) Relative standard deviation

Figure F.26: D_w^{3D} estimated mean and relative standard deviation in the radial cross-section at $Z1$ for IBE with 3D and finer discretized thermal-hydraulic channels coupling study in PWR core.

- **Y3 cross-section**

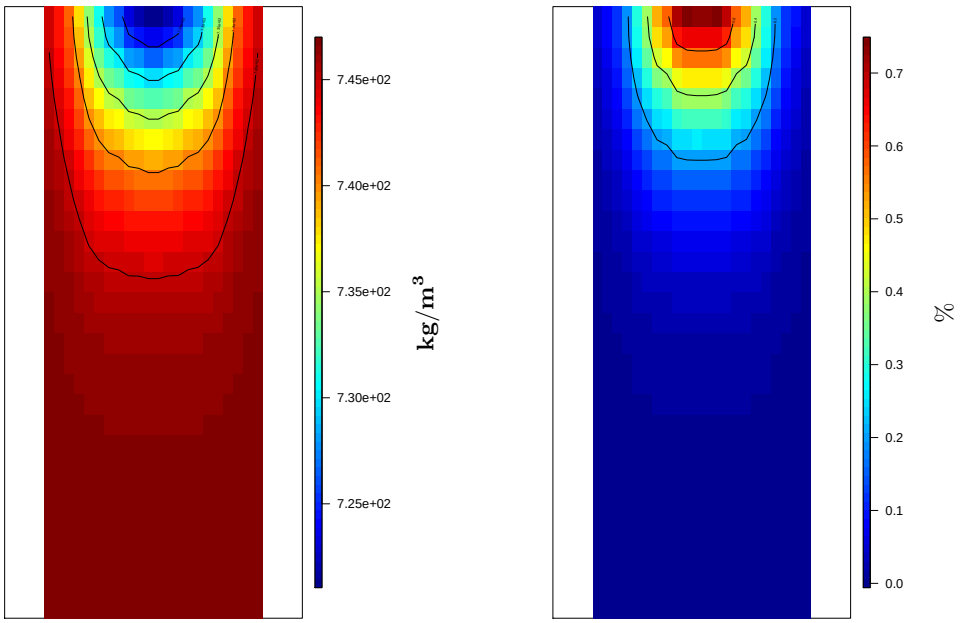

(a) Mean (b) Relative standard deviation

Figure F.27: D_w^{3D} estimated mean and relative standard deviation in the axial cross-section at $Y3$ for IBE with 3D and finer discretized thermal-hydraulic channels coupling study in PWR core.

- **Z15 cross-section**

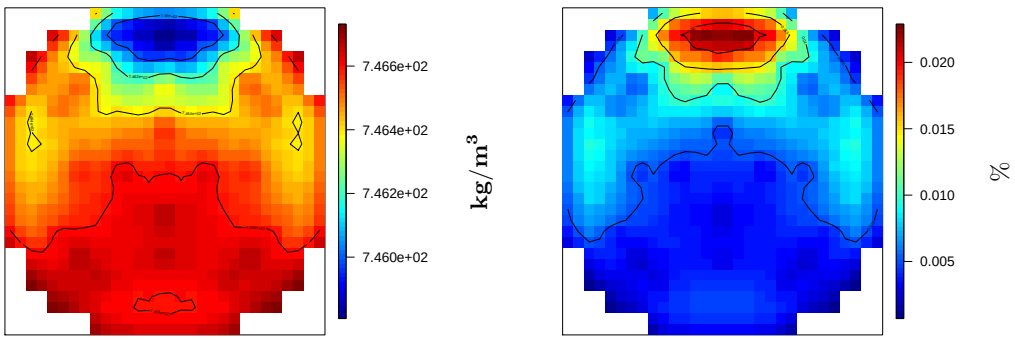

(a) Mean (b) Relative standard deviation

Figure F.28: D_w^{3D} estimated mean and relative standard deviation in the radial cross-section at $Z15$ for IBE with 3D and finer discretized thermal-hydraulic channels coupling study in PWR core.

- **Y16 cross-section**

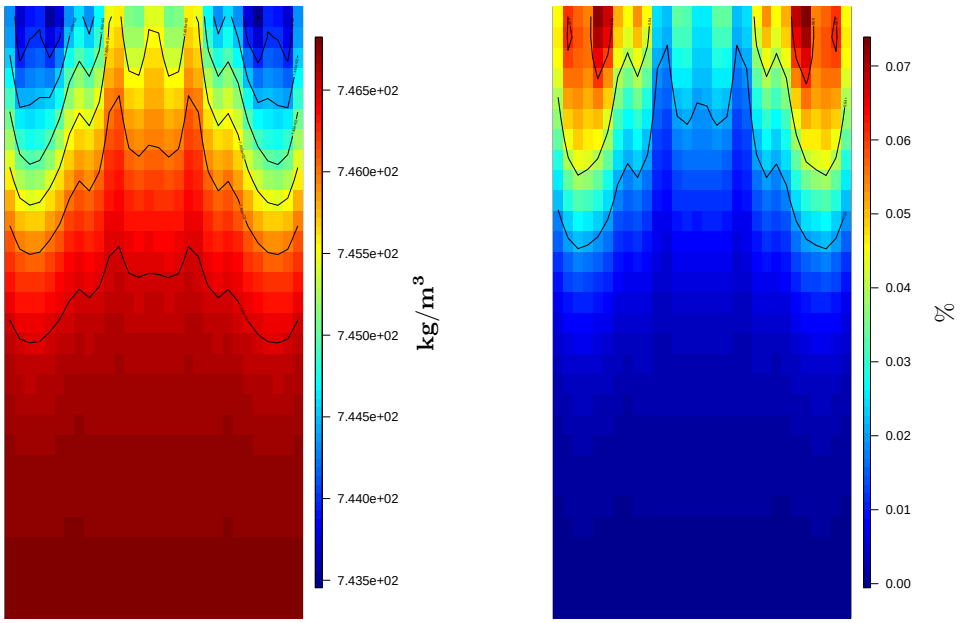

(a) Mean (b) Relative standard deviation

Figure F.29: D_w^{3D} estimated mean and relative standard deviation in the axial cross-section at $Y16$ for IBE with 3D and finer discretized thermal-hydraulic channels coupling study in PWR core.

- **Z30 cross-section**

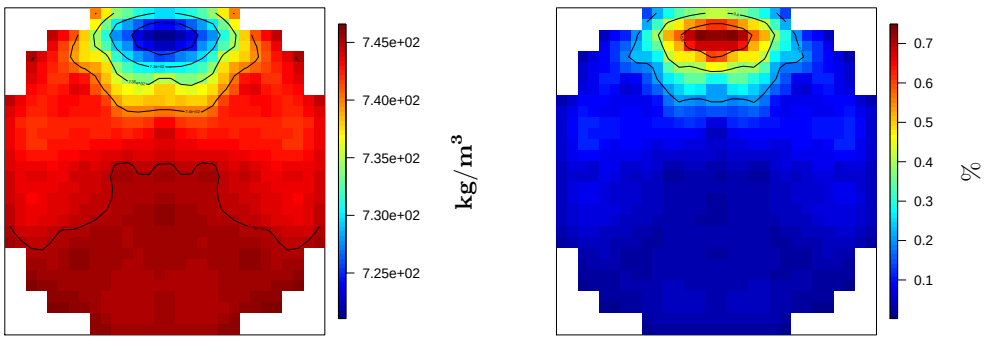

(a) Mean (b) Relative standard deviation

Figure F.30: D_w^{3D} estimated mean and relative standard deviation in the radial cross-section at $Z30$ for IBE with 3D and finer discretized thermal-hydraulic channels coupling study in PWR core.

In general for all the $3D$ fields one main difference arises from the fact that $Y3$ is at an assembly that is different from the one identified in Appendix E due to the finer discretization. We cannot thus make comparisons for this cross-section.

from investigating all the other cross-sections we can conclude that for all the $3D$ fields there is no significant impact of the 3D thermal-hydraulics modeling with finer radial discretization. The only main impact is at the cross-section of the maximum linear power that was presented in Section 4.7.4.

What is interesting is the fact the we managed to include large $3D$ fields in our Uncertainty Quantification Methodology. The are a total of 23160 meshes in each field increasing the difficulty of their treatment. As we are entering a world of Big Data and Machine Learning many perspectives open for the handling of such $3D$ fields. However, maybe the most important is first to assess in which situations we really need such large fields and what new can they bring on the table for industrial applications.

Résumé

Durant les dernières décennies, l'évolution de la puissance de calcul a conduit au développement de codes de simulation en physique des réacteurs de plus en plus prédictifs pour la modélisation du comportement d'un réacteur nucléaire en situation de fonctionnement normal et accidentel. Quand les phénomènes physiques les plus importants sont modélisés avec des approximations et hypothèses maitrisées, les modélisations sont qualifiés *Best Estimate* (BE). Le caractère BE implique la prise en compte des sources d'incertitudes sous la forme de biais et de variance. Un cadre d'analyse d'incertitudes cohérent avec l'utilisation de modélisations BE a été développé pour bien prendre en compte ces incertitudes. On parle d'approche *Best Estimate Plus Uncertainties* (BEPU) et cette approche donne lieu à de nombreux travaux de R&D à l'international en simulation numérique. L'étude BEPU d'un transitoire multi-physique avec fort couplage comporte de nombreux défis tant en modélisation physique qu'en analyse d'incertitudes. Les plus importants sont: les augmentations du temps de calcul et du nombre d'entrées-sorties associées au couplage multi-physique BE, les dépendances et interactions entre les entrées et les non-linéarités de comportement des sorties.

Dans cette thèse, on étudie la quantification d'incertitudes multi-physiques dans le cas d'un transitoire d'Éjection de Grappe de contrôle (REA- *Rod Ejection Accident*) dans un Réacteur à Eau Pressurisée (REP). Il s'agit d'un transitoire avec de forts effets de couplage entre les comportements neutronique, thermohydraulique et thermique du combustible. La modélisation BE actuellement disponible au CEA est réalisée en couplant les codes APOLLO3 ® (netronique) et FLICA4 (thermohydraulique-thermique du combustible) dans l'environnement SALOME/CORPUS.

Dans la première partie de la thèse, on examine différents outils statistiques disponibles dans la littérature scientifique dont la réduction de dimension, l'analyse de sensibilité globale, des modèles de substitution et la construction de plans d'expérience. On utilise ces outils pour aborder certains de ces défis prélistés pour finalement développer une méthodologie de quantification d'incertitudes pour une modélisation multi-physique BE d'un transitoire REA. On met l'accent sur deux points: la prise en compte des sorties fonctionnelles et la réduction de la dimension des entres pour faciliter la construction des modèles de substitution. Pour le premier point, des indices Shapley agrégés ont été utilisés pour l'analyse de sensibilité globale. Pour le deuxième, deux méthodes ont été développées. La première méthode a pour but d'identifier des sous-espaces des entrées importants par rapport aux différents sorties d'intérêt, basée sur des mesures de dépendance (indices HSIC). La deuxième méthode optimise des plans d'expérience *space-filling* dans l'espace complet des entrées et des sous-espaces important identifiés par la méthode précédente. Les modèles de substitution sont construits dans ces sous-espaces en incluant l'erreur de la réduction de dimension dans leur erreur d'approximation.

Dans la deuxième partie de la thèse, on améliore la modélisation du comportement du combustible. Un couplage *Best Effort* pour la simulation d'un transitoire REA est disponible au CEA. Il comprend le code ALCYONE V1.4 qui permet une modélisation fine du comportement thermomécanique du combustible. Cependant, l'utilisation d'une telle modélisation conduit à une augmentation significative du temps de calcul du transitoire REA ce qui rend actuellement difficile la réalisation d'une analyse d'incertitudes à partir d'une approche *Best Effort*. Pour cela, une méthodologie de calibrage d'un modèle analytique simplifié pour le transfert de chaleur pastille-gaine (Hgap) basée sur des calculs ALCYONE V1.4 découplés a été développée. L'incertitude du modèle est quantifiée basée sur l'erreur de calibrage en prenant en compte l'incertitude de l'état initial. Le modèle calibré est finalement intégré dans la modélisation BE pour améliorer sa prédictivité sans augmenter le temps de calcul. Cette modélisation est appelée IBE (*Improved Best Estimate*).

Les deux méthodologies développées sont maquettées initialement sur un cœur de petite échelle représentatif d'un REP puis appliquées sur un cœur REP à l'échelle 1 dans le cadre d'une analyse multi-physique d'un transitoire REA. Les conclusions des applications montrent que les entrées dominantes sont les

paramètres neutroniques: sections efficaces et fraction effective des neutrons retardés. L'écart à la crise d'ébullition est très sensible à la modélisation du Hgap. En améliorant sa modélisation et sa quantification d'incertitudes entre BE et IBE, l'importance du Hgap est fortement diminuée. Finalement, on a utilisé la modélisation IBE pour propager les incertitudes et effectuer une analyse de sensibilité globale sur des sorties fonctionnelles 3D.

Mots-clés: Quantification d'incertitudes, Couplage Multi-Physique, Éjection de Grappe (REA), Best Estimate Plus Uncertainty (BEPU)

université PARIS-SACLAY
ÉCOLE DOCTORALE
INTERFACES
Approches Interdisciplinaires : Fondements, Applications et Innovation

Titre : Développement d'une méthodologie de Quantification d'Incertitudes pour une analyse Mutli-Physique Best Estimate et application sur un Accident d'Éjection de Grappe dans un Réacteur à Eau Pressurisée

Mots clés : Quantification d'incertitudes, Couplage Multi-Physique, Éjection de Grappe (REA), Best Estimate Plus Uncertainty (BEPU)

Résumé : Durant les dernières décennies, l'évolution de la puissance de calcul a conduit au développement de codes de simulation en physique des réacteurs de plus en plus prédictifs pour la modélisation du comportement d'un réacteur nucléaire en situation de fonctionnement normal et accidentel. Un cadre d'analyse d'incertitudes cohérent avec l'utilisation de modélisations *Best Estimate* (BE) a été développé. On parle d'approche *Best Estimate Plus Uncertainties* (BEPU) et cette approche donne lieu à de nombreux travaux de R&D à l'international en simulation numérique. Dans cette thèse, on étudie la quantification d'incertitudes multi-physiques dans le cas d'un transitoire d'Éjection de Grappe de contrôle (REA- *Rod Ejection Accident*) dans un Réacteur à Eau Pressurisée (REP). La modélisation BE actuellement disponible au CEA est réalisée en couplant les codes APOLLO3 ® (netronique) et FLICA4 (thermohydraulique-thermique du combustible) dans l'environnement SALOME/CORPUS. Dans la première partie de la thèse, on examine différents outils statistiques disponibles dans la littérature scientifique dont la réduction de dimension, l'analyse de sensibilité globale, des modèles de substitution et la construction de plans d'expérience. On utilise ces outils pour développer une méthodologie de quantification d'incertitudes. Dans la deuxième partie de la thèse, on améliore la modélisation du comportement du combustible. Un couplage *Best Effort* pour la simulation d'un transitoire REA est disponible au CEA. Il comprend le code ALCYONE V1.4 qui permet une modélisation fine du comportement thermomécanique du combustible. Cependant, l'utilisation d'une telle modélisation conduit à une augmentation significative du temps de calcul ce qui rend actuellement difficile la réalisation d'une analyse d'incertitudes. Pour cela, une méthodologie de calibrage d'un modèle analytique simplifié pour le transfert de chaleur pastille-gaine basé sur des calculs ALCYONE V1.4 découplés a été développée. Le modèle calibré est finalement intégré dans la modélisation BE pour améliorer sa prédictivité. Ces deux méthodologies sont maquettées initialement sur un cœur de petite échelle représentatif d'un REP puis appliquées sur un cœur REP à l'échelle 1 dans le cadre d'une analyse multi-physique d'un transitoire REA.

Title : Development of an Uncertainty Quantification methodology for Multi-Physics Best Estimate analysis and application to the Rod Ejection Accident in a Pressurized Water Reactor

Keywords : Uncertainty Quantification, Multi-Physics coupling, Rod Ejection Accident (REA), Best Estimate Plus Uncertainty (BEPU)

Abstract : The computational advancements of the last decades lead to the development of numerical codes for simulating the reactor physics with increasing predictivity allowing the modeling of the behavior of a nuclear reactor under both normal and accidental conditions. An uncertainty analysis framework consistent with Best Estimate (BE) codes was developed in order to take into account the different sources of uncertainties. This framework is called Best Estimate Plus Uncertainties (BEPU) and is currently a field of increasing research internationally. In this thesis we study the multi-physics uncertainty quantification for Rod Ejection Accident (REA) in Pressurized Water Reactors (PWR). The BE modeling available in CEA is used with a coupling of APOLLO3 ® (neutronics) and FLICA4 (thermal-hydraulics and fuel-thermal) in the framework of SALOME/CORPUS tool. In the first part of the thesis, we explore different statistical tools available in the scientific literature including: dimension reduction, global sensitivity analysis, surrogate modeling and design of experiments. We then use them in order to develop an uncertainty quantification methodology. In the second part of the thesis, we improve the BE modeling in terms of its uncertainty representation. A Best Effort coupling scheme for REA analysis is available at CEA. This includes ALCYONE V1.4 code for a detailed modeling of fuel-thermomechanics behavior. However, the use of such modeling increases significantly the computational cost for a REA transient rendering the uncertainty analysis prohibited. To this purpose, we develop a methodology for calibrating a simplified analytic gap heat transfer model using decoupled ALCYONE V1.4 REA calculations. The calibrated model is finally used to improve the previous BE modeling. Both developed methodologies are tested initially on a small scale core representative of a PWR and then applied on a large scale PWR core.

Université Paris-Saclay
Espace Technologique / Immeuble Discovery
Route de l'Orme aux Merisiers RD 128 / 91190 Saint-Aubin, France